

THE ACCELERATED LIFE CYCLE TESTING AND MODELLING OF LI-ION CELLS
USED IN ELECTRIC VEHICLE APPLICATIONS

BY

CLAIRE ANGELA ROSSOUW
STUDENT NUMBER: 20001542

Submitted in fulfilment of the requirements for the degree of Masters in Science in
the Faculty of Chemistry at the Nelson Mandela Metropolitan University

January 2012

Supervisor: Dr E.E. Ferg
Co-Supervisor: Prof P. Loyson

Abstract

Li-ion batteries have become one of the chosen energy storage devices that are used in applications such as power tools, cellular phones and electric vehicles (EV). With the demand for portable high energy density devices, the rechargeable Li-ion battery has become one of the more viable energy storage systems for large scale commercial EVs because of their higher energy density to weight or volume ratio when compared to other current commercial battery energy storage systems.

Various safety procedures for the use of Li-ion batteries in both consumer and EV applications have been developed by the international associations.

The test procedures studied in this dissertation demonstrated the importance of determining the true capacity of a cell at various discharge rates. For this, the well known Peukert test was demonstrated. The study also showed that cells with different battery geometries and chemistries would demonstrate different thermal heating during discharge and slightly different Ragone results if different test methods were used as reported in the literature. Accelerated ageing tests were done on different cells at different Depth-of-Discharge (DoD) regions. The different DoD regions were determined according to expected stresses the electrode material in a cell would experience when discharged to specific DoD that follows the discharge voltage profile. Electrochemical Impedance Spectroscopy (EIS) was used to measure various electrochemical changes within these cells. The EIS results showed that certain observed modelled parameters would change similarly to the ageing of the cell as it aged due to the accelerated testing. EIS was also done on cells at different State-of-Charge (SoC) and temperatures. The results showed that EIS can be used as an effective technique to observe changes within a Li-ion cell as the SoC or temperature changed.

For automotive vehicles that are powered by a fuel cell or battery, a supercapacitor can be coupled to a battery in order to increase and optimize the energy and power densities of the drive systems. A test procedure in the literature that evaluated the use of capacitors with Pb-acid batteries was applied to Li-ion type cells in order to quantify the increased power due to the use of a supercapacitor with a Li-ion cell. Both a cylindrical LiCoO₂ cell and a VRLA Pb-acid cell showed some additional charge acceptance and delivery when connected to the supercapacitors. A LiMn₂O₄ pouch cell showed significant charge acceptance and delivery when connected to

supercapacitors. The amount of additional charge acceptance and delivery of the different combinations could be explained by EIS, in particular, the resistance and capacitance of the cell in comparison to the combination of the cell and supercapacitor. A large capacity LiCoO_2 cell showed high charge acceptance and delivery without connection with a supercapacitor. The study proved that EIS can be used to model the changes within cells under the different conditions and using different test procedures.

Acknowledgements:

1. My Lord and Saviour Jesus Christ, for the strength and knowledge to complete this study.
2. Dr Ferg for the continuous support and drive throughout this study.
3. Prof Loyson for his guidance and suggestions in this study.
4. HySA Systems and the Nelson Mandela Metropolitan University for the financial contribution.
5. Dr W. Fuls from Optimal Energy for all the advice and guidance during this study.
6. Willard Batteries for the use of some of the channels of their Battery Tester. Without this assistance some of the tests would not have been completed in time.
7. My husband, Riaan, and our parents for all the love, support and patience during this study.
8. Charmelle Snyders for assistance and encouraging words.
9. WetTest for internet usage and printing of relevant journal papers, reports and dissertation copies.

Related publications by the Author:

Parts of this work were presented at:

1. The 40th SACI National Convention conference in Johannesburg, South Africa, January 2011.

Titled: Testing Procedures of Lithium-ion batteries for use in EV applications.

CA Rossouw, EE Ferg and P. Loyson

2. The International Battery Association conference in Cape Town, South Africa, April 2011.

Titled: Testing of batteries with supercapacitors for EV applications. CA

Rossouw, EE Ferg and P. Loyson

3. The Advanced Automotive Battery Conference in Mainz, Germany, June 2011.

Titled: The DoD window cycle testing of Lithium-ion cells used in EV

applications. CA Rossouw, EE Ferg, P Loyson and W. Fuls

Declaration:

I, Claire Angela Rossouw (20001542) hereby declare that the dissertation for the degree of Magister Scientiae (Chemistry) is my own work and that it has not been previously submitted for assessment or completion of any postgraduate qualification to another University or for another qualification.

Mrs. C.A. Rossouw

Table of Contents

CHAPTER 1:	- 1 -
Introduction	- 1 -
1.1. Lithium – element properties and applications.	- 1 -
1.2. History of lithium-ion batteries and other rechargeable battery chemistries.	- 2 -
1.3. Chemistry of Lithium-ion cells:	- 7 -
1.4. Lithium-ion crystal structure and movement of ions mechanism	- 8 -
1.5. Future Lithium-ion cell development.....	- 16 -
1.6. Limitations to Lithium-ion batteries	- 17 -
1.6.1. Failure mode due to the Solid Electrolyte Interface (SEI):.....	- 18 -
1.6.2. Failure due to thermal conditions.	- 20 -
1.7. Lithium-ion cell testing:.....	- 21 -
1.7.1. Capacity fade due to Calendar life or Cycle life losses:	- 22 -
1.7.2. Techniques available for testing of ageing effects:	- 24 -
1.8. Supercapacitors	- 30 -
1.9. Test procedures focused on in this study.	- 32 -
1.9.1. Review and some theoretical considerations of the electrochemical testing procedures:.....	- 33 -
1.9.1.1. Peukert tests:.....	- 33 -
1.9.1.2. Ragone Tests:.....	- 35 -
1.9.1.3. Electrochemical Impedance Spectroscopy (EIS):	- 37 -
1.9.1.4. Batteries with Supercapacitors tests:	- 50 -
1.10. Workshops on Lithium-ion batteries and literature review:	- 51 -
1.10.1. Workshop presented by Walter van Schalkwijk. July 2010, Cape Town, South Africa	- 51 -
1.10.2. SACI ElectrochemSA workshop IV was presented by various speakers. February 2011, Port Elizabeth, South Africa.....	- 55 -
1.10.3. The International Battery Association (IBA) conference, April 2011, Cape Town, South Africa.....	- 56 -
1.10.4. The Advanced Automotive Battery Conference (AABC). June 2011, Mainz, Germany	- 57 -
1.11. Literature Review:	- 61 -
1.12. Objectives of this Dissertation:.....	- 69 -
CHAPTER 2:	- 71 -
2.1. The instrumentation.....	- 71 -
2.2. Experimental procedures	- 71 -
2.2.1. Peukert Tests:.....	- 73 -
2.2.1.1. Cautions that need to be considered with the Bitrode Tester:.....	- 73 -

2.2.2. Ragone Tests:.....	- 74 -
2.2.3. DoD window tests:	- 76 -
2.2.4. Electrochemical Impedance Spectroscopy (EIS):	- 77 -
2.2.4.1. Caution required for EIS analyses:	- 77 -
2.2.4.2. Calibration:.....	- 78 -
2.2.5. High rate charge & discharge tests using supercapacitors and Li-ion cells and Pb-acid cells.....	- 79 -
CHAPTER 3:	- 87 -
Peukert and Ragone Tests on Li-ion cells.....	- 87 -
3.1. Peukert Test.....	- 87 -
3.1.1. Peukert Test with Temperature Results for the 20Ah Pouch cell and 2Ah cylindrical cell:.....	- 88 -
3.1.2. Peukert Test with Temperature Results for the 1Ah pouch cell	- 96 -
3.2. Ragone Tests	- 98 -
3.2.1. 2Ah Li-ion constant current & constant Power Method Results:	- 98 -
3.2.2. 20Ah Li-ion constant current & constant power method results:	- 100 -
3.2.3. 5Ah Pb-acid constant current & constant power method results:.....	- 102 -
3.2.4. Comparison of the different chemistry cells using the different Ragone test methods:	- 103 -
CHAPTER 4:	- 107 -
Electrochemical Impedance Spectroscopy on Li-ion cells.....	- 107 -
4.1. EIS study of Li-ions cells at various temperatures and State of Charge:.....	- 114 -
4.1.1. 20Ah pouch cell at different States-of-Charge (SoC)	- 114 -
4.1.2. 1Ah pouch cell at different SoC.....	- 120 -
4.1.3. 2Ah cylindrical cell at different SoC.....	- 126 -
4.1.4. 20Ah pouch cell at different Temperatures	- 133 -
4.1.5. 1Ah pouch cell at different Temperatures	- 138 -
4.1.6. 2Ah cylindrical cell at different Temperatures	- 143 -
4.2. Capacity Ageing tests together with EIS:	- 150 -
4.2.1. 20Ah Li-ion pouch cell capacity ageing results:	- 150 -
4.2.2. 2Ah Li-ion cylindrical cell capacity ageing results:	- 169 -
CHAPTER 5:	- 183 -
Supercapacitors connected to Li-ion cells and a comparison with Pb-acid cells -	183 -
5.1. 2.4Ah Li-ion cylindrical cell with two 10F Supercapacitors	- 186 -
5.2. 5.21Ah VRLA Pb-acid cell with two 10F supercapacitors.....	- 195 -
5.3. 1Ah Li-ion pouch cell with two 3.3F supercapacitors	- 206 -
5.4. 20Ah Li-ion pouch cell.....	- 213 -
CHAPTER 6:	- 216 -

Conclusion	- 216 -
References	- 220 -

List of abbreviations

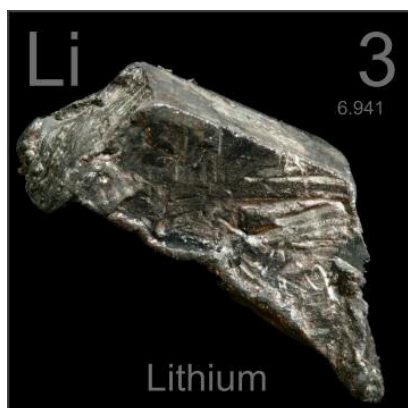
Li-ion	Lithium ion battery
NiCd	Nickel Cadmium battery
NiMH	Nickel Metal Hydride battery
Pb-acid	Lead-acid battery
VRLA	Value regulated Lead-acid battery
EV	Electric Vehicle
HEV	Hybrid Electric Vehicle
PHEV	Plug-in Hybrid Electric Vehicle
SEI	Solid Electrolyte Interface
DoD	Depth-of-Discharge
SoC	State-of-Charge
EIS	Electrochemical Impedance Spectroscopy
Z	Impedance (real and imaginary)

CHAPTER 1:

Introduction

1.1. Lithium – element properties and applications.

Lithium is alkali metal with many versatile uses.



Electron Configuration: [He]2s¹

Atomic Weight: 6.941 g/mol

Density: 0.535 g/cm³

Melting Point: 180.54 °C

Boiling Point: 1342 °C

Lithium does not exist in nature in its metallic form and is found in small quantities in a range of ores of igneous rocks and in salts from mineral springs or sea water as lithium salts.

It was first discovered by a Brazilian chemist José Bonifácio de Andrada e Silva in 1800 in a mine on the island of Utö, Sweden¹. It was only in 1817 that Johan A. Arfvenson, then working as a chemist, detected the presence of the new element when analysing petalite ore.

The usefulness of the material in various applications came about only in the middle of the 19th century, where it is now commonly used in applications such as Li-ion primary and rechargeable batteries, coolant in nuclear breeder reactors, lithium carbonate as a mood-stabilizing drug; lithium chloride and bromide are used as desiccants and lithium stearate as an all-purpose high-temperature lubricant. Lithium is a strong oxidizing agent². Metallic lithium will react with nitrogen, oxygen and water vapour in the air. Lithium hydroxide represents a potentially significant hazard as it is extremely corrosive. This will limit the use of metallic lithium in most applications. The main lithium compound used in applications is lithium hydroxide. These applications include the pottery industry and in medicine as antidepressant³.

1.2. History of lithium-ion batteries and other rechargeable battery chemistries.

The very first voltage-producing systems used only as demonstrations go back to Galvani, Volta, Daniell and Bunsen during the late 1800s. In 1860, the Frenchman Gaston Planté invented the first version of a rechargeable battery –based on the chemistry of lead and lead dioxide in sulphuric acid⁴. Scientific progress and applications of the energy storage systems came about in the 1900s. At first only primary cells such as manganese dioxide-zinc cells, the wet Leclanché, dry zinc-carbon cells and NiCd (Nickel Cadmium) were developed in different sizes and shapes and were used in many home applications. A leap in technology was then seen around the 1960s leading to the more powerful alkaline manganese dioxide-zinc cells that were being used for flashlights and electronic devices. These cells showed good shelf life and were able to operate in hot typical climates⁵.

The first published research work carried out in the field of Li-ion primary battery began with the work of Harris in 1958. This work eventually led to the development and commercialization of a variety of primary lithium cells during the 1970s. Some of the chemistries that were studied included the lithium/sulfur dioxide (Li/SO₂), lithium-thionylchloride (Li/SOCl₂) and lithium-manganese dioxide (Li/MnO₂) to name a few. During the 1980s, many attempts to develop a rechargeable lithium battery were undertaken; the difficulties of the early rechargeable batteries were the recharging step of the metallic lithium anode: this led to safety issues that resulted in cells exploding and burning. These issues were due to the reactivity of the metallic lithium (especially electrodeposited lithium with the electrolyte solutions) which resulted in dendrite formation which often pierced the separator. The piercing of the separator allowed the electrodes to be in contact with each other, which caused short circuits. The reactions of the lithium electrode were studied and a number of strategies were developed in order to modify the reactivity of the Li-solution interface and thus improve its utility and safety. The first high-rate Li-ion cells manufactured burned down a Sony factory, as very little was known about charging the cells, what caused dendrite formation and why there was oxygen evolution from the cathode. Very little was known at the time about thermal management.

Further research of the anode material saw the move from metallic lithium to a carbon/graphite anode material. During that time Steele investigated the use of

graphite and layered sulfide TiS_2 instead of the metallic lithium anodes. The metallic lithium anodes showed safety concerns. These new Li alloy anodes were seen as potential candidates for anode electrodes of the Li-ion battery based on non-aqueous liquid electrolytes⁶. Carbon/Graphite as an anode material was investigated as it proved to have many more advantages such as it is mildly oxidised by oxygen, carbon dioxide or ozone. Metals and metal oxides can be deposited onto the graphite layer such as aluminium, silver, copper and its oxides. These composites as anode materials show considerably improved electrochemical performance⁷. Lithium intercalation occurs between carbon planes up to a maximum ratio of one Lithium atom to six carbon atoms⁶. It has been found that excess charge is consumed during the first charge. Unlike metallic lithium, there is no further irreversible loss⁶. During the initial charging cycle, a thin protective Solid Electrolyte Interface (SEI) is formed on the anode. This SEI layer insignificantly limits the ability of the Li-ions to freely move through the anode pores, but reduces some of the charging ability of the cell. Metallic lithium anodes were at this stage known to form these dendrites during charging which led to short circuits within the cell which could lead to smoke and fires.

Further research into the cathode materials was carried out by Whittingham, who reviewed the properties and preparation of many insertion compounds and discussed their intercalation reaction⁶. The most common chemistries that were discussed at the time included the V_2O_5 , V_6O_{13} and MnO_2 cathode materials. Some years later other transition metals were investigated for the cathode electrodes: these included Ni, Co or Mn. These are common metals used today in LiMO_2 where $\text{M} = \text{Ni, Co and/or Mn}$. At about that time the concept of a Li-ion cell was tested in a laboratory with two insertion electrodes cycling Li ions between them.

During the late 1970s and early 1980s, rechargeable lithium batteries were developed. The first cells using lithium insertion compounds as positive electrodes appeared when Exxon and Moli Energy tried to commercialise the Li/TiS_2 and Li/MoS_2 systems respectively. These were low voltage units with an operating voltage of less than 2V. During the 1990s, a lot of research went into advanced battery systems based upon the insertion and removal of Li ions into host compounds serving both electrodes. In 1991, Sony introduced the first commercial Li-ion cell based on C/LiCoO_2 . The cells had an open circuit potential of 4.2V and an operational voltage of 3.6V.



These first designs by Sony of a Li-ion battery were known as the 18650 cell; meaning a cell that is 65mm in length and has a diameter of 18mm⁸.

Figure 1.1 Li-ion 18650 cell design.

Another cell design that was and is still used in small portable consumer applications such as PDAs, watches, camcorders, digital cameras and many others is the coin cell design.



Figure 1.2. Li-ion coin cell design.

The coin cells were developed to give relatively good energy density with an average voltage of about 3V. These cells are able to maintain their higher voltage for a longer period of time when compared to similar alkaline cells.

They were used for typical memory back-up power supply in computer systems.

Soon the rechargeable coin Li-ion cell was replacing the NiCd battery. These cells had excellent charge/discharge cycle characteristic with long-term reliability⁹.

Another system that was developed for use as a rechargeable battery was the Nickel-Metal-Hydride (NiMH) battery. The NiMH chemistry replaced most applications where NiCd batteries had previously been used. The NiMH is a commercially important rechargeable battery both for the consumer and for industrial applications where these cells have some good design flexibility, excellent power and energy densities, few environmental and recyclable concerns and currently, a lower cost per unit due to their high production volume¹⁰.

When considering rechargeable batteries, the Pb-acid battery chemistry has been around for many decades. Pb-acid batteries have important applications in the automotive industry as starting, lighting and ignition (SLI) batteries. Their application as traction (propulsion) batteries are currently used to power golf carts, forklifts and modern hybrid electric vehicles (HEV) such as the Honda Civic in the USA. However these batteries have low energy-to-weight and low energy-to-volume ratios which makes them unfavourable for full electric vehicles (EV) as the weight and volume of the batteries needed to be as low as possible¹¹.

The rechargeable Li-ion battery has become one of the more viable energy storage systems for commercial EV because of their higher energy density to weight or

volume ratio when compared to other battery energy storage systems¹². In a paper in 1996, the US Department of Energy predicted a power density goal of 1.7kW/kg for the automotive industry¹³. The batteries have on average a higher cell voltage per cell when compared to other battery systems and have shown to be able to discharge a relatively high rates providing on average between 500 to 1000 full discharge/charge cycles under ambient conditions. Li-ion batteries do not suffer from capacity “Memory effects” that are common with NiMH batteries nor from any electrode sulphation due to partial state of capacity cycling experienced with Pb-acid batteries. However, some of the disadvantages of typical Li-ion cells include their need for over discharge or over charge protection, the use of organic electrolyte, improved thermal safety and longer cycle life. Some of the main research focus involves changing the chemistry of the electrodes by combining different transition metals in order to improve the thermal safety and cycle life¹².

In figure 1.3, a comparison is made between the different energy densities vs. power densities for the different energy storage devices. The different energy storage devices discussed include various battery chemistries such as Pb-acid, NiCd, Li-ion as well as capacitors. The Pb-acid, NiCd and Li-ion are the most commercially available battery types. In terms of their power densities, an increase is seen from left to right, with the Li-ion having the highest power density and the Pb-acid battery having the lowest power density. However the capacitors show a greater power density than all the battery types. A change in energy density is also seen with the batteries, where Li-ion shows the greatest battery energy density and Pb-acid having the lowest energy density. The ultracapacitor (capacitor having a capacitance of more than 1 Farad) showed a similar energy density to the Pb-acid battery, but lower than the Li-ion and NiCd batteries. An ordinary capacitor showed the lowest energy density of all the energy storage devices. In the EV market, a battery that has the highest energy to weight ratio is required. A combination of a high energy density battery together with a high power density supercapacitor is also being investigated in order to make use of each device’s advantage. The time, in hours, (Figure 1.3) illustrates how fast the energy storage device discharges, with the capacitors showing a fast discharge in comparison to the battery systems that would take longer to discharge.

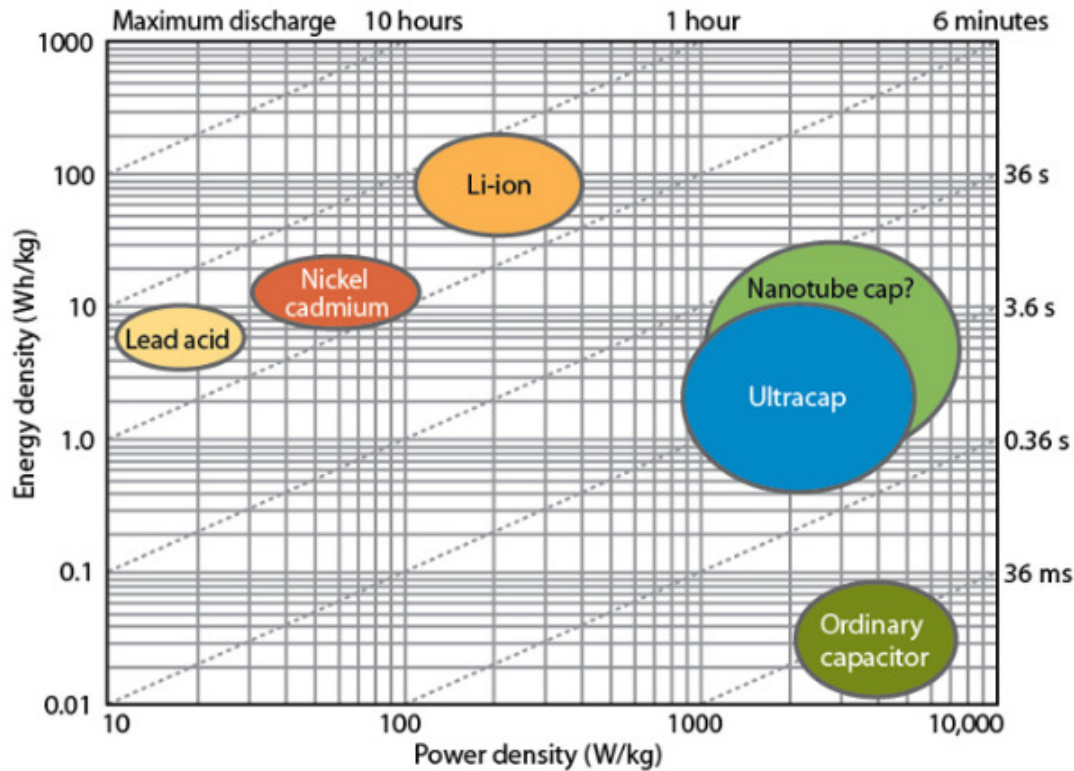


Figure 1.3. Energy vs. power densities of the different battery chemistries and supercapacitors¹⁴.

In the present global energy economy, the need for fossil fuels as the main form of fuel and energy has increased significantly, where their demand has outstripped their supply. Unfortunately there is a limit to these fossil fuels that has led to the need for alternative and renewable energy sources in order to sustain the current global energy demands. There has also been evidence that the increasing level of atmospheric CO₂ that results from the combustion of fossil fuels has a detrimental effect on the environment in terms of global warming¹⁵. As part of the requirements for alternative renewable energy sources, energy storage devices such as batteries form a crucial part especially with the introduction of Hybrid Electric Vehicles (HEV) and Electric Vehicles (EV). A HEV or Plug-In Hybrid Electric Vehicle (PHEV) entails that a vehicle is driven by both an electric motor powered by a battery and/or supercapacitor, as well as an internal combustion engine (petrol or diesel). An EV would be considered as solely driven by an electric motor and powered by a battery and/or supercapacitor. The different hybrid vehicles can be further classified according to cost savings, longer distance range and include functions such as stop-start and regenerative braking¹⁶.

1.3. Chemistry of Lithium-ion cells:

The half cell reduction potential (which occurs at the cathode of a cell) of a Li-ion cell can be described as:

$\text{Li}^+ (\text{aq}) + \text{e}^- \rightarrow \text{Li} (\text{s})$ with a Standard Reduction Potential (E°) of -3.04V.

In an electrochemical cell, an electric potential is created between two dissimilar substances. This potential is a measure of the energy per unit of charge which is available from the oxidation/reduction reactions to drive the reaction and can be expressed by the well known Nernst Equation in terms of the standard cell potential, temperature and species concentration¹⁷.

$$E = E^\circ - \frac{RT}{nF} \ln Q$$

In this equation E = total energy of the system, E° = the standard cell potential, R = Gas constant which is 8.314 (volt/coulomb)/(mol-K), T = Temperature in Kelvin, n = no of moles of electrons exchanged in the electrochemical reaction, F = Faradays constant, which is 96500 coulombs/mol and Q = reaction quotient, which are the equilibrium concentrations of the participating chemical species⁵.

When looking at battery chemistry in particular the values of temperature and the redox materials play an important role in the cell type to give sufficient energy density so as to be commercially viable. In order for cathode materials to be suitable for Li-ion cells, the material must accept and release the Li-ions repeatedly and quickly in order to ensure recharging and high current capability¹⁸. The cathode material must remain thermally stable for its application. Further important properties of a cathode material include oxidative stability and conductivity. LiCoO_2 for example has been shown to be relatively oxidative unstable in comparison to LiFePO_4 . However LiFePO_4 , in comparison, is seen to be relatively poorly conductive when compared to LiCoO_2 . Thus research is being carried out in order to improve these properties by combining different transition metals in certain ratios¹⁹.

1.4. Lithium-ion crystal structure and movement of ions mechanism

A wide range of possible cathode materials for Li-ion cells has been studied. However, only a few have shown any significant commercial value. The suitable cathode materials can be grouped into the 3 most common crystal structural classes:

- Olivine – 1D structure²⁰. 1D meaning that the Li-ions move in one direction.

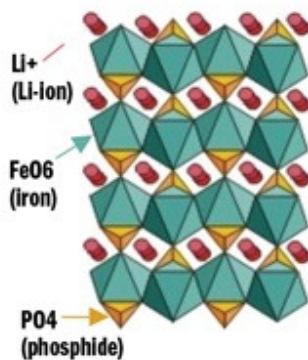


Figure 1.4. Olivine crystal structure

Examples of cathode material that have this structure include: LiFePO_4 , $\text{LiAlFe(PO}_4)_2$ and LiMnPO_4

- Layered crystal structure – 2D structure²⁰. The Li-ions in a 2D structure are able to move along the plane in two directions.

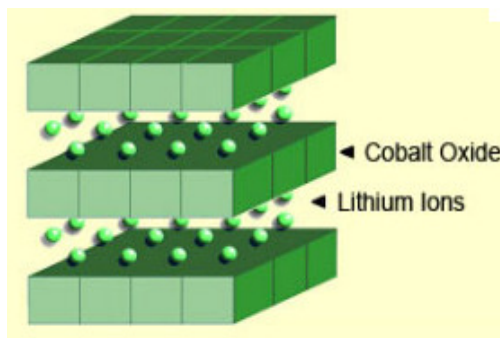


Figure 1.5 Layered crystal structure

Examples of cathode material that have this structure include: LiCoO_2 , $\text{LiNi}_{1/3}\text{Mn}_{1/3}\text{Co}_{1/3}\text{O}_2$ and $\text{LiNi}_{0.8}\text{Co}_{0.15}\text{Al}_{0.05}\text{O}_2$

- Spinel – 3D structure²⁰. Due to the 3D structure the Li-ions are able to move in 3 directions, i.e. along the x, y and z-axis planes.

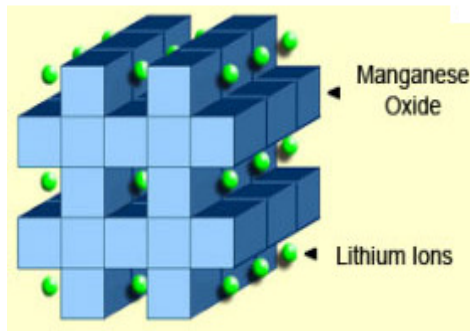
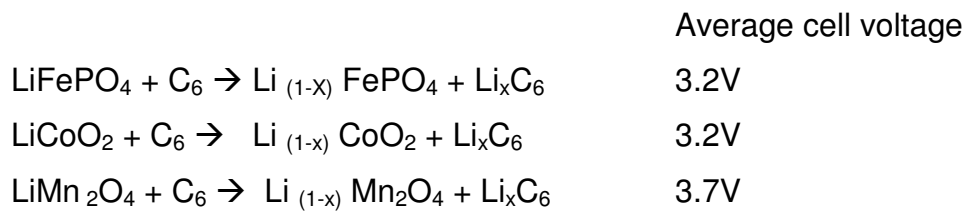


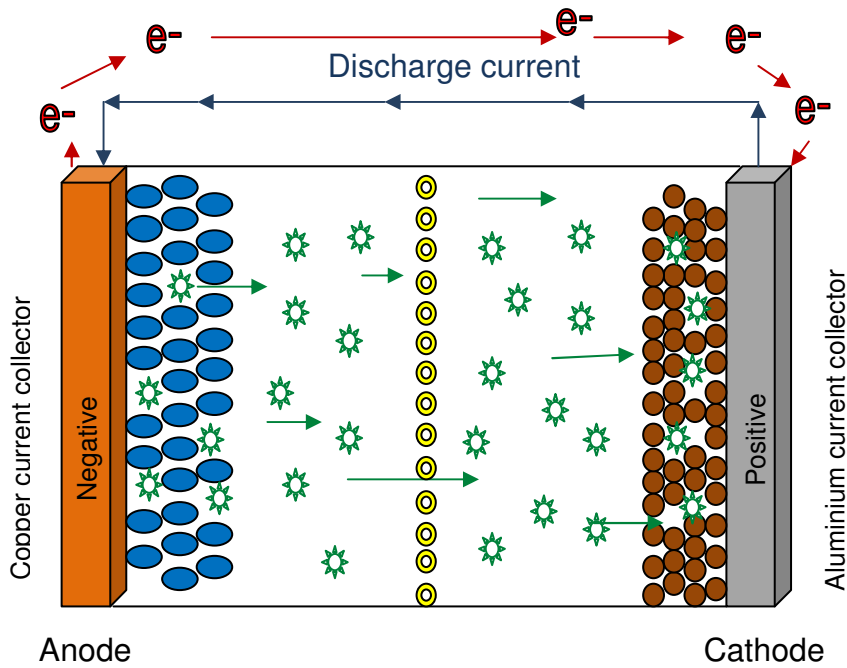
Figure 1.6 Spinel crystal structure

Examples of cathode material that have this structure include: LiMn_2O_4 and $\text{Li}_7\text{Ti}_5\text{O}_{12}$

During the charge and discharge processes, the Li ions are reversibly intercalated between the cathode and the anode as they pass through the electrolyte. During charging, Li ions move from the cathode via the electrolyte through the separator and fill the pores in the anode layer. The opposite is true for discharging. The overall cell reaction can be described by J Li, E Murphy, J Winnick, PA Kohl²¹ and is shown graphically in figure 1.7:



During Discharge reaction:







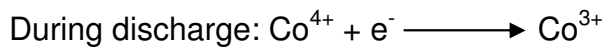
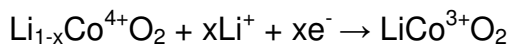
-  Li⁺ ions
 -  Separator
 -  Cathode consisting of Cobalt and oxygen ions
 -  Anode consisting of graphite
- Clear space – organic electrolyte

Figure 1.7a Diagram showing the discharge mechanism of a Li-ion cell.

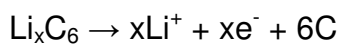
Electrons and Li-ions move from the anode to the cathode during discharging.



Reduction occurs at the cathode and Li-ions move from the negative electrode (anode) to the positive electrode (cathode).



Oxidation occurs at the anode



Charging reaction:

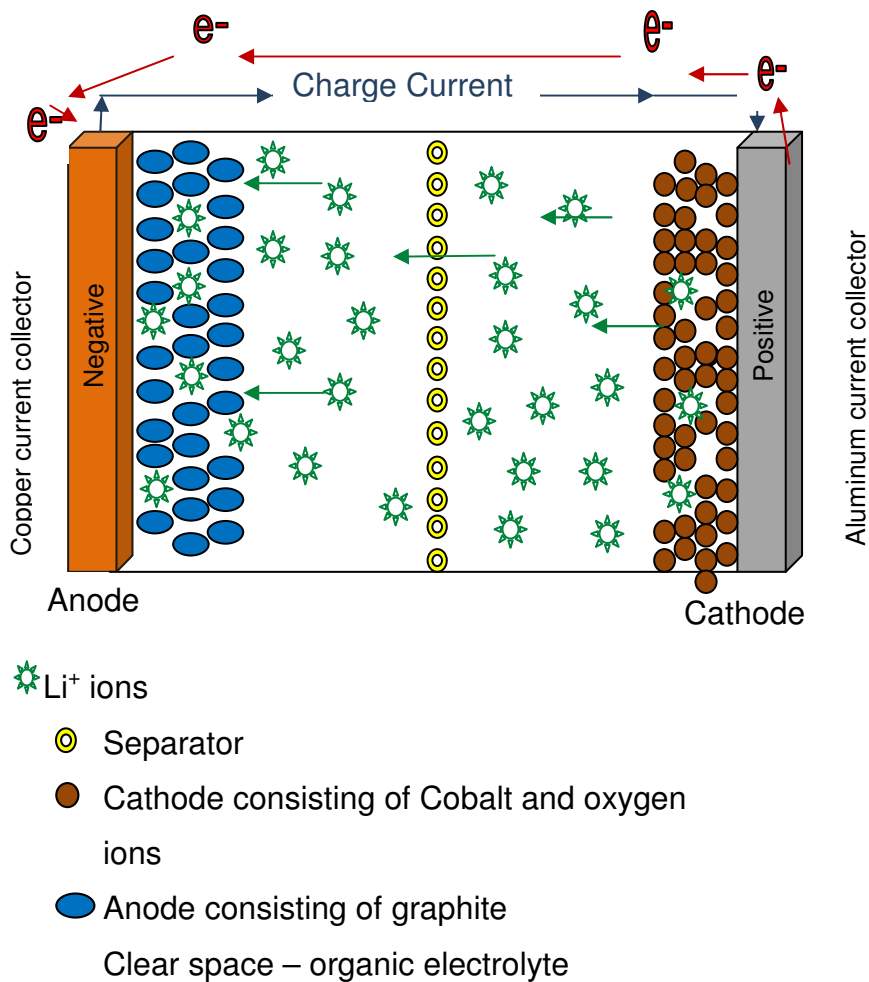
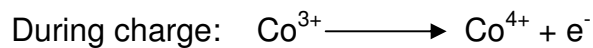


Figure 1.7b Diagrams showing the charge mechanism of a Li-ion cell.

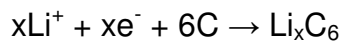
Electrons and Li-ions move from the cathode to the anode during charging.



Oxidation occurs at the cathode and Li-ions move from the positive electrode (cathode) to the negative electrode (anode).



Reduction occurs at the anode



The anode electrode is usually formed from graphite. Graphite has advantages over other anode materials, such as metallic lithium or carbon, due to its relatively high specific capacity, low relative constant voltage plateau and low cost. Some disadvantages of graphite include the fact that graphite is sensitive to electrolyte solvent uptake; there is a risk of Lithium plating onto its surface and it has a limited charging rate at low temperatures. A copper current collector is used with the anode. Copper is used as dendritic formation allows for better adhesion of the graphite onto the copper current collector²².

The separator for Li-ion cells is a porous membrane which is used to prevent the physical contact between the anode and the cathode in the cell. However it is porous in order to allow sufficient ionic transport of the Li-ions. Commonly used separators used include cellulose, glass fiber which are non-woven materials; inorganic composite membranes such as Separion[®] and microporous polymer membranes such as polyolefines (polyethylene and polypropylene). Considerations made when choosing a separator include: cost, porosity, a thermal shut-down mechanism, electrolyte uptake and electrolyte wetting. No separator commercially available meets all considerations. Binders are also included within the Li-ion cell. Binders work as an adhesive but flexible link between the electrode particles. Various binders include: Teflon, Polyvinylidene difluoride (PVdF) based binders and Sodium Carboxymethylcellulose (CMC)²².

When electrolytes are chosen for use in Li-ion cells, there are a few priorities that the electrolyte needs to meet. These priorities include an electrolyte that supports the formation of effective interphases within the cell; it contributes to the cell safety and conducts the Li-ions well. It must protect against irreversible material and charge losses, however minimal losses will always be experienced. The electrolyte also needs to be conductive and of a certain viscosity to ensure wetting. A common electrolyte salt used in Li-ion cells is LiPF₆. However due to thermal and chemical instability, this electrolyte salt will need to be replaced. A possible replacement for this salt would include Partially Fluorinated Solvents such as fluoro ethylene carbonate (FEC). The advantages of FEC include a good wetting ability, low temperature performance and low flammability. However FEC is relatively costly and recycling of the material is limited. Electrolyte additives can also be added to the electrolyte in order to improve anode passivation, cathode protection, overcharge protection, flame retardation and improvement of the electrolyte conductivity²². Any

moisture in the Li-ion cell will react with the electrolyte salt LiPF_6 resulting in HF acid. This HF will cause damage to the separator, electrodes and current collectors resulting in short circuits. For this reason aqueous electrolytes cannot be used in Li-ion cells⁸.

The cathode electrode in Fig 1.7 consists of LiCoO_2 material. Various other cathode materials can be found as the cathode material. Cobalt material is selected due to its relatively high capacity and flat voltage range. Due to its small atomic size, cobalt is lighter than some other transition metals, which allows for a better energy density for the cell. However cobalt is relatively expensive and the trend shown by industry indicates that Li-ion cells in future will be manufactured with less cobalt and more nickel. LiCoO_2 cells have shown stability deterioration during cycling as well as some thermal instability. Thus nickel is used to dope the cathode material which ensures better stability. The other cathode materials commonly used in Li-ion cells include: LiMn_2O_4 and LiFePO_4 . The advantages of using Li-ion cells containing LiMn_2O_4 cathode material include: low cost of manufacturing the cells, the cells are able to work at high voltages and produce high power. These cells are also relatively thermally safe. However this cathode material has a low calendar and cycle life when a graphite anode layer is used. The manganese contaminates the Solid Electrolyte Interface layer of the anode due to dissolution of Mn^{x+} at higher temperatures. The LiMn_2O_4 cathode material also has a low capacity and lower specific energy values. The LiFePO_4 cathode material shows excellent thermal and electrochemical stability. This material has a good cycle life when cycled at room temperature and high rate capability. However this cathode material only cycles at low voltages and the manufacturing of this material is more difficult which results in high manufacturing costs. Various blends of transition metals for use in the cathode material are being researched. The current collector for the cathode material is aluminium²².

The different cell chemistries each have a set of charge and discharge voltage limits also referred to as the working voltage window. For example the chemistry of LiCoO_2 has a limit of 3.0V to 4.2V. Overcharging or over-discharging outside these voltage windows will result in abuse of the cell. This abuse can occur accidentally or intentionally. Further abuse of the battery will result in the electrolyte continuing to reduce at the unprotected cathode. A phase transition occurs and the structure of the unit cells of the material begins to change. Resulting in pores on the electrode becoming inaccessible which leads to accelerated cell failure¹². During the initial

manufacturing of Li-ion cells, the cell is allowed to undergo a charge and discharge regime in order for a formation of a protective film to be deposited onto the anode surface. This film also known as the Solid Electrolyte Interface (SEI), allows for stability of the cell during continuous charge and discharge cycles in typical applications.

Within the voltage window, discussed previously, lie three regions that will influence the stresses within the cell during cycle testing. The greatest stress lies near the voltage limits of the cell. Each region will have an effect on the amount of stress that the cell will undergo. The stresses can be defined as decreasing the cathode material particle size. This decrease in particle size will result in narrowing of the miscibility gap between the lithiated and delithiated phases and a decrease in the equilibrium potential hysteresis²³. This will result in an increase in internal impedance of the cell, resulting in a decrease in overall capacity.

During cycling within the normal voltage window, the active material of the electrodes in the battery can undergo changes for three reasons: (i) Expansion and contraction of the host materials due to lithium intercalation, (ii) Electrode volume increase caused by irreversible reaction deposits, and (iii) Dead volume and pressure changes within the cell case depending on the battery structure and construction. The volume thickness of the active material due to the expansion and contraction results from changes within the graphite and lithium transition metal oxide structures. Expansion of the graphite layer is more pronounced than the lithium transition metal oxide layer. This expansion of the graphite layer can greatly vary depending on the structure of the graphite. In some cases, the natural graphite can change its unit cell volume by as much as three times more than the lithium transition metal oxide. These changes are more pronounced in a cell made by the strip-wound process than the stacked-design²⁴.

The three areas of stress that the electrode active materials in the cell can experience during a typical discharge voltage step in a LiCoO₂ cell can be described as certain Depth of Discharge (DoD) window regions on the curve (Fig 1.8). These include the low DoD that corresponds to the voltage region of 3.94V to 4.2V. The active material in this region would typically experience a middle stress region because of the high end cell voltage where damage to the cathode material can take place. The middle DoD window region would correspond to a voltage region of 3.58V to 3.94V, where minimal active material expansion occurs as the ions are being

moved between the cathode and anode materials and finally a high DoD window region that would correspond to the voltage region of 3.0V to 3.58V. In this region, the active material would experience a high degree of stress that would primarily occur at the anode and a possible increase in the SEI layer.

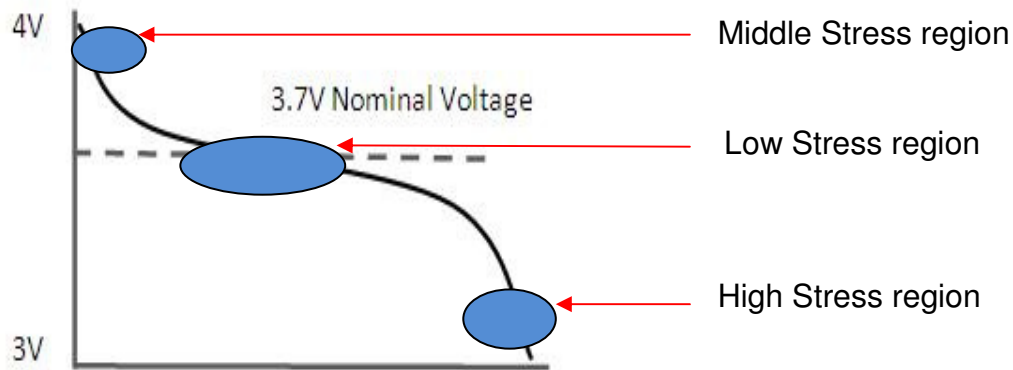


Figure 1.8: Discharge curve of a typical LiCoO_2 cell showing the 3 regions.

These stresses and strains result as cycling occurs producing a change in the volume between fully and partially lithiated phases. During some of the resulting expansions the strain energy will drive the particle fracture, as energy that is absorbed by the material as a result of work done on it will lead to deformation. The strain will cause fractures within the SEI layer, which will allow for further decomposition of the electrolyte into the SEI layer. Interference by the SEI layer with the transport and reactions will result in increases of the interfacial resistance, finally resulting in irreversible removal of Li. As the SEI layer increases, the cell begins to fade²⁵. In Figure 1.8, the various regions correspond to different regions of stress of the active material. Ideally, in order to optimize the longevity of Li-ion batteries, electronic devices should limit the battery's use to work within the middle DoD region. However, this would limit the available discharge capacity and would require frequent recharging during the life of the battery. When placing a number of cells in series, the best performance of that series will depend on the capacity and voltage range of the weakest cell. If there is an imbalance in the cell voltages and capacities within a bank of batteries, the discharging and charging to the minimum and maximum voltage limits would gradually cause some of the cells to overcharge or over discharge. This will result in placing more strain on the remaining cells thereby reducing the life cycle ability of the entire battery pack.

The expected life of the Li-ion battery pack also needs to be known, as the EV and HEV manufacturers need this info in order to give a guarantee on their batteries. These manufacturers would also need to know what could possibly go wrong during the life of the battery and perhaps when this may occur. This will not only enable them to budget correctly for these batteries but also ensure safety for their customers. The expectations of the batteries in Hybrid EV, EV and Fuel cell EV are different due to the different nature of the systems and their requirements.

1.5. Future Lithium-ion cell development

The cathode materials that are commonly being manufactured for applications such as PDAs, laptops and cellular phones are LiCoO_2 , LiFePO_4 , Li_xMnO_2 (as indicated by “we are here” in Fig 1.9). These cathode materials are manufactured with an anode material of graphite.

The most commonly used Li-ion cathode material is the LiCoO_2 . This is a successful cathode material which has been extensively used in typical applications such as cellular phones, laptops and PDAs. Alternative materials such as $\text{LiNi}_{1/3}\text{Mn}_{1/3}\text{Co}_{1/3}\text{O}_2$ and $\text{LiNi}_{0.8}\text{Co}_{0.15}\text{Al}_{0.05}\text{O}_2$ are being developed in order to reduce the cost and improve the stability of the material. Cobalt is a limited resource in the world and thus more expensive than other transition metals such as manganese, nickel and iron. The LiCoO_2 structure is also not stable and can easily undergo performance degradation or failure with overcharging. This degradation can be caused by the cobalt dissolving into the electrolyte when the electrode is delithiated during charging²⁶.

The cobalt oxide structure can be stabilized by doping the material with other transition metals such as Ni, Mn and Al. For example: $\text{LiNi}_{1/3}\text{Mn}_{1/3}\text{Co}_{1/3}\text{O}_2$ and $\text{LiNi}_{0.8}\text{Co}_{0.15}\text{Al}_{0.05}\text{O}_2$. The additional elements stabilize the layered structure and enhance the cycling stability²⁷.

The substitution of other transition metals into the cathode material would bring structural and thermal stability. This in turn would improve the cyclability but to the expense of achievable discharge capacity⁶.

New materials are being researched to increase the cell voltages and are not yet commercially available. These new materials would result in higher cell voltages leading to higher power and energy densities as illustrated by an increase in potential vs. Li/Li^+ . These improvements in potential can be made by adding different

transition metals to the existing commercial chemistries, i.e. LiCoO_2 , LiFePO_4 and LiMnO_2 . Each transition metal that is added to the basic Li-ion chemistry adds some advantage to the overall cathode materials, for example, by adding iron to the material, the cathode material is able to operate at higher temperatures. However there is a limit to what can be added and the quantity of each metal⁸.

Figure 1.9 summarizes some examples of the different cathode materials that are currently being researched:

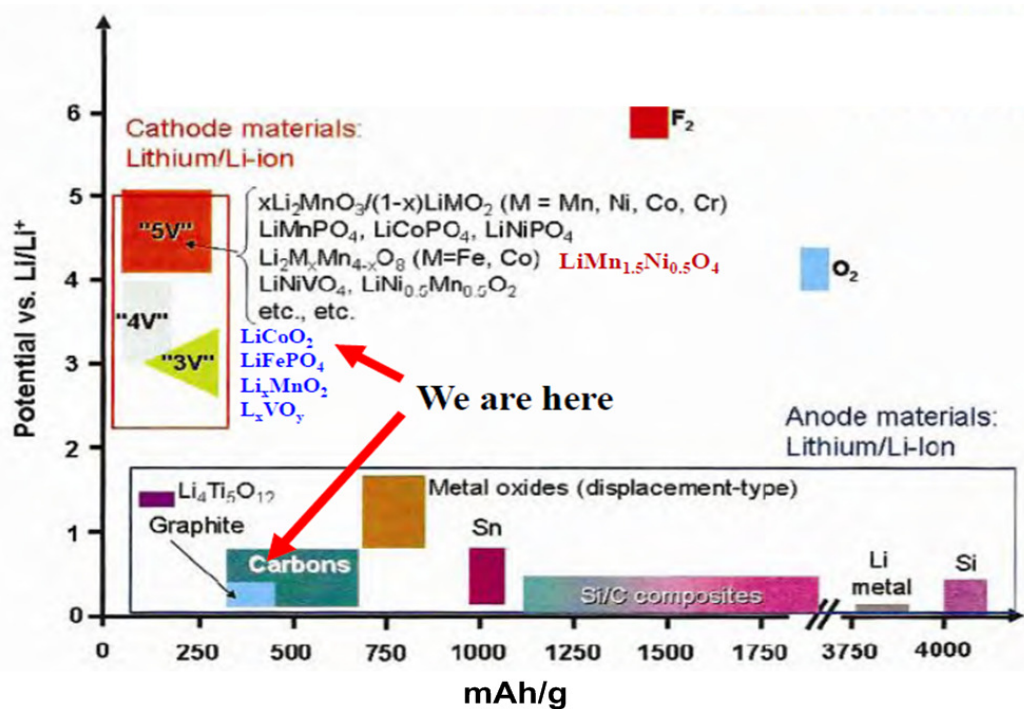


Figure 1.9: the different cathode and anode materials under investigation⁸.

Research is also being carried out in possibly substituting the graphite anode material with other materials, such as lithium titanates and lithium tin materials. When investigating changes to the anode material, metallic lithium is still being researched for use only in the lithium air batteries. However care must be taken if this metallic lithium were to be used as the anode material, due to the spontaneous reactivity of the metal in oxygen²⁸.

1.6. Limitations to Lithium-ion batteries

The introduction of Electric Vehicles (EV) would significantly reduce the use of fossil fuel and the local CO_2 emissions. However they are limited by the distance the vehicle can achieve before having to recharge, which often can take a few hours. Another concern is the safety of a large numbers of cells that are stacked together in

order to produce a battery within the limits and requirements of a passenger vehicle. This requires a good understanding of the management and performance abilities of the battery in a vehicle system as well as the application load implications on the chemistry on the cell design. In particular, the expectant life span or calendar life under different environmental conditions and user applications needs to be understood in order to alleviate consumer fears of premature battery failure and unrealistic life expectancy²⁹.

As Li-ion batteries are used in the consumer application industry such as laptops, cellular phones and PDAs, a life span of about 2-3 years can be considered as sufficient. For the market requirements Li-ion batteries in EV and HEV applications, the life span expectancy is for 7 to 10 years with a considerably larger power capability requirements and higher safety and costs than for batteries that are typically used in powering a laptop³⁰. Some of the more common failures that occur in Li-ion batteries can be described as follows.

1.6.1. Failure mode due to the Solid Electrolyte Interface (SEI):

The failure mode in Li-ion batteries can be primarily described as chemical or electrical. The chemical failure is understood as the loss of electrode active material integrity due to the expansion and contraction of the unit cell of the active material during discharging and charging processes. This results in a stress and strain evolution, which causes a resistance of the cell resulting in solute diffusion limitations. The resistance is seen due to the SEI layer becoming too thick and the Li-ions are restricted in their movement which will result in reduction of the capacity. The end result will be seen when the Li-ions within this layer become trapped. Electrical failure includes the overcharge or over discharge, dendrite formation, electrolyte deterioration and the increase of the Solid Electrolyte Interface (SEI). The SEI layer caused by use and sometimes abuse should not be confused with the thin protective SEI layer that is formed on the anode during the initial charging process. The rate of SEI growth can be equated to the rate of change of the lithium concentration at the surface. This accounts for SEI damage by expansion/contraction of the active materials³¹.

Example of some of the changes that occur at the anode/electrolyte interface can be summarized by:

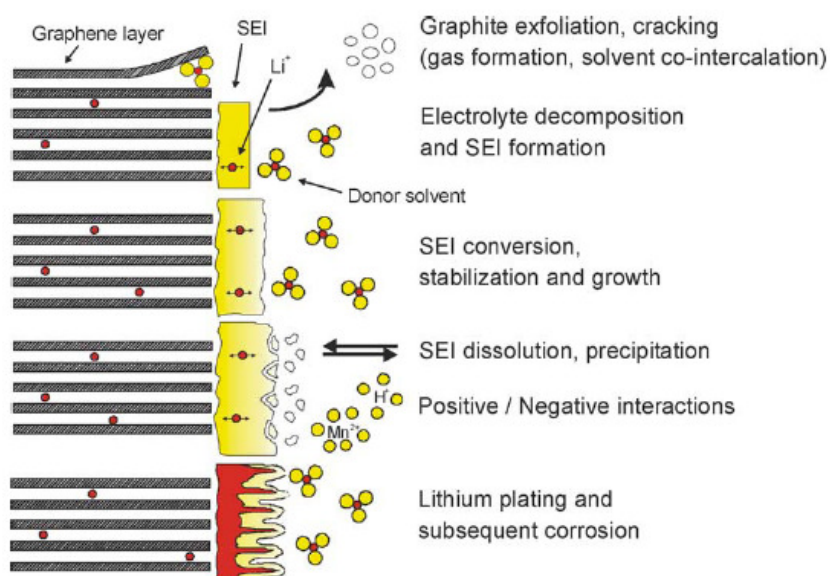


Figure 1.10: the possible changes that can occur at the anode/electrolyte interface³¹. Changes at the electrode/electrolyte interface due to reactions of the anode with the electrolyte are considered by researchers to be a major source of ageing of the anode. As the SEI layer increases on the electrodes, in particular the anode, it becomes difficult for the Li-ions to pass through into the pores of the electrodes, thus causing cell failure. Any additional SEI growth will cause further insertion of lithium into the graphite layer resulting in an increase of the lattice volume. An increase in volume causes the surface of the film to be stretched or even destroyed. The capacity retention and lifetime of the cell depend on the structural stability of the electrode materials which will change as the crystal structures are distorted during abusive situations or prolonged periods of cycling. As the Li ions move between the electrodes, ohmic drop, electrolyte decomposition and interfacial properties between the electrodes start to fade the cell's ability to capacity cycle. These structural changes will affect the electrochemical behaviour of the electrodes as can be measured by Electrochemical Impedance Spectroscopy (EIS) analysis³¹. This damage can only be repaired by a chemical reaction of the lithium, resulting in irreversible capacity loss.

1.6.2. Failure due to thermal conditions.

One of the most important safety considerations for Li-ion cells/batteries are their thermal stability under various applications whether these are for ordinary use or abusive conditions such as exposure to over-heating or external short-circuits. These factors need to be considered when scaling up the cell design. There are several exothermic reactions that take place within the cell during discharge and would cause the cell to heat up and accumulate within the cell or battery pack. This will have an effect on the acceleration of the reactions within the cell thereby increasing the internal temperature of a cell. If this heat is not dissipated effectively to the environment, it may cause the cell temperature to rise too quickly, thereby risking a thermal run-away. A typical example of thermal effects of Li-ion cells made with different chemistries is summarized in figure 1.11. A thermal run-away is considered when the battery reaches a certain temperature (in most cases) of about 60°C and above where the battery would continue to heat up rapidly leading to explosions and combustion of the organic material³².

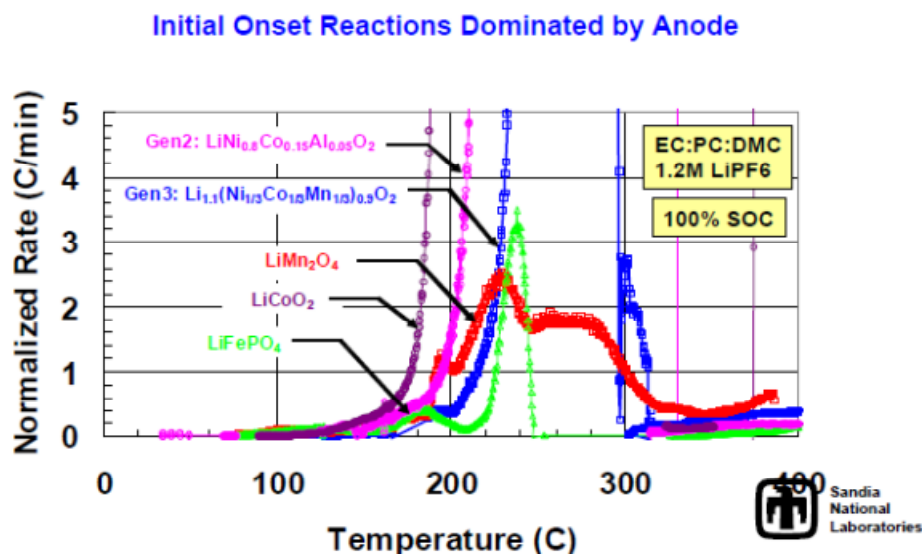


Figure 1.11: Thermal runaway graph for the different lithium ion chemistries³³.

Studies carried out by Sandia National Laboratories showed that there are three sources of heat that is caused during thermal run-away. The first source of heat generation is due to the chemical reaction of the cell during discharge and is called the 'reversible' heat. The second source of heat generation is due to ohmic resistance and polarization and is known as 'irreversible' and would typically occur with over discharging. The third source of heat generation is caused by 'side

reactions' such as corrosion, overcharge and short circuits due to chemical failures (dendrites) which will also lead to 'irreversible' heat³³.

A number of models were developed that could describe the sources of heat to allow for effective safety measures to be put in place. The one model considers the structural chemistries of the different oxides and their bonding ability to the oxygen (Fig 1.12).

LiFePO₄ doesn't thermally runaway as easily as the other chemistries.

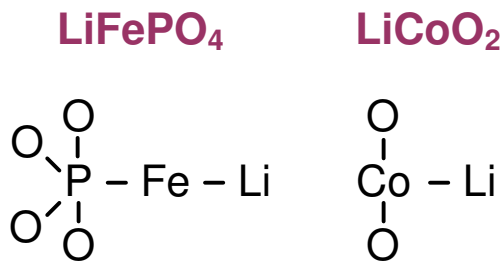


Figure 1.12.: the bonding of oxygen to different atoms in the different chemistries³³.

This diagram shows why LiFePO₄ doesn't show thermal runaway at lower temperatures: in LiFePO₄ the oxygen atoms are bonded covalently to the phosphorous and the phosphate is then bonded to the metal by ionic bonding.

However in LiCoO₂ the oxygen atoms are covalently bonded directly onto the metal. The oxygen atom that is bonded directly to the metal becomes easier to cleave during high temperatures thereby feeding the decomposition reactions.

Some improvements in thermal safety have been made by adding small quantities of other metals such as aluminium and nickel to the LiCoO₂ cathode material which adds stability and increases the onset thermal runaway temperature (Fig 1.12).

1.7. Lithium-ion cell testing:

Safety procedures for the use of Li-ion batteries in both consumer and EV applications were developed by the Underwriters Laboratories (UL-1642), the United States Advanced Battery Consortium (USABC), the Electrochemical Storage System Abuse Test Procedure Manual and the Japan Storage Battery Association (JBA).

This has led to safety-related studies, suggestions on protection mechanisms and new coatings over the cathode materials³⁴. The FreedomCAR group forms part of the U.S. Department of Energy specialising in vehicle technology programs. The FreedomCAR group focuses on test procedures similar to the USABC³⁴.

The main aims of the USABC and the FreedomCAR groups included:

- System developments. Items such as cost, battery life, battery performance and abuse tolerance needed to be investigated.
- Technology assessment. Emerging technologies needed to be investigated prior to full system development. The overall capabilities of the technology, as well as the technical claims needed to be validated through independent testing.
- Benchmark Testing. Working with national laboratories and independent tests against the manufacturer's specifications.

1.7.1. Capacity fade due to Calendar life or Cycle life losses:

Capacity fade refers to the loss in primary and secondary material (mainly carbon), as well as a difference in rate capability. Both calendar life loss and cycle life loss are responsible for ageing of the cell but should be tested separately.

Capacity loss consists of irreversible and reversible components. Reversible loss refers to when the battery capacity loss is due to 'self-discharge'. This loss can be recovered again once the battery is recharged. Irreversible capacity loss is due to degradation of the battery as it is used and cannot be recovered.

Cycle life losses refers to the battery showing a decrease in capacity when it is active, i.e. as the battery is charged or discharged at different rates between the voltage limits. The number of cycles a battery can achieve is usually defined as the ability to discharge at a constant current or rate until it reached a certain predefined State of Charge (SoC) such as 80% in EV applications.

Calendar life losses refers to the battery losing its capacity even when it is inactive, such as when it is in storage or in stand-by applications for certain periods of time.

The effects of cycling will have a greater effect on capacity loss than the effects caused due to calendar loss. Capacity fade results due to two major processes: the loss of active material (lithium) at the negative electrode and an impedance growth at both the cathode and anode. The battery will undergo irreversible loss. These losses will be influenced by the application of the battery and how the user operates the battery³⁵. Figure 1.13 shows the capacity loss over time.

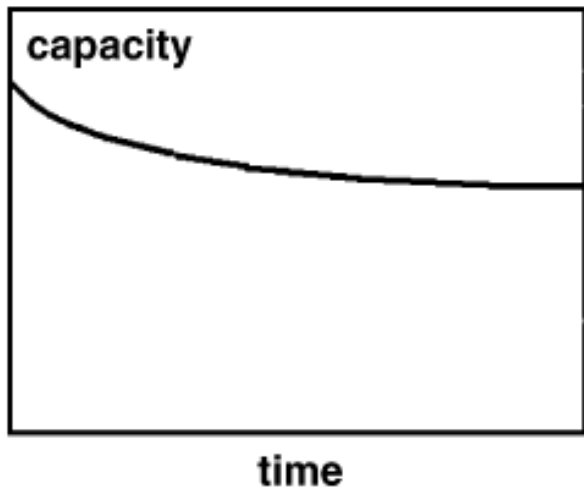


Figure 1.13 typical capacities vs. time for storage test.

Calendar life loss:

The rate by which a Li-ion battery will age is influenced by the temperature that it is exposed to and the State of Charge (SoC), and is summarized in Table 1.1³⁶.

Table 1.1: Recommended storage charge levels at different temperatures and State-of-Charge.

Storage Temperature (°C)	40% charge level (Recommended storage charge level)	100% charge level (typical user charge level)
0	98% after 1 year	94% after 1 year
25	96% after 1 year	80% after 1 year
40	85% after 1 year	65% after 1 year
60	75% after 1 year	60% after 1 year

Capacity loss increases with increasing temperatures. Capacity loss will also be influenced by level of charge that the battery is stored at; a recommended level of 40% charge will ensure that the battery loss is reduced over the time of storage. In general Li-ion batteries have a calendar life of about 2-4 years at present.

Cycle life loss:

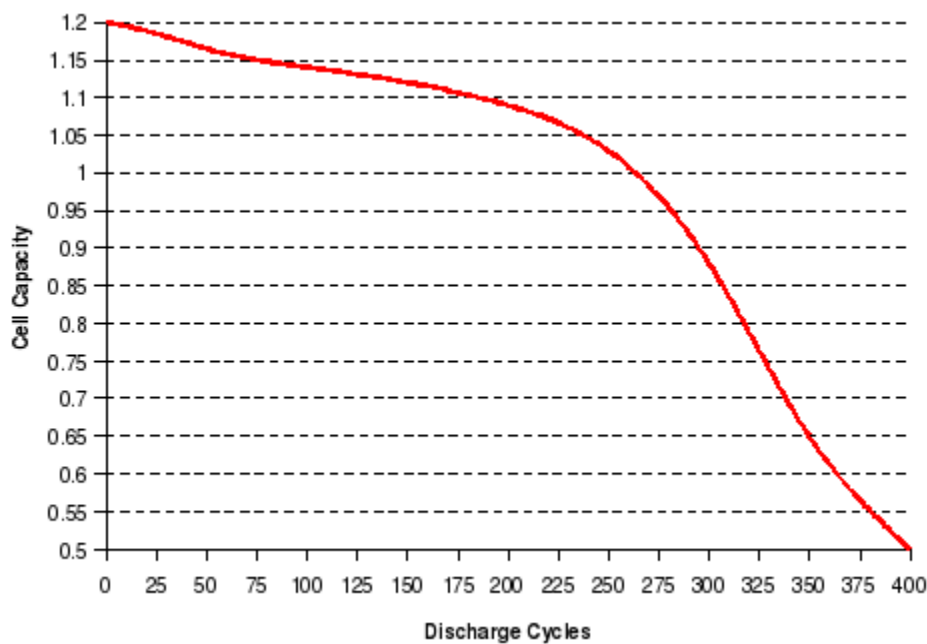


Figure 1.14: Generic discharge curve of lithium ion cell showing the change in cell capacity over no of discharge cycles³⁷.

In figure 1.14, a decrease in cell capacity is seen as the no of discharge cycles increases. Ageing of the cell during cycling is as a result of irreversible degradation of active materials during lithium insertion⁸.

The possible mechanisms for capacity fading during cycling include:

- Degradation of the crystalline structure of the positive material. A mechanical modification of the composite electrode structure can occur during cycling due to volume changes of this structure. This would lead to the active material disconnecting from the conductive network. This mechanical modification effect is limited, as the volume change of insertion material is small.
- Graphite exfoliation of the negative electrode
- Build-up of passivation film on both electrodes, thus limiting the active surface area and clogging the electrodes' pores (this can occur during storage).

1.7.2. Techniques available for testing of ageing effects:

It is important to characterize the ageing of a cell, thus allowing for reduction of the amount of batteries needed for certain applications such as portable applications, which saves money and reduces environmental waste. However this is only possible

if simple and reliable methods for testing and battery management are available that can be used by manufacturers.

There are several destructive and non-destructive techniques available for the characterization of the ageing effects in Li-ion cells. They will differ in accuracy, complexity and the ability to give meaningful results that can be translated into battery durability and longevity in application.

The destructive techniques include the testing of the cells safety aspects such as short circuiting, puncture tests, impact tests, vibration tests and deformation tests where the cell is bent. The characterisation of the active material in the cell would involve the cutting open of the cell. Techniques will then be used to study the chemical composition of the active material surface films of the electrodes, separators and the electrolyte. Techniques such as scanning electron microscopy (SEM) and Powder X-ray diffraction (PXRD) are used to provide information on the changes in chemical composition.

Electrochemical destructive techniques involve testing the battery using a series of charge and discharge steps at a particular C-rate that would simulate as close as possible the real application of the battery. However, life expectancies of batteries in the field can be up to 10 years, therefore accelerated laboratory tests are often required that can extrapolate battery life expectancies from relatively short testing procedures. Most methods are also unable to distinguish between the different ageing effects and where within the battery the failures occur: at the electrodes, separator and/or electrolyte degradation which are difficult to categorize.

The non-destructive techniques include voltammetry that can be used with a cell that allows for a suitable reference electrode to be included with the working and counter electrodes. This technique provides information about the electrode polarization curves that may be of interest in characterizing the ageing effects. It is also useful in evaluating the electrochemical stability of the electrolyte, comparison of different electrolytes against the electrodes and to study the influences of varying salts, solvents and polymer within the cell. However this technique is time-consuming and because two different electrodes are used in batteries, the voltammetric response will be affected by the charge/discharge reactions³⁸. Thus not all ageing effects can be determined using this technique.

The most common accelerated testing for predicting the calendar life of a battery is to expose the battery to different temperatures and states of charge (SoC). These

cells or batteries are then exposed to these conditions for a period of time where the results would typically show a decrease in the cell capacity. Work carried out by I. Bloom et al³⁹ carried out a test where 6 cells were exposed to each of the four temperatures (i.e. 40, 50, 60 and 70 °C) and to each of two SoCs (60 and 80%). Four additional cells were exposed to each of the four temperatures but each at 40% SoC. The different effects on the cells or batteries will then be compared³⁹. They concluded that temperature accelerated the cell performance degradation. The area-specific impedance (ASI) was influenced the most by higher temperatures and cells at 60% SoC.

The most common electrochemical performance of a Li-ion battery supplied by the manufacturers is the so called discharge curves at different rates under ambient conditions shown in Fig 1.15.

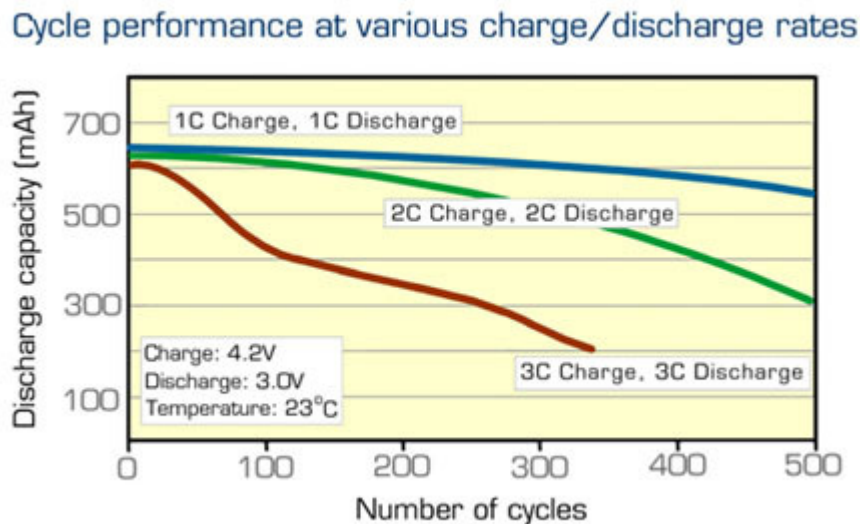


Figure 1.15. Cycle performance of a Li-ion cell cycled at different charge and discharge rates²⁰.

The capacity cycling ability is usually expressed as the number of cycles that the cell can undergo at certain discharge capacity under ambient conditions. As can be seen in figure 1.15, at higher charge and discharge rates the cell is only able to complete fewer cycles before the discharge capacity becomes too low²⁰.

In addition, these tests can also be performed at different temperatures as was done by the authors: Stuart Bowden and Christiana Honsberg, from the Solar Power Labs at the Arizona State University (Fig1.16)⁴⁰. Their results showed that as the temperature increased, the number of cycles that the cell was able to complete

decreased. It should also be noted that as the %DoD increased, the number of cycles that the cell was able to complete also decreased. However, an increase in temperature had a greater influence on the number of cycles the cell was able to complete.

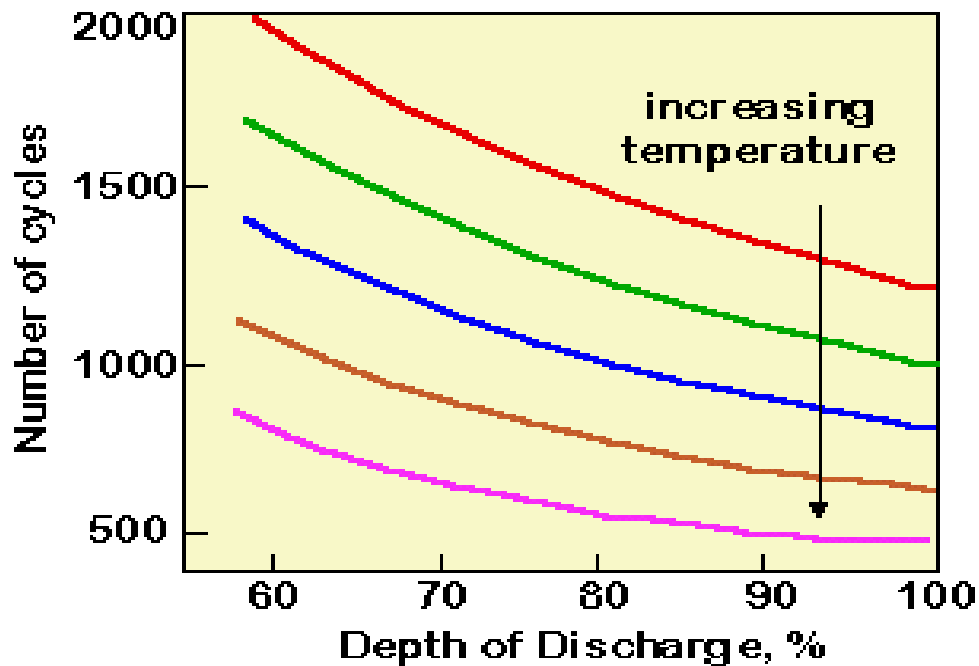


Figure 1.16: Capacity testing at different temperatures and % DoD⁴⁰.

More complicated testing sequences are employed that try and simulate driving conditions of Electric Vehicles that include the Dynamic Stress Test³⁴. The Dynamic Stress Test (DST) is an example of a test procedure established by the U.S. Advanced Battery Consortium (USABC). This test aims at simulating expected demands on an EV battery during real driving conditions such as high climbing, acceleration during overtaking and stop-start and can be employed in order to determine the capacity fading of a cell and give some comparative evaluation of different battery types studied under similar conditions.

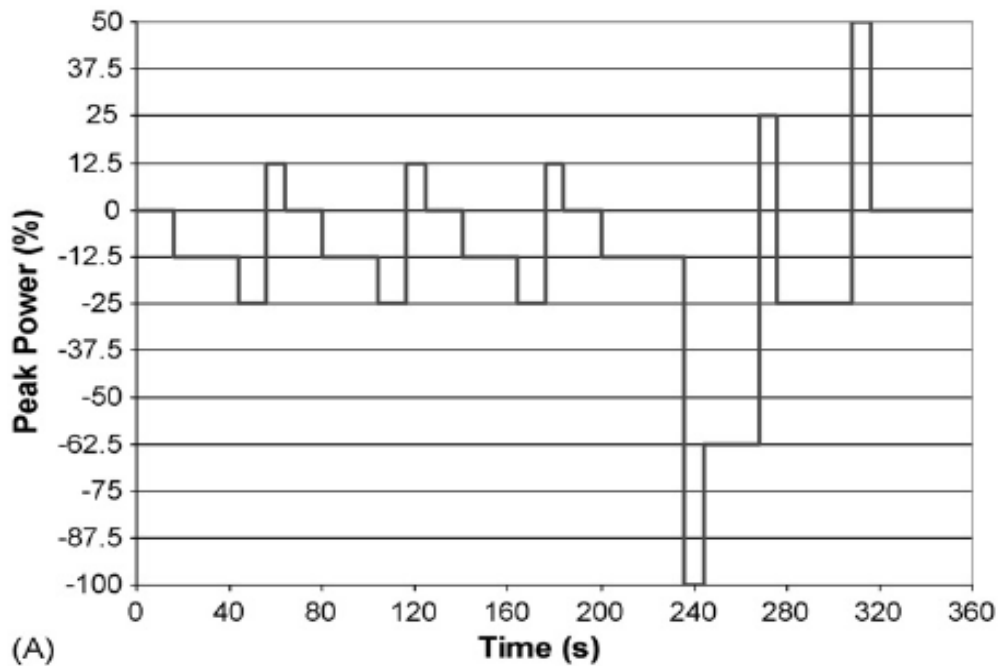


Figure 1.17: Dynamic Stress test procedure³⁴.

A DST test is described by the USABC Test procedures as a variable power discharge cycle calculated by a Peak Power Test. The DST uses a 360 second sequence of power steps with only 7 discrete levels³⁴. A Peak Power Test is quoted by USABC as “the maximum discharge power which a battery can produce into a load for 30 seconds (at a given depth of discharge) without allowing the voltage to drop below $\frac{2}{3}$ of its open circuit value (OCV) at that DoD. The discharge voltage is also restricted to be above a Discharge Voltage Limit (DVL). This DVL is determined as the higher of either $\frac{2}{3}$ of the OCV at 80% DoD at the beginning of life of the cell or the manufacturer’s specified minimum discharge voltage. Limiting the voltage under load to $\frac{2}{3}$ OCV or the DVL is carried out for efficiency and propulsion system design considerations”³⁴.

The modelling of the DST tests can be described as being more generic and does not necessarily simulate every possible application where cells within a bank of batteries are often non-linear in terms of their actual capacity, state of health and SoC and are highly dependent on parameters such as temperature, batteries overall SoC and short-term history. The implementation of battery models are very difficult where often only approximations can be achieved⁴¹.

With the DST test a standard usage cycles has been developed to provide a basis for comparison, however it should be noted that the typical user does not necessarily drive according to these cycles and may most likely accelerate twice as fast as allowed for in the standard test.

However according to a paper by Steven T. Mayer, a DST test of small Li-ion cells showed that the system delivered high energy (65Wh/kg maximum with a 4.3 hr run time) with a reasonable cycle-life (375-480 cycles) under the full USABC mid-term DST conditions. At a 44% DoD (with the %DoD based on the maximum possible DST energy available) a much higher cycle life of 2800 cycles was achieved. This value would correspond to DST driving for 1.9 hours every day for 7.7 years. Both the DoD and charging voltage will affect the delivered energy and cell life⁴².

One other test that can be used involves the Incremental capacity variation test⁴³. This test depicts the change in capacity associated at a voltage step. Each peak in the incremental capacity curve has a unique shape, intensity and position. It will exhibit an electrochemical process taking place in the cell. This test involves different discharge rates and the curves that are formed at these rates. As the number of cycles that the cell has undergone increases these curves will change position, shape and intensity and is shown in figure 1.18.

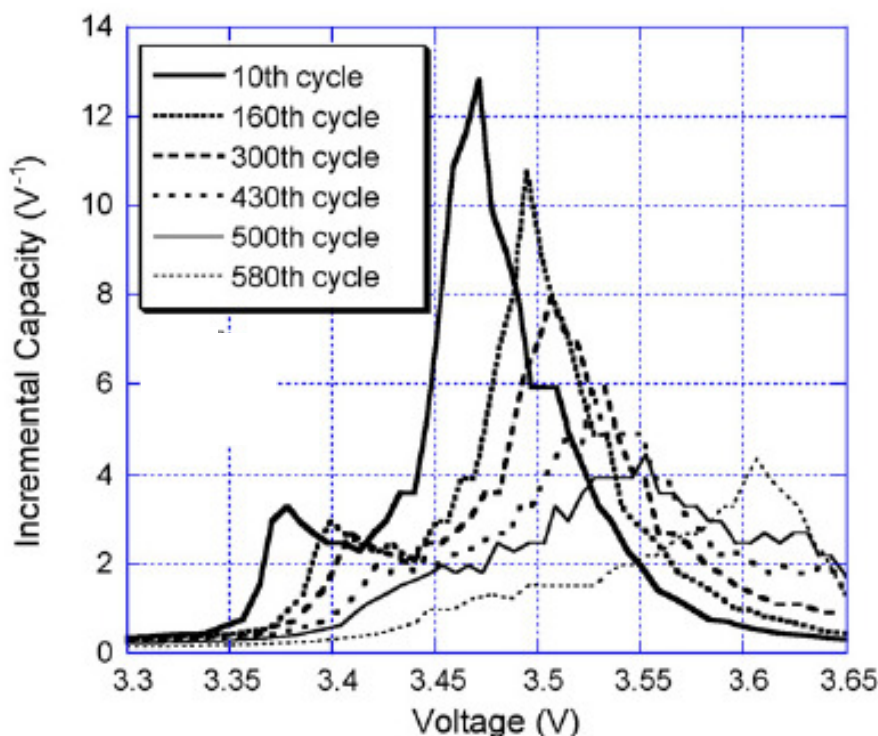


Figure 1.18: Incremental capacity variation graphs⁴³.

However, the testing procedures are often only applicable to specific applications where currents and environment conditions are more predictable such as portable electronic devices and one often requires different simulation tests for different applications such as EV, HEV and PHEVs. Also, the results of the test procedures seldom give an indication of the expected life in terms of years of the battery. Thus a reliable and accurate algorithm for the Battery Management System (BMS) needs to be developed. This algorithm would need to take into account the state-of-charge (SoC) and state-of-health (SoH) as the battery capacity fades and degradation mechanisms come into effect. Unfortunately Li-ion cells are subject to a significant loss of capacity and rate capability fade due to cycling as well as long periods of storage. Therefore the BMS needs to ensure that the parameters that are affected the most during cycling and storage are highlighted, and that the BMS can correct for these changes. The limiting voltages, available power and energy would need to be accurately and reliably calculated into the algorithm by making use of in situ and non-destructive methods. The voltage limits are important in order to ensure safety and making use of the maximum amount of available energy for the system will ensure relatively lower costs.

Many EV manufacturers are also required to place a warranty onto the battery system, where the possibility of the state of health of the battery is required under different types of applications with different cell stresses when used by the consumer. This info would be factored into the battery management system which takes into account battery degradation which may lead to an early warning system which may then help to extend the battery life or allow it to be used in other types of applications.

1.8. Supercapacitors

Capacitors are known as Electro-chemical, Double-layer, super or ultra capacitors. They fall into two groups: namely a standard capacitor (capacitance of μF or pF ranges) and a super or ultra capacitor (capacitance of anything exceeding 1 Farad). For the automotive industry, a supercapacitor can be coupled up to a cell or battery in order to increase the energy and power densities of the systems. A capacitor is able to deliver more power to the system than the conventional system of the battery alone⁴⁴. Supercapacitors designs are already used in a number of vehicle

applications such as the stop-start technology being developed by PSA (Peugeot Citroen Group)⁴⁵; the system reduces the fuel consumption of the vehicle during long traffic stopping periods and can reduce the size of the common battery by 30%, providing more torque during the restarting step. Another design discussed included the KERS (Kinetic Energy Recovery Systems) as used by the different F1 competitors. The kinetic energy of a moving vehicle is recovered under braking and is stored in a reservoir (for example a battery, supercapacitor or flywheel) to be used at a later stage under acceleration¹⁶.

Supercapacitors are able to fully charge within 5-10s, while high power batteries with the same settings charge fully in 5-10 minutes. Another advantage of supercapacitors is that their cycle life is usually longer than most batteries and supercapacitors have excellent reversibility (90 to 95% or higher)⁴⁶. Supercapacitors are also able to work at very low temperatures such as -40 °C. A limitation of supercapacitors is their limited charge retention and capacity.

A capacitor functions by storing the electrical energy in the interface between the electrode and the electrolyte. The electrodes of the capacitor need to have the correct pore size if carbon is being used as the electrodes. If the pores are too small to allow easy access to the electrolyte ions, they will not contribute to the double layer effect that is needed.

The electrolyte can be manufactured from 2 materials, namely organic or aqueous. Organic materials allow for higher workable voltages, usually 2 – 2.5V but the resistivity is relatively high. Aqueous materials have lower voltages, usually 1V, but have a better conductance than the organic materials.

The separator is used to prevent the occurrence of electrical contact between the two electrodes. It does however allow the ions to pass through it: ion-permeable material such as paper or polymers for the organic electrolytes and ceramic or glass fibre for the aqueous electrolytes can be used. The separator needs to be ion-permeable, have a high electrical resistance and a low thickness and the types can be summarized in table 1.2.

There are 3 types of capacitors⁴⁶:

1. Electrostatic capacitor;
2. Electrolytic capacitor; and
3. Electro-chemical capacitor.

Table 1.2 summarises the different characteristics of each:

Electrostatic capacitor	Electrolytic capacitor	Electro-chemical capacitor
Two metal electrodes separated by a dielectric.	Two metal electrodes separated by a dielectric, but have a conductive electrolyte salt in contact with the metal electrodes.	Porous electrode structure, thus increasing the capacitance per unit volume. Also uses electrolyte solutions.
Operating voltage depends on the strength of the dielectric material	Oxide layer serves as the dielectric	Very small surface area.
	For safety reasons, if polarity is reversed, the oxide layer dissolves the electrolyte and becomes short-circuited.	

Table 1.2. Classification of the different capacitors according to electrode type, operating voltage and safety.

Common testing procedures of supercapacitors include: power density, charge/discharge cycles and capacitor voltage windows. These tests are carried out in order to determine the capacitance and resistance of that specific capacitor at a constant current.

Further testing of capacitors includes a constant current charge/discharge test in order to determine the capacitance and resistance during the discharge step at various periods of time, a Pulse test to determine the resistance of each capacitor and a Ragone test to determine the power densities of the capacitor.

1.9. Test procedures focused on in this study.

This research project was carried out in collaboration with the HySA Systems initiatives for the development of Fuel cell technology in South Africa and in particular for applications in Fuel cell drive vehicles where the need for an integrated

Li-ion battery with a supercapacitor is required. These areas required research in terms of manufacturing these products and the various testing procedures for each. Research into testing procedures on combinations of these products was also needed.

Some of the testing that were considered for this study are described now in more detail and include:

- Peukert tests
- Ragone tests
- Electrochemical Impedance Spectroscopy Analysis (EIS).
- DoD window Tests
- Supercapacitors & Battery Tests

1.9.1. Review and some theoretical considerations of the electrochemical testing procedures:

1.9.1.1. Peukert tests:

The prediction of State-of-Charge (SoC) of a battery is vital in many applications. Many engineers and scientists base their SoC prediction on the Peukert equation. This equation relates to the available capacity of a battery and is often used to describe the discharge rates of Pb-acid batteries for a constant current discharge. The use of the Peukert equation dates back to a paper published by Peukert in 1897⁴⁷. Peukert performed constant current discharge tests on several different Pb-acid batteries from different manufacturers. He found that a simple equation was sufficient to describe the capacity and discharge rates for all Pb-acid batteries⁵⁰.

$$C = I^n t. \quad \text{(Equation 1.1)}$$

where C = capacity of the battery for a load of I amperes, expressed in Ah, I = Current, expressed in Amps, n = Peukert constant, t = time, expressed in hours.

In this study the Peukert equation was also applied for a variety of Li-ion battery types and used to show how the capacity of a cell can vary with the applied discharge rate. Very few authors describe the use of the Peukert relationship for Li-ion batteries. K. Striebel et al studied the use of the Peukert plot to describe the studies of variable rate discharges for the half-cell reactions of LiFePO₄ cathodes⁴⁸. Another paper by A.M. Lackner et al described the Peukert relationship of high-

energy plastic type Li-ion cells with improved cathode material types of cells at 55 °C and how it influenced the calendar life on the discharge capacity of a cell⁴⁹.

A Peukert constant closer to 1 of a cell would show less deviation in the cells capacity at different discharge rates. However the Peukert equation should be interpreted with care: as even when the cell is discharged at high current discharge rates, this does not imply that the entire cell's available material has been utilized. It is also important to note that the discharging of a cell is an exothermic reaction, which will have an influence on the available capacity. At a high rate of discharge, there will be a marked increase in temperature which may lead to an increase in available capacity of that cell at the specific rate⁵⁰.

In figure 1.19, the battery temperature plays an important role in determining battery parameters such as capacity and cycle life over long term operation. Significant amounts of heat are generated during high discharge rates⁵¹.

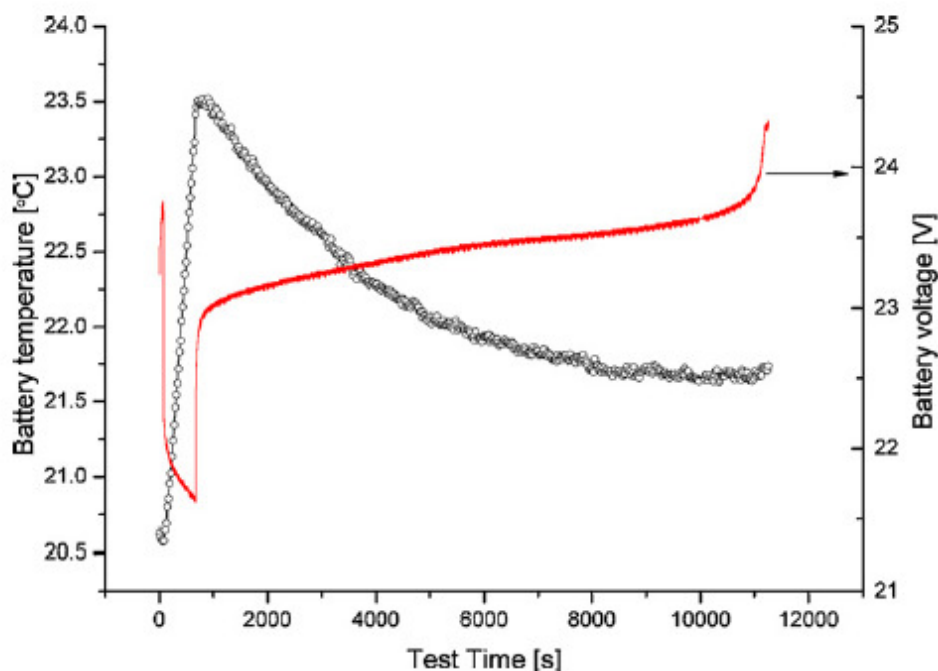


Figure 1.19: a typical measurement of battery temperature and voltage during a typical discharge and charge cycle according to a paper by V. Yufit and N.P. Brandon⁵¹.

It is recommended that a battery in high power discharge applications requires sufficient time to cool down between successive capacity cycles and this should be taken into account in overall system designs⁵¹. Most literature reviewed; simply

report the discharge curves and the achieved capacity with little or no information on the respective increase in the battery or cells temperature during high rate discharge. In figure 1.20, it is shown that as the discharge rate increased, the temperature on the surface of the battery also increased. During the study, the temperature increase during high rate discharges will be noted and compared.

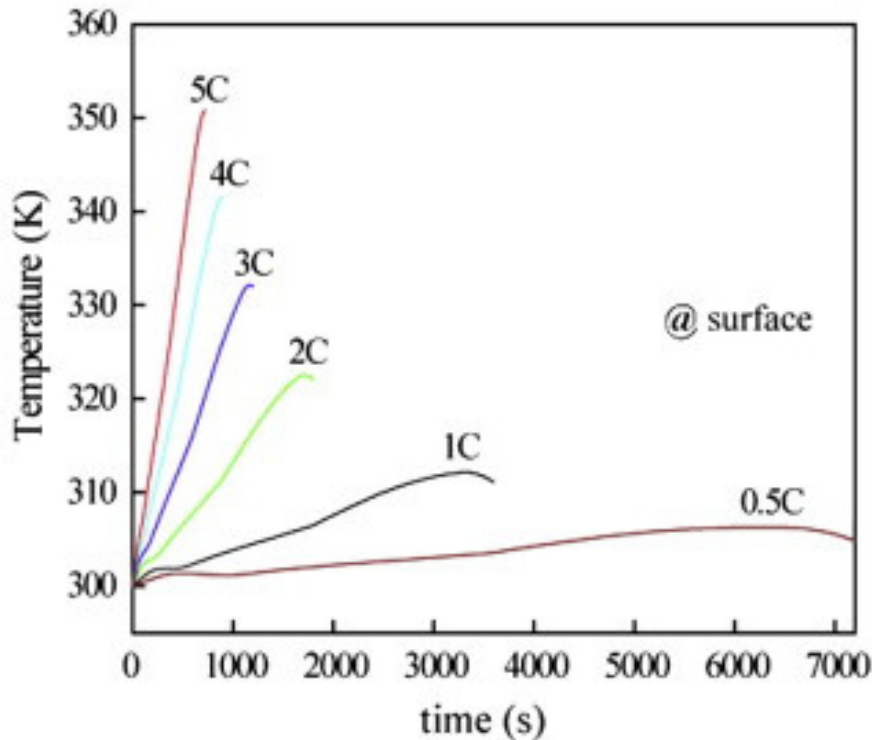


Figure 1.20. Surface temperature profiles of a Li-ion cell at discharge rates of 0.5C, 1C, 2C, 3C, 4C and 5C⁵².

As can be seen from the graphs above, there is a greater change in temperature over the different C rates.

1.9.1.2. Ragone Tests:

During the past 30 years, the relationship with specific power-density and specific energy-density has been empirically plotted, often on logarithmic scales. Such plots originated in a paper by Ragone at the May 1968 meeting of the Society of Automotive Engineers in Detroit, MI⁵³. In Ragone's paper the behaviour of battery systems for electrically powered vehicles was already considered. Ragone plots usually have a hooked shape corresponding to the fall-off of energy-density as the power-density is increased in the discharge of the battery. The reason for this shape

could be due to the increasing cell polarisation as the high power demands are made on the electrochemical storage device. Ragone plots of different electrochemical storage devices such as Ni/Cd, electrochemical capacitors and Pb-acid were made by the Idaho National Engineering Laboratory in 1996 for comparison of the different electrochemical storage devices according to their energy-densities and power-densities¹³.

Ragone Plots can be used to compare the energy-densities and power-densities of different electrochemical storage devices as seen in figure 1.21. The larger the energy density of a cell, the more power that cell would be able to deliver for its size¹³.

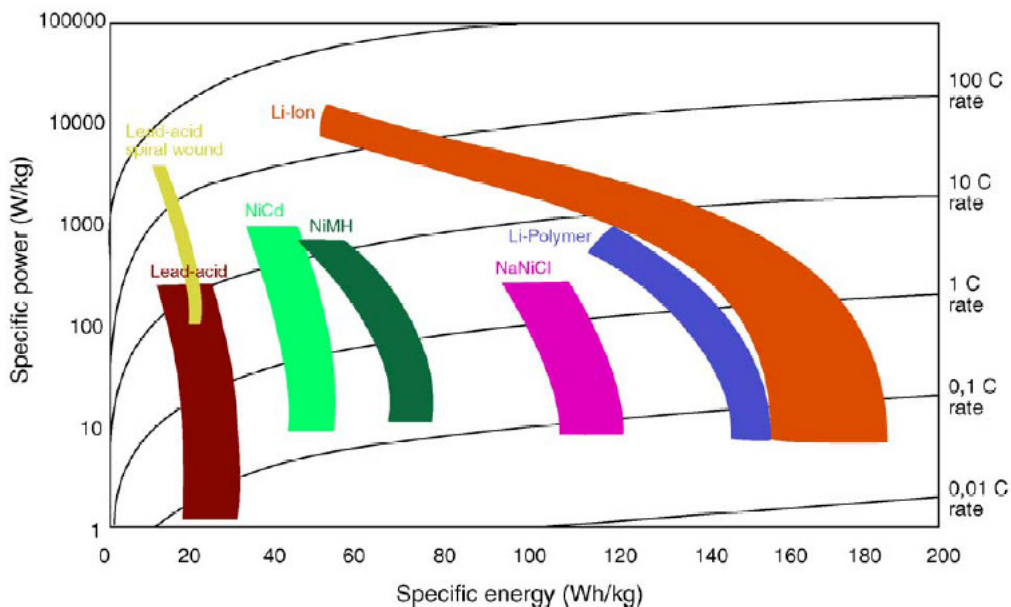
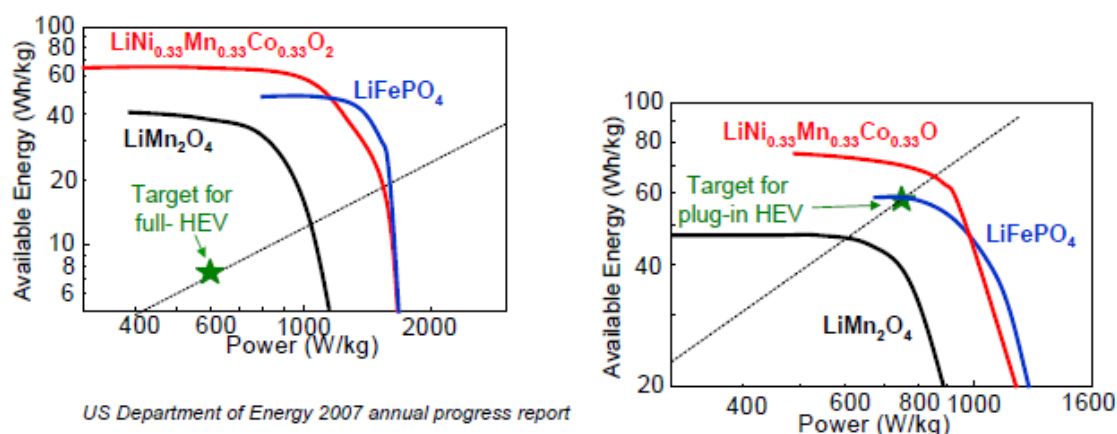


Figure 1.21. The Ragone Plots of different battery chemistries⁵⁴.

The results in figure 1.21 show that the Pb-acid battery system has the lowest specific energy and specific power when compared to the other electrochemical storage devices. The Li-ion shows a wider spread of specific energy and specific power since there are a large range of different cathode materials available. The other electrochemical storage devices such as NiCd and NiMH fall between Pb-acid and Li-ion batteries in their specific energy and power.

Ragone Plots can be used to explain the dependence of energy-density (ED) and power-density (PD) on the current drain for a battery and the behaviour of electrochemical capacitors. Non-traditional Ragone Plots are also seen when different graphite anode materials are compared and comparison of different cathode materials⁵⁵.



US Department of Energy 2007 annual progress report

Figure 1.22. Ragone Plots of different cathode materials⁵⁵.

In figure 1.22, the target values as specified by the U.S. Department of Energy for specific energy and power of full-HEV and plug-in HEV are indicated. According to the study, in 2007 the Li-ion battery that contained LiFePO_4 as the cathode material was starting to meet the required target for the plug-in HEV⁵⁶.

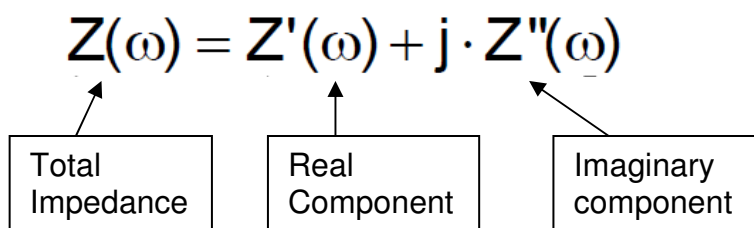
In literature, two different test methods are described to obtain the Ragone Plot. These methods include: constant power method and another where a constant current are measured.

The constant power method makes use of a constant power discharge at different C/rates, whereas the constant current method uses a constant current at this same discharge C/rates⁵⁷. The constant current method is similar to the Peukert test⁵⁸.

1.9.1.3. Electrochemical Impedance Spectroscopy (EIS):

EIS is a non destructive analytical technique that doesn't alter the sample and consists of the application of a small alternating current or voltage to an electrochemical system that then measures the response of the system to the signal. EIS is a technique that provides a large amount of information over a relatively short measurement time; however the interpretation of the information can be relatively complex where mathematical and graphing techniques need to be employed in order to interpret the information correctly⁵⁹. The advantages of using modern EIS instrumentation includes the ability to work over a very wide frequency range (10 μ Hz to 1 MHz). With a suitable reference electrode, the method can evaluate the electrochemical properties of one electrode and measure various subcomponent properties while the electrochemical system remains intact⁶⁰. For typical applications,

the impedance measurements are often done at one or two frequencies only or by using certain pulse methods that can give relatively fast results of the status of the electrochemical system. However, most of these techniques are comparative in nature, where a fair amount of laboratory analysis over a range of systems needs to be done in order to develop a suitable and reliable model for field application. The response obtained can be described as impedance (Z) which is a ratio or transfer function of the voltage to the current. Because this signal is so small, the response of the system can be regarded as linear, and the same transfer function should result whether the applied signal is a potential difference or current. As some processes are related to time derivatives of potential and concentration rather than upon the magnitude of the variables themselves, some part of the system will be in-phase with the perturbation (a real component) and another part will be out-of-phase with the applied signal (an imaginary component) and can be summarized by the following equation.

$$Z(\omega) = Z'(\omega) + j \cdot Z''(\omega)$$


The diagram shows the equation $Z(\omega) = Z'(\omega) + j \cdot Z''(\omega)$ with three boxes below it. The first box, labeled 'Total Impedance', has an arrow pointing to $Z(\omega)$. The second box, labeled 'Real Component', has an arrow pointing to $Z'(\omega)$. The third box, labeled 'Imaginary component', has an arrow pointing to $Z''(\omega)$.

Figure 1.23: The components that make up the total Impedance of a system⁶¹.

Helmholtz in 1879, considered the double layer formed when charging an electrode in solution and assumed that a layer of counter ions would be immobilized on the surface by electrostatic attraction, which would neutralise the surface charge⁶². In a Helmholtz model, the electric potential falls from its initial value ϕ_m at the surface of the electrode to zero in the bulk solution (the bulk solution being some distance from the electrode), over the thickness of the layer of counter ions, as shown in Figure 1.24. However later Gouy and Chapman argued that the ions are subject to random thermal motion which would mean that they would not be immobilized on the surface⁶³. They suggested that the ions which neutralise the surface charge are spread out in solution, forming a diffuse double layer.

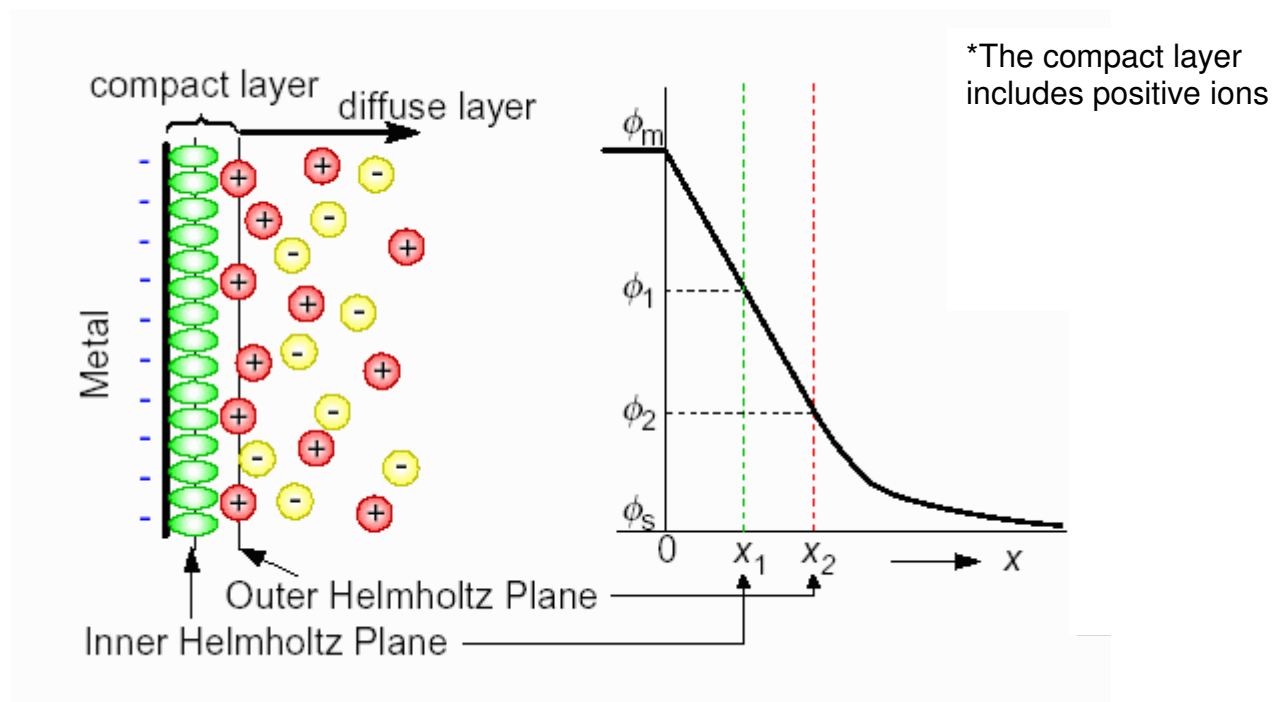


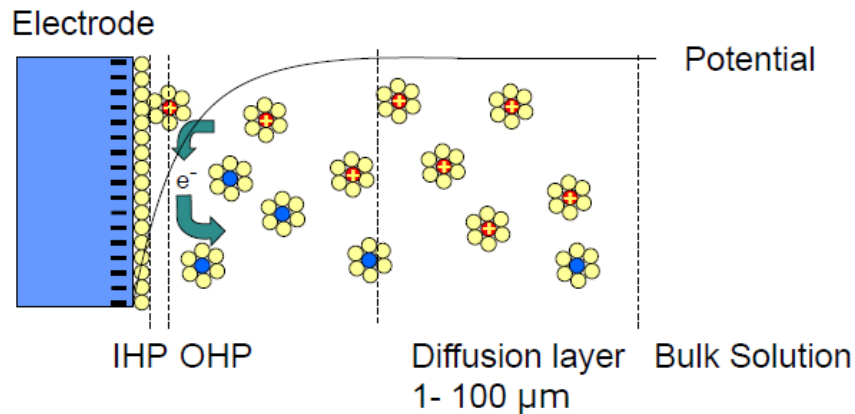
Figure 1.24 The Helmholtz double layer⁶⁴.

In 1924, the study done by Stern disagreed with both the Helmholtz and Gouy-Chapman models and stated that the true model is possibly a combination of the two models⁶³. Some ions are indeed immobilized on the surface (as Helmholtz suggested), but usually not enough to totally neutralise the charge. Thus the rest of the charge is neutralised by the diffuse layer (Gouy-Chapman model) that extends out into the solution.

Recent models of the double layer take into account the physical nature of the interfacial region, as well as the volume between the electrode and the bulk of the solution, which is a parameter that can be described and modelled from data determined by EIS measurements⁶⁵.

An electric double layer on the surface of an electrode can be described as a charged surface that comes into contact with an electrolyte solution. This charged surface is expected to attract ions of the opposite charge and repel ions of like charge, thus establishing an ion atmosphere in the immediate vicinity of the electrode surface. Two parallel layers of charge are then formed, and this is known as the double layer capacity. An example of this double electric layer is shown in figure 1.25, the interaction between the electrode and the electrolyte.

ELECTROCHEMICAL INTERFACE



IHP Inner Helmholtz plane: ion adsorbed onto metal surface

OHP Outer Helmholtz plane: closest ions free to move within the electrolyte

Figure 1.25: The electrochemical interface⁶¹.

A charge transfer reaction takes place at the particle surface. The electrolyte particle interface is modelled usually by using the Randle's model approach (fig 1.26). This model contains the charge transfer resistance (R_{ct}), double layer capacity (C_{dl}) and the Warburg (W) coefficient of the particle. This model is used as the starting point to explain the impedance characteristics of electrochemical storage devices in using EIS information.

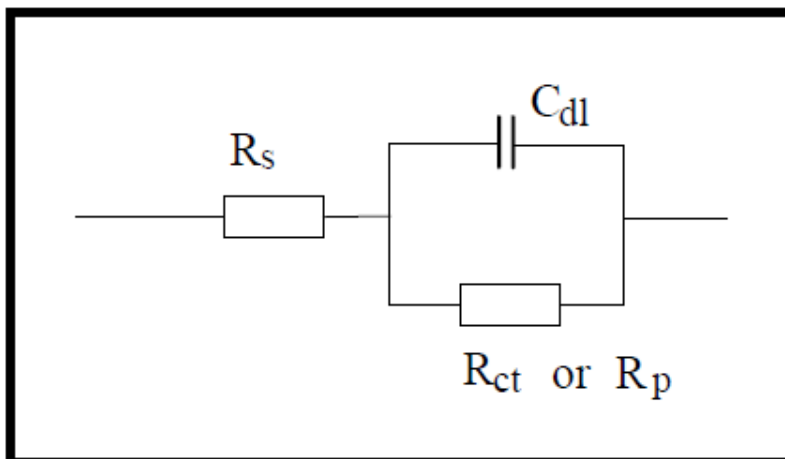


Figure 1.26. Simplified Randles Cell Schematic Diagram.

Insight into the resulting various regions of the EIS spectrum can provide information such as charge-transfer, double-layer and solid-phase diffusion processes that occur at the electrode interface⁶⁶. By scanning over a wide frequency range from 10^6 to 10^{-2} Hz, an experiment can take a while and certain information could be distorted especially if the study is done during the cells discharge or charge state⁶³. New

methods that make use of multi-Sine measurements can measure several frequencies at once without losing information at either high or low frequencies⁶⁰. The impedance data obtained after analysis can either be represented as a Bode plot or a Nyquist plot (Fig 1.27 and 1.28)⁶⁷. The Bode spectra would provide information on the change of the impedance and the phase shift with frequency whereas the Nyquist plot would provide information on the mixture of resistance and capacitance at high and low frequencies.

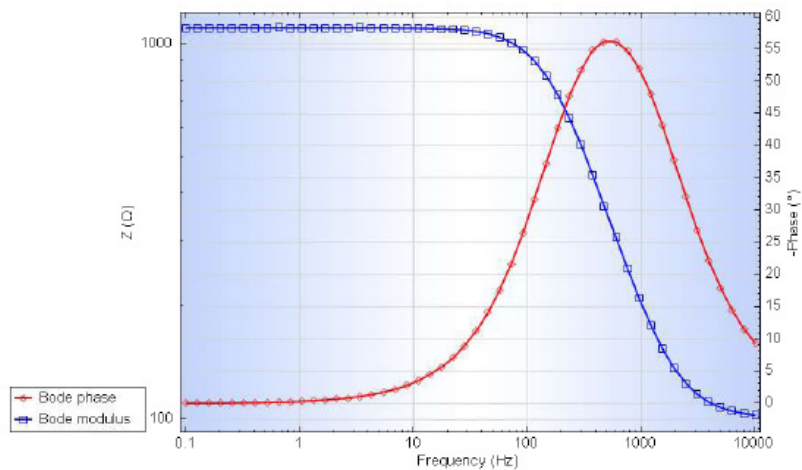


Figure 1.27: Bode plot showing the Bode phase and the Bode modulus.

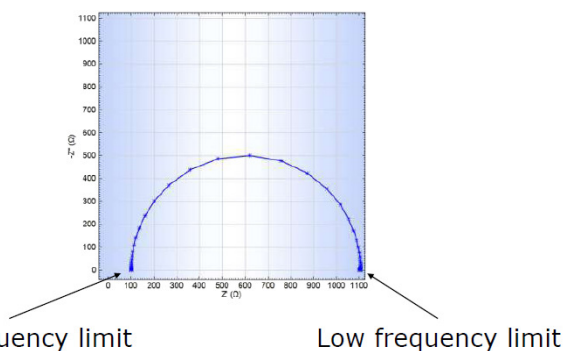


Figure 1.28: Nyquist plot showing different frequency limits⁶⁰.

Both the Nyquist plot and Bode plot have individual charge transfer processes that can be resolved by an equivalent circuit model. In the Nyquist plot, small impedances can be swamped by large impedances unlike the Bode plot which is able to provide information on both the small and large impedances.

The technique of EIS is very sensitive and is often difficult to obtain reproducible results due to variations in instrumental, cell connection and sample composition. Various tests are carried out in order to test for linearity, causality, stability and

consistency of the analyzed data. These tests include a Lissajous plot and a Kramers-Kroning (K-K) test.

A condition for linearity is that the applied AC amplitude must be small enough so that the response of the cell can be assumed to be linear where the system must obey Ohm's Law ($E = iZ$). The value of Z is independent of the magnitude of the perturbation. A typical Lissajous plot can be plotted in order to test for linearity of the spectra obtained⁶⁰.

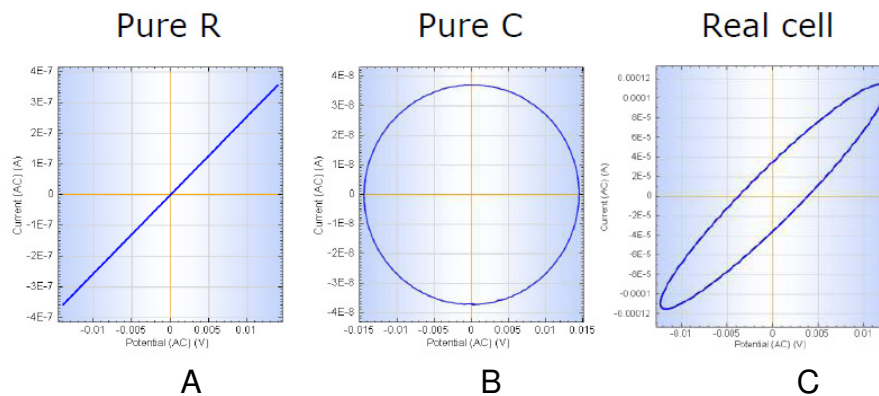


Figure 1.29: Lissajous plots⁶⁰.

For a sample that comprises a pure resistance, a straight line can be obtained for current versus potential (Fig 1.29A). If the sample comprises a pure capacitor, a perfect circle would be observed (Fig 1.29B). Samples that are a combination of resistances and capacitance such as in the case of a typical battery, the current versus potential plots would result in a symmetric oval shape graph (Fig 1.29C). Non-linear behaviour can be easily observed and could imply that the measurement system needs to be calibrated or that a poor measurement system design was used for a particular application (Fig 1.30A and B).

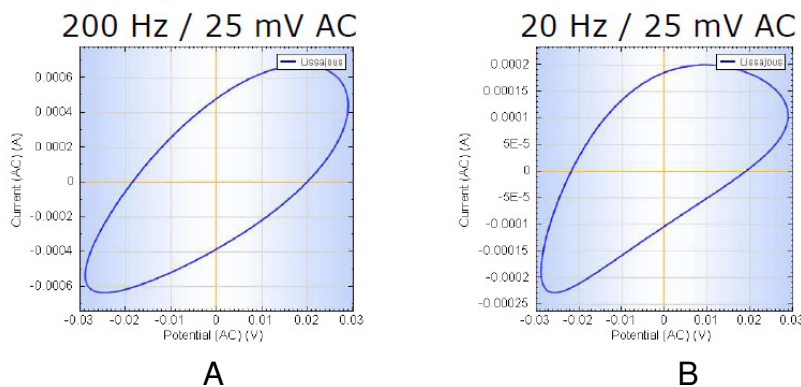


Figure 1.30: Non-linear Lissajous plots⁶⁰.

Another factor that needs to be considered in EIS measurements is the causality condition. This condition means that the measured AC response of the system must be directly correlated to the applied AC stimulus. The system should not be affected by outside disturbances, which will affect the measured AC response.

A Kramers-Kronig (K-K) test can be carried out in order to check consistency and stability of the data. The K-K test is a basic test for data validation and the equation links the real and imaginary components of complex quantities for systems fulfilling the conditions of linearity, causality and stability.

Stability means that the overall state of the system should not significantly change during the acquisition of the data.

An example of inconsistent and unstable results is shown in figure 1.31 and this shows that the experimental points do not follow the graphical representations.

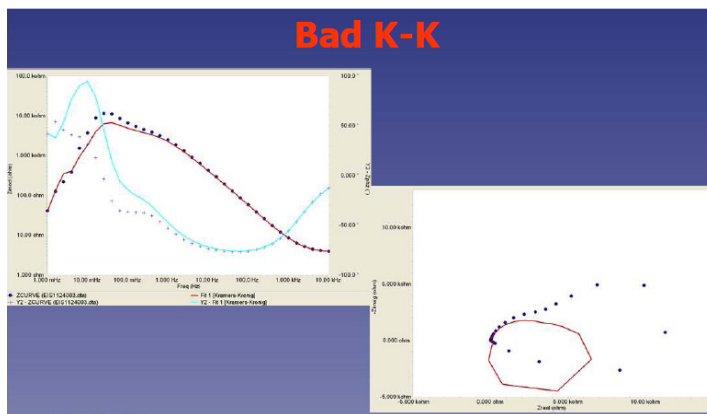


Figure 1.31: Bad K-K examples⁶⁰.

The K-K transform is usually applied to the EIS data and is performed by fitting a general model to the spectral data. If the general model as selected by the Gamry Analyst matches to the spectral data with a confidence value of 1×10^{-6} and smaller, the experimental setup and system under study can be considered as stable and linear⁶⁷.

A typical Nyquist plot for a battery chemistry system can provide certain characteristic information that is described by the different regions (Fig 1.32)⁶⁸.

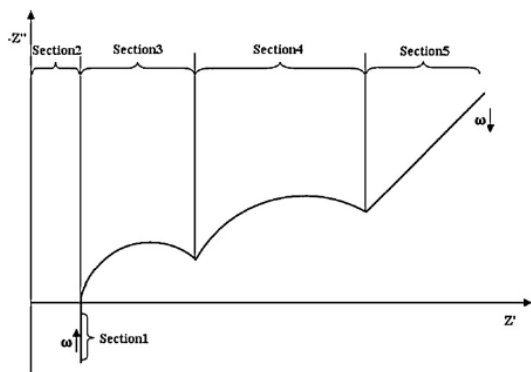


Figure 1.32: Different sections of an ideal EIS spectrum for a battery system⁶⁸.

The region shown as section 1 which could have negative impedance and would be due to the Inductance (L) of the cell. The inductance is usually indicated by the “tail” of the spectrum that is shown along the negative y-axis. The inductance occurs at high frequencies and is due to the inductive reactance that results from the metallic elements of the cell and sampling leads.

Section 2 of the spectrum is due to the sum of Ohmic resistances (R_1) of the current collectors, active material, electrolyte and the separator. This region occurs where the graph intersects the real impedance axis (x-axis). The distance from the imaginary impedance (y-axis) along the real impedance (x-axis) typically increases as the internal impedance increases due to the ageing processes of the battery. The third region includes the first semi-circle (Z_{arc1}) of the spectrum which is usually associated with the SEI layer that is formed on the anode during cycling. This semi-circle will change as the cell ages. The fourth region includes the second semi-circle (Z_{arc2}) which represents the double layer capacity and charge transfer resistance of the electrodes. This semi-circle will also change as the cell ages. The final region (Section 5) can be described by the Warburg element (Z_w) which is due to the diffusion processes in the active material of the electrodes at very low frequencies. A Warburg element in an equivalent circuit model can in simple terms being described as the distance the diffusing reactants travel within the cell. At high frequencies, the Warburg element is small as the diffusing reactants don't need to travel very far; however at low frequencies, the Warburg element is larger as the diffusing reactants need to move further. In Li-ion cells a bonded Warburg element can be used that takes the nature of the separator that is found in these cells into consideration⁶⁰.

The 5 regions modelling can be summarised in Figure 1.33.

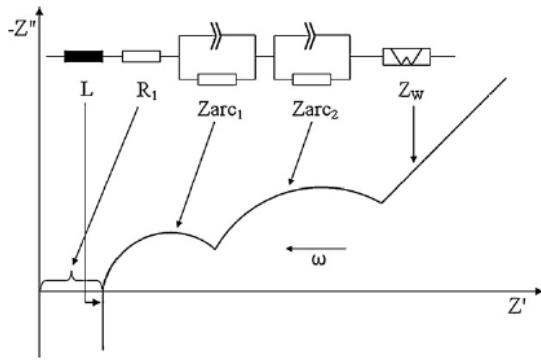


Figure 1.33: Ideal impedance spectrum of a Li-ion cell and an EC with Z_{arc} and Warburg element⁶⁹.

In laboratory examples where the electrochemical properties of the electrode material are researched, half cells are measured using EIS using typical half-cell impedance analysis where the reference electrode is an external electrode such as a lithium wire that serves as both the working and reference electrodes. However in the EIS study of sealed manufactured cells the observed spectra are a result of both the positive and negative electrode chemistries where the reference electrode could not be inserted into the sealed Li-ion cell and would be connected to the anode. Hence, the changes observed in spectra needs to take into consideration that the reference electrode could drift due to the electrochemical changes at the anode. The working electrode is usually connected to the cathode and the sensing electrode is connected to the graphite anode⁷⁰. When mixed cell chemistries are measured, it becomes difficult to differentiate which effects were due to either negative or positive electrode chemistry. The resulting semi-circle in the impedance spectrum would correspond to the combination of effects from the two electrodes (anode and cathode) in the battery⁷¹.

Various suppliers have software that can be used to obtain an Equivalent Circuit Model where the various components would then have suitable starting parameters to allow a least square refinement of the model and its parameters to a set of experimental data (Fig 1.34).

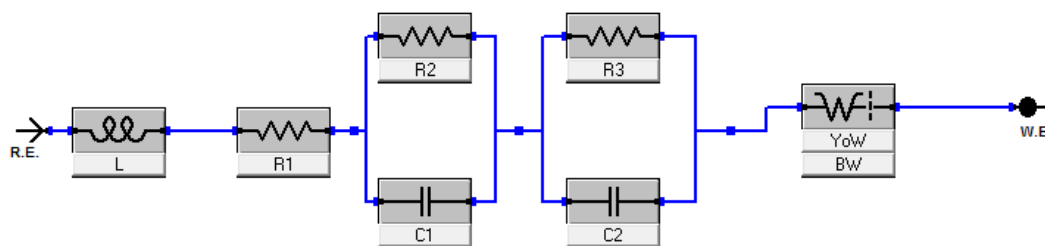


Figure 1.34: EIS model used to analyse EIS spectra of typical Li-ion cell chemistry⁶⁸.

EIS model parameter	Parameter description
L (H)	Inductance of circuit
R1 (ohm)	Resistance of circuit
R2 (ohm)	Resistance associated with the SEI as formed on the anode during cycling
C1 (F)	Capacitance associated with the anode
R3 (ohm)	Resistance associated with the double layer capacity and charge transfer resistance at the electrodes
C2 (F)	Capacitance associated with both electrodes
YoW (S*s ^a) and BW	Porous Bonded Warburg section of the cell

Table 1.3: Parameters used in the EIS model in Fig 1.34⁶⁹.

The changes in the different sections of the EIS spectrum can be modelled and the trends observed can possibly explain changes in the physical and chemical properties that occur for example during life cycle capacity ageing experiments. The electrochemical changes that are typically associated with such studies include the charge-transfer and the double layer charging that occur at the surface of the electrodes and the solid-phase diffusion inside the particle and an open-circuit potential which will vary as a function of the intercalant concentration. The model can also be used to examine the effect of an insulating film surrounding the particle (Fig 1.35)⁶⁶.

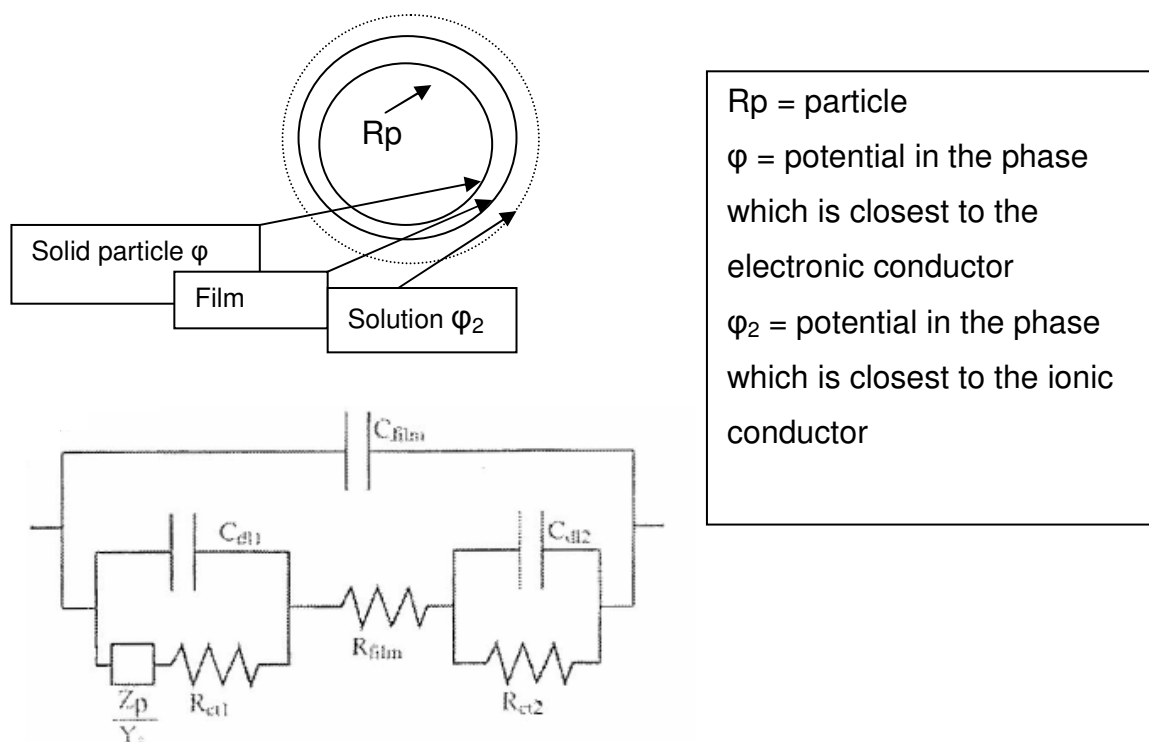


Figure 1.35. Schematic diagram of intercalation particle and an equivalent-circuit diagram of the interfaces⁶⁶.

A number of studies have reported the use of EIS to study the effect of porous electrodes⁶³. Most electrode structures do not have well-defined pores and consists of rather irregular network of interconnected spaces between the particles filled with electrolyte. Due to the absence of well-defined pores, there are some deviations of the description of the electrolyte impedance within the electrode active material. In porous metallic electrodes, where the metal-particle resistances are low such effects can often be neglected. However for batteries, both the electronic resistance of particles and the ionic resistance of the electrolyte in the pores are important and it is difficult to distinguish between the various conductivity contributions that make up a cell. Despite the inability to distinguish between these various contributions, information about the combined specific resistance of a porous electrode can be useful⁶³.

Any adsorption processes at the electrode surface, surface reaction, chemical modification or thermal changes while carrying out an EIS spectra can be seen when the data loops back on itself at the lower frequencies. For example in studies done at low temperatures (-20 °C) the cell's can show spectra that show the typical loop back

effect implying that the cell could be warming up during the EIS spectra scan (Fig 1.36).

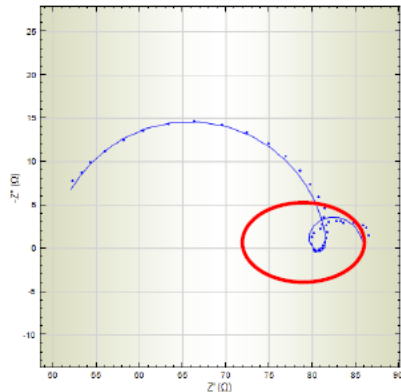


Figure 1.36: EIS spectra with a typical looping back of a cell studied at -20°C ⁶⁰. Other studies have shown that care needs to be taken when doing EIS studies at various temperatures. In addition to the ageing effect of the battery on the EIS spectra, the temperature will be giving competing effects in EIS spectra (Fig 1.37)⁶⁹.

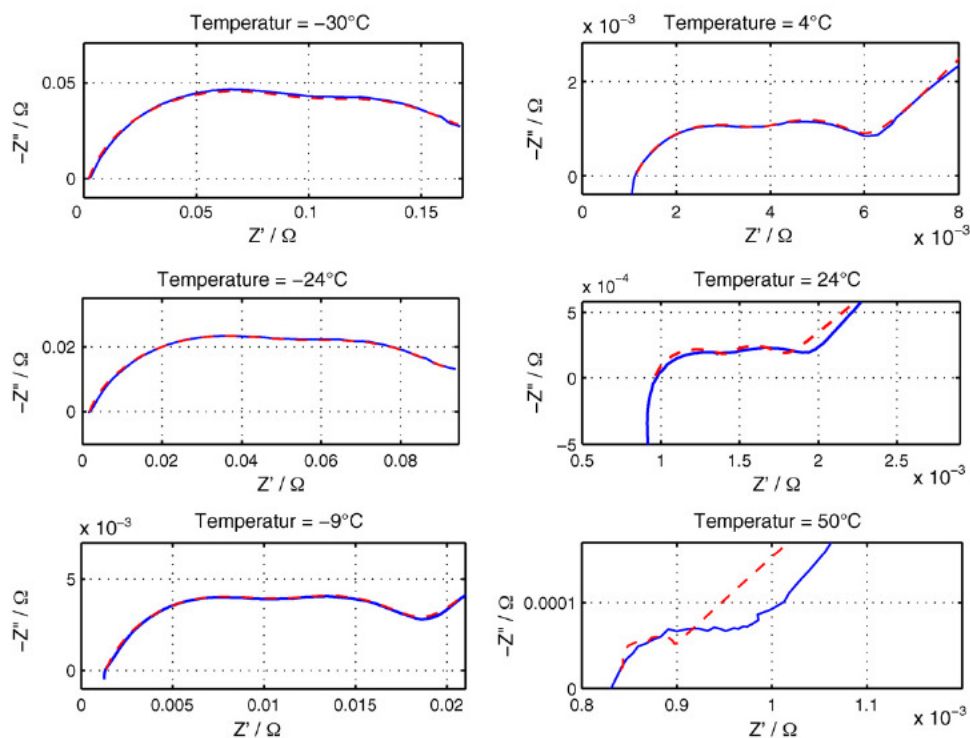


Figure 1.37: Comparison of a measured and simulated EIS data at different temperatures. The cell was at a 60% SoC. The solid line represents the measured spectra and the dashed line represents the simulated spectra⁶⁹.

At lower temperatures, the spread of the semi-circles can be observed (Fig 1.37 a). This was explained by the sequence of slower chemical processes that correspond

to higher cell impedances. The ohmic resistances of the cell increases showing that the diffusion processes are strongly depend on temperature. At elevated temperatures the semi-circles tend to grow together and cannot be clearly distinguished from each other.

A Li-ion cell or battery that is at different States-of-Charge (SoC) would also show considerable differences in their respective EIS spectra (Fig 1.38).

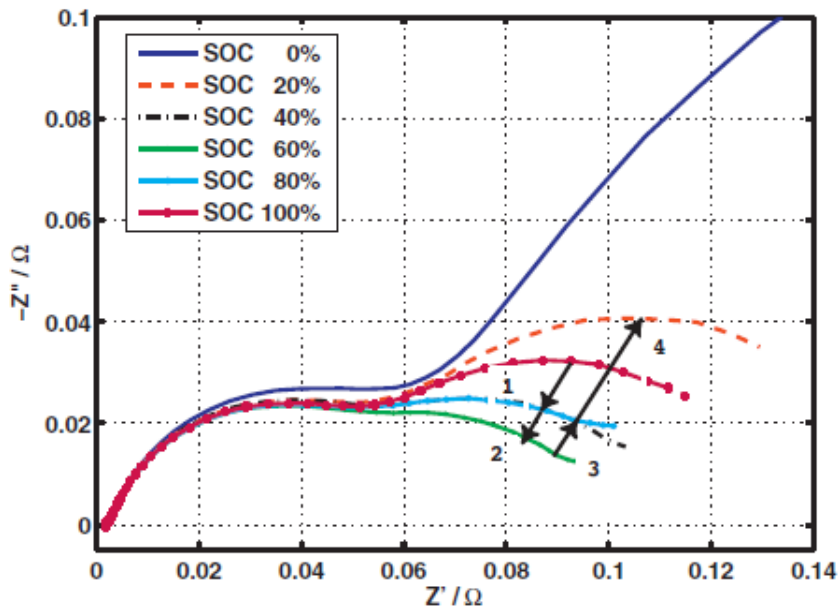


Figure 1.38: EIS spectra for different SoC at a temperature of -24°C ⁶⁸.

The study showed that for all the different SoC of the cell, the first semi-circle seemed to remain relatively the same. However the second semi-circle showed considerable variation with change in SoC implying that the resistance of the SEI is not necessary a function of SoC, but rather that the active materials charge transfer and diffusion resistance is dependant and higher in relation to a lower cell voltage. A number of studies have shown that there is a correlation between the deterioration of the cell's capacity that occurs with an increase in capacity cycle number to the overall cell impedance (Fig 1.39)⁷².

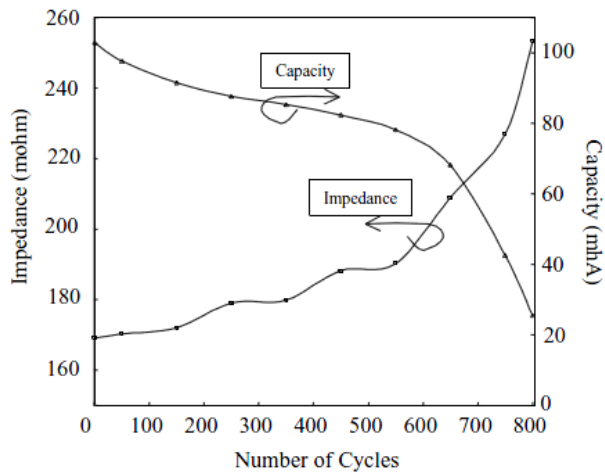


Figure 1.39 Deterioration characteristics of the battery capacity and impedance (1kHz)⁷².

In this study, EIS was used to study the changes that occur in the EIS spectra as the cell ages with cycling at different Depths-of-discharge. From the changes in the spectra due to the ageing of the cell i.e. the thickening of the SEI layer on the anode or cathode, an increase in the overall cell impedance will be seen.

In this study EIS was used to investigate the changes in impedance properties of a cell at different temperatures and States-of-charge (SoC).

1.9.1.4. Batteries with Supercapacitors tests:

Due to the small size and high energy density of Li-ion batteries they show great potential for EV and HEV applications. However, the battery is limited in its ability to accept large amounts of charge over a short period of time. In order to allow a system to absorb excessive energy during fast charging and discharging batteries are usually then oversized for a particular application that then adds unnecessary weight and cost to the system⁵⁸.

The supercapacitor has shown to be effective in absorbing large amounts of energy that is generated during applications such as regenerative braking, where a system that uses a battery only, would not be able to utilize all the energy that is produced. This study considered the combination of capacitor with cells and their ability to accept certain power input supplied from the EV systems of the vehicle such as regenerative braking. This procedure was done by combining different battery types to typical supercapacitors that would form part of the overall EV management system. A study in the literature had shown an efficient test method to determine the

effectiveness of a capacitor with a Pb-acid battery⁷³. This study considered a similar procedure for Li-ion cells where possible direct comparisons could be made.

When combining supercapacitors and batteries for testing, in order to increase the capacitance, the supercapacitors should be connected in parallel with the batteries. Not only is the capacitance increased but the overall equivalent series resistance of the bank is decreased, while connections made in series in order to increase the voltage rating will result in an increase in resistance. Defining n_p as the number of parallel capacitors and n_s as the number of series capacitors, the following equation can be used to define a configuration index m .

$$m = n_p / n_s \quad \text{(Equation 1.2)}$$

If $m > 1$ there were more parallel connections than series connections and if $m < 1$ the opposite is true⁷⁴. Depending on the application, different ratios of supercapacitors to batteries in parallel and series can be used.

1.10. Workshops on Lithium-ion batteries and literature review:

During this study of Li-ion cells and related chemistries, a number of workshops and conferences were attended. The main findings learnt as well as some important literature reviews are briefly discussed.

1.10.1. Workshop presented by Walter van Schalkwijk. July 2010, Cape Town, South Africa

In summary, the workshop focused on the basics of the battery chemistry that included the half cell reaction equations and the application of the Nernst Equation and their importance to battery chemistry. A short history of Li-ion battery chemistry was also presented and relevant in terms of current technologies and application. In terms of the electrode materials, discussion was presented on the different crystal structures and how Li-ions migrate between the anode and cathode during charging and discharging. It was noted that the electrons move via the outside circuit. It was important to note that often different Li-ion chemistries are used for different applications. For example, LiCoO_2 as the cathode is commonly used in laptops and

cell phones. LiFePO_4 is used in batteries that are used in buses. The LiMn_2O_4 , due to its three-dimensional structure improves the flow of ions between the electrodes and due to the ease of flow which allows for low internal resistance, the LiMn_2O_4 cell can be discharged to 20-30A with a very small increase in temperature. This battery was being used in some of the automotive manufacturers such as GM for their Volt EV. Each application would have its own set of testing procedures and voltage profiles that will suit the use of the battery.

The workshop also discussed the use of graphite and its limitations as the anode material in the charging of a Li-ion cell. Other anode materials were also discussed such as lithium titanate. When the lithium titanate is combined with LiCoO_2 , it was able to deliver 140-145 mAh.g^{-1} over 150 cycles with almost no fade – an impressive performance. The lower energy density of the anode material may detract from the overall cell capacity but the energy density improves the stability and possibly the safety of the battery.

Thermal runaway that can occur under various situations was discussed in more detail where the different temperatures limits for the different Li-ion chemistries were shown and precautions to reduce the possibilities of thermal run-away and why LiFePO_4 has a different thermal runaway profile.

Cells should not be used if they have been discharged below 3V, as some irreversible changes may have occurred at the electrodes resulting in early failure. However the dangers of over-discharging the cell below 1V were emphasized and clearly discussed where if a cell is discharged below 1V; the copper from the current collector begins to dissolve. If the cell is then subsequently recharged, the copper will begin to plate out on the electrode, which may form sharp dendrites that can then pierce the separator, resulting in short circuits which may lead to explosions or fires. A cell should never be recharged if it was discharged below 1V.

There were also potential problems if a cell is over-charged. The internal impedance of the cell would significantly increase if a cell is charged above the manufacturer's maximum voltage limit. This increase in internal impedance was due to too many solvated Li-ions moving towards the electrode surface. The high impedance could lead to lithium plating on the electrode, which would also form dendrites that may pierce the separator, causing short-circuits and excessive gassing that could result in the popping of the seam on a pouch cell.

Different mixtures of solvents are often used for different reasons, such as a mixture that will ensure that the battery can work at high temperatures and higher rate. A common salt that is used in Li-ion cells is LiPF_6 . Most solvents such as ethers will disintegrate at a voltage of 3.8V and higher. Research is currently conducted to find better solvents in cells that could possibly work at voltages as high as 5V. For these, a combination of ionic liquids is often considered.

The function of the Solid Electrolyte Interface (SEI) was discussed. The functions of the SEI being a protective layer that forms on the anode and thus prevents the further decomposition of the solvent but still allowed the movement of Li-ions in and out of the electrode active material. This SEI layer is formed during the initial two cycles of the cell just after manufacture. During application and extensive use, cracking of the SEI layer will cause more graphite to be exposed, which will react further with the electrolyte thereby increasing the SEI layer. Once the layer becomes too thick, the diffusion of the Li-ions in and out of the electrode active material is significantly reduced, resulting in a lower capacity of the cell. High rate charging will also increase the SEI layer growth.

Some of the manufacturing aspects of cells and batteries were discussed. Care must be taken during manufacture, in order to prevent contamination. An example of contamination was seen when a small amount of moisture is trapped within a cell that can react with the LiPF_6 salt to form LiF crystals, PF_5 and HF. The crystals would cause blockages within the active material pores, the PF_5 would react further with the cathode active material and the HF can corrode the current collectors that are made from Cu and Al. All these factors would result in damage to the cell.

Temperature changes will have an effect on the internal impedance of the cell, but by keeping a battery cool, but not in a freezer during storage, would ensure that the battery would have a longer shelf life. During cycle tests, it was not recommended that the cell is cycled at 1C below temperatures of 5°C. It was also not recommended that the cell is cycled above 45°C, as going beyond these cycling limits will speed up the capacity fade. In order to accelerate ageing of the cell, 1 month of heating the cell in a hotbox is equivalent to 8 months of ageing. It should be noted that during cycle testing, after the discharge cycle step, the Open Circuit Voltage (OCV) would increase slightly. This increase was due to the cell voltage evening out throughout the cell. A sharp dip in the voltage during cycle tests indicated a possible short circuit within the cell and thus the voltage should be

carefully monitored. If only temperature was monitored during the tests, a short circuit may not be quickly determined as the temperature effects lag in time. When deciding on which tests to carry out on cells or batteries, basic cycling tests can be carried out but it is important to measure current, voltage, time, temperature, internal resistance/impedance during the tests. These parameters would provide information of the cell as it ages. Cycle testing should be carried out at different temperatures, for example 0, 5, 10, 20, 30, 40, 50 and 60 °C. If the cells were cycled at temperatures of 5 °C and lower, this will have a dramatic effect on the ageing. Cycling at higher temperatures than 40 °C would also have an effect on the capacity of the cells. Testing the cell at 55 °C for 6 continuous weeks is equivalent to 48 weeks of age testing.

It is important to test cells/batteries at the 3 stages of life of a cell/battery, i.e. beginning of life, middle of life and end of life. These tests could include cycling at 100% DoD or at different %DoD. Very few tests were carried out when the cell/battery is at its end of life and thus many manufacturers don't know how long the cells would last for a particular application.

Other tests included mechanical, environmental and vacuum tests. One other test included the self-discharge tests that can also be carried out on cells where the cell is left to discharge over time without any charging. This test is carried out in order to determine if there is a 'leakage' of current, which would mean that the cell will never be fully charged.

When testing new materials, a coin cell can be made. When manufacturing the coin cell, the aluminium foil should be weighed prior to manufacture. This was carried out in order to calculate the weight of the active material. The cathode and anode materials would then be coated on to the current collectors and the coin cell sealed. The coin cell should then be fully charged, using the relevant chemistry voltage limits. Then discharge the coin cell over a 10 hour cell, once again using the relevant voltage limit. The cell should be weighed. Then cycle the cell at different C-rates in order to determine the energy density of the coin cell.

Two further tips were given when working with Li-ion cells: use a non-metallic cutting tool to cut cells open in a glove box. This will prevent shocking yourself and moisture contamination. It was also recommended that Vermiculite (can be purchased at garden stores, as it is used to condition soil) be placed in a container that holds your cells during testing. This would prevent the laboratory catching fire.

1.10.2. SACI ElectrochemSA workshop IV was presented by various speakers. February 2011, Port Elizabeth, South Africa

The basic concepts of Electrochemical Impedance Analysis (EIS) were discussed and presented amongst other topics of applied electrochemistry at a two day workshop. It was stated that EIS data may be displayed as either a vector or a complex quantity. A vector is defined by the impedance magnitude and the phase angle. A resistor will shift the phase by 0° , a capacitor will shift the phase by -90° and an inductor shifts the phase by $+90^\circ$. The complex quantity on the other hand is equal to $Z_{\text{total}} = Z_{\text{real}} + Z_{\text{imag}}$. Both the vector and complex quantities are different representatives of impedance and are mathematically equivalent. The difference between the Bode and Nyquist plots were also discussed. Electrochemical cells can be modelled as a network of passive electrical circuit elements. This network is called an "equivalent circuit". The EIS response of an equivalent circuit can be calculated and compared to the actual EIS response of the electrochemical cell. A Randles equivalent circuit is the simplest model that EIS data can be modelled against but systems such as seen with batteries will have an effect known as the Warburg effect. Another element which may be placed into an equivalent circuit is known as a Constant Phase Element (CPE). However this is a very general element of an equivalent circuit and great care must be taken when using a CPE, as this parameter represents a change within a cell and must still be explained. It is not acceptable to simply add elements until a good fit is obtained. Another important concept to EIS was the cable setup, for systems that will undergo 100Ω or less as seen in figure 1.40, the inductance of the wiring can be minimised by twisting the cables. With the current pair (red and green cables) on one side and the sense pair (white and blue cables) on the other side, as seen in the diagram below:



Figure 1.40. Cable setup during an EIS test.

It should be noted that all instruments have their limits and you must ensure that you know where your system lies, for example in energy devices such as batteries which have low impedances.

Advantages to using EIS were discussed such as the technique being a non-destructive technique. The information content of EIS is much higher than DC techniques and it is able to distinguish between two or more electrochemical reactions that are taking place simultaneously. EIS can identify diffusion-limited reactions, and EIS provides information on the capacitive behaviour of the system. EIS on energy devices were then discussed, and it should be noted that it is important to know what materials make up the energy device. By knowing what materials are involved in the system, it becomes easier to identify processes and what may have failed. Porous electrodes are known to complicate modelling. If a reference electrode is incorporated into the test system, this reference electrode must be very similar to the working electrode.

Various examples of spectra and modelling were shown on energy devices. These energy devices included fuel cells, porous electrode system, such as batteries and dye sensitized solar cells. Multi-Sine measurements can be used to measure several frequencies at once and are able to speed up the EIS measurements without losing information at either high or low frequencies.

EIS on corrosion and coatings were also discussed, for example carbon steel in aerated water, Stainless steel in acid and insulating coatings. Finally examples of EIS spectra of thermal cycling were observed.

1.10.3. The International Battery Association (IBA) conference, April 2011, Cape Town, South Africa

The conference began with a presentation that focused on the South African manufactured electric vehicle, Joule and the challenges of the battery management system. This was followed by presentations on a brief history of Li-ion batteries, future developments of the battery chemistry and market opportunities. The use of batteries in electric and hybrid electric vehicles was discussed.

A presentation entitled material properties and their influence on cell performance for automotive applications followed. It was seen that by adding manganese to the Li-ion cathode material, cycling at higher temperatures was possible. Manganese reduces the cracking of the active material, which allows for the higher temperature cycling. The disadvantage of adding manganese to the material, to increase resistance of the cell. Nickel can also be added to the cathode material in order to improve the cycling at higher temperatures. When working at low temperatures, the electrode materials

will be influenced. However the electrolyte resistance doesn't have an effect at these low temperatures.

Much information was presented on the research into Li-air batteries, where we have been, current research and future expectations. Current battery research in South Africa was discussed, and the manufacturing of Li-ion pouch cells that are presently being carried out by HySA Systems.

Presentations on various cathode material research followed. The presentations also included techniques in manufacturing of cells and doping of cathode materials.

These discussions were then followed by presentations on various anode materials and electrolyte research. It was seen that TiO_2 can be added to the electrode material as a safety measure against overcharging, and that different electrodes, in particular different anodes have different diffusion coefficients.

A presentation on insights into Li^+ -carbon interactions together with the technique of Raman Spectroscopy followed. New electrode materials, anode and cathode, as well as electrolytes for high power applications were discussed at the conference.

Various testing procedures of cells or batteries were not well discussed.

1.10.4. The Advanced Automotive Battery Conference (AABC). June 2011, Mainz, Germany

The AABC Conference focused on Li-ion batteries research, development and strategic implications for the automotive industry in particular. The other fields that were covered during the conference included Li-ion batteries for E-Bikes and energy storage for the grid system. Research and development on materials and applications for the supercapacitor industry was also covered at the conference.

There were also two tutorials sessions that were presented on the first day, these included:

Introduction into Lithium Battery Materials. Presented by Prof Martin Winter from the University of Muenster²².

The tutorial covered the 5 main groups of components needed for a battery, these groups include the anode material, cathode material, electrolyte, separator and case vents. These groups were then further divided into active and inactive materials. The anode and cathode materials were being classified as the active materials and the rest of the components being classified as the inactive materials. All the materials are critical for the proper functioning of the battery. A typical battery has 49.75%

active material and the other 50.25% as inactive material. The active material is responsible for the energy of the battery. When looking at an 18650 cell that is commonly used in laptops and cellular phones which weighs about 45g. 0.51g is active Li from the cathode and 0.11g is inactive Li from the electrolyte salt. The elements involved in a Li-ion battery are light, namely lithium, carbon and a small percentage of transition metals such as manganese, iron and/or nickel. Due to the advantage of these lightweight elements and a small size, a Li-ion battery is considered to have a high energy density when comparing with lead-acid and Nickel Metal Hydrides (NiMH) batteries. Energy density is defined as the amount of energy stored within a given volume. A lead-acid battery for example will need to have a larger volume of space to accommodate the same amount of energy output as a Li-ion battery.

The workshop also went into the history of the different active cathode materials, from the original LiCoO_2 chemistry and its limitations, through to the chemistries being developed today. These chemistries included structured oxides of materials that contain cobalt, manganese, nickel and iron. The different anode materials were also discussed from metallic lithium to typical graphite to lithium titanates. The different lithiation reaction mechanisms and the basic structures of the cathode materials were explained in more detail classifying them into the layered (eg: LiCoO_2 , $\text{LiNi}_{1/3}\text{Mn}_{1/3}\text{Co}_{1/3}\text{O}_2$ and $\text{LiNi}_{0.8}\text{Co}_{0.15}\text{Al}_{0.05}\text{O}_2$), spinel (eg: LiMn_2O_4) and the olivine (eg: LiFePO_4 and LiMnPO_4) structures. New materials that are being developed include the doping of the oxides which was shown to improve the stability and cost of the active cathode material. Higher voltages and more capacity can be achieved when combining different elements in the cathode material.

The electrode active material design can be complex and parameters such as structure stability, redox potential, thermal stability, size effects, surface effects and others need to be carefully considered and monitored when manufacturing this electrode active material.

The workshop also discussed aspects of the inactive materials in a battery. These included the different electrolytes that can be used in a battery, different separators, current collectors and binders. It is important to select the correct electrolyte in order to ensure that the Li ions are able to travel between the electrodes, that the electrolyte contributes to cell safety and that the electrolyte forms a stable but thin Solid Electrolyte Interface (SEI) that will protect the electrodes but still allow Li ions

to flow. There are different separator materials available which must offer good chemical resistance, temperature stability, high wettability and battery safety. In general, the achievable energy is only one parameter of a battery; there are other parameters such as performance and cost that need to be considered when designing and optimizing batteries.

The 2nd workshop was on the engineering of Supercapacitor Storage Systems. Presented by Dr. Roland Gallay from Garmanage¹⁶.

Supercapacitors can be used in various industries; these include medium size wind turbines, static energy storage systems, electronic consumer products such as digital cameras, hybrid electric buses and automotive hybrids. All automotive manufactures have hybrid programmes, where they may have a form of a hybrid in the market or are currently developing a hybrid for the market. The different hybrids can be classified as full hybrid (good cost saving, biggest voltage range and are responsible for the functions of stop-start, regen, active boost, electrical drive and auxiliary users of the vehicle); active hybrid (similar to a full hybrid but not responsible for the auxiliary users); mild hybrid (fewer functions, less savings and lower voltage range) and finally a micro hybrid which is only responsible for the stop-start function of the vehicle, provides very little saving and has a small voltage range.

Different supercapacitor designs are currently being developed by the different automotive manufactures. Such as the stop-start technology being developed by PSA, this system reduces the fuel consumption of the vehicle, reduces CO₂ emissions, reduces the size of the battery by 30%, and provides more torque and other advantages. Another design discussed included the KERS (Kinetic Energy Recovery Systems) as used by the different F1 competitors. The kinetic energy of a moving vehicle is recovered under braking and is stored in a reservoir (for example a battery, supercapacitor or flywheel) to be used at a later stage under acceleration. The design of a supercapacitor was then discussed. It is important to note that each layer within a supercapacitor needs to be connected to a current collector that can deliver the energy from the supercapacitor. This is carried out in order to reduce the internal resistance of the supercapacitor. In a supercapacitor all of the following adds resistance to the overall system: conductors, collector, carbon, separator and electrolyte. Many equations were discussed that describe the power available for a supercapacitor when considering the internal resistance.

A website was given that can be used when deciding on a supercapacitor for a particular application. Voltages, energy requirements, power ratio, temperatures, current etc are all taken into account in the spreadsheet on this website:

http://garmanage.com/atelier/index.cgi?app=sizing_scap

The rest of the week involved 20 minute presentations by experts in their fields' specific to Li-ion batteries and their application. Sessions were run concurrently dealing with topics on Li-ion batteries and supercapacitors. Some of the highlights of the presentations given are summarized as follows:

- Li-ion battery presentations:

A talk on the pricing of LiCoO₂ chemistry in the last decade was presented. The LiCoO₂ chemistry was the chemistry of choice for the last decade as it was used in the 18650 cell design. The 18650 cell design was used in most applications. However as the price of cobalt increases, manufacturers are looking at reducing the amount of Co in their batteries, and replacing with Ni, Mn and/or Fe. A prediction was made on how the markets would grow and which chemistries will see growth patterns by 2020. This was followed by a talk on recent advances in cathode materials for automotive applications by Toda Energy Materials Company. Once again the development of Li-ion battery chemistry containing Ni, Fe, Co and Mn were shown to be where the markets were moving. A new cathode material of using stabilized Nickelate Cathode Material for high-energy and high-power automotive Li-ion cells was discussed. Tiax has developed and owns the IP on this chemistry. Presentations were made on the effect of coating and drying processes on the electrode structure and performance. Once again, progress and challenges of Li-air battery technology were discussed. Finally presentations showing Li-ion batteries in other markets such as E-Bikes and Energy storage was discussed. The strategic implications of Li-ion batteries for automotive applications were discussed and some new developments by the different manufacturers shown.

- Supercapacitor presentations:

Presentations focused on how to increase the specific energy of electrochemical capacitors by changing the electrode material. Applications of supercapacitors in city buses and trains were discussed as well as the combination of a supercapacitor with

a Li-ion battery for use in the automotive industry. When designing the combination of supercapacitor with Li-ion battery, a well designed Battery Management System (BMS) needs to be carried out. Without the BMS, a very small increase in current storage and delivery will be achieved.

1.11. Literature Review:

The following reviews are of articles found in the literature which are relevant and of interest to the study.

Ageing of lithium-ion batteries. Guy Sarre, Philippe Blanchard, Michel Broussely. Journal of Power Sources 127 (2004) pages 65-71

Li-ion batteries containing liquid electrolytes are considered as having a long life and providing reliability. Li-ion batteries have for the last 10 years provided tremendous growth in the field of consumer applications such as mobile phones or portable computers. The new challenges exist that this technology must now be viable and compete with other battery chemistries in the fields of standby, automotive or space and defence applications. The Li-ion battery must be able to provide better life cycle cost and show excellent life behaviour on real configuration where floating, cycling and OCV storage are combined.

This paper showed results obtained until now by Saft with a cell design that was based on lithiated nickel oxide as the positive electrode. Some basic mechanisms were used to explain ageing phenomena on both the negative and positive sides. All these cells were built with the standard active materials and components. High energy (HE) cells and a high rate power (HP) cells were selected in order to illustrate the compromise between power ability and energy content. The two types of ageing situations that were selected included storage and the operational use according to charge and discharge profile corresponding to the applications. While cycling generally damages the materials reversibility, ageing that is caused by storage is widely caused by interactions between the electrolyte and the active materials. The impact of the cycling behaviour on the energy (or capacity) and power can be described according to the effect on the different cells. The HE cell was cycled according to a typical EV profile which was obtained from the DST cycle. The cell was cycled between a fully charged cell and an 80% DoD. The results showed that

after 1000 cycles, the cell showed negligible loss of energy and about 3% of the power was lost under the test at 80% DoD under a 30s peak current of 150A.

The HP cell was subjected to a hybrid vehicle profile according to the PNGV (Partnership for a New Generation of Vehicles) specifications that consisted of a discharge at 1.5% SoC regeneration around the 50% SoC for the cell. After 350 000 cycles, the capacity and power values remained the same.

During storage tests, both the HE and HP cells were stored at different temperatures and voltages typical of the working SoC were obtained, i.e. 100% SoC for the HE and 50% SoC for the HP cell.

After a period of 22 months the capacity and power of the HE cell was stable at 20 °C, and showed a loss of 4% at 40 °C. After 1 year of storage even at high temperatures, the HP cell provided the same performance.

The ageing phenomena of Li-ion batteries can be attributed to the reaction of the active materials with the electrolyte at the electrode interface. The phenomenon is also due to self degradation of the active material structures on cycling and ageing of non-active components contributes to the ageing.

The kinetics of the reactions will vary with different types of Li-ion systems (whether they are nickel, cobalt or manganese) and will also depend on the reactivity of the materials and the electrolyte. The presence of impurities; the manufacturing processes both for the raw materials and the complete cell and cell design will all have an effect. The application and operating profile will also have an effect.

When looking at the negative side of the cell, the stability of the passivation layer, which is built at the electrolyte/electrode interface, is a key to the ageing. A very low electronic conductivity should be maintained. However the ionic Li^+ conductivity must be maintained at a high level in order to ensure that there is a sufficient discharge rate. The film growth caused by electron tunnelling through the layer is irreversibly consumed lithium, which is formed during the first charge, but is self-inhibiting due to the thickness increase. Metallic impurities caused by the reduction of soluble ions may have a very detrimental effect by increasing the electronic conductivity. This will increase the cell impedance.

On the positive side, unlike lithiated graphite electrode, the positive oxidation power depends on the SoC. Ageing at high voltage will lead to oxidation of the electrolyte components which may induce insulating solid deposits which will reduce the active

surface. This will result in an increase in the actual reaction current density. This phenomenon will be enhanced by temperature.

In conclusion, it can be found that this chemistry shows reliable and long life behaviour as the more than 1000 deep cycles were carried out. Several thousands of shallow cycles were also performed. According to application and operating, a minimum life prediction of about 6-20 years can be obtained.

Investigation of battery end-of-life conditions for plug-in hybrid electric vehicles. Eric Wood, Marcus Alexander, Thomas H. Bradley. Journal of Power Sources 196 (2011) pages 5147-5154

An advanced vehicle technology such as the Plug-in hybrid electric vehicles (PHEVs) has the capability to improve the near-term sustainability of the transportation energy sector. This technology is able to store energy on-board in the forms of gasoline and electricity, PHEVs offer the potential to significantly reduce greenhouse gas emissions and improve national energy security.

However PHEVs need to be tested in order to determine the life cycle cost and consumer acceptability. The question was asked - can test procedures from the USABC be used? The USABC standards, established for the End-Of-Life (EOL) for Battery Electric Vehicles (BEV), state that specific failure criteria is met when “the net delivered capacity of a cell, module, or battery is less than 80% of its rated capacity when measured on the DST” or “the peak power capability determined using the Peak Power Test is less than 80% of the rated power at 80% DoD.

USABC last updated its battery EOL testing procedure in January 1996. However since then, much progress has been made in the field.

Between 2005 and 2009, a PHEV battery pack was degraded in a laboratory over 4323 charge/discharge (CD) cycles using a PHEV specific test profile. The profile is shown in the figure 1.42 below:

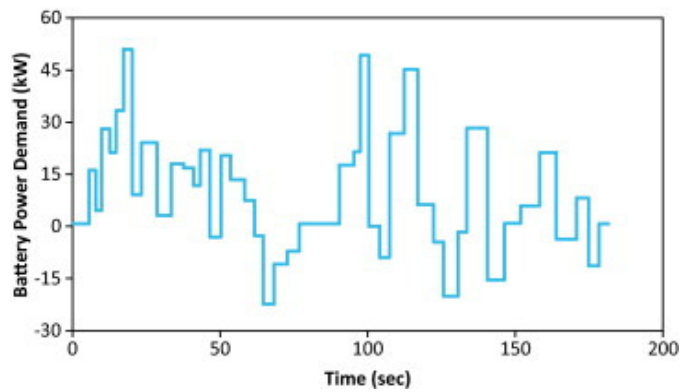


Figure 1.41 PHEV CD test profile used to define PHEV-specific battery degradation test procedure⁷⁵.

The PHEV specific test profile is made up of a series of CD, CS (charge sustaining) steps. These tests were used to simulate the types of battery usage common to PHEVs.

Reference Performance Tests (RPTs) were conducted before the start of the life cycle test, and at periodic intervals every 240 test cycles. 240 test cycles is equivalent to approximately two months of testing. These RPTs were carried out in order to characterise the performance of the battery.

Two degradation control strategies (DCS) were presented in order to demonstrate ways in which vehicle level efficiency and performance change with battery degradation.

The 1st DCS method used a degradation test based on capacity-based SoC. The results that were obtained showed a decrease in Peak Power over 4000 cycles. The internal resistance during discharge increased over 4000 cycles. The same trends were observed at 60% DoD, 70% DoD and 80% DoD. The effect was more pronounced at 80% DoD. This test is known as the static DCS test as the SoC remains constant.

The 2nd DCS method used a degradation test based on using t-SoC. The t represents a change in SoC, as determined after the RPT tests. Similar trends were observed with the t-Soc as with the capacity-based SoC. This test can also be described as a dynamic DCS test, as the SoC changes after the RPT.

Using the two DCS, the following diagram shows how the fuel consumption will be affected by the battery degradation.

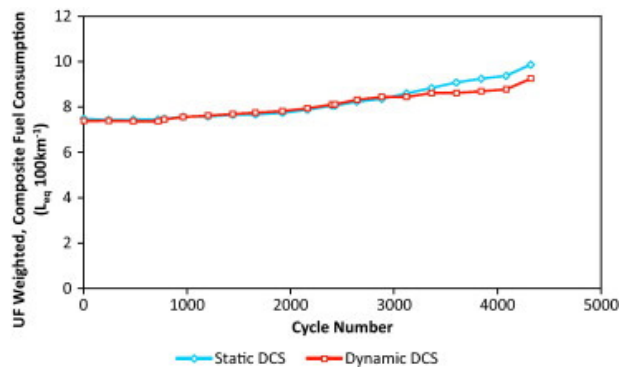


Figure 1.42 PHEV fuel consumption as a function of cycle number⁷⁵.

As can be seen from the graph, the static DCS test showed an increase in fuel consumption as the battery degrades.

When examining the cost of ownership the cost of batteries in PHEVs had to be investigated.

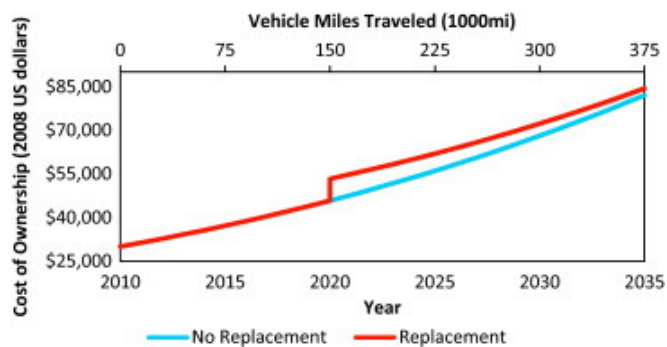


Figure 1.43 Cost of ownership model demonstrating the cost of battery replacement in PHEVs⁷⁵.

With no replacement the cost steadily increases, however when the battery is replaced, there will be an increase in cost, as it is a new battery, but the cost will gradually decrease again and match the cost of not replacing the battery. A variety of studies assume that PHEV battery life can be predicted by the USABC cycle life test procedures. However this assumption has dramatic effects on the PHEV lifecycle costs and consumer acceptability. When looking at the results, it is unlikely that the USABC definition for battery EOL will be predictive of how customers and vehicle manufacturers will approach battery replacement.

PHEVs differ from BEV, as they are designed to sense battery degradation and subsequently increase the degree to which they are blended to make up the power difference. Consequently the battery will need to be replaced when the fuel saving is greater than the battery replacement cost.

Finally, due to the disconnection between the existing test method and modern PHEV battery requirements and control capabilities, the USABC needs to consider revising their test procedures. Specific battery designs or battery applications should have their own testing procedure.

Characterization of high-power lithium-ion batteries by electrochemical impedance spectroscopy. I. Experimental investigation. D Andre, M. Meiler, K. Steiner, Ch. Wimmer, T. Soczka-Guth, D.U. Sauer. Journal of Power Sources 196 (2011) pages 5341-5348

During the next few years the automotive sector will face a challenging change from the internal combustion engine to the electrified power trains. However this will be a long and tough change as there are many technical issues that need to be resolved. One of the main tasks of the battery in HEVs will be to provide sufficient amounts of power for acceleration, and thus reducing the CO₂ emission at all operating conditions. The performance of all batteries is measured by their open circuit voltage (OCV), nominal capacity and impedance (Z). Whereas OCV and cell capacity are only affected at low temperatures, the impedance is strongly temperature as well as SoC dependent.

Both State-of-Charge and temperature will have an influence on the performance of a commercial high-power Li-ion cell. This influence can be investigated using electrochemical impedance spectroscopy (EIS). Cells were subjected to a complete range of automotive applications and the cell impedance measured and analysed. A strong nonlinear temperature correlation was shown for all frequency ranges. The ohmic resistance was nearly unaffected by the variation in SoC, but the mass transport impedance reduces between 100% to 60% SoC, and then increases again for lower SoCs.

EIS is a widely used experimental technique that is used to gain insight into the electrochemical systems. If all the internal processes are ignored, the cell voltage will drop linear as described by Ohm's Law. However, in reality, the voltage declines in three parts. These three parts include ohmic loss, which will take effect without any time delay after the current pulse. The second one is the voltage loss which is caused by charge transfer runs after a time delay, which is determined by the double layer capacity into a steady voltage. The third and final one is the voltage loss

caused by insufficient diffusion of Li-ions into the active material which increases till the end of the voltage drop.

The EIS method involves applying a sinusoidal signal and measuring the characteristic response from the cell which will depend on the cell impedance. This input signal can either be current (galvanostatic) or voltage (potentiostatic). A typical current or voltage curve for EIS has the form of a Lissajous figure.

Various graphs were plotted and graphed for tests involving testing the cell at different SoC and temperatures simultaneously. Both the Bode and Nyquist plots were examined during the analysis.

The influence of temperature on the analysis: a very strong spread of both semi-circles was observed for decreasing temperatures. This indicated that there was an increase in the SEI resistance. The double-layer resistance increased with decreasing thermal energy. The intersection with the real axis occurs at lower frequencies for higher temperatures, but the impedance caused by the diffusion phenomena starts at higher frequencies with increasing temperatures. Temperature will have a strong impact on ohmic resistance. Within the temperature range the resistance almost triples over these automotive applications. Typical vehicle operations are in the range of a few seconds and therefore comparable with impedance values at 0.1Hz. This additional consideration of charge transfer and diffusion yields into an even higher impedance. The consequence is insufficient amount of power at low temperatures. This will result in either higher fuel consumption or even issues of cranking if no additional starter battery is provided. Therefore the battery and power train need to be specially designed to accommodate these consequences even at low temperatures.

The influence of SoC on the analysis: a strong effect on the impedance spectrum affecting the second semi-circle is especially visible for SoCs below 30%. This semi-circle is associated with charge transfer and diffusion resistance. As the SoC drops below 30%, the charge transfer and diffusion resistance increases. In contrast to temperature, SoC has a small influence on the ohmic resistance. Thus the measurement of internal resistance is not suitable as an online SoC indicator of the cell.

In conclusion, it is noted that temperature has a greater effect on cell impedance and only a small influence is due to the SoC.

Characterization of high-power lithium-ion batteries by electrochemical impedance spectroscopy. II. Modelling. D Andre, M. Meiler, K. Steiner, Ch. Wimmer, T. Soczka-Guth, D.U. Sauer. Journal of Power Sources 196 (2011) pages 5356-5363

A common way to model Li-ion batteries is to apply equivalent circuit (EC) models. In this paper two different EC models were built up and parameterized for a commercial 6.5Ah high-power Li-ion cell. The measured EIS data depended on temperature and SoC.

The first EC model consisted of ohmic resistance (R), an inductor (L), and three RC-elements (a parallel connection of a capacitor (C) and a resistor). The second EC model consisted of one R, one L, two Zarc elements and a Warburg element. The estimated parameters were used to develop two empirical electrical cell models which could be used to predict the voltage of the cells depending on the current, temperature and SoC. A Butler-Volmer adjustment was made as no DC-offset was used for the EIS measurements and the effect of current on cell overvoltage was unknown. However this adjustment is important for charge transfer.

Different current profiles were used to determine their performance over a wide SoC and temperature range. These profiles were then used to validate the models. The first validation was carried out to test the models in the whole SoC range by comparing the results of cell characterisation tests for simulation and measurement. The models were tested and analysed for several cycling profiles and finally validated against data recorded during a HEV drive.

The next validation was carried out against drive cycles at five different temperatures measured in a laboratory.

The results of the modelling showed that for the 1st model, it was not possible to reproduce the measured data even with optimized parameters sufficiently. It was too simple. The second model reproduced the spectra very accurately. The validations however showed that both models predict the cell voltage very precisely. However the 1st model was not able to reproduce the impedance curves but did predict the voltage precisely.

Comparisons of both models showed a 20% higher mean error for the 1st model against the 2nd model. However this mean error is in the range of a few mV.

Therefore it can be concluded that the impedance fitting plays a role for the simulation quality, but the influence is small.

In conclusion, both models allow for precise prediction of the battery voltage and battery performance. Thus you can use both models for simulations of for example consumption, vehicle range, cooling requirements and battery lifetime prognosis.

1.12. Objectives of this Dissertation:

The objective of this dissertation is to develop and evaluate various testing procedures on different Li-ion battery chemistries and battery designs used in Electric Vehicles, with the aim to determine end-of-life predictions and how the cell internally ages. The various test procedures selected included:

- Peukert tests on all cells prior to commencing with any other test procedure.
- Ragone tests via the constant current and the constant power methods. This test was carried out on two LiCoO₂ cell designs, namely pouch and cylindrical. The tests were also carried out on a Pb-acid cell.
- DoD window tests at the three regions of a LiCoO₂ discharge curve. These tests were also carried out on pouch and cylindrical cells. As part of this study, an alternate test procedure was developed, that investigated the different stresses within a cell at different regions of a discharge curve of that cell chemistry. Capacity cycling the Li-ion cells within three different voltage windows allows the electrode material to experience different levels of material stress. An understanding of the battery behaviour and the stress that the battery undergoes at the various regions of the discharge curve, allows the EV manufacturer to optimise their on-board battery management system. Since the state-of-health of the cell will be affected by these different regions on the discharge curve and how often the cell remains in these regions, Electrochemical Impedance Spectroscopy would be used to record these changes. This will allow an optimization of the achievable capacity for the duration of the battery life. EIS studies can then be carried out in order to monitor the change in certain parameters as an indication of the health of the cell with cycle time.
- EIS analysis would be used on cylindrical and pouch cells at different temperatures and SoCs in order to investigate to what extent the cell design had an influence on certain parameters.

- High rate charge/discharge tests will be carried out on combinations consisting of supercapacitors and Li-ion pouch cells, supercapacitors and Li-ion cylindrical cells and finally supercapacitors and Pb-acid cells. A test procedure from literature has been used in this study in order to compare the current acceptance and delivery of a battery alone against a battery connected with a supercapacitor⁷³.

CHAPTER 2:

2.1. The instrumentation

The battery cycling tests were carried out on a Bitrode LCV50 Battery Tester. The Bitrode Battery Tester was supplied with thermocouples for each channel. These thermocouples were used to measure the outside surface temperature of the cell during cycling. The various test procedures were programmed using the Bitrode software that was supplied with the Battery Tester. The Electrochemical Impedance Spectroscopy spectra on the lithium-ion cells were carried out on a Gamry Instruments Potentiostat 3000. The EIS spectra obtained were analysed using Echem Analyst version 5.6 supplied by Gamry Instruments.



Figure 2.1. Bitrode Battery Tester.



Figure 2.2. Gamry Impedance Analyser connected to a 20Ah pouch cell.

2.2. Experimental procedures

The study was carried out on three types of Li-ion cells. These three types included: a 2Ah Samsung CGR18650CG lithium cobalt oxide cell (code: MH12210), a HySA Systems manufactured 1Ah lithium manganese oxide pouch cell and an anonymously supplied 20Ah lithium cobalt oxide pouch cell. HySA Systems is located at the University of the Western Cape (UWC). In addition, 7Ah VRLA Lead-

acid batteries supplied by Powertech were also used for some testing procedures. The supercapacitors used in the study included 10F, 2.5V Electric Double Layer Capacitors (Gold capacitors) manufactured by Panasonic (otherwise known as Matsushita Electric Industrial Co in the Far East). 3.3F, 2.5V Electric Double Layer Capacitors (Gold capacitors)/HW Radial lead type manufactured by Panasonic.



Figure 2.3.
20Ah
pouch cell.



Figure 2.4
2Ah
cylindrical
cell.



Figure 2.5. 10F, 2.5V supercapacitor.



Figure 2.6. 3.3F, 2.5V supercapacitor.



Figure 2.7.
7Ah VRLA Pb-
acid cell.

2.2.1. Peukert Tests:

Each cell was analyzed by a number of different discharge rated steps matching C/1, C/2, C/5, C/10 and C/20 rates in order to obtain a Peukert relationship⁵⁰. The temperature change during the Peukert analysis was measured for all the cells tested by means of a thermocouple that was attached to the Bitrode Battery Tester. The thermocouple was externally taped to the cell housing.

The parameters used for each cell type during the Peukert Test:

	C rate	Current (A)	Voltage limits (V)
20Ah pouch cell	C/1	20	3.0 to 4.2V
	C/2	10	
	C/5	4	
	C/10	2	
	C/20	1	
2Ah cylindrical cell	C/20	0.1	3.0 to 4.2V
	C/10	0.2	
	C/6	0.34	
	C/4	0.5	
	C/2	1	
	C/1	2	

Table 2.1 Parameters used for each cell type.

2.2.1.1. Cautions that need to be considered with the Bitrode Tester:

All cells must be tightly fitted to the cables before the test procedures were carried out, in order to prevent short-circuits. Voltage limits were programmed into all charge and discharge steps in order to prevent the cell from overcharging or over discharging. The voltage limits used on Lithium-ion cells tested included: 3.0 as the lower voltage and 4.2V as the upper voltage limits. The Bitrode Battery Tester had 5 LCV channels that were able to carry 50 A of current limits There were 2 sets of 8 channels on the MCV unit that had 10 A current limits. The 20Ah pouch cells were connected to the Battery Tester using a suitable bolt and nut to 50A units. The 2Ah and 1Ah cells were connected to the lower rated testing units using suitable bolts and nuts to the 10 A units.

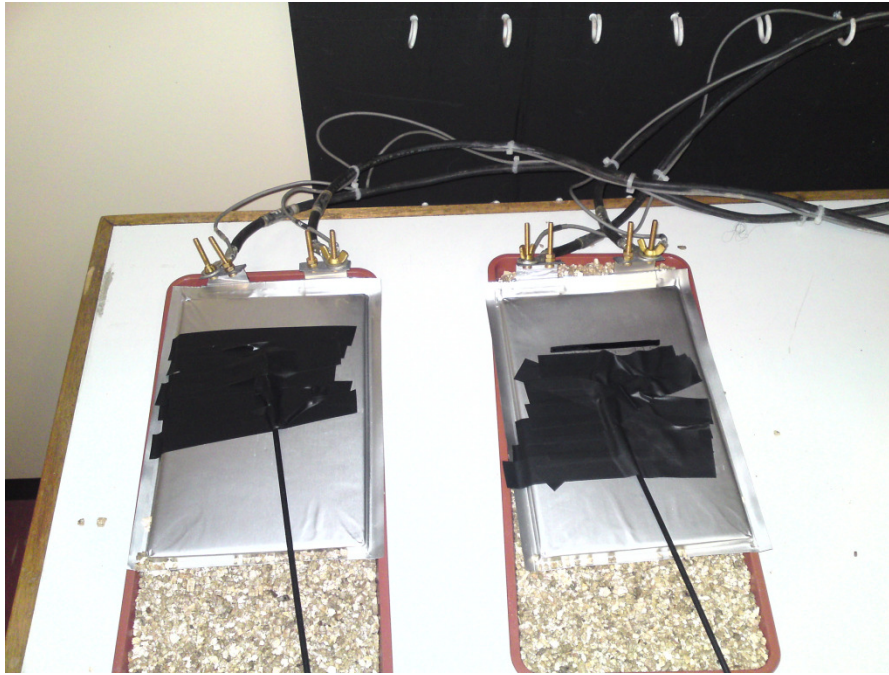


Figure 2.8. 20Ah pouch cells connected to the Bitrode battery Tester.

Vermiculite was placed around the cells in order to reduce the risk of a fire due to cell short-circuiting during the testing procedures.

Each channel on the Battery Tester was calibrated by the manufacturer's appointed service technician.

2.2.2. Ragone Tests:

A Ragone test was performed to determine the energy and power densities for the different Li-ion battery configurations (cylindrical and pouch) and to compare two different battery chemistries (Li-ion and Pb-acid). In theory, the larger the energy density of a cell, the more power that cell would be able to deliver for its size. There were two methods described in the literature that could be used: either a test at constant power or at constant current¹³. Both were done in this study to determine possible differences between them.

Constant current Ragone Test method comparison between different capacity cells:

A comparison was made by using the 20Ah Li-ion pouch cell, 2Ah Li-ion cylindrical cell and 7Ah VRLA Pb-acid cell. The test method was used in order to show the different energy densities of the different capacity cells. The values used for the comparison were obtained from a Peukert Test as seen in table 2.1. Additionally the

values used for a constant current Ragone Test method for the 7Ah VRLA Pb-acid cell can be seen in Table 2.2.

	Current	Voltage limits (V)
7Ah VRLA Pb-Acid cell	0.35 A	1.75 to 2.4V
	0.7 A	
	1.4 A	
	3.5 A	
	7 A	

Table 2.2. Parameters for the 7Ah VRLA Pb-acid cell during the constant current Ragone test method.

Constant power method comparison between different capacity cells:

The same cells were then tested via the constant power Ragone test method⁷⁶. The power values used for the comparison were calculated from the Peukert test.

Parameters of each cell type when completing the constant power Ragone test method:

	Power (W)	Voltage limits (V)
20Ah pouch cell	3	3.0 to 4.2V
	6	
	12	
	30	
	60	
2Ah cylindrical cell	0.15	3.0 to 4.2V
	0.3	
	0.6	
	1	
	1.5	
7Ah VRLA Pb-acid cell	0.15	1.75V to 2.4V
	0.3	
	0.6	
	1	
	1.5	

Table 2.3 Parameters for each cell type.

Graphs were drawn showing the power densities vs. energy densities of each cell at the different discharge steps based on the cell mass.

2.2.3. DoD window tests:

The Li-ion cells were subjected to a discharge test at different DoD window regions that occur on a typical discharge curve for a Lithium Cobalt oxide cell (Fig 2.9).

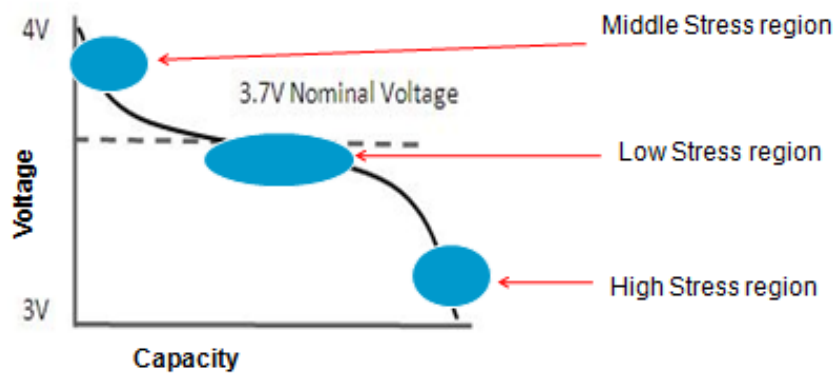


Figure 2.9. Discharge curve of a typical LiCoO₂ cell showing the 3 stress regions. The 20Ah pouch cell and 2Ah cylindrical cell were subjected to cycling tests within three different regions (Table 2.4).

DoD window region	Voltage region	Stress region
Low	3.94V to 4.2V	Middle
Middle	3.58V to 3.94V	Low
High	3.0V to 3.58V	High

Table 2.4. The different DoD window regions showing the voltage range and degree of stress.

For the pouch and cylindrical cells, a C/1 discharge step was carried out before the cycle loop testing. This was done in order to determine the constant discharge power value.

For the 20Ah pouch cells, the cycling loop sequence consisted of a charge step at a 0.1C (2A) and the discharge at a constant power (74W) between the desired voltage limits. A test unit consisted of 50 loops before the cells C/1 capacity was determined again.

For the 2Ah cylindrical cells, the cycling test sequence was different in that the loop sequence consisted of a constant power discharge (7W) between the desired voltage limits followed by a 20 minutes rest step. No charge step was included during the loop sequence in order to accelerate the cell deterioration within the

various “stress regions” of the discharge curve. A test loop sequence consisted of 200 loops within the voltage limit ensuring that all available materials capacity within the cell was depleted.

2.2.4. Electrochemical Impedance Spectroscopy (EIS):

Electrochemical Impedance Spectroscopy Analyses (EIS) were done on the cells at the specific intervals of the DoD window tests. An EIS spectrum was done using the fully charged cells after every 50 cycles for the 20Ah pouch cells and after 200 cycles for the 2Ah cylindrical cells. This test was done in order to determine the change in possible internal cell impedance during the cycling within the various stress regions of the discharge curve.

EIS analysis was done on a cylindrical and pouch cells at different temperatures⁶⁸ and States-of-Charge (SoC)⁶⁸. The different temperatures included: -20 °C, -10 °C, 0 °C, 10 °C, 20 °C, 30 °C, 40 °C and 50 °C and the different SoC included: 100%, 80%, 60%, 40%, 20%, 10%, 5% and 0% SoC. The 100% SoC corresponds to a fully charged cell and 0% SoC corresponding to a fully discharged cell. The intermediate SoC were achieved by discharging the fully charged cell at the C/1 rate to the % capacity of the fully discharged cell.

The test parameters used for the Galvanostatic EIS analysis are summarized in table 2.5:

DC current (A)	0
AC current (A rms)	0.05
Initial Frequency (Hz)	60 000
Final Frequency (Hz)	0.025
Points per decade	10

Table 2.5 Parameters for the Galvanostatic EIS analysis.

2.2.4.1. Caution required for EIS analyses:

Ensure that the working lead and working sense cables are connected to the positive electrode. The counter, working sense and reference leads are connected to the

negative electrode. The working sense and reference leads cables should be intertwined in order to reduce the effect of inductance due to the external cables. The Gamry Reference 3000 is a floating ground instrument that required the cell cables to contain only a floating ground lead (black clip) connected to the Faraday cage⁶⁹.

2.2.4.2. Calibration:

It was important that the instrument be regularly calibrated. The Gamry Impedance Analyser was supplied with a calibration unit and standard test procedure. A calibration was done according to the test procedure on the software and the cables were connected as per the calibration test plate. A Dummy cell was used in order to determine if the system was measuring the samples reliably. The various tests such as the K-K test, as described in chapter 1, were done in order to ensure repeatability and accuracy.

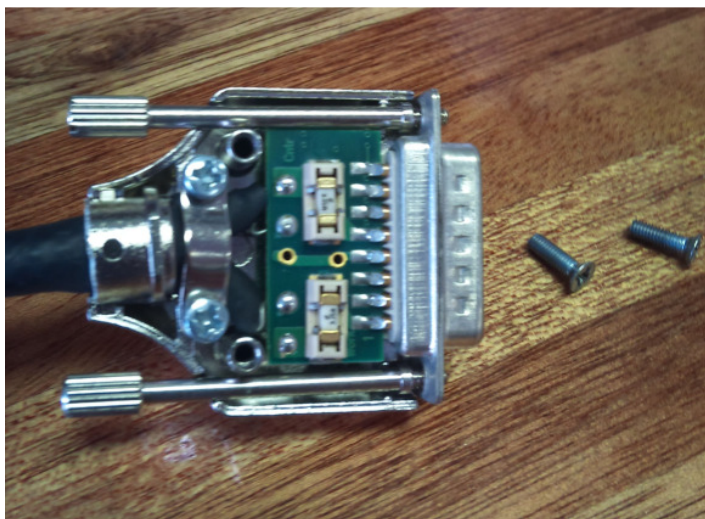


Figure 2.10. Fuse area on counter/working cable.

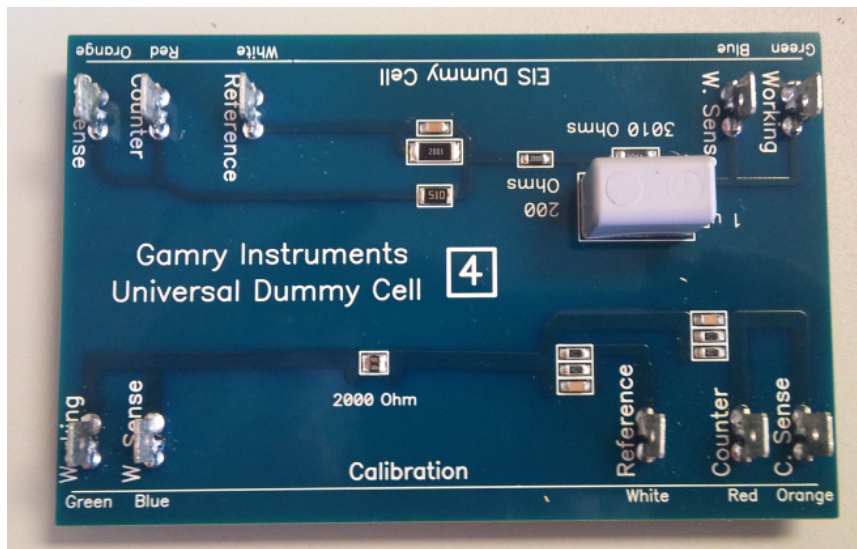


Figure 2.11. Calibration and dummy cell.

2.2.5. High rate charge & discharge tests using supercapacitors and Li-ion cells and Pb-acid cells.

The study was done on the three types of cells, a Lithium Cobalt oxide spiral cell, a Lithium Manganese oxide pouch cell and the Lead-acid VRLA cell. The Lithium Cobalt oxide cell was a Samsung manufactured 18650 spiral cell with a capacity rating of 2.4Ah. The Lithium Manganese oxide pouch cell was an UWC manufactured cell with a capacity rating of 1Ah. The Lead-acid VRLA cell with a true capacity rating of 5.21Ah. A 20Ah Lithium Cobalt Oxide pouch cell was also tested, but without the supercapacitors. The testing procedure was carried out in order to compare the charge acceptance and discharge ability of a battery alone against a system consisting of a battery and a supercapacitor.

Their voltage and current configuration relative to the capacitor size were determined and similar to the study done by M. Fernández et al⁷³. A ratio of 2F to 1Ah was used⁷³.

In order to ensure that the different cell types and chemistries could be compared, the cells were configured to have similar capacities and cell voltages. Two 5.2Ah lead-acid cells were connected in series in order to increase the voltage to 4.8V. A set of two 10F supercapacitors were connected in series in order to increase their voltage. The cells were then connected in parallel to the set of 10F supercapacitors.

Two 2.4Ah Lithium-ion cells were connected in parallel in order to increase their cell capacity to 4.8Ah. These were then connected to a similar set of supercapacitors in parallel as for the Pb-acid cell configuration.

A set of two 3.3F supercapacitors were connected in series in order to increase their voltage. The one 1Ah Li-ion cell was then connected in parallel to the set of 3.3F supercapacitors.

Each cell was subjected to a program which included discharging to a particular State-of-Charge (SoC), followed by a 5s high rate charge or a 10s high rate discharge⁷³. The test procedure for each cell type is described below:

	Current	Time	Voltage limit	
Discharge to 80% SOC	2.4A	12 minutes	3.0V	
Rest		10 minutes		
Charge	50A	5 seconds	4.2V	Measure Power
Rest		10 minutes		
Charge	10A		4.2V	Charge till 0.45Ah (cell fully charged again)
Discharge to 60% SOC	2.4A	24 minutes	3.0V	
Rest		10 minutes		
Charge	50A	5 seconds	4.2V	Measure power
Rest		10 minutes		
Charge	10A		4.2V	Charge till 0.90Ah (cell fully charged again)
Discharge to 40% SOC	2.4A	36 minutes	3.0V	
Rest		10 minutes		
Charge	50A	5 seconds	4.2V	Measure power
Rest		10 minutes		
Charge	10A		4.2V	Charge till 1.75Ah (cell fully charged again)
Discharge to 20% SOC	2.4A	48 minutes	3.0V	
Rest		10 minutes		
Charge	50A	5 seconds	4.2V	Measure power
Rest		10 minutes		
Charge	10A		4.2V	Charge till 1.75Ah (cell fully charged again)

Table 2.6. High rate charge test procedure for 4.8Ah Li-ion cells.

	Current	Time	Voltage limit	
Discharge to 80% SOC	2.4A	12 minutes	3.0V	
Rest		10 minutes		
Discharge	2.4A	10 seconds	3.0V	Measure Power
Rest		10 minutes		
Charge	10A		4.2V	Charge till 0.45Ah (cell fully charged again)
Discharge to 60% SOC	2.4A	24 minutes	3.0V	
Rest		10 minutes		
Discharge	2.4A	10 seconds	3.0V	Measure power
Rest		10 minutes		
Charge	10A		4.2V	Charge till 0.9Ah (cell fully charged again)
Discharge to 40% SOC	2.4A	36 minutes	3.0V	
Rest		10 minutes		
Discharge	2.4A	10 seconds	3.0V	Measure power
Rest		10 minutes		
Charge	10A		4.2V	Charge till 1.72Ah (cell fully charged again)
Discharge to 20% SOC	2.4A	48 minutes	3.0V	
Rest		10 minutes		
Discharge	2.4A	10 seconds	3.0V	Measure power
Rest		10 minutes		
Charge	10A		4.2V	Charge till 1.75Ah (cell fully charged again)

Table 2.7. High rate discharge test procedure for 4.8Ah Li-ion cells.

For the 20Ah pouch cell, the same test procedure as tables 2.16 and 2.17 were used, except the discharge current was 20Ah. The maximum charge and discharge rate steps were 200A instead of 50A as used in the 2Ah cylindrical cell. For the 1Ah pouch cell, the same test procedure as tables 2.16 and 2.17 was also used, except the discharge current was 1Ah. The maximum charge and discharge rate steps were similar to the currents used during the 2Ah cylindrical cell tests.

	Current	Time	Voltage limit	
Discharge to 80% SOC	Using 5.21A	12 minutes	3.5V	
Rest		10 minutes		
Charge	50A	5 seconds	5.3V	Measure Power
Rest		10 minutes		
Charge	10A		4.8V	Charge till 1.25Ah (cell fully charged again)
Discharge to 60% SOC	5.21A	24 minutes	3.5V	
Rest		10 minutes		
Charge	50A	5 seconds	5.3V	Measure power
Rest		10 minutes		
Charge	10A		4.8V	Charge till 2.50Ah (cell fully charged again)
Discharge to 40% SOC	5.21A	36 minutes	3.5V	
Rest		10 minutes		
Charge	50A	5 seconds	5.3V	Measure power
Rest		10 minutes		
Charge	10A		4.8V	Charge till 3.76Ah (cell fully charged again)
Discharge to 20% SOC	5.21A	48 minutes	3.5V	
Rest		10 minutes		
Charge	50A	5 seconds	5.3V	Measure power
Rest		10 minutes		
Charge	10A		4.8V	Charge till 5.0Ah (cell fully charged again)

Table 2.8. High rate charge test procedure For Pb-Acid cell.

	Current	Time	Voltage limit	
Discharge to 80% SOC	Using 5.21A	12 minutes	3.5V	
Rest		10 minutes		
Discharge	50A	10 seconds	3.3V	Measure Power
Rest		10 minutes		
Charge	10A		4.8V	Charge till 1.25Ah (cell fully charged again)
Discharge to 60% SOC	5.21A	24 minutes	3.5V	
Rest		10 minutes		
Discharge	50A	10 seconds	3.3V	Measure power
Rest		10 minutes		
Charge	10A		4.8V	Charge till 2.50Ah (cell fully charged again)
Discharge to 40% SOC	5.21A	36 minutes	3.5V	
Rest		10 minutes		
Discharge	50A	10 seconds	3.3V	Measure power
Rest		10 minutes		
Charge	10A		4.8V	Charge till 3.76Ah (cell fully charged again)
Discharge to 20% SOC	5.21A	48 minutes	3.5V	
Rest		10 minutes		
Discharge	50A	10 seconds	3.3V	Measure power
Rest		10 minutes		
Charge	10A		4.8V	Charge till 5.0Ah (cell fully charged again)

Table 2.9. High rate discharge test procedure High rate discharge test for the Pb acid cell.

The chemistry of Pb-acid cells allowed for high rate charging to a higher voltage limit than 4.8V and high rate discharging to a lower voltage limit than 3.5V. For Li-ion cells, the upper voltage limit of 4.2V and the lower voltage limit of 3.0V were strictly adhered to in order to prevent damage to the cell. The different high rate current charge and discharge were then plotted for each cell.

CHAPTER 3:

Results and Discussion:

Peukert and Ragone Tests on Li-ion cells

3.1. Peukert Test

The Peukert Test was done on all new cells received in order to determine the true capacity that is required for the various electrochemical studies. When purchasing cells, the manufacturer would provide mechanical characteristics of the cell, such as length, width, weight and thickness of the cell, as well as the electrical characteristics of the cell such as nominal voltage and nominal capacity. The true capacity is usually a few Ah higher than the rated nominal capacity.

The true capacity of a cell at a specific discharge rate was established by discharging the cell at different rates such as the C/20, C/10, C/5, C/2 and C/1 rate. The actual discharge currents used in discharge tests were calculated from the cells nominal capacity specified by the manufacturer. Once the results are obtained, the true capacity and the variation in capacity at different discharge rates were calculated using the Peukert Equation⁵⁰:

$$C = I^n t \quad (3.1)$$

C being the capacity, I being the discharge current, n is the Peukert constant and t being the time taken for the discharge step.

The constant charge and discharge current of a battery is measured in terms of the C-rate. For example: a battery that is rated at 1000mAh should provide at least 1000mA for 1 hour. The same battery discharged at 0.5C should provide 500mA for two hours. At 2C, the same battery should deliver 2000mA for 30minutes. However, as Peukert showed in his studies⁵⁰ of the Pb-acid battery system, this relationship was not linear and similar results were observed for the Li-ion cells studied. In addition, the Li-ion cells showed a notable increase in cell temperature at the higher discharge rates. Peukert tests together with temperature measurements were done on 2Ah cylindrical cells, 20Ah pouch cells and 1Ah pouch cells that were made by UWC.

3.1.1. Peukert Test with Temperature Results for the 20Ah Pouch cell and 2Ah cylindrical cell:

Each cell was subjected to a series of charge and discharge steps with an example shown in Figure 3.1.

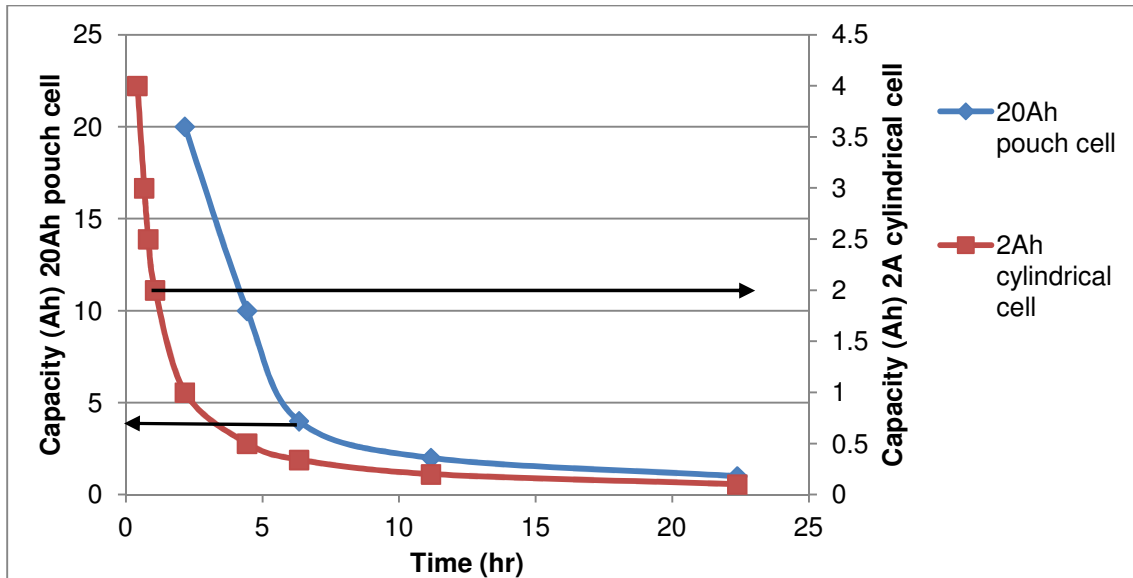


Figure 3.1 Capacity (Ah) vs. time (hr) for both the 20Ah pouch cell and 2Ah cylindrical cells.

The results showed that the time taken for each C rate discharge step decreases as the discharge current increases. In order to calculate the Peukert constant for each type of cell, a graph depicting \ln current vs. \ln time is drawn in Fig 3.2.

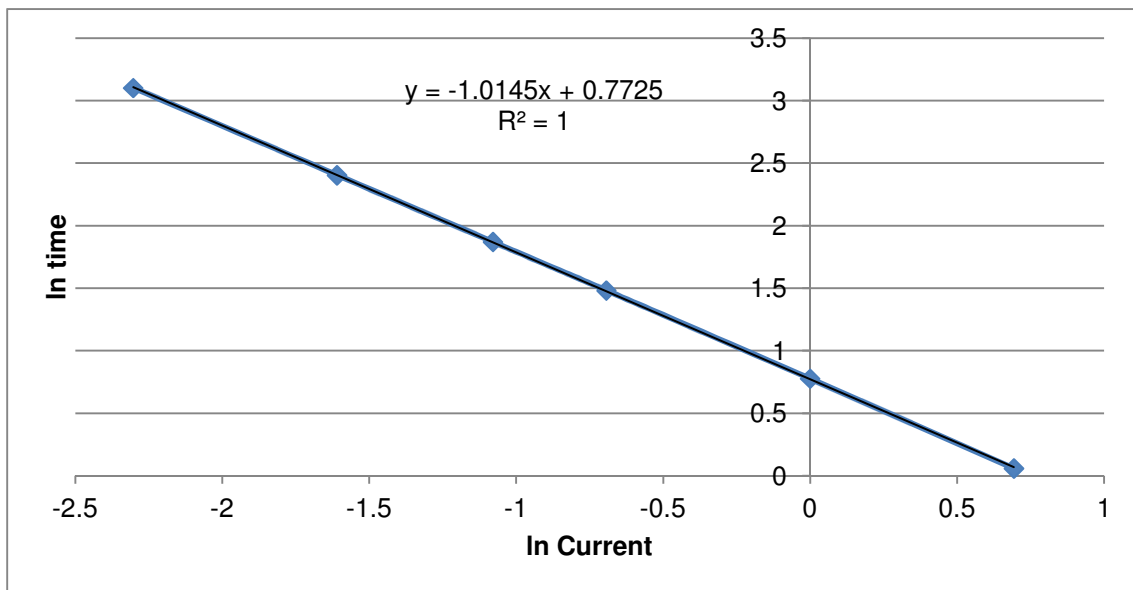


Figure 3.2. Graph depicting \ln time vs. \ln current for the 2Ah cylindrical cell.

The Peukert constant would be equal to the negative slope of the graph, which in this example was 1.0145. The capacity and Peukert constant for five cells were calculated and shown in Table 3.1.

Current (A)	Cell 1 (Ah)	Cell 2 (Ah)	Cell 3 (Ah)	Cell 4 (Ah)	Cell 5 (Ah)	Ave Capacity /discharge (Ah)	Std Deviation
0.1	2.22	2.19	2.24	2.25	2.28	2.24	0.03
0.2	2.21	2.20	2.23	2.24	2.28	2.23	0.03
0.34	2.21	2.19	2.22	2.24	2.28	2.23	0.03
0.5	2.20	2.19	2.22	2.23	2.27	2.22	0.03
1	2.18	2.17	2.06	2.19	2.23	2.16	0.07
2	2.12	2.13	2.14	2.14	2.12	2.13	0.01
Peukert Constant	1.0145	1.0090	1.0161	1.0162	1.0215		
Ave Peukert Constant	1.0155						
Std Deviation	0.0045						

Table 3.1. Capacity and Peukert constants for five 2Ah cylindrical cells.

In a typical large battery application, there are usually many cells connected in series. The battery would be required to discharge at certain rates. If the above five cells were used as an example for a battery, at the discharge current of 0.1 A, the standard deviation was 0.03 with the average capacity being 2.24 Ah. The lowest capacity for the group of cells was cell 2 at 2.19 Ah and the highest capacity being cell 5 at 2.28 Ah. These differences in capacities of the cells at a particular discharge rate will have an influence on the health of the cells within the battery pack. If the battery is discharged to the lower voltage limit, this could result in the cell with the lower capacity to discharge below the recommended voltage limit. This would lead to irreversible active material damage and premature ageing of the cell. This in turn would place more strain on the other four cells in the particular power application resulting in possible reduced long term life cycle usage.

The standard deviation from the Peukert constants for the five cells was shown to be 0.0045. In order to determine if the standard deviation calculated showed a small variation from the Peukert constant mean (the data points were close to the mean), at a 95% confidence level, a T-test was done. The true Peukert Constant average lies between 1.0099 and 1.0210 with 95% confidence. The slight variation in the

Peukert constant between the cells would imply that the cells would have a slightly different discharge profile under variable current applications. This again would imply that some cells would behave slightly differently in terms of high current discharge applications to the other cells within a battery pack. This becomes particularly relevant in battery systems that have several hundred cells in series, where the careful balance of the cells true capacity would be required in order to reduce the risk of premature cell damage and possible reduced battery life cycle capability. A similar example for a 20Ah pouch cell showed the Peukert constant to be 1.0394 (Fig 3.3) and the results for a set of five cells studied with respect to their capacity are shown in table 3.2.

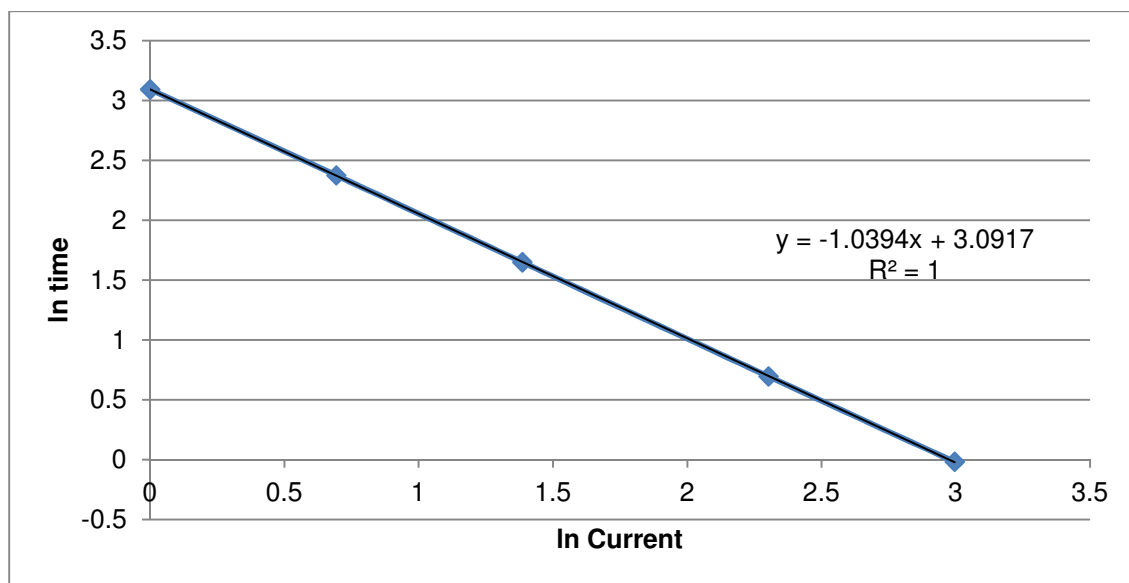


Figure 3.3. Graph depicting ln time vs. ln current for the 20Ah pouch cell.

Current (A)	Cell 1 (Ah)	Cell 2 (Ah)	Cell 3 (Ah)	Cell 4 (Ah)	Cell 5 (Ah)	Ave Capacity /discharge (Ah)	Std Deviation
1	22.39	22.39	21.98	22.02	22.20	22.20	0.20
2	21.79	21.84	21.38	21.48	21.91	21.68	0.23
4	20.99	21.07	20.68	20.80	21.54	21.02	0.33
10	19.73	19.79	19.89	20.04	20.89	20.07	0.47
20	18.83	18.95	19.46	19.63	20.21	19.41	0.55
Peukert Constant	1.0589	1.0571	1.0417	1.0394	1.0312		
Ave Peukert Constant	1.0457						
Std Deviation	0.0119						

Table 3.2. Capacity and Peukert constants for five 20Ah pouch cells.

Once again each cell within the battery will be affected at the different discharge rates. If the five cells above were used to make up a battery, the average capacity at the discharge rate of 1A was 22.20 Ah, with the lowest capacity being cell 3 at 21.98 Ah and the highest capacity being cells 1 & 2 at 22.39 Ah each. The standard deviations for the five cells at the different discharge rates were larger for the 20Ah pouch cell than the standard deviations of the 2Ah cylindrical cells. The largest standard deviation was seen for the five cells at the discharge rate of 20A. A steady increase in standard deviation was seen as the cells were discharged to higher capacity rates. These differences in capacities would have an effect on the health of a battery if all these cells were connected in series and subjected to variable high power application. For example at a discharge rate of 20A, cell 1 would discharge the quickest to the lower voltage limit that could result in a faster ageing of the cell and increased strain on the other cells. In a typical EV application where these types of cells would be used, a battery would consist typically of 95 cells in series. Here, the importance of the cells having similar actual capacities and discharge rates at higher currents would be important in order to maintain the expected life application of 7 to 10 years.

Notably the pouch cells were rated at 20Ah by the manufacturer. The results of the Peukert test showed that at the 1A discharge, the cells achieved capacities above 20Ah. However, at discharge currents of 20A, the capacities were significantly less than the manufacturer's rated capacity of 20Ah. This again emphasizes the importance of knowing the true capacity of a cell at a particular rate. In practical applications, this can often be difficult, where variable current strengths are used. For these cells, the true Peukert Constant average lies between 1.0309 and 1.0605 with 95% confidence. Both the cylindrical cells and the pouch cells showed very small confidence intervals, which indicated a small variation between the Peukert constants and the mean Peukert constant. It would be beneficial to have a set of cells whose Peukert constant of a cell was closer to 1 and thus would show less deviation in the cells capacity at different discharge rates.

In this study, the cell's temperature at different discharge rates showed an increase with increased discharge rate. An example of the change in temperature of a 2Ah cylindrical cell and a pouch cell at different discharge currents are shown in Figure 3.4 and 3.5 respectively.

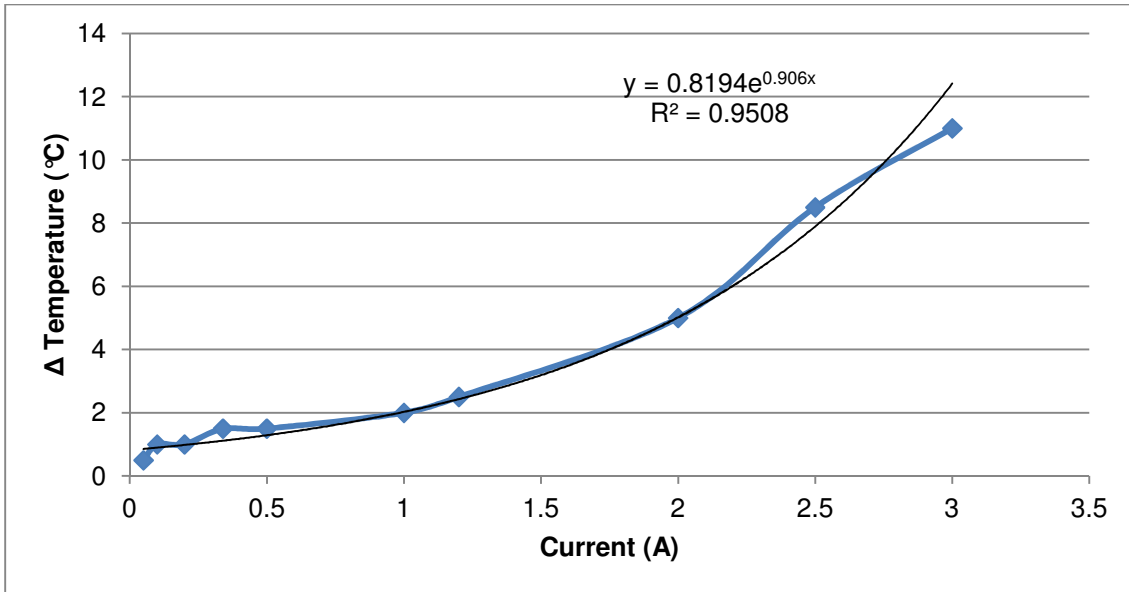


Figure 3.4. Change in temperature ($\Delta^{\circ}\text{C}$) vs. discharge current (A) of the 2Ah cylindrical cell.

A significant increase in the cells surface temperature was seen for the cylindrical cells at currents greater than 2A, which equalled the C/1 rate. The results showed an exponential increase in the temperature with increase in current, whereas the results of the 20Ah pouch showed a more linear increase over the current range (Fig 3.5). This implies that the cell design has significant influence on the ability of the cell to dissipate heat during high rate discharges.

The results were repeatable and the change in temperature for three cylindrical cells and five pouch cells are shown in tables 3.3 and 3.4 respectively.

Current (A)	cell 1 (Change in Temp °C)	cell 2 (Change in Temp °C)	cell 3 (Change in Temp °C)
0	0	0	0
0.05	0.5	1	1
0.1	1	1	1
0.2	1	1	1
0.34	1.5	1.5	1.5
0.5	1.5	1.5	1.5
1	2	2	2
1.2	2.5	2.5	3
2	5	6	6
2.5	8.5	11.5	9.5
3	11	12.5	12
4	13	12	13

Table 3.3. Table of current (A) vs. change in temperature (°C) of three 2Ah cylindrical cells.

These results are similar to findings reported by Dong Hyup Jeon and Seung Man Baek⁵². They studied the skin temperature of an 18650 1.5Ah cylindrical cell at different discharge rates. At lower discharge rates, the skin temperature of the cells increased slightly. At higher temperatures the skin temperature of the cells had increased significantly. These increases in temperature at higher discharge rates were due to entropy changes of LiCoO_2 and LiC_6 . As the discharge rates increased, the temperature gradient was steep because the contribution of heat generation due to joule heating was high⁷⁷. The contribution of heat generation due to entropy changes was dominant at low discharge rates, whereas the joule heating was significant at higher discharge rates⁷⁷. Entropy is a thermodynamic quantity that changes in a reversible process by an amount equal to the heat absorbed or emitted, divided by a thermodynamic temperature⁷⁷. Joule heating is also known as ohmic resistance or resistive heating. Joule heating is the process by which the passage of an electric current through a conductor releases heat⁷⁸. At higher discharge rates, there would be a higher resistance build-up as the Li^+ ions are forced to move from the anode to the cathode at faster rates than at lower discharge rates, thus increasing the heat generation.

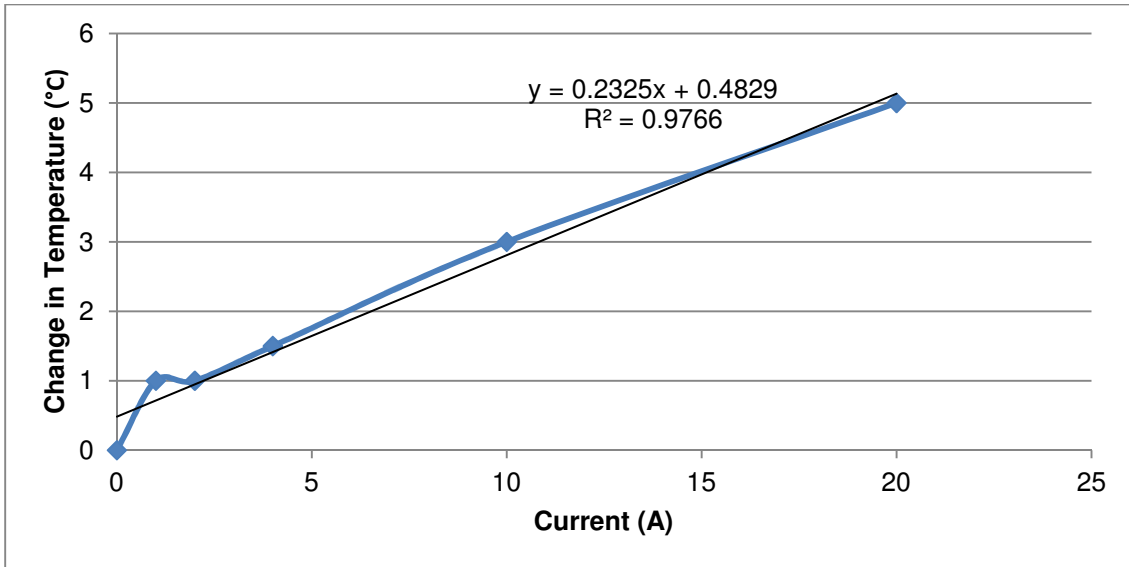


Figure 3.5 Change in temperature ($\Delta^{\circ}\text{C}$) vs. discharge current (A) of a 20Ah pouch cell.

A table of current vs. change in temperature for five pouch cells is shown in table 3.4.

Current (A)	Pouch 1 (Change in Temp $^{\circ}\text{C}$)	Pouch 2 (Change in Temp $^{\circ}\text{C}$)	Pouch 3 (Change in Temp $^{\circ}\text{C}$)	Pouch 4 (Change in Temp $^{\circ}\text{C}$)	Pouch 5 (Change in Temp $^{\circ}\text{C}$)
0	0	0	0	0	0
1	1	1	1	1	0.5
2	1.5	1.5	1	1	1
4	1.5	1.5	1.5	1	1.5
10	3	1.5	3	2	2
20	5	4	5	4	5.5

Table 3.4. Table of current (A) vs. change in temperature ($^{\circ}\text{C}$) of five 20Ah pouch cells.

For the 20Ah pouch cell, the change in temperature corresponded to a linear change in temperature as the discharge rate increased. The heat distribution during discharging of a cylindrical and pouch cell are different due to their shape, as well as the way in which the cathode, separator and anode are arranged within the cell, i.e. in a cylindrical cell the anode and cathode are wound around in a circle reducing the effective heat dissipation from the core of the cylinder during discharge (Fig 3.6)⁵². In a pouch cell the anode and cathode are stacked on top on each other in a sheet type arrangement, allowing for better heat distribution to the environment (Fig 3.7)⁷⁹.

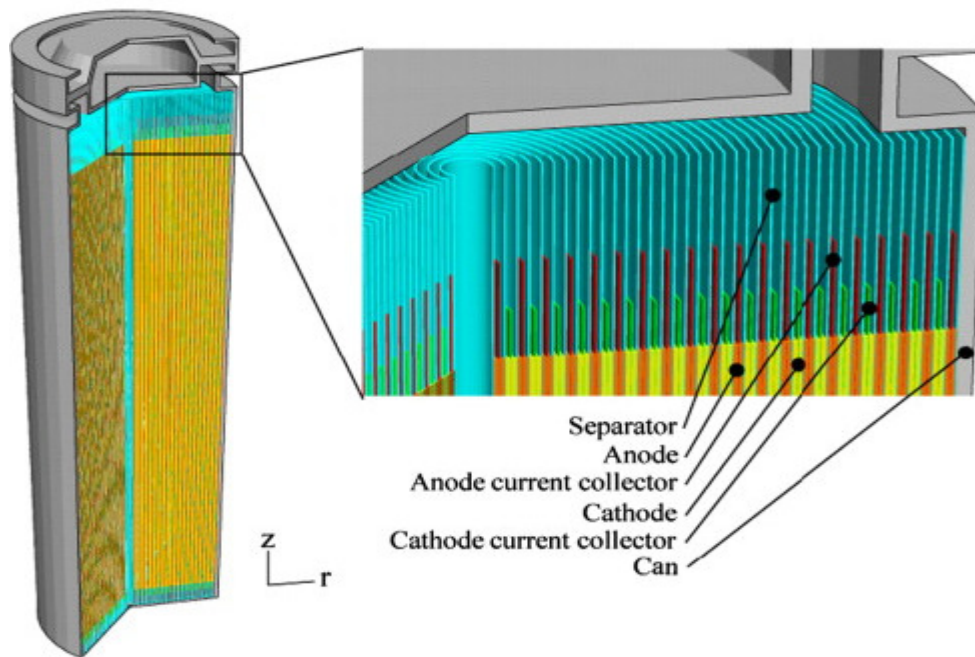


Figure 3.6. Schematic diagram of a cylindrical Li-ion battery⁵².

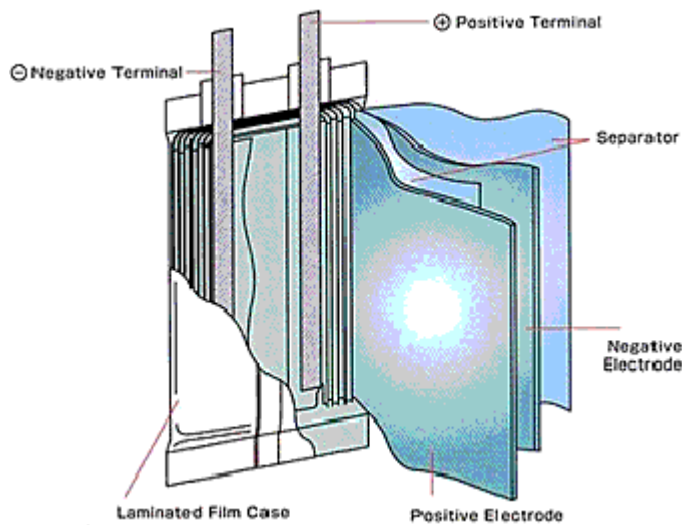


Figure 3.7. Schematic diagram of a Li-ion pouch cell⁷⁹.

The results of this study showed that care should be taken when assembling cells into battery packs to ensure sufficient heat dissipation during high rate discharge applications with the cylindrical cell requiring more cooling due to its shape⁵². Ideally each cylindrical cell would need to be cooled separately, whereas the pouch cells could be arranged in rows with the cooling running along the length of the row. Research into better ways of cooling and stack configurations of cells in a battery pack for EVs are being carried out by engineers in the field.

3.1.2. Peukert Test with Temperature Results for the 1Ah pouch cell

Five 1Ah pouch cells were manufactured and supplied by the University of the Western Cape (UWC). Peukert tests were carried out on each cell and the results for one of the cells are shown in figure 3.8 and the results of the other cells are shown in table 3.5.

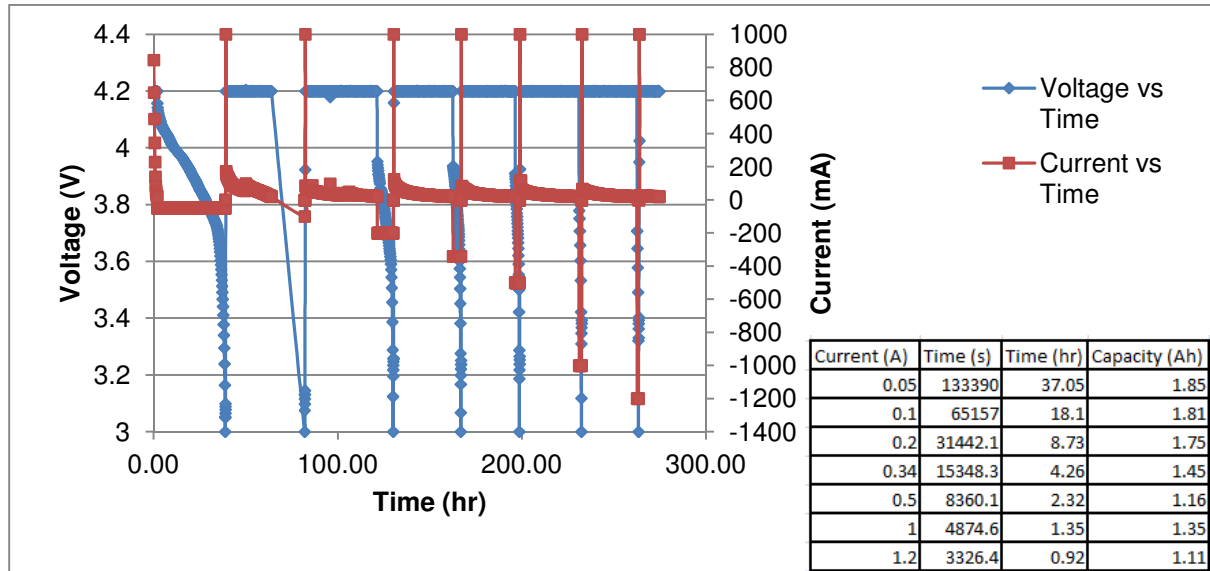


Figure 3.8. Voltage (V) vs. time (hr) and current (A) vs. time (hr) graph for a 1Ah pouch cell. A table showing the numerical values from the graph is shown.

Only one of the five pouch cells were able to achieve significant capacity, implying that the others could have failed due to electrical short circuit within the cell assembly. Disassembling of the failed cells to determine the failure analysis was not done.

Peukert tests were carried out on the other four 1Ah pouch cells. The capacities at the different discharge currents are shown in table 3.5.

Current (A)	Cell 1: (Ah)	Cell 2: (Ah)	Cell 3: (Ah)	Cell 4: (Ah)	Cell 5: (Ah)
0.05	1.89	1.85	3.86	3.31	1.06
0.10	0.00	1.81	3.82	0.00	0.00
0.20	0.11	1.75	0.00	0.00	0.35
0.34	0.00	1.45	0.00	0.00	0.14
0.50	0.00	1.16	0.05	0.00	1.29
1.00	0.00	1.35	0.00	0.00	0.06
2.00	0.00	1.11	0.25	0.00	0.02

Table 3.5. The capacities of the five 1Ah pouch cells at the different discharge currents.

The Peukert results of the one cell were carried out in duplicate (Fig 3.9).

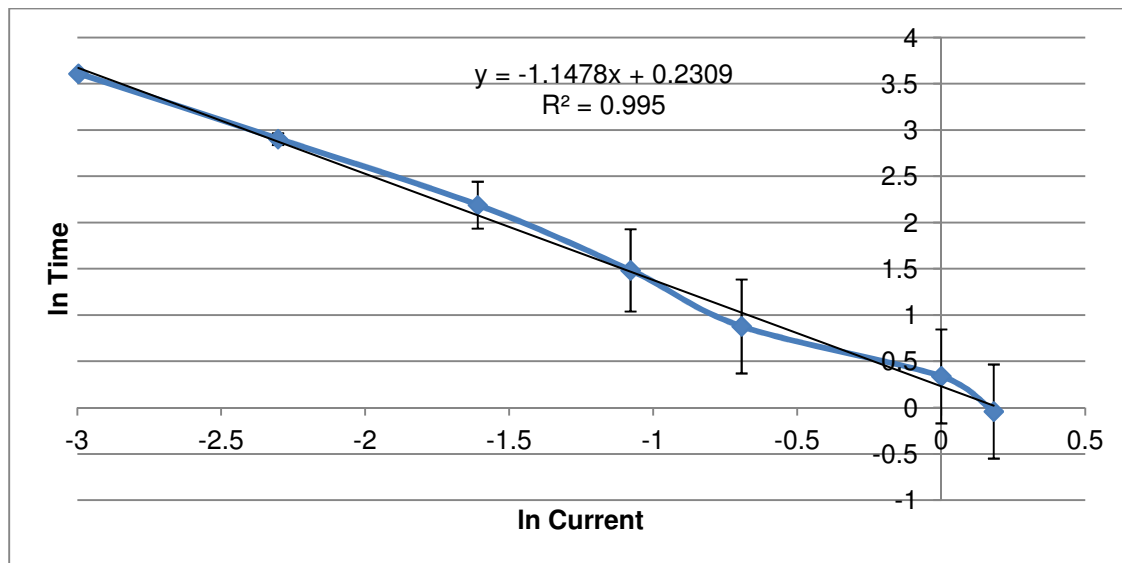


Figure 3.9. Graph depicting ln time vs. ln current.

The Peukert constant would be equal to the negative slope of the graph, which in this example was 1.1478. The higher Peukert Constant would imply a higher deviation in capacity at the higher rates of discharge. The cell was assembled with thicker electrodes within the cell when compared to conventional cell assembly. It was expected that cells with thicker electrodes would give lower capacities at higher current applications.

The temperature change during the various current discharge steps showed that there was very little change in temperature during the high current discharge rates (Fig 3.10).

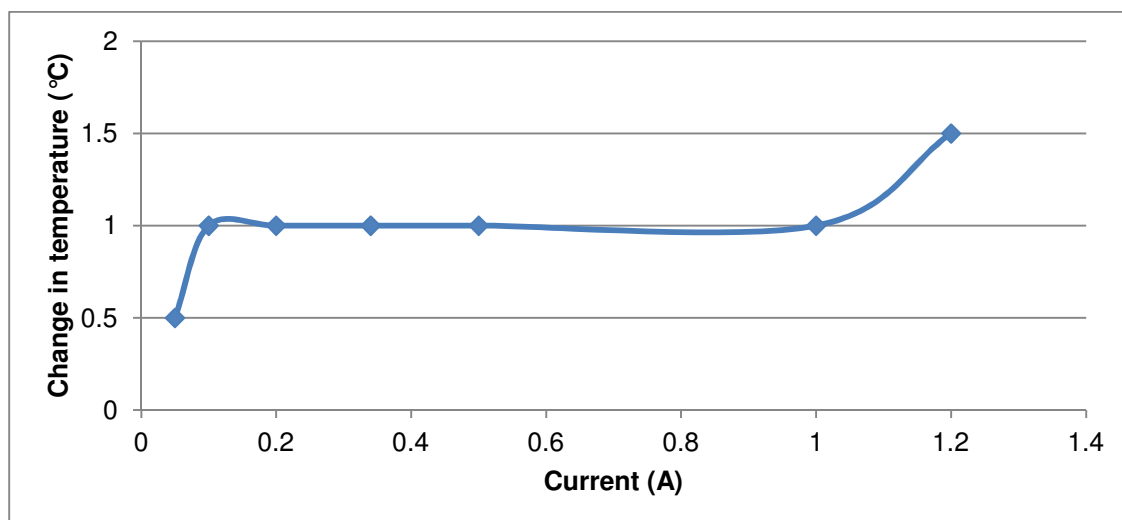


Figure 3.10. Change in temperature (°C) over the different discharge steps for 1Ah pouch cell.

Care was taken during the Peukert tests of the 1Ah pouch cells, as many of these pouch cells supplied failed during testing. The 1Ah pouch cell was not subjected to discharge rates higher than C/1 as was done with the 2Ah Li-ion cylindrical cells in order to prevent failure of this cell. If the cell had been subjected to higher discharge rates, possibly larger changes in temperature may have been seen.

3.2. Ragone Tests

Ragone Tests were carried out in order to compare the energy densities and power densities of two different types of Li-ion cells, namely the 20Ah pouch cell and the 2Ah cylindrical cell. The results from these Li-ion tests were then compared to results obtained from a VRLA Pb-acid cell. For comparison purposes, the Ragone tests were done by using the constant current and the constant power method⁵⁸. The study for each cell type was done in duplicate.

3.2.1. 2Ah Li-ion constant current & constant Power Method Results:

An example of the constant current and constant power method results of a 2Ah cylindrical cell was shown in Figure 3.11 and the average of two set of cells are shown in tables 3.6 and 3.7.

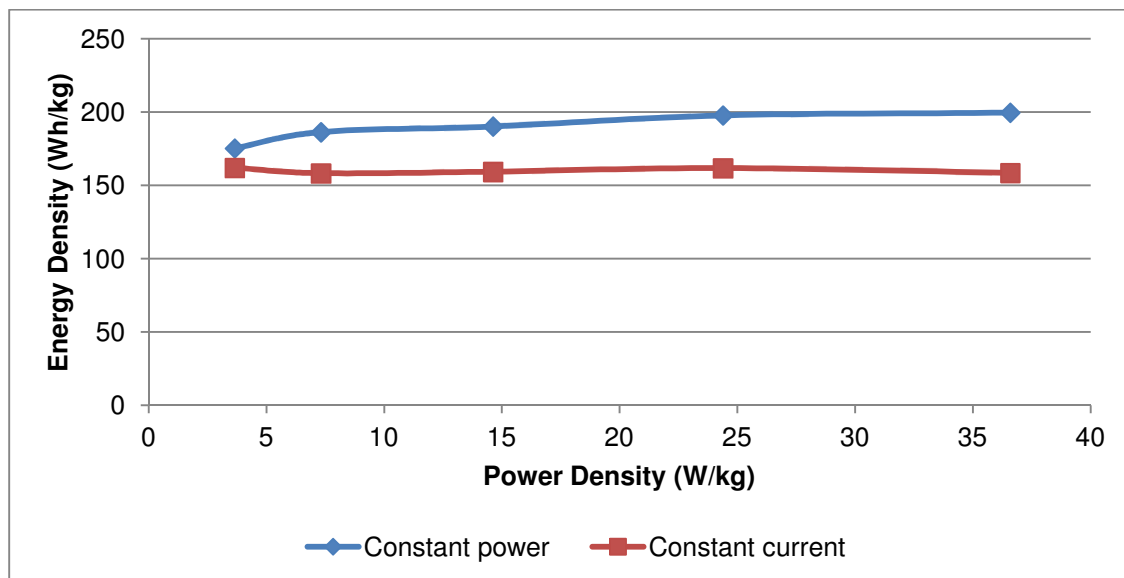


Figure 3.11. Energy and Power densities at Constant current and constant power Ragone tests of a 2Ah cylindrical cell.

Constant current method:

All cells Power Density (W/kg)	Cell 1 Energy Density (Wh/kg)	Cell 2 Energy Density (Wh/kg)	Mean	Std deviation
3.66	161.87	164.90	163.39	2.14
7.32	158.17	162.22	160.20	2.86
14.63	159.17	161.88	160.53	1.92
24.39	161.66	160.37	161.02	0.91
36.59	158.44	162.91	160.68	3.16

Table 3.6. Power densities and energy densities of two 2Ah cylindrical cells during the constant current method.

Constant power method:

All cells Power Density (W/kg)	Cell 1 Energy Density (Wh/kg)	Cell 2 Energy Density (Wh/kg)	Mean	Std deviation
3.66	175.21	178.36	176.79	2.23
7.32	186.30	182.48	184.39	2.70
14.63	190.14	189.23	189.69	0.64
24.39	197.71	204.48	201.10	4.79
36.59	199.59	195.23	197.41	3.08

Table 3.7. Power densities and energy densities of two 2Ah cylindrical cells during the constant power method.

Similar differences were seen between the energy density values of the different cells using the constant power method when compared to the constant current method of the 2Ah cylindrical cells.

According to literature, these results can be plotted two ways, i.e. energy density (y-axis) vs. power density (x-axis) as shown in a paper by Andrew Chu and Paul Braatz⁵⁸ or power density (y-axis) vs. energy density (x-axis) as shown in a paper by W.G. Bell and B.E. Conway¹³. However, in this study, the data were plotted as energy density vs. power density allowing for easier comparison. In the work published by W.G. Bell and B.E. Conway, the focus was on the resistance of the cells at different energy and power densities and not directly comparable to the data obtained during this study.

The results showed similar power density and energy density values for both methods. The energy density and power values reported by Andrew Chu and Paul Braatz⁵⁸ showed energy density values between 40 and 200 Wh/kg for Li-ion cells. For the Sony Li-ion cell used in their study, the energy density values decreased

sharply after the cell had reached power density values of 100 W/kg and higher. This would indicate that the cell was discharged at high discharge rates, e.g. discharging a 2Ah cell at discharge current of 5A. The time taken for this discharge would be short and the overall energy density (Wh/kg) would be low. During this study the 2Ah cylindrical cells were tested using currents of 100mA to a maximum of 2A during the constant current method. During the constant power method the 2Ah cylindrical cells were tested using power values of 0.15W to 1.5W. The maximum current value of 2A and the maximum power value of 1.5W correspond to the C/1 rate of the cell. The Sony cell was discharged at considerable higher discharge rates above C/1. The small increase in energy density values between the constant power method and constant current method was explained by W.G. Bell and B.E. Conway¹³ in a paper that stated that in order to calculate energy and power, the following equations should be used:

$$\text{Energy: } E = Q (\Delta V) \quad (3.2)$$

$$\text{Power: } P = I (\Delta V) \quad (3.3)$$

ΔV is the potential difference established between the two electrodes of a cell with Q being the charge stored. In practical applications it was shown that the discharge decreased faster at higher power application. This can be explained by non-uniformity of discharge and/or isolation of some of the active material at high currents. During this study, the charge stored (Q) at the potential difference was greater than during the constant power method, which resulted in the time for each discharge step of constant power method to be slightly longer.

3.2.2. 20Ah Li-ion constant current & constant power method results:

An example of the constant current and constant power method results of a 20Ah pouch cell was shown in Figure 3.12 and the results of two cells in tables 3.8 and 3.9.

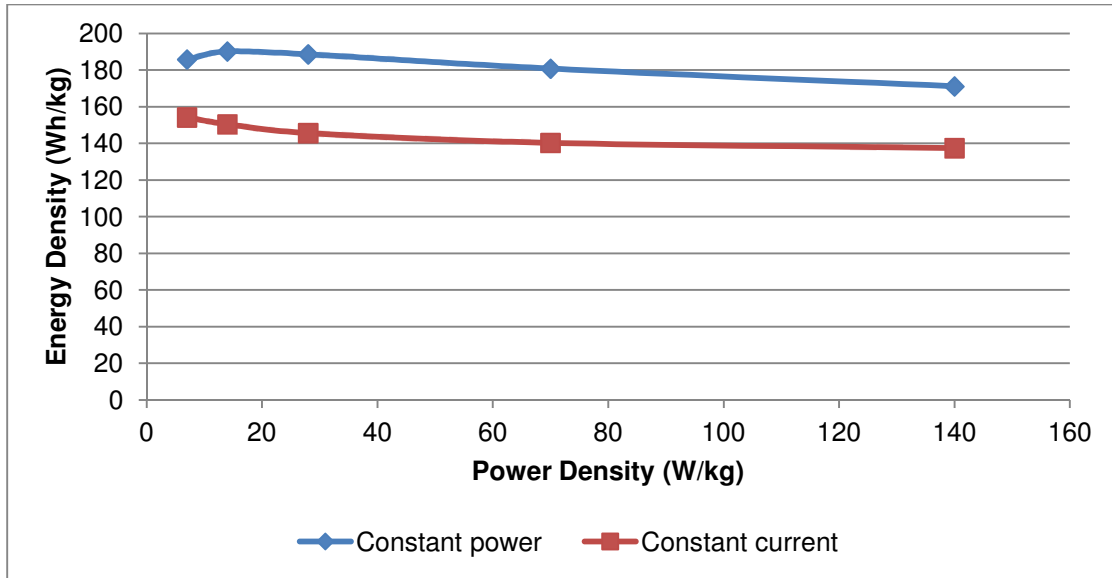


Figure 3.12. Energy and Power densities of Constant current and constant power Ragone tests for a 20Ah pouch cell results.

Constant current method:

All cells Power Density (W/kg)	Cell 2 Energy Density (Wh/kg)	Cell 2 Energy Density (Wh/kg)	Mean	Std Deviation
7	154.13	153.92	154.03	0.15
14	150.39	149.71	150.05	0.48
28	145.59	144.78	145.19	0.57
70	140.27	139.24	139.76	0.73
140	137.43	136.26	136.85	0.83

Table 3.8. Power densities and energy densities of two 20Ah pouch cells during the constant current method.

Constant power method:

All cells Power density (W/kg)	Cell 2 Energy density (Wh/kg)	Cell 2 Energy density (Wh/kg)	Mean	Std Deviation
7	185.81	185.84	185.83	0.02
14	190.17	190.18	190.18	0.01
28	188.59	188.95	188.77	0.25
70	180.79	181.10	180.95	0.22
140	171.06	173.16	172.11	1.48

Table 3.9. Power densities and energy densities of two 20Ah pouch cells during the constant power method.

Once again similar energy density trends were seen when compared to the results by Andrew Chu and Paul Braatz⁵⁸ when using a constant power method. The explanation that the constant power method energy density values were higher than

the constant current method are similar to the results obtained with the 2Ah cylindrical cell.

3.2.3. 5Ah Pb-acid constant current & constant power method results:

An example of the constant current and constant power method results of a 7Ah Pb-acid cell was shown in Figure 3.13 and the results of two cells shown in tables 3.10 and 3.11.

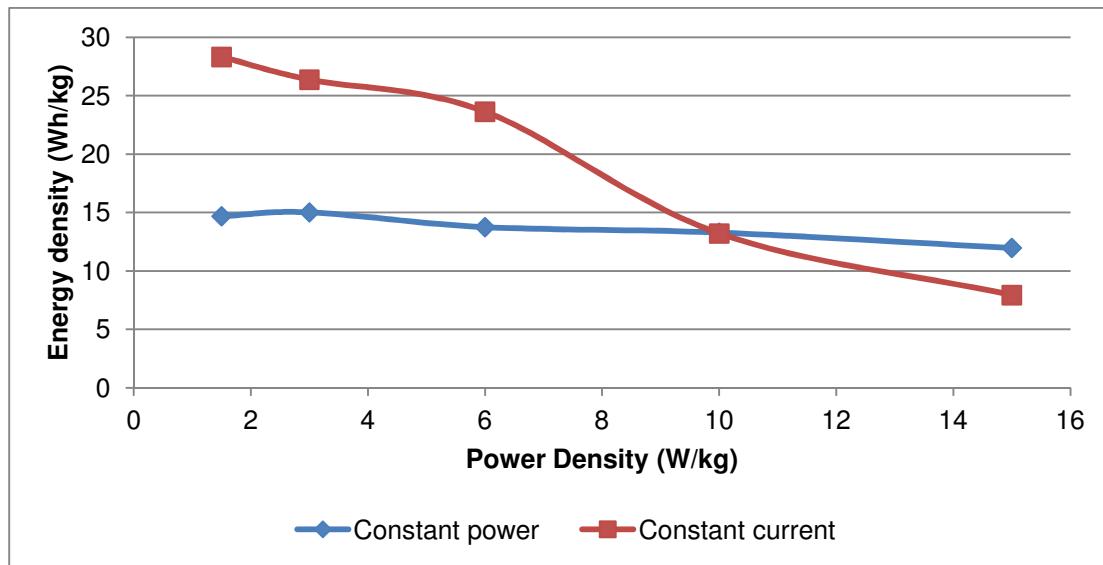


Figure 3.13. Energy and Power densities of Constant current and constant power Ragone tests for a 7Ah Pb-acid cell results.

All cells Power Density (W/kg)	Cell 1 Energy Density (Wh/kg)	Cell 2 Energy Density (Wh/kg)	Mean	Std Deviation
1.5	28.31	28.15	28.23	0.11
3	26.36	25.75	26.06	0.43
6	23.62	23.71	23.67	0.06
10	13.2	13.03	13.12	0.12
15	7.93	8.4	8.17	0.33

Table 3.10. Power densities and energy densities of two 7Ah Pb-acid cells during the constant current method.

Constant power method:

All cells Power Density (W/kg)	Cell 1 Energy Density (Wh/kg)	Cell 2 Energy Density (Wh/kg)	Mean	Std Deviation
1.5	14.68	15.23	14.96	0.39
3	15.01	14.97	14.99	0.03
6	13.75	13.31	13.53	0.31
10	13.28	13.00	13.14	0.20
15	11.97	11.85	11.91	0.08

Table 3.11. Power densities and energy densities of two 7Ah Pb-acid cells during the constant power method.

A similar energy density trend was seen when comparing the Pb-acid Ragone test results to a paper by Peter Van den Bossche et al⁵⁴. The paper was based on life cycle tests of different batteries chemistry which considered the constant current method. The values in the paper indicated power density values of between 2 and 100 W/kg and energy density values of 20-30 Wh/kg. The paper indicated that at higher power densities, the energy density decreases, which was seen in this study for both methods. However for the constant current method the decrease in energy density at the same power densities was more pronounced. This could be explained in part by the use of higher charge currents which resulted in lower energy efficiencies for Pb-acid type cells as was discussed by work published by Tomohiko Ikeya et al⁸⁰. However it is not mentioned in the paper whether the same effect will be seen with constant current discharge.

3.2.4. Comparison of the different chemistry cells using the different Ragone test methods:

The Energy and Power density of the three types of cells can be compared to each other and is shown in Fig 3.14.

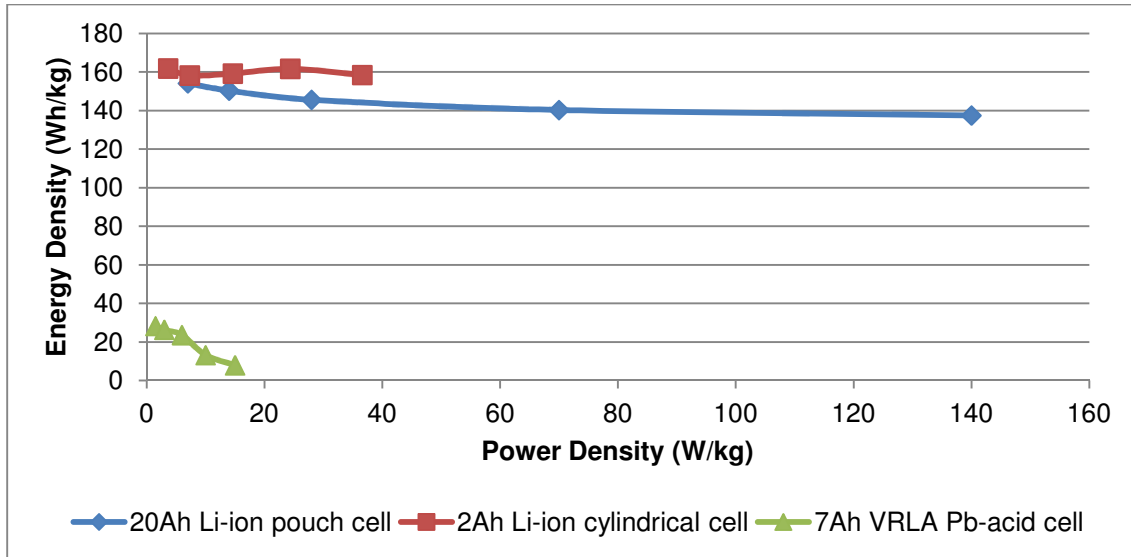


Figure 3.14. The power densities and energy densities for each cell type chemistry and using the constant current Ragone test method.

The results showed very clearly that the Pb-acid cell had comparatively small power and energy densities in relation to the two Li-ion cells. The 2Ah Li-ion cell showed similar energy densities to the 20Ah Li-ion pouch cell. The power densities were different for the Li-ion cells as the one cell was a 20Ah cell and the other cell 2Ah cell. By carrying out the same discharge current rates on the 2Ah cylindrical cell, would result in failure of the cell, as the discharge current rates would be too high. With the 7Ah VRLA Pb-Acid cell having the greatest ohmic resistance and/or kinetic/activation polarization and is considerably heavier in mass, the energy density was much lower. The low energy density of a Pb-acid battery can also be explained by the use of lead as both the grid material and the internal connectors and the poor utilization of the active materials⁸¹.

In the constant current method, the power density was calculated using equation 3.2. The power and energy density values would depend on the ΔV , which depends on both the ohmic resistance and kinetic/activation polarisation.

In the constant power method, the power discharge value was maintained till the cell reached the voltage limit. Even though the constant discharge power value was calculated from the constant current method, the results showed that for the Li-ion cells tested, each discharge step took longer in time than the method where a constant current was used. The following graph (Fig 3.15) can be used to show the

power density vs. energy density ratio for each different chemistry and capacity, when constant power was used for the Ragone Test.

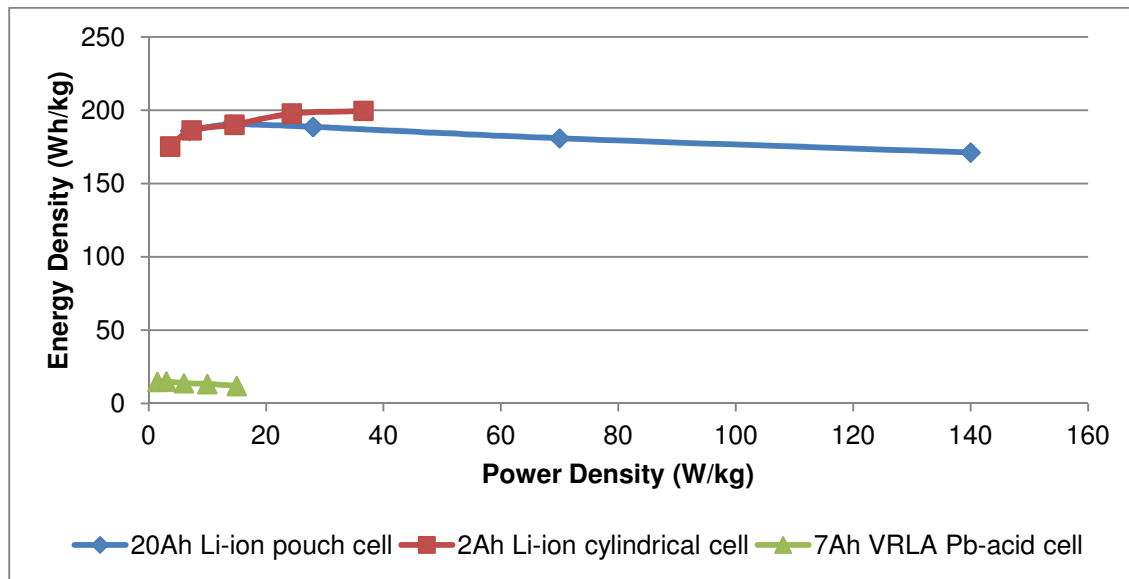


Figure 3.15. The power densities to energy densities at the different steps for each chemistry and capacity using the constant power Ragone test method.

The results showed that the 7Ah Pb-acid cell had the smallest energy densities and power densities. During the constant power Ragone test method of Li-ion cells, the current and the voltage will change in order to maintain the constant power value, i.e. during discharge the voltage will slowly decline and the current would increase in order to maintain the same power. A similar pattern for the cells at the constant power method was seen in comparison to the constant current method.

In this chapter, the Peukert tests were used to determine the true capacities of the different cells of different designs with the same capacity rating. The study showed that there were slight differences between the true capacities at a certain rate when compared to the specified capacity by the manufacturer. For both the 2Ah Li-ion cylindrical cells and the 20Ah Li-ion pouch cells, the true capacity at the relative low currents was higher than the manufacturer's rated capacity. The true capacity at the various rates would be used in further electrochemical testing in subsequent chapters.

The Peukert constant for both the 20Ah pouch cell and the 2Ah cylindrical cell were close to the value of 1 indicating that these cells would only show a slight deviation in the cell's capacity at the different discharge rates. The 1Ah pouch cells made by

UWC showed a relatively larger Peukert constant giving an indication that the utilization of the active material would decrease with increase in discharge rates. This in part can be explained by the active material, coated on the electrode current collectors, being comparatively thicker than commercial cells⁸². The study also showed that an increase in the change in temperature was seen as the discharge rate increased. An exponential increase in temperature over the discharge rates was seen for the 2Ah cylindrical cells. A linear increase in temperature over the discharge rates for the 20Ah pouch cells was seen. The difference in change in temperature at different discharge rates for the cylindrical and pouch cells was explained by the difference in geometry and layout of electrodes within the different cells. Very small increases in temperature were seen over the discharge rates for the 1Ah pouch cell. Ragone tests can be carried out via the constant current and constant power methods to calculate the energy and power densities for different cell types and capacities. The Ragone test results showed that the Li-ion cells showed similar energy densities, while the Pb-acid cells showed much lower energy densities. The energy densities of both Li-ion cells and the Pb-acid cells fell within the values seen in literature. The power densities of the 2Ah cylindrical cell were smaller than the power densities of the 20Ah pouch cell as the cylindrical cell could not be discharged to the discharge current rates used in testing of the 20Ah pouch cell. However both Li-ion cell types' as well as the Pb-acid power densities fell within the values seen in literature.

CHAPTER 4:

Results and Discussion:

Electrochemical Impedance Spectroscopy on Li-ion cells

Electrochemical Impedance Spectroscopy (EIS) can be used to determine changes within a Li-ion cell non-destructively. Typical Lissajous plots were seen during the EIS spectrum acquisition. These plots can be used to monitor the spectrum as it is being acquired for any abnormalities. These abnormalities could result from the EIS instrument being incorrectly connected to the battery via the EIS instrument cables and clips, and possible overcharging or unstable charging of the battery prior to the EIS measurements⁸⁵. An example of the Lissajous plot during an EIS analysis is shown in Fig 4.1.

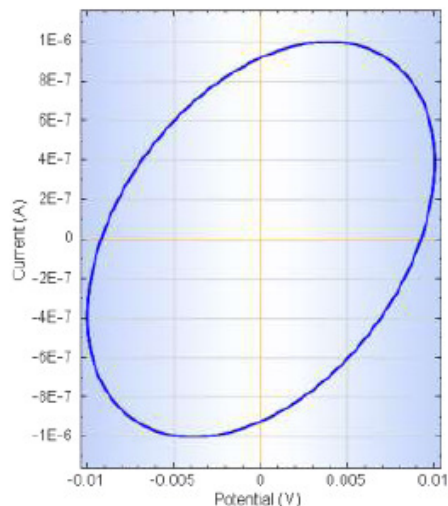


Figure 4.1. An example of a Lissajous plot during an EIS analysis⁶¹.

Most EIS analyses followed similar patterns across the screen, thus indicating linearity within the spectrum.

Examples of a Bode and Nyquist plots of a resistor and capacitor are shown in Fig 4.2 and 4.3 respectively.

10Ω Resistor:

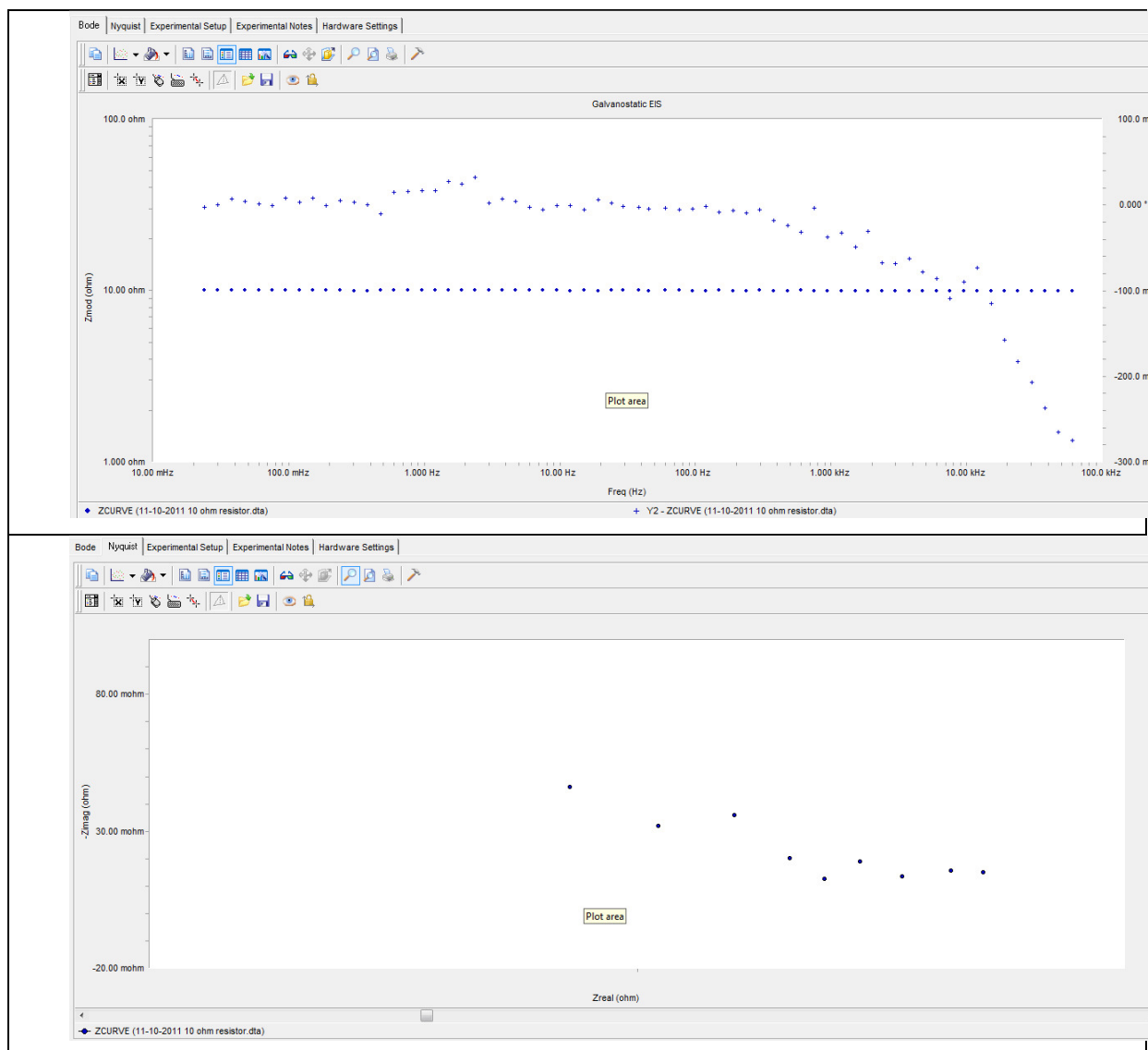


Figure 4.2. Bode and Nyquist plot of a 10Ω resistor.

The upper diagram being a Bode plot and the lower diagram being a Nyquist plot of the 10Ω resistor. According to a Technical Note⁸³ from Gamry Instruments, the magnitude of an ideal resistor's impedance is independent of frequency and the phase is zero. As the resistor used in this example was not an ideal resistor, a small amount of impedance was measured and a small Nyquist plot could be plotted (Nyquist plots illustrate the frequency responses as well as phases). The Bode plot would show two straight lines if an ideal resistor was used. The Bode plot example shows some phase characteristics indicating a practical resistor.

10F Capacitor:

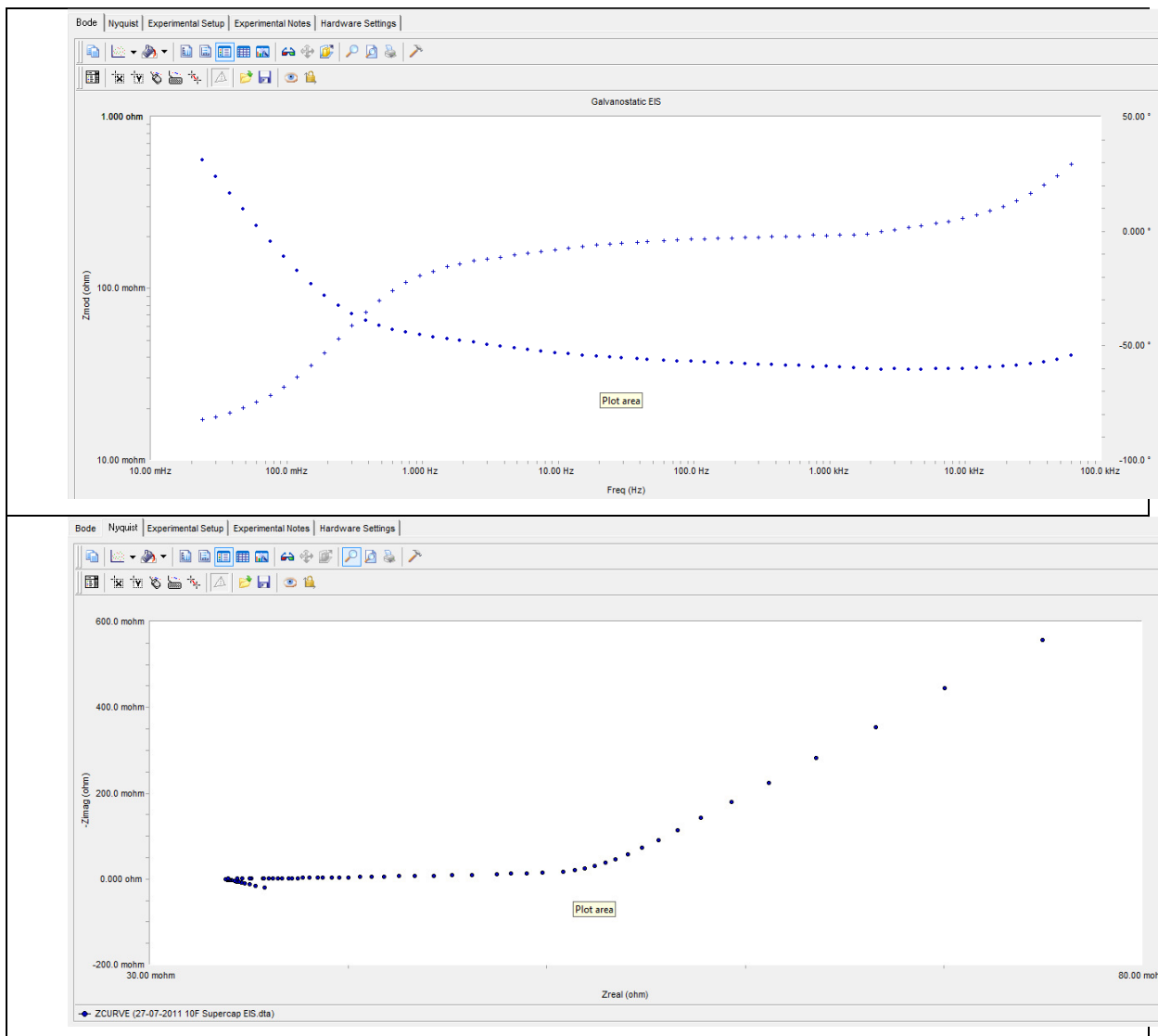


Figure 4.3. Bode and Nyquist plot of a 10F capacitor.

The upper diagram being a Bode plot and the lower diagram being a Nyquist plot of the 10F capacitor. According to a Technical note by Gamry Instruments⁸⁴, the Bode plot of a capacitor includes three regions: above 10Hz the magnitude of a capacitor frequency and phase approach 100mΩ and 0°. In the region between 100μHz and 10Hz, capacitance controls the impedance. In this region the magnitude vs. frequency was linear on the log-log Bode plot. Below 10μHz, the impedance begins a transition back towards a resistive behaviour as leakage resistance becomes dominant. The Nyquist plot shows both the frequency and phase responses common to a capacitor. The results showed that different EIS spectra can be seen for the different types of electrochemical devices.

A Kramers-Kronig (K-K) test was done to check consistency and stability of the data. The K-K test is a basic test for data validation and the equation links the real and imaginary components of complex quantities for systems fulfilling the conditions of linearity, causality and stability⁸⁵.

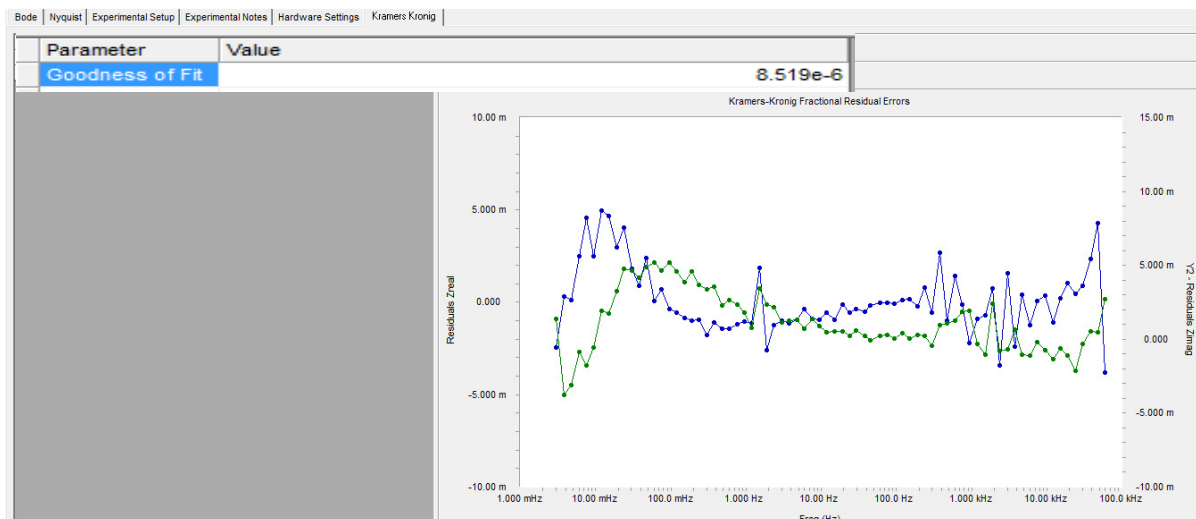


Figure 4.4. An acceptable K-K test result with a Goodness of Fit of 8.52×10^{-6} .

A K-K test result close to $\pm 1 \times 10^{-6}$ is considered to be a good result⁸⁵.

For comparison purposes, a poorer K-K test result is shown in Figure 4.5 where the Goodness of Fit was significantly larger than 1×10^{-6} . Reasons for this could include that the magnitude to frequency of the EIS spectrum was non-linear or that the test was unstable.

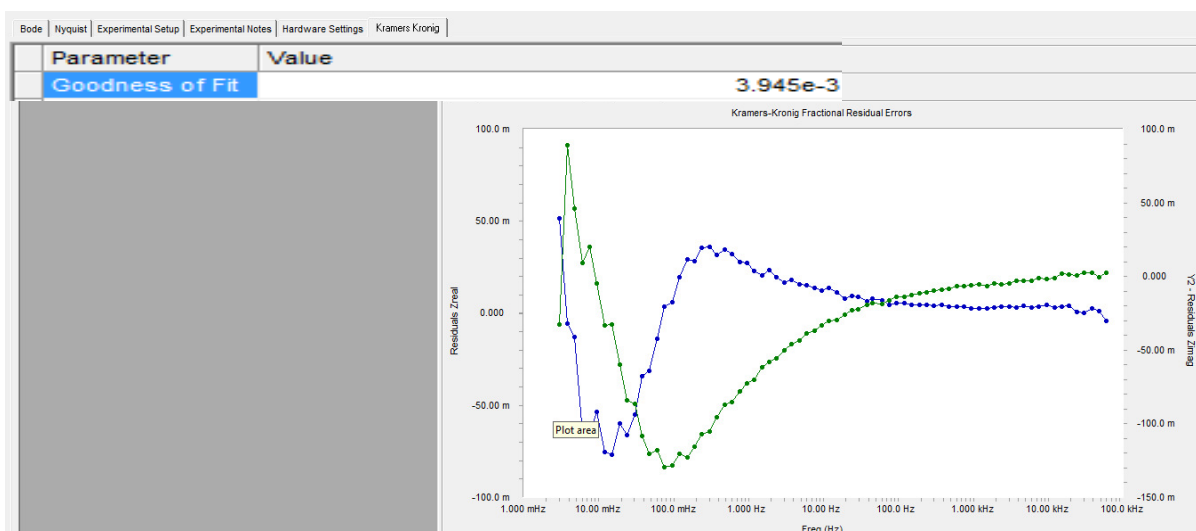


Figure 4.5. Example of a bad K-K test result.

A number of other experimental errors can be controlled in EIS analysis, such as ensuring that the cells are maintained at constant temperature. This was especially true if spectra are required at different temperatures. Care needed to be taken when

EIS measurements were done at temperatures below 0°C and at temperatures above 30°C. For example, the EIS scan of a Li-ion cell that was done at -20°C is shown in Fig 4.6.

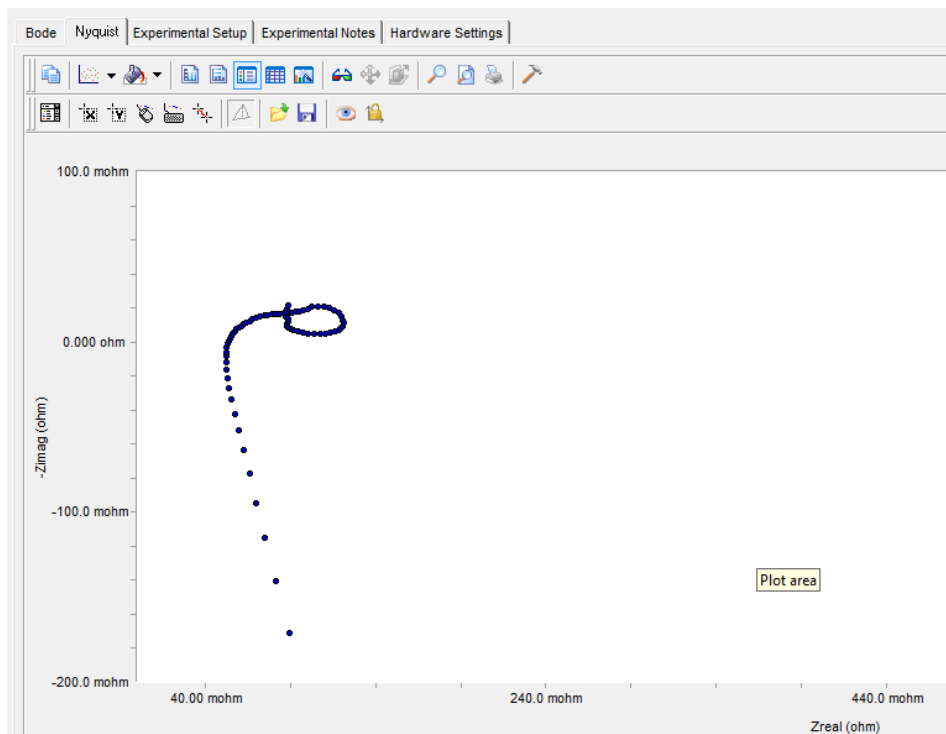


Figure 4.6. A Nyquist plot showing an EIS spectrum looping back on itself.

The cell was cooled to -20°C and removed from the freezer followed by the EIS analysis which could take up to 10 minutes. As the cell began to warm, some adsorption processes at the electrode surface, surface reactions, chemical modification or thermal changes may have occurred that resulted in the EIS spectra showing a typical looping back in the Nyquist plot. All subsequent analysis at lower or higher temperatures than room temperature would have to be done at the set temperature. Care also had to be taken to ensure that all surrounding electric interferences, in particular the cooling generator of the freezer or heating element of an oven, needed to be switched off.

An EIS model was used to analyse the EIS spectra obtained. The parameters that were measured within the cell during EIS analysis included: the inductance and resistance of the circuit, resistance associated with the SEI as formed on the anode during cycling, resistance associated with the double layer capacity and charge transfer resistance of the electrodes, the capacitance associated with the SEI layer

at the anode and the capacitance associated with the double layer capacity at both electrodes and the porous Warburg function.

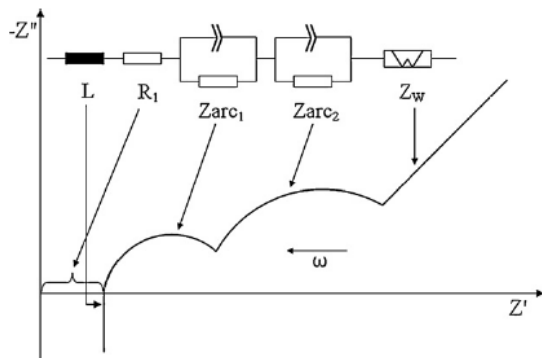


Figure 4.7. Ideal EIS spectrum with a decrease in frequency in ohms along the x-axis from left to right.

At very high frequencies of the spectrum shown in fig 4.7, the inductance parameter was measured. The inductance took into account inductive reactants of the metallic elements in the cell and wires. The ohmic resistance of the cell was measured at the intersection with the real axis of the spectrum. The circuit resistance measured the resistances of current collectors, active material, electrolyte and separator. The first semi-circle seen on the spectrum was associated with the solid electrolyte interface (SEI) that formed on the surface of the anode during cycling. The second semi-circle represented the double layer capacity and charge transfer resistance seen at both electrodes. The Warburg element was seen at low frequencies of the spectrum and took place due to diffusion processes in the active material of the electrodes⁶⁸. A measure of the time taken for the reactant to diffuse across the Nernst Diffusion layer⁸⁶ was characterized by one of the parameters (YoW) from the model. The Nernst Diffusion layer is a virtual layer, within which the gradient of the ion concentration is constant and equal to the true gradient at the electrode-electrolyte interface. This is shown in Figure 4.8.

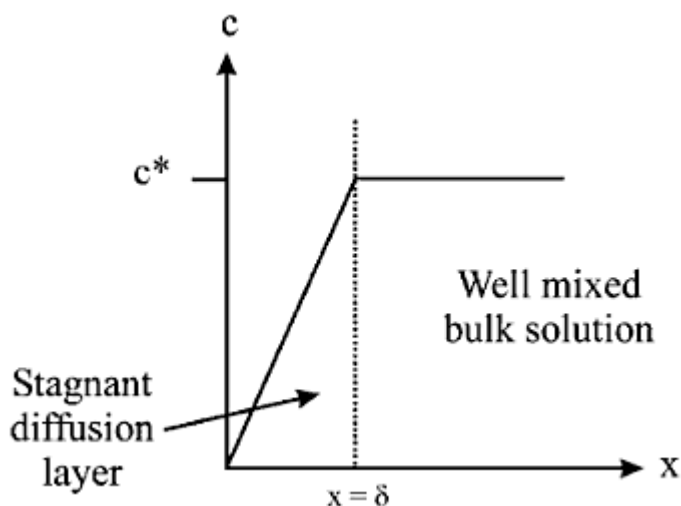


Figure 4.8: Nernst Diffusion layer⁸⁷.

The thickness of the Nernst Diffusion layer may be measured graphically as the ion concentration vs. the distance from the electrode surface⁸⁷.

The equivalent circuit diagram used to determine these parameters can be drawn as shown in Figure 4.9.

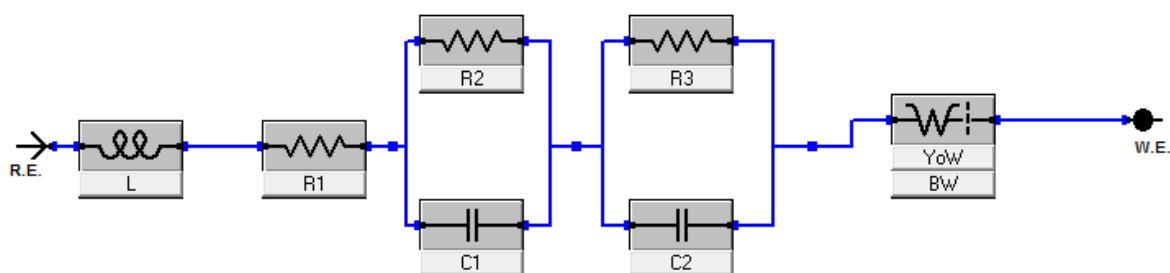


Figure 4.9. Equivalent Circuit diagram used to determine the different parameters of an EIS spectrum.

The diagram was drawn using the Gamry Analyst software.

The different symbols in Fig 4.9 can be explained in table 4.1.

EIS model parameter	Parameter description
L	Inductance of circuit
R1	Resistance of circuit
R2	Resistance associated with the SEI as formed on the anode during cycling
C1	Capacitance associated with the anode
R3	Resistance associated with the double layer capacity and charge transfer resistance at the electrodes
C2	Capacitance associated with both electrodes
YoW & BW	Porous Bonded Warburg section of the cell

Table 4.1 EIS model explanation⁶⁸.

EIS measurements of Li-ion cells that were discharged to different States-of-Charge (SoC) were done at room temperature. Three different types of Li-ion capacity cells were measured, namely the 20Ah LiCoO₂ pouch cell, the 1Ah LiMn₂O₄ pouch cell and the 2Ah LiCoO₂ cylindrical cell. EIS measurements were also done on these three types of Li-ion cells at different temperatures. The EIS model described above was used to analyse all the EIS spectra obtained at the different SoC and different temperatures.

4.1. EIS study of Li-ions cells at various temperatures and State of Charge:

4.1.1. 20Ah pouch cell at different States-of-Charge (SoC)

A 20Ah pouch cell was fully charged and then discharged at C/1 rate based on the cells true capacity to 80% 60% 40%, 20%, 10%, 5% and 0% SoC respectively. The cell was allowed to stabilize for 10-20 minutes before subjecting it to an EIS analysis. The cell was then fully charged after each SoC test and subsequently discharged to the next SoC. EIS results are shown in Fig 4.10.

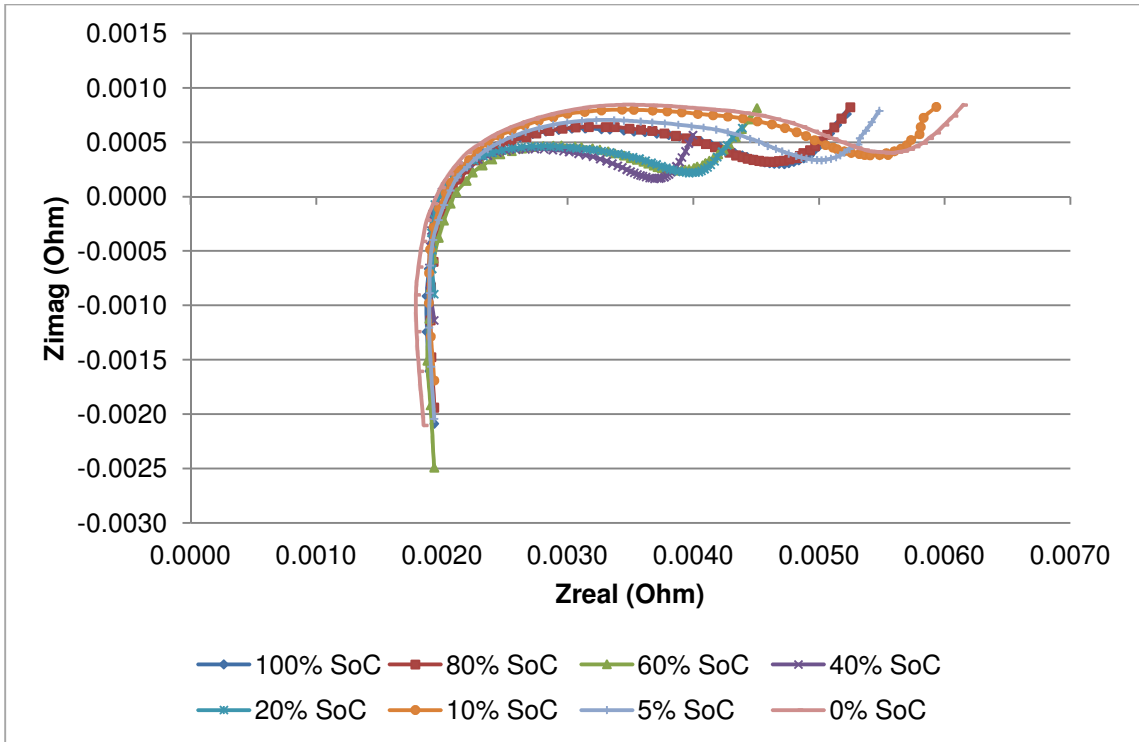


Figure 4.10. EIS Nyquist plot of a 20Ah pouch cell at different SoC done at room temperature.

Very small changes along the Zreal axis were seen for the different SoC.

The various model parameters of importance were plotted. Large semi-circles were seen at 20% and 0%, and in order to investigate this area better, EIS were also done at 10% and 5% SoC.

Resistances due to current collectors, electrolyte resistance and electrode material resistance were modelled collectively under the circuit resistance parameter of the EIS model selected. The circuit resistance at different SoC is shown in Fig 4.11.

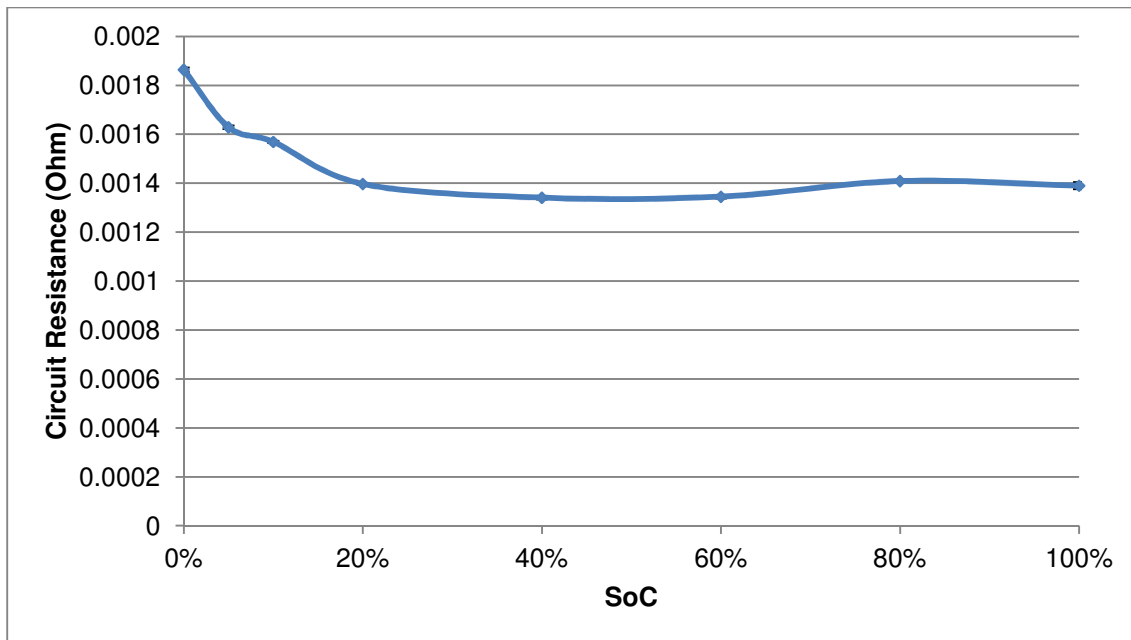


Figure 4.11. Circuit resistance at different SoC.

The slightly higher resistance values were seen at 0%, 5%, 10%, 80% and 100% SoC. The higher circuit resistances at 0%, 5% and 10% SoC could be due to higher resistances at the anode which contributed to the overall circuit resistance. As the SoC decreased, more oxidation would occur at the anode which resulted in higher resistances. At 80% and 100% SoC, the overall charge is increased and more Li-ions can be found at the cathode, which resulted in higher resistances due this charge at the cathode. The overall resistance was influenced more by the anode than the cathode.

A similar resistance pattern was seen for the resistance associated with the SEI layer at the anode.

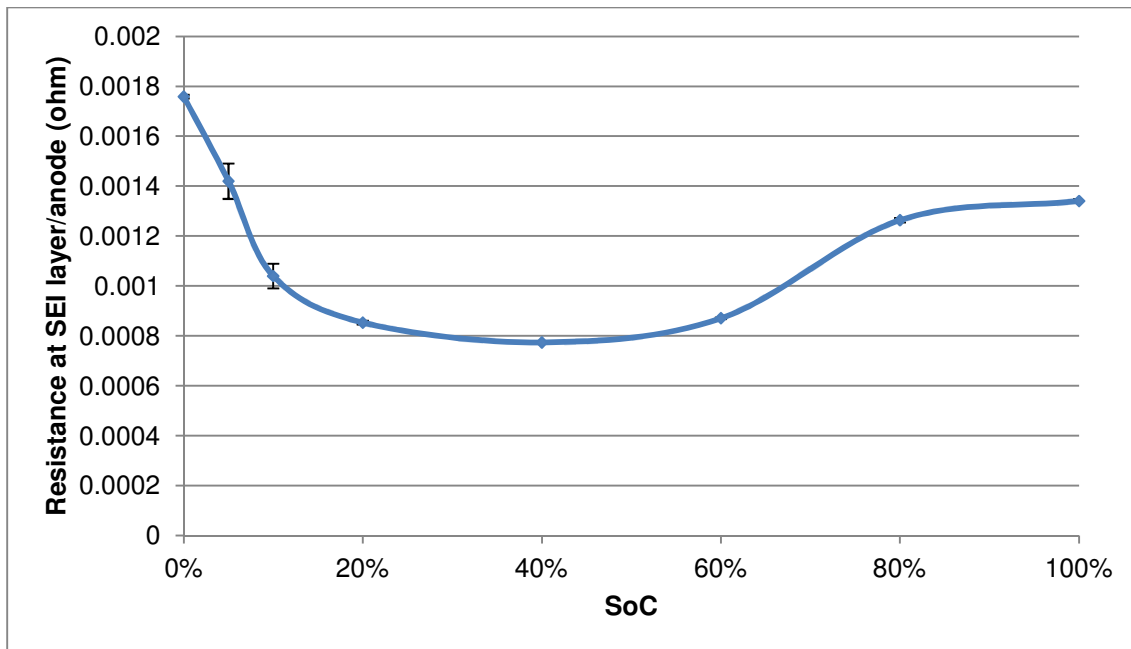


Figure 4.12. Resistance associated with the SEI layer at the anode at the different SoC.

Similar trends were seen in the resistance associated with the SEI layer at the anode results as seen for the circuit resistance results, with an increase in resistance at 80% and 100% SoC. The resistances peaked at lower SoC and higher SoC with smaller values of resistance were shown for 20%, 40% and 60% SoC. The peak at lower SoC could be due to resistance by the SEI layer at the anode in aiding further lithiation. The peak at higher SoC could be due to the SEI layer preventing full delithiation of the anode.

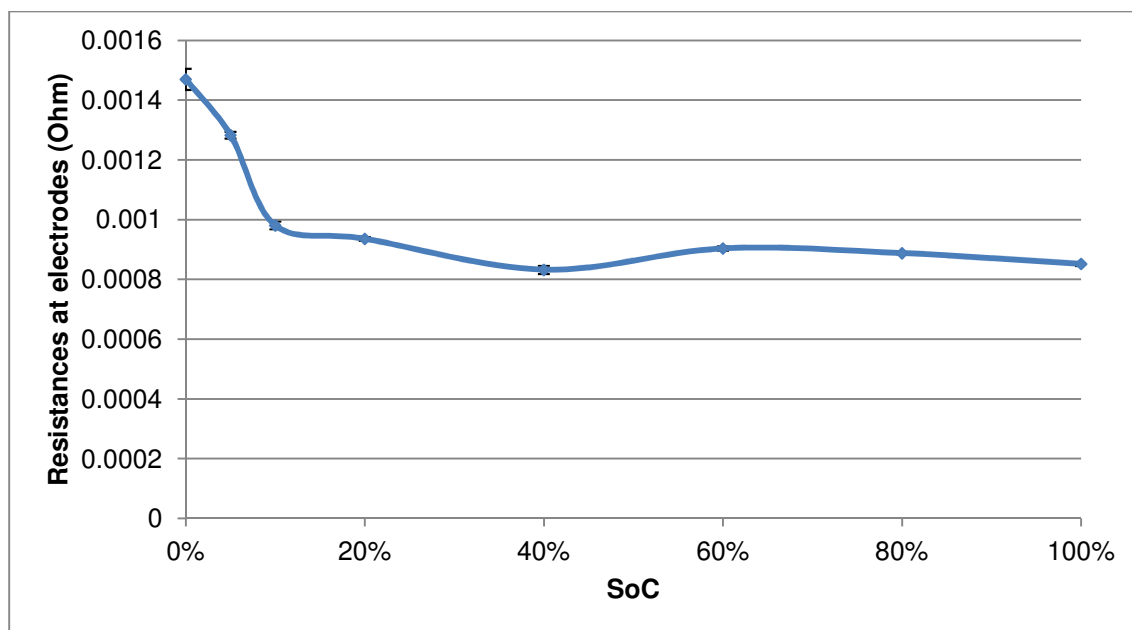


Figure 4.13. Resistance associated with the double layer capacity and charge transfer resistance at the electrode at the different SoC.

The largest resistance was seen at 0% SoC. The resistance then decreased to 40% SoC. A slight increase in resistance was seen at 60% SoC, and then the resistance decrease again. The trend matched the results seen in a paper by D. Andre et al⁶⁸. The peak at the lower SoC was influenced by the resistance at the anode. If an overall resistance trend was drawn using the results obtained due to the SEI layer at the anode and the resistance results at both electrodes, a similar trend to the circuit resistance would be seen.

The capacitance associated with the SEI layer at the anode and the capacitance associated with both electrodes are shown in Fig 4.14 and 4.15 respectively.

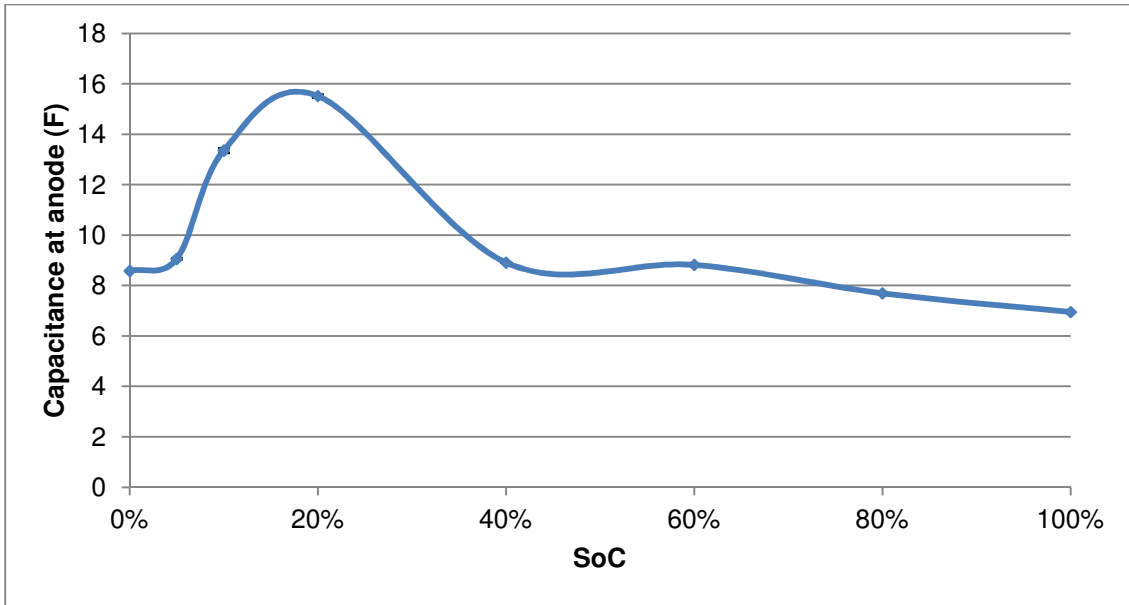


Figure 4.14. Capacitance associated with the SEI layer at the anode at different SoC.

A peak of capacitance associated with the SEI layer was seen at 20% SoC. Capacitance is the ability of the battery to store energy. At 20% SoC, the battery had a low charge and would be able to undergo charging and thus store more energy. At 20% SoC, the resistance due to the SEI layer was lower than at 0%, 5% and 10% SoC, which would also influence the capacitance of the cell.

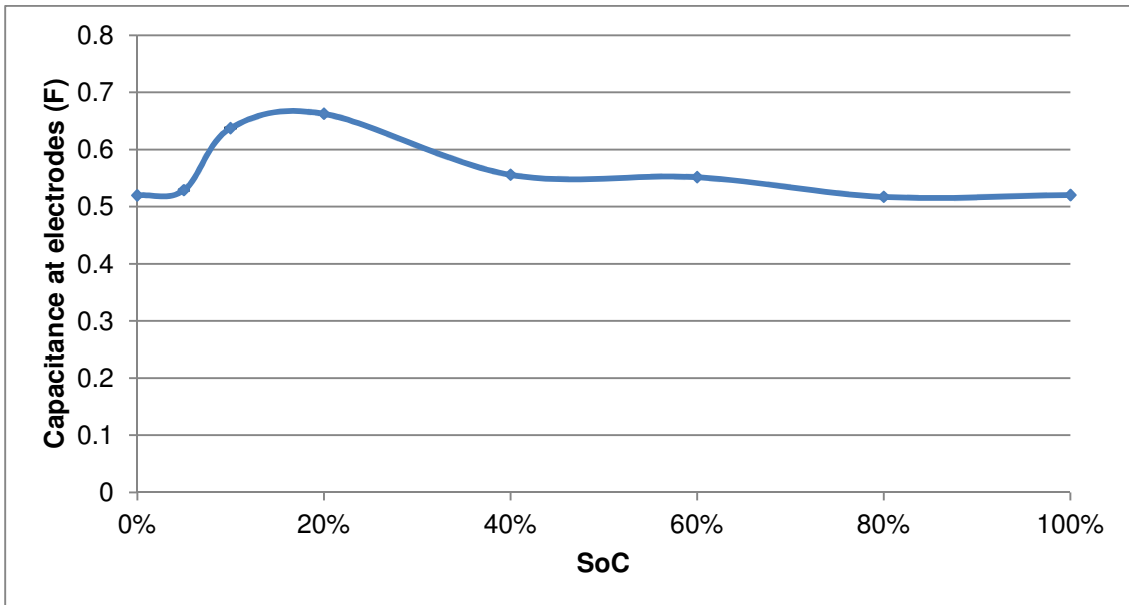


Figure 4.15. Capacitance associated with the double layer capacity and charge transfer at both electrodes at different SoC.

A similar trend to the capacitance associated with the SEI layer was seen for the capacitance associated with both the electrodes.

The Warburg effect was measured at the different SoC and shown in Fig 4.16.

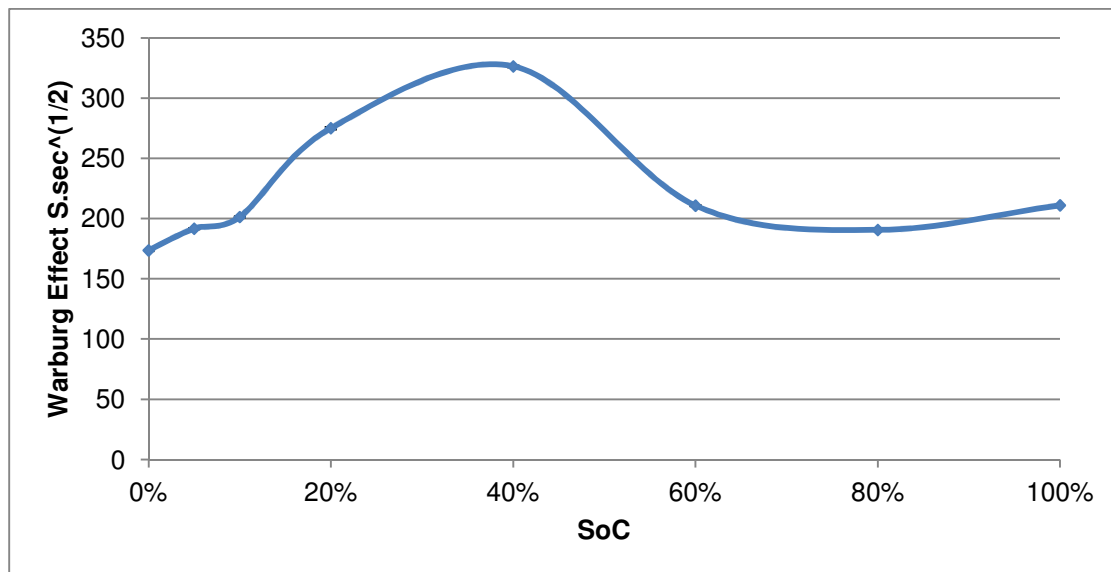


Figure 4.16. Time taken for the reactant to diffusion through the Nernst Diffusion layer at the different SoC.

The Warburg effect depends on the diffusing ability of the reactants to diffuse through the Nernst Diffusion layer. At 40% SoC, the reactants took the longest to diffuse through this Nernst Diffusion layer. When an electrode is polarized, the surface concentration of the species that is either being oxidized or reduced falls to zero, thus ensuring more material will then diffuse to the electrode surface towards this lower region of concentration⁸⁷. At 40% SoC, the electrodes are almost equally oxidized/reduced, thus ensuring that the more material diffuses towards the electrodes, which would result in higher diffusion rates. The slight inconsistencies in the change in the Warburg constant at the lower SoC could not be explained.

4.1.2. 1Ah pouch cell at different SoC

A 1Ah pouch cell was fully charged and then discharged at C/1 rate based on the cells true capacity to 80% 60% 40%, 20%, 10%, 5% and 0% SoC respectively. The cell was allowed to stabilize for 10-20 minutes before subjecting it to an EIS analysis. The cell was then fully charged after each SoC test and subsequently discharged to the next SoC. EIS results are shown in Fig 4.17.

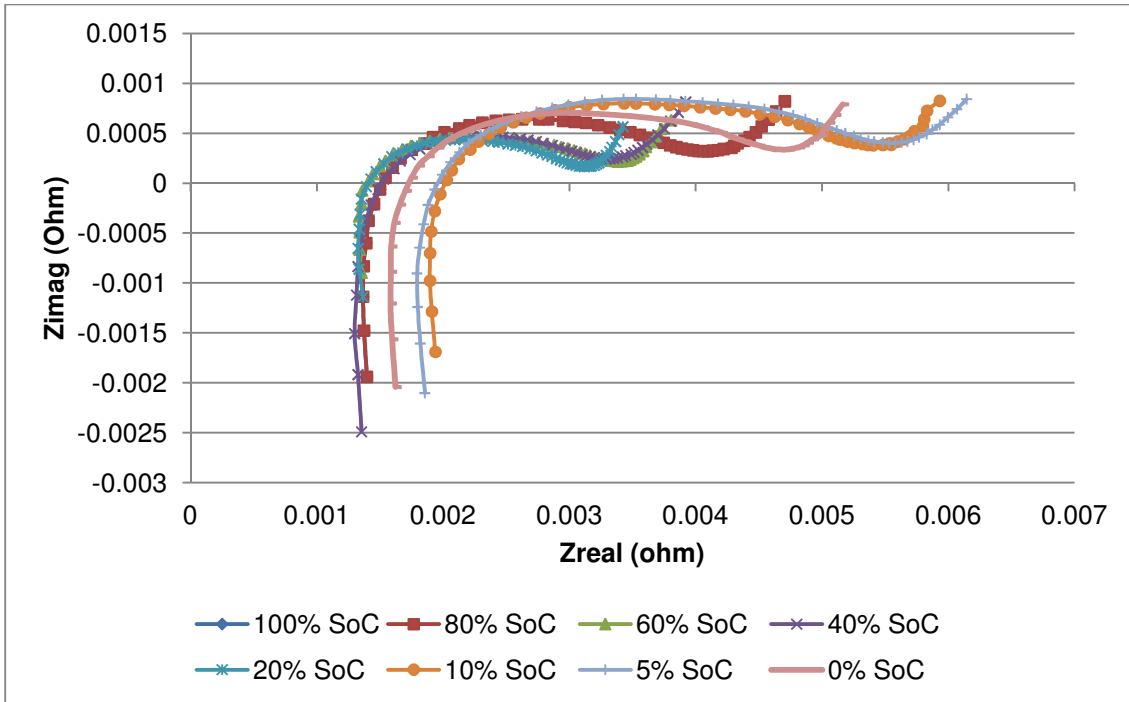


Figure 4.17. EIS spectra of a 1Ah pouch cell at different SoC.

There were small changes seen along the Zreal axis at the different SoC with the spectra obtained at 10%, 5% and 0% SoC showing larger Zreal values. These differences indicate differences in circuit resistances within the 1Ah pouch cell at the different SoC.

The EIS spectra were modelled using the EIS model previously discussed. Once again, EIS spectra were taken at 10% and 5% SoC in order to determine if there were any significant changes between 20% and 0% SoC.

The resistances for the different areas within the cell were plotted. Resistances due to current collectors, electrolyte resistance and electrode material resistance were modelled collectively under the circuit resistance parameter of the EIS model selected. The circuit resistance at different SoC is shown in Fig 4.18.

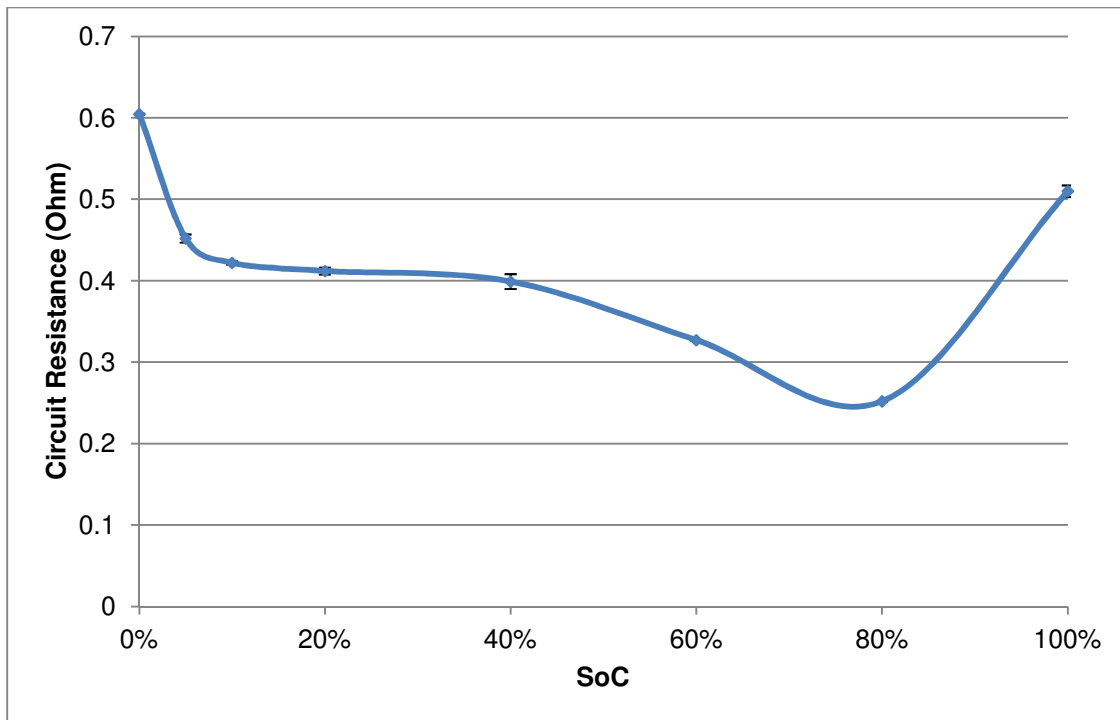


Figure 4.18. Circuit resistance at different SoC.

The highest resistance values were seen at 0%, 5%, 10% and 100% SoC. This trend was similar to the trend seen in the results obtained in the 20Ah pouch cell. However there was a larger decrease in circuit resistance from 40% to 80% SoC than seen for the 20Ah pouch cell. This inconsistency could not be explained and might be due to poor cell / circuit connections.

The resistance associated with the SEI layer at the anode is shown in Fig 4.19.

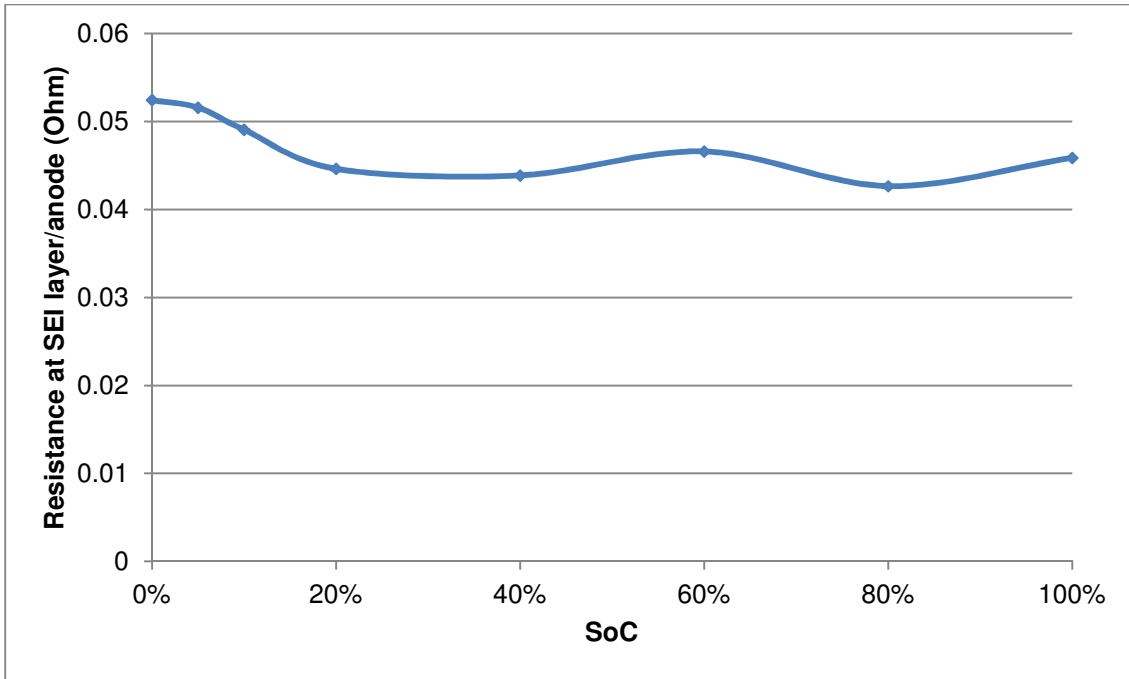


Figure 4.19. Resistance associated with the SEI layer at the anode at the different SoC.

Higher resistances were seen for the lower SoC, as was expected due to the SEI layer playing a role in the resistance at this SoC. However there were small changes in resistance associated with the SEI layer for all the SoC.

The resistance associated the double layer capacity and charge transfer resistance at the electrodes shown in Fig 4.20.

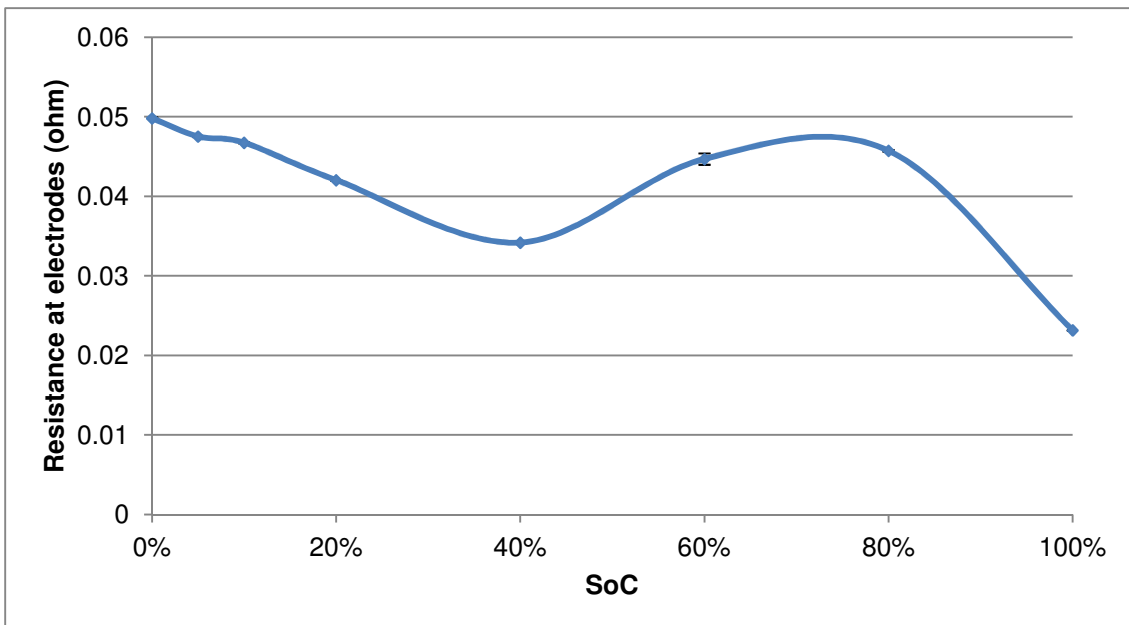


Figure 4.20. Resistance associated with the double layer capacity and charge transfer resistance at the electrode at the different SoC.

The resistance associated with the double layer capacity and charge transfer at both electrodes was the highest at 0%, 5% and 10 % SoC. The resistance continued to drop from 10% SoC till 40% SoC, with a slight increase again to 60% and 80% SoC. On average, an increase in the resistance was observed with a decrease in the SoC of the cell. Once again a similar trend was seen for the 20Ah pouch cell, however the resistance values were slightly higher for the 1Ah pouch cell and the peaks and valleys of the values was more significant than for the 20Ah pouch cell. As the cell was smaller in dimension and the electrode connections were closer in proximity to each other in comparison to the 20Ah pouch cell, additional connections and wiring between the cell and the EIS instrument were used in order to prevent short circuits. These additional connections and wiring could have caused some experimental errors which resulted in these differences seen in the results. Ageing of the cell may have highlighted the changes seen in the 1Ah pouch cell.

Capacitance was measured and the results are shown in Fig 4.21 and 4.22.

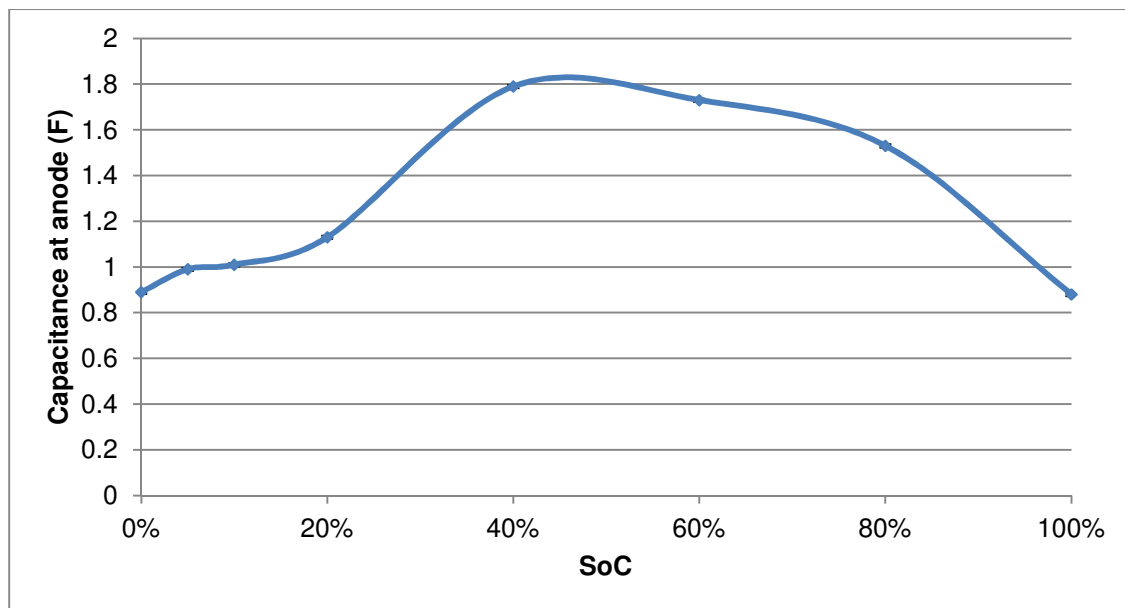


Figure 4.21. Capacitance associated with the SEI layer at the anode at different SoC.

There was an increase in capacitance at 40% SoC as associated with the SEI layer at the anode. At 40% SoC, the cell would have the ability to accept charge, thus having a higher capacitance. The capacitance was seen to decrease as the SoC increased after 40% SoC. The highest value was seen at 40% SoC. The anomalies in the change in capacitance with decrease in SoC could be due to the refinement model chosen to fit the model to the experimental data. Slight increases in

capacitance at lower SoC were also seen in the results where the cell was tested with supercapacitors and are discussed later in chapter 5. The results are shown in Fig 5.33 and 5.34. The results indicate that the capacitance built up till 40% SoC, followed by a sudden drop in capacitance from 20% SoC. The voltage of a cell is also known as the electromotive force (emf). The emf can be thought of as the pressure that causes the charges to flow through the circuit of the battery⁸⁸. In this case, at 20% SoC the emf of this cell may place too much pressure on the charge and the capacitance drops.

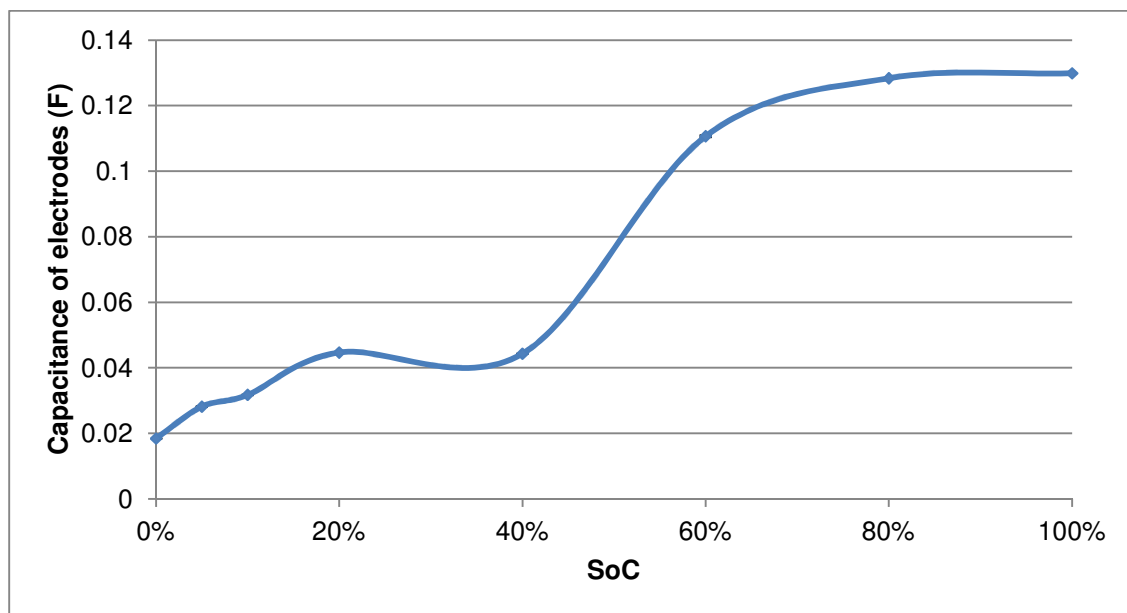


Figure 4.22. Capacitance associated with the double layer capacity and charge transfer at both electrodes at different SoC.

The capacitance steadily increased as the SoC increased after 40% SoC. This trend was different to the one seen for the capacitance associated with the SEI layer at the anode. However these capacitance values were smaller than the capacitance associated with the SEI layer at the anode values, which indicated that this capacitance had a smaller influence on the overall capacitance of the cell. The above capacitance is associated with the double layer capacity and charge transfer resistance at both electrodes. As the cell is charged the Li-ions lithiate the anode more than the cathode, thus increasing the capacitance at the cathode.

The time taken for the reactant to diffuse through the Nernst Diffusion layer is plotted in Fig 4.23.

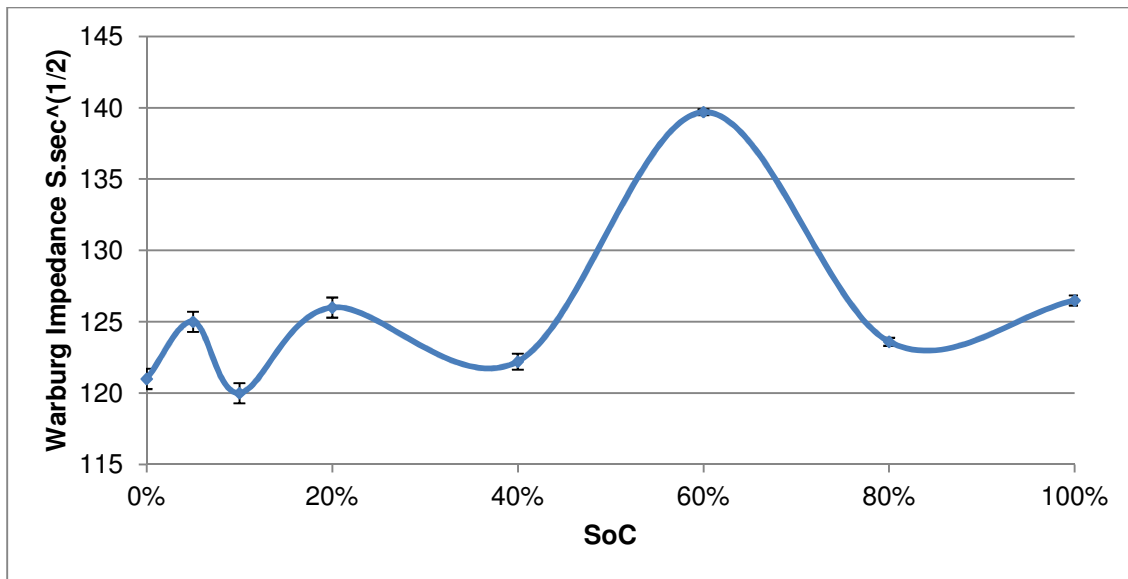


Figure 4.23. Time taken for the reactant to diffusion through the Nernst Diffusion layer at the different SoC.

A higher Warburg effect was seen at 60% SoC, indicating the time taken for the reactants to diffuse through the Nernst Diffusion layer was the highest at 60% SoC. This higher value at 60% SoC could be due to a poorly fitted EIS model, as the other SoC values shift between 120 and 127 S.sec^(1/2).

4.1.3. 2Ah cylindrical cell at different SoC

A 2Ah cylindrical cell was fully charged and then discharged at C/1 rate based on the cells true capacity to 80% 60% 40%, 20%, 10%, 5% and 0% SoC respectively. The cell was allowed to stabilize for 10-20 minutes before subjecting it to an EIS analysis. The cell was then fully charged after each SoC test and subsequently discharged to the next SoC. EIS results are shown in Fig 4.24.

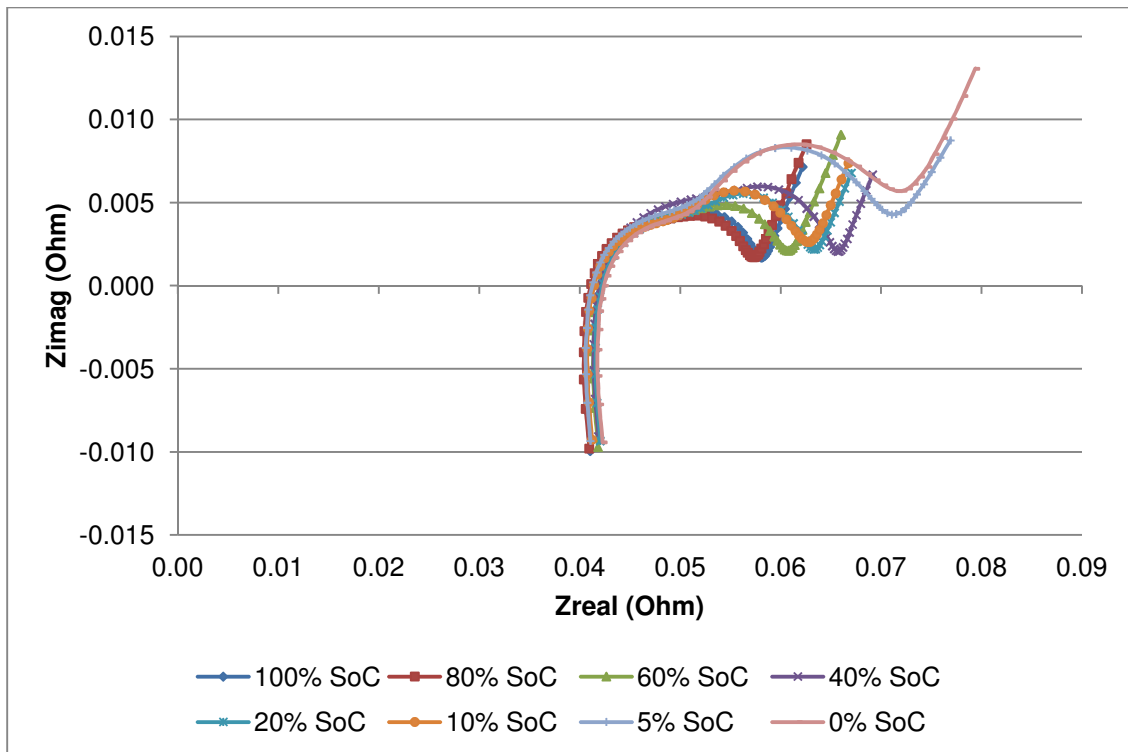


Figure 4.24. EIS spectra of a 2Ah cylindrical cell at different SoC.

Very small changes along the Zreal axis were seen for the different SoC. However, significant changes within the semi-circles were seen. These changes were modelled using the EIS model previously discussed. Larger differences along the Zreal axis were seen during the 1Ah pouch cell tests. The various model parameters of importance were plotted.

Larger semi-circles were seen at 20% and 0%, and in order to investigate this area better, EIS were also taken at 10% and 5% SoC.

The resistances for the different areas within the cell were plotted. Resistances due to current collectors, electrolyte resistance and electrode material resistance were modelled collectively under the circuit resistance parameter of the EIS model selected. The circuit resistance at different SoC is shown in Fig 4.25.

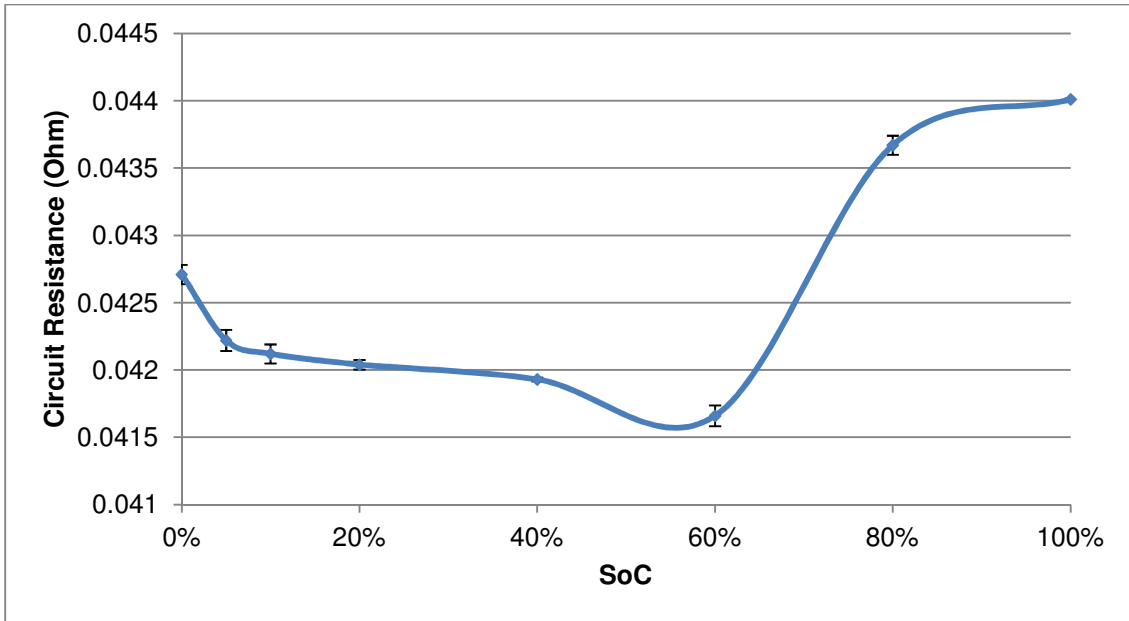


Figure 4.25. Circuit resistance at different SoC.

The resistance values steadily decreased from 0% SoC to 60% SoC. There was an increase in resistance to 100% SoC. The circuit resistance values seen in the 2Ah cylindrical cell results were higher than the circuit resistance values seen during the 20Ah pouch cell tests. The reason could be attributed to a different cell design or possibly the 2Ah cylindrical cell had aged more before the testing.

The resistance associated with the SEI layer at the anode is shown in Fig 4.26.

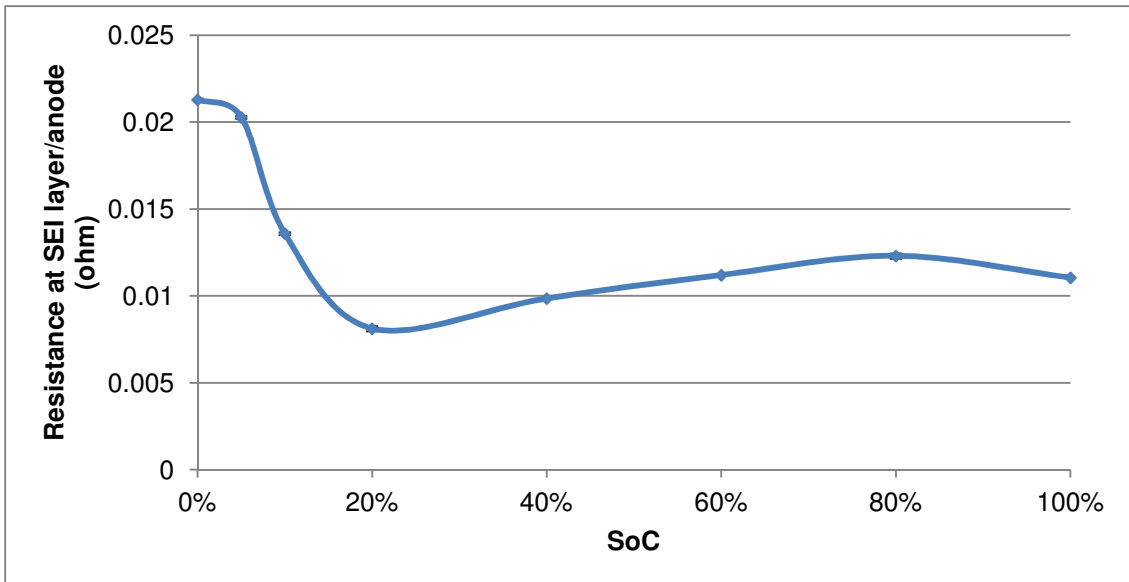


Figure 4.26. Resistance associated with the SEI layer at the anode at the different SoC.

The highest resistance values were obtained at 0% and 5% SoC. A decrease in resistance values was then seen. The 2Ah cylindrical cell showed a small increase in resistance from 20% SoC to 80% SoC with a small decrease in resistance at 100% SoC.

The resistance associated with the double layer capacity and charge transfer resistance at the electrodes is shown in Fig 4.27. Higher resistances were seen at 0%, 5% and 40% SoC.

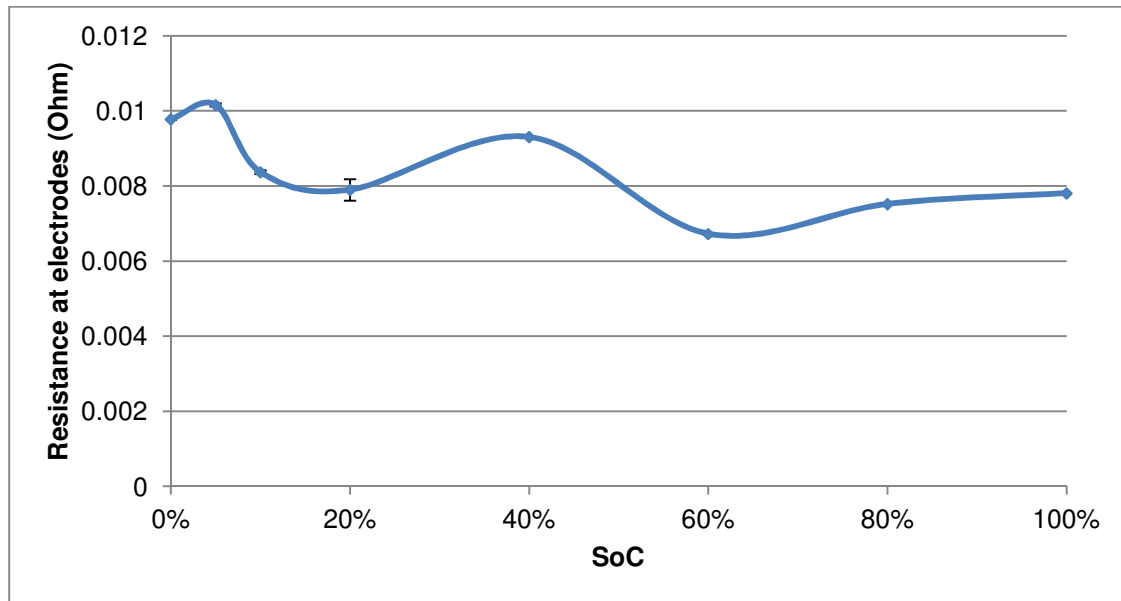


Figure 4.27. Resistance associated with the double layer capacity and charge transfer resistance at the electrode at the different SoC.

The trend seen in figure 4.27 explains the large second semi-circle seen in the EIS spectra, where higher semi-circles were seen at 0%, 5% and 40% SoC on the EIS spectra obtained. This indicated that there were higher resistances associated with the double layer capacity and charge transfer resistance at lower SoC.

The capacitance was measured and is shown in fig 4.28 and 4.29.

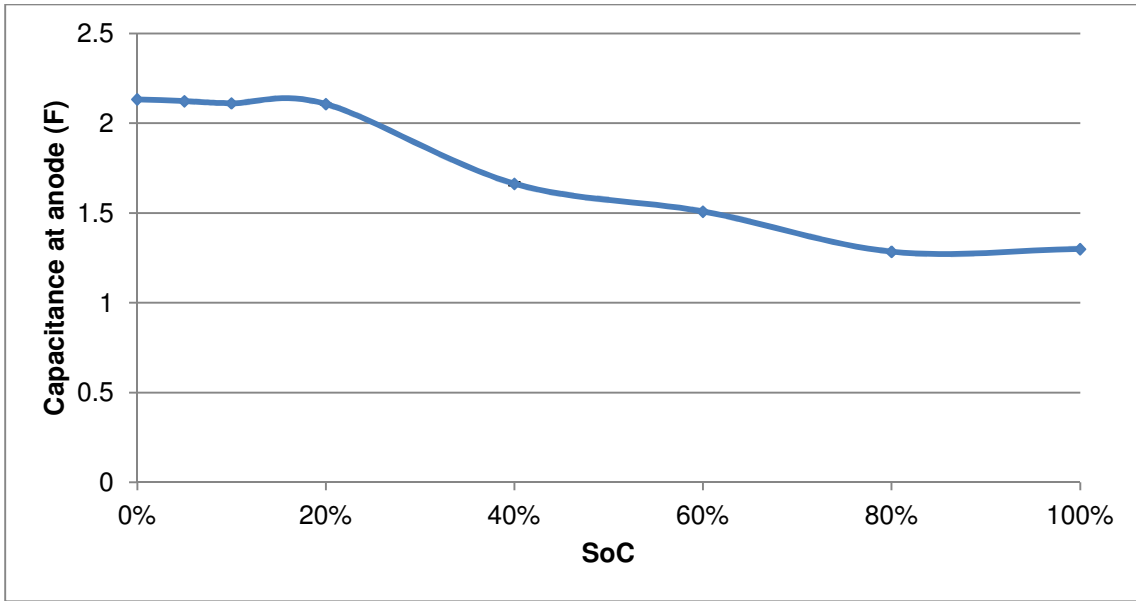


Figure 4.28. Capacitance associated with the SEI layer at the anode at different SoC.

Unlike the other results obtained for the capacitance of the 20Ah and 1Ah pouch cells, the capacitance slowly decreased as the SoC increased. This indicated that the resistance of the cell played almost no significant role in the capacitance of the cell. As the cell SoC decreased, the cell was able to accept more charge and thus the capacitance also increased.

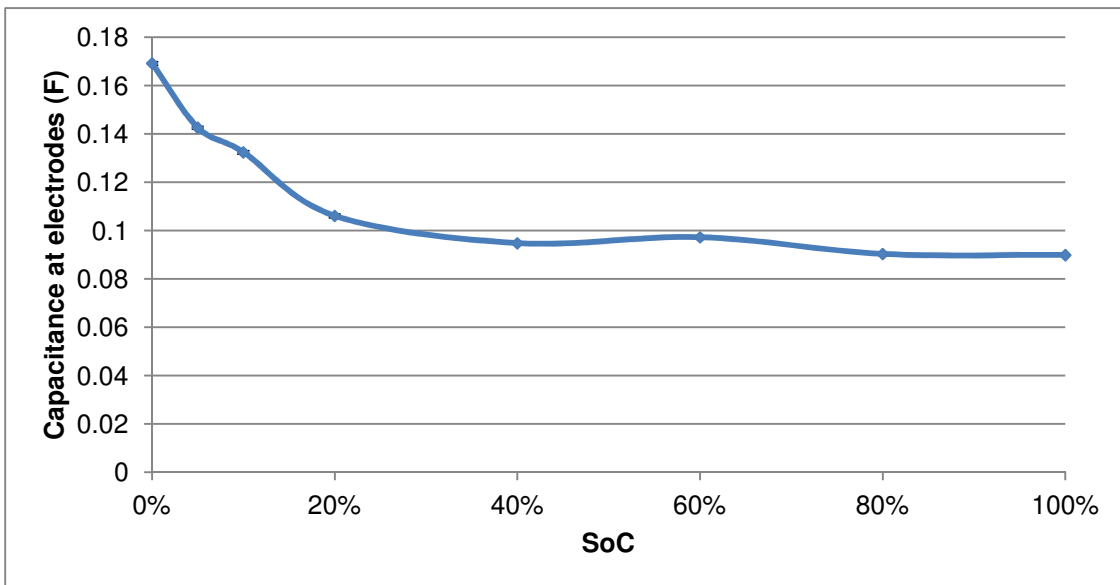


Figure 4.29. Capacitance associated with the double layer capacity and charge transfer resistance at both electrodes at different SoC.

The similar trend was seen for the capacitance associated with the double layer capacity and charge transfer resistance at both electrodes as for the capacitance associated with the SEI layer at the anode. However the capacitance at 0%, 5% and 10% SoC gradually decreases unlike the capacitance associated with the SEI layer at the anode that remained the same.

The time taken for the reactant to diffuse through the Nernst Diffusion layer is shown in Fig 4.30.

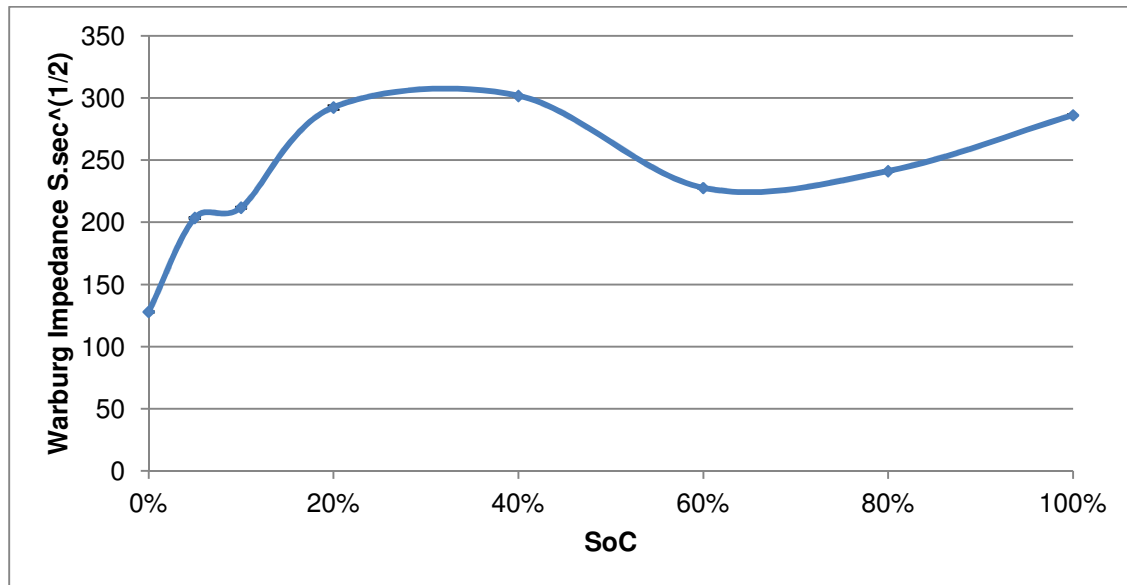


Figure 4.30. Time taken for the reactant to diffusion through the Nernst Diffusion layer at the different SoC.

Once again the Warburg effect was similar to the trend seen during the testing of the 20Ah pouch cell with the greatest value being at 40% SoC. This parameter was sensitive to the experimental setup and the use of the model and fitting of it to the EIS spectra obtained.

Observations made during EIS testing at different SoC:

The inductance values for the three different cells were plotted (Fig 4.31). Very small values were seen for all three cells which indicated small inductance due to the connectors used, cables and instrumental changes.

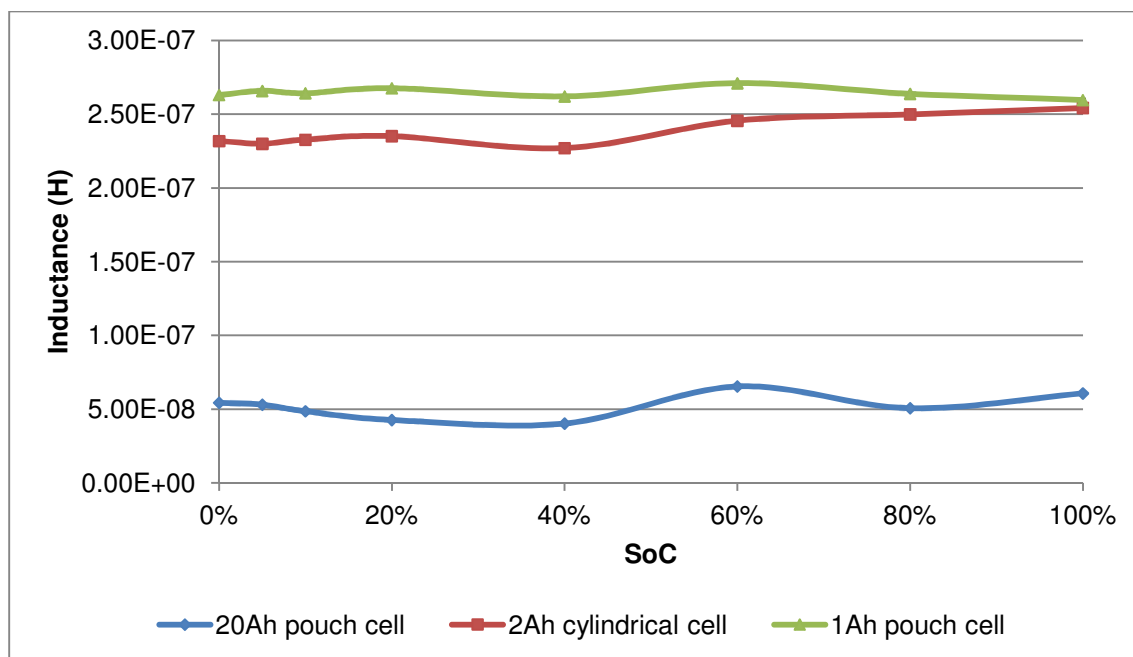


Figure 4.31. Inductance of three different cells at different SoC.

From 50% to 100% SoC the EIS spectra showed larger semi-circles in the EIS spectra. This observation matched a paper by K. Takeno et al⁷². The inductances of all the EIS spectra showed very small values, which indicated very little changes associated with the connections of the cells with the Gamry EIS instrument. Similar trends in circuit resistance were seen for all cells with higher resistances values at 0%, 5%, 10% and 100% SoC. The resistance associated with the SEI layer at the anode showed similar trends for all the cells with the 1Ah pouch cell showing smaller changes along the trend. The resistance associated with the double layer capacity and charge transfer resistance at the electrodes showed a gradual decrease in resistance for the 20Ah pouch cell, a slight increase in resistance at 60% SoC for the 1Ah pouch cell and the cylindrical cell showed slightly higher resistances at 40% SoC. The 20Ah pouch cell trends matched a paper by D. Andre et al⁶⁸. The capacitance associated with the SEI layer at the anode for the 20Ah pouch cell showed an increase till 20% SoC, followed by a decrease in capacitance. The 1Ah pouch showed an increase in capacitance till 40% SoC, followed by a gradual decrease. The 2Ah cylindrical cell showed a steady decrease in capacitance as the SoC increased, with a small peak in capacitance at 20% SoC. The capacitance associated with the double layer capacity and charge transfer resistance at both electrodes showed an increase in capacitance till 20% SoC followed by a decrease in capacitance from 20% SoC as the SoC increased for the 20Ah pouch cell. The

1Ah pouch cell showed a gradual increase in capacitance as the SoC increased. The 2Ah cylindrical cell showed a gradual decrease in capacitance as the SoC increased. These differences could be explained by the differences in cell geometry and chemistry. The two LiCoO₂ cells showed similar trends in comparison to the 1Ah LiMn₂O₄ pouch cell, which indicated that the chemistry of the cells played a larger role in the trends seen. Both the LiCoO₂ cells showed a higher Warburg effect at 40% SoC, while the 1Ah pouch cell showed an increase at 60% SoC.

4.1.4. 20Ah pouch cell at different Temperatures

A fully charged cell was placed in a freezer at -20 °C for 1hr to equilibrate. The EIS of the cell was measured inside the freezer ensuring that the power to the freezer was switched off. The lower temperature studies were repeated at temperatures of -10 °C, 0 °C, 7 °C and 18 °C respectively. The fully charged cells were placed in an oven at 30 °C, 40 °C and 50 °C respectively. After allowing the cells to equilibrate after 1hr, the EIS analyses were done with the cell inside the oven. The power to the oven was switched off during the analysis procedure. All the tests were repeated in duplicate for statistical calculations.

The results of the EIS at the different temperatures are shown in Fig 4.32.

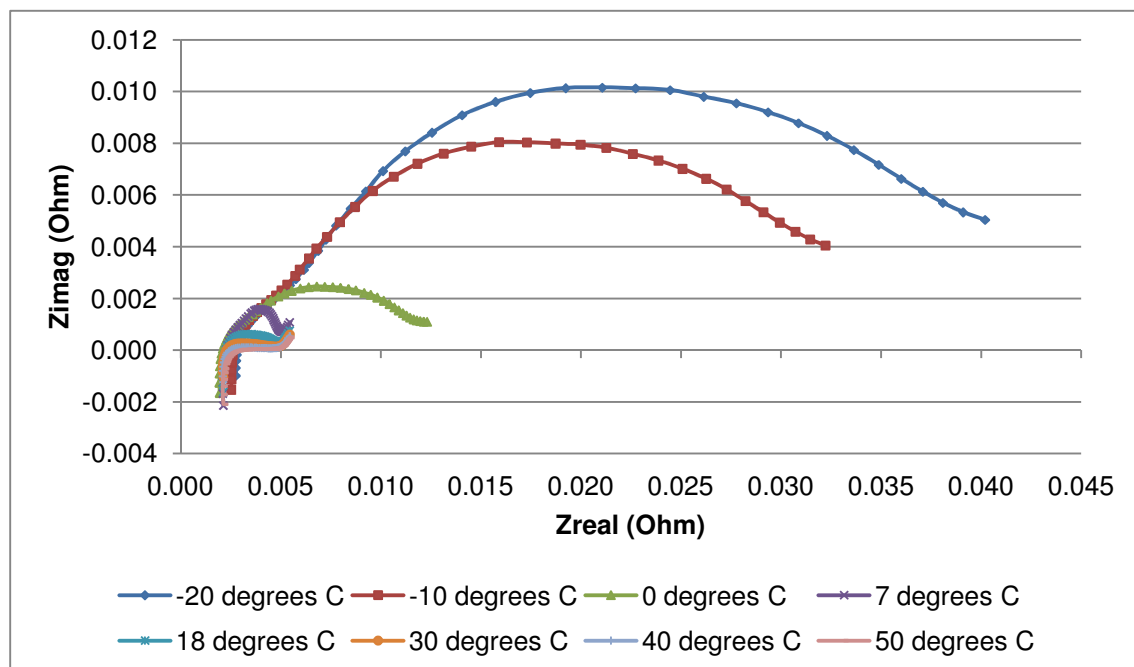


Figure 4.32. EIS spectra of a 20Ah pouch cell at different temperatures.

Very small changes along the Zreal axis were seen for the different temperatures. However significant changes within the semi-circles were seen. These changes were modelled using the EIS model previously discussed. Larger semi-circles were seen at -20 °C, -10 °C and 0 °C.

The resistances for the different areas within the cell were plotted. Resistances due to current collectors, electrolyte resistance and electrode material resistance were modelled collectively under the circuit resistance parameter of the EIS model selected. The circuit resistance at different temperatures is shown in Fig 4.33.

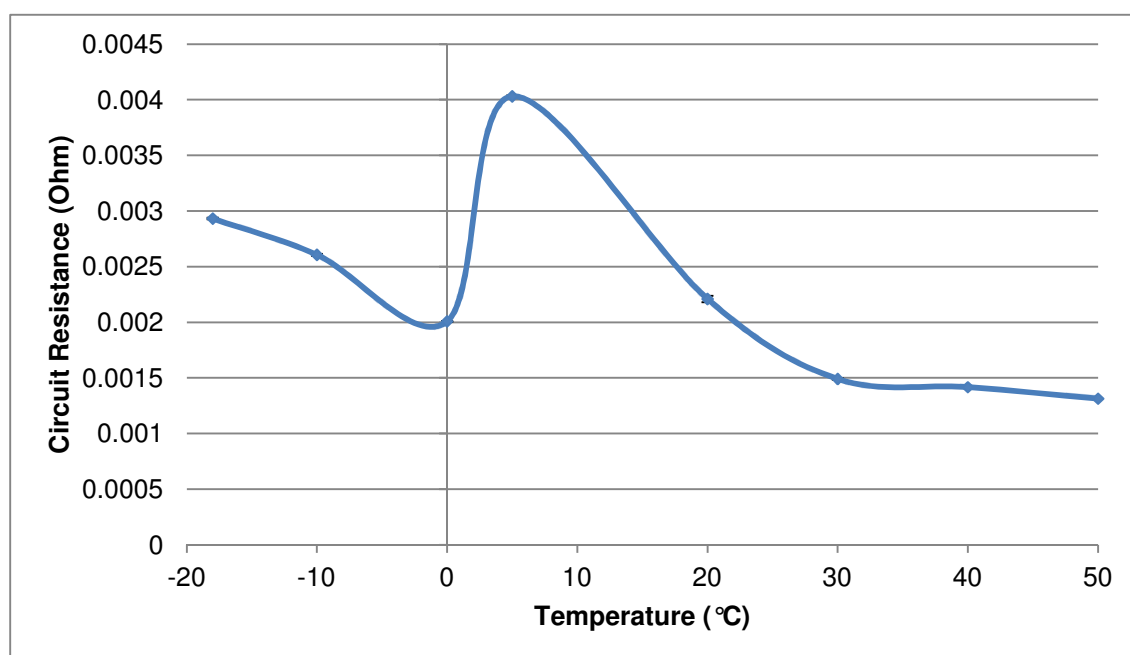


Figure 4.33. Circuit resistance at different temperature.

The highest resistance values were seen at -20 °C, -10 °C and 10 °C. A slightly lower resistance was seen for the 0 °C. Overall the resistance values were small and could be due to experimental setup errors.

The resistance associated with the SEI layer at the anode is shown in Fig 4.34.

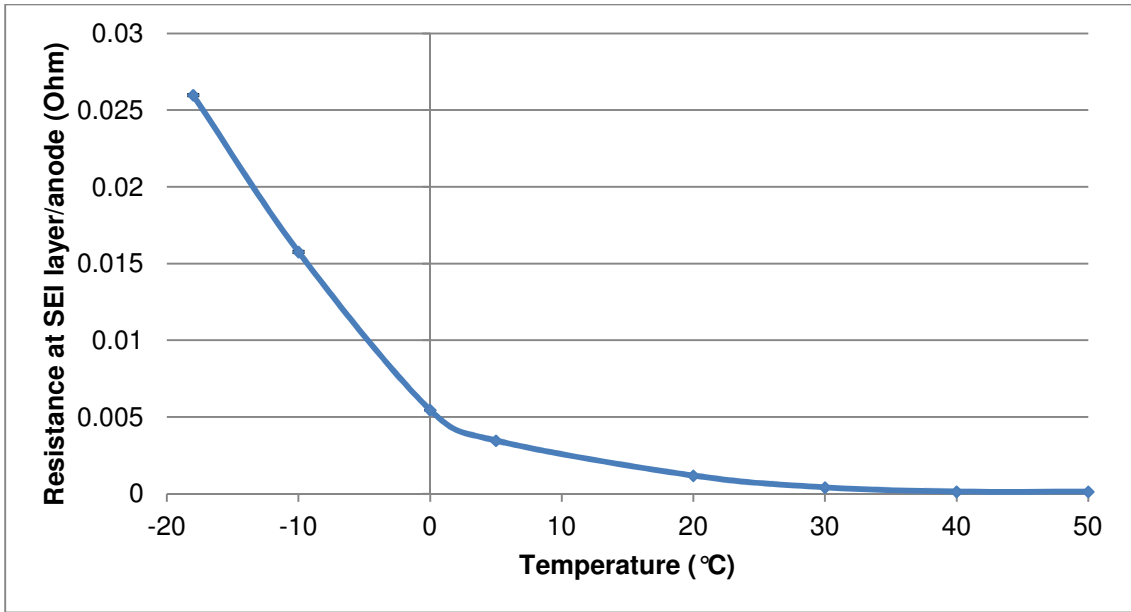


Figure 4.34. Resistance associated with the SEI layer at the anode at the different temperatures.

The resistance gradually decreased from -20 °C to 50 °C. This resistance was responsible for the increase in the first semi-circle seen for the all EIS spectra at the different temperatures. As the temperature increased, the Li-ions became more energized and were able to move through the SEI layer, thus reducing the resistance in this area.

The resistance associated with the double layer capacity and charge transfer resistance at the electrodes is shown in Fig 4.35.

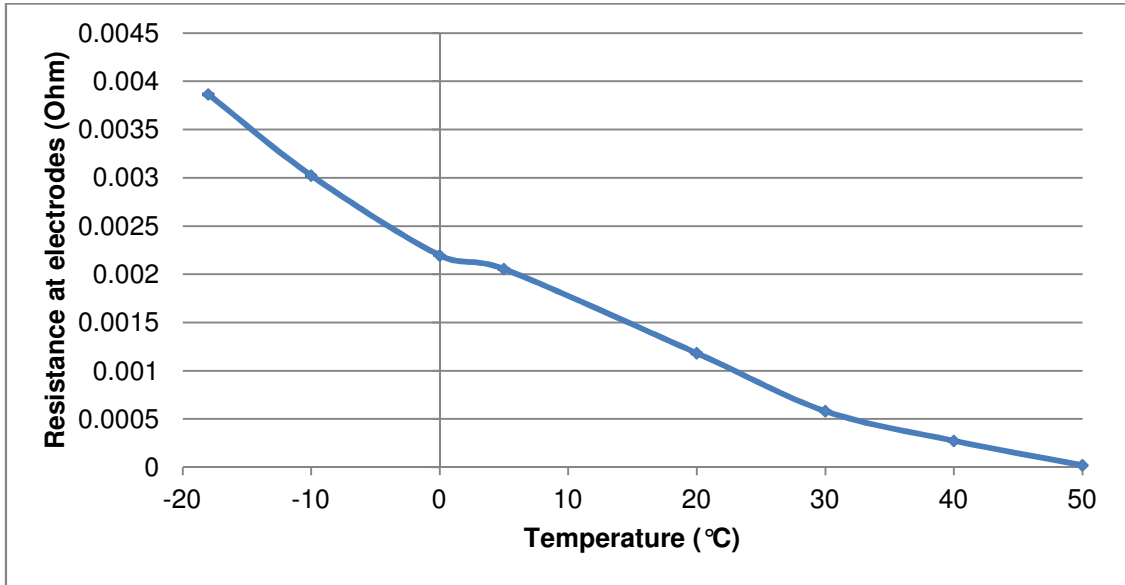


Figure 4.35. Resistance associated with the double layer capacity and charge transfer resistance at the electrode at the different temperatures.

The resistance gradually decreased from -20 °C to 50 °C. Once again as the cell heated up, the Li-ions were able to flow faster between the electrodes. Very small values of resistance were observed as contributed by both electrodes.

The capacitance at the various areas within the cell was measured and is shown in Figures 4.36 and 4.37.

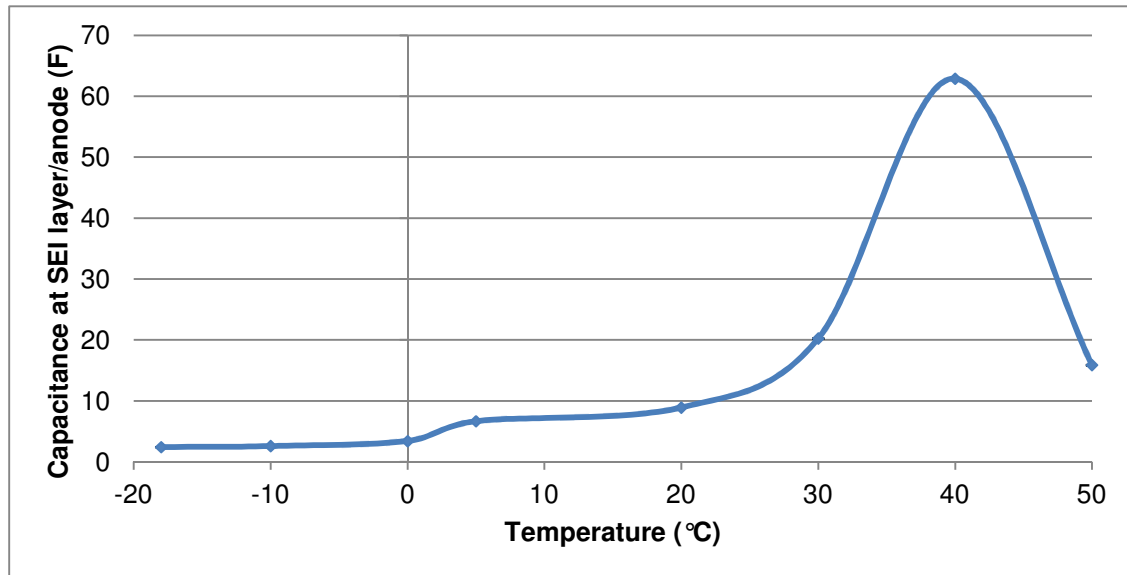


Figure 4.36. Capacitance associated with the SEI layer at the anode over the different temperatures.

The capacitance of the cell gradually increased from 0 °C to 40 °C. Below 0 °C, the capacitance was small, as the cell was cold and the movement of the Li-ions was restricted. Above 40 °C, the capacitance values dropped indicating that the cell became too hot. The heat within the cell restricted the Li-ion movement.

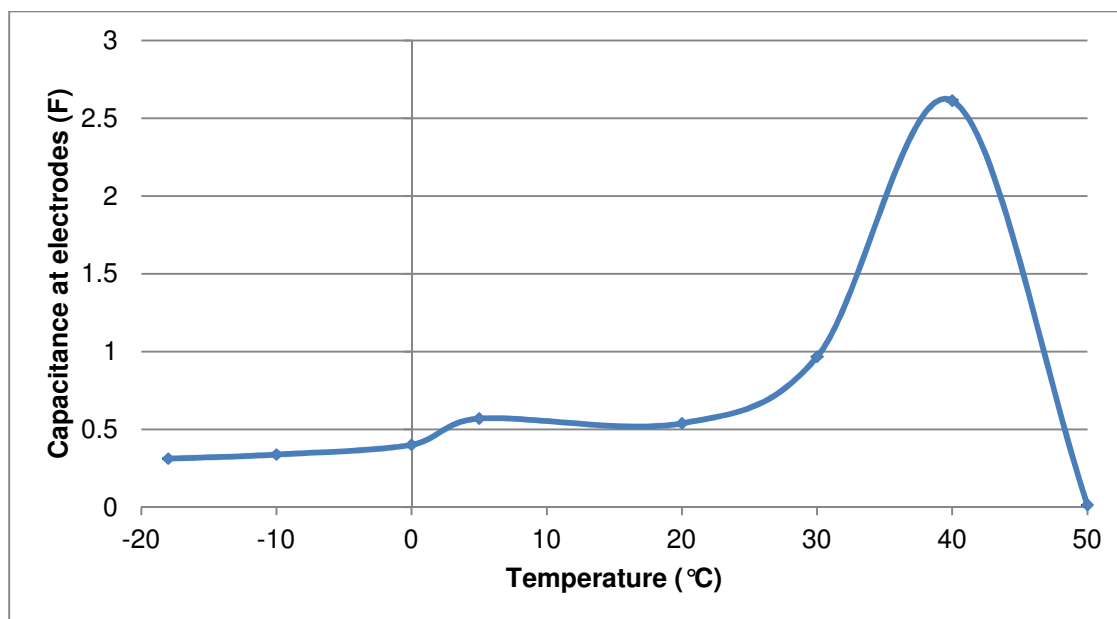


Figure 4.37. Capacitance associated with the double layer capacity and charge transfer resistance at both electrodes over the different temperatures.

A similar trend is seen for the capacitance associated with both electrodes as seen with the capacitance associated with the SEI layer at the anode. Once again, the temperature of the cell played a role in the movement of the Li-ions and the overall capacitance of the cell. Possible reasons for the large increase in capacitance value at 40°C could be due to an error in the fitting of the model to the EIS data. Another factor for the drop in capacitance at 50°C could be due to the electrolyte activity and possible side-reactions within the cell. According to a paper by W.B. Gu et al⁸⁹, the heat effect at high ambient temperatures may cause side-reactions to occur which would play a role in the capacity of the cell significantly. As a result, the cell temperature will further increase and may lead to thermal runaways. Careful thermal management needs to be taken to ensure safety of large Li-ion cells.

The time taken for the reactant to diffuse through the Nernst Diffusion layer is shown in Fig 4.38.

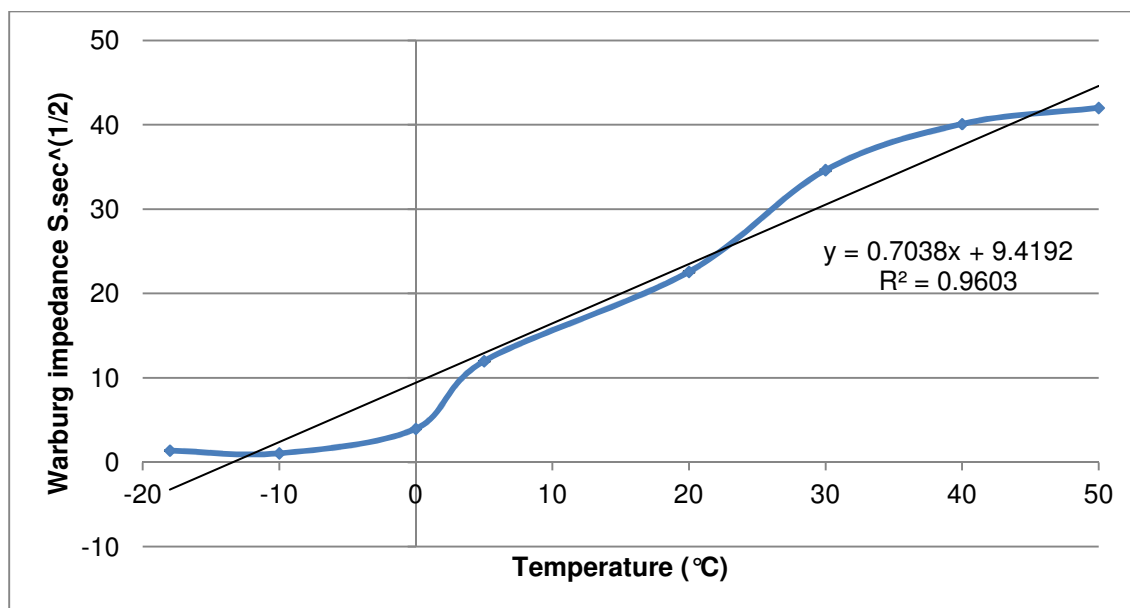


Figure 4.38. The Warburg effect over the different temperatures.

The Warburg effect gradually increased as the temperature of the cell increased. This increase in the Warburg effect matched the trend seen in a paper by Jamie Gomez et al⁹⁰ where the Warburg effect increased as the temperature increased at various SoC, including a fully charged cell as used in this study.

4.1.5. 1Ah pouch cell at different Temperatures

A fully charged cell was placed in a freezer at -20 °C for 1hr to equilibrate. The EIS of the cell was measured inside the freezer ensuring that the power to the freezer was switched off. The lower temperature studies were repeated at temperatures of -10 °C, 0 °C and 16 °C respectively. The fully charged cells were placed in an oven at 30 °C, 40 °C and 50 °C respectively. After allowing the cells to equilibrate after 1hr, the EIS analyses were done with the cell inside the oven. The power to the oven was switched off during the analysis procedure. All the tests were repeated in duplicate for statistical calculations.

The results of the EIS at the different temperatures are shown in Fig 4.39.

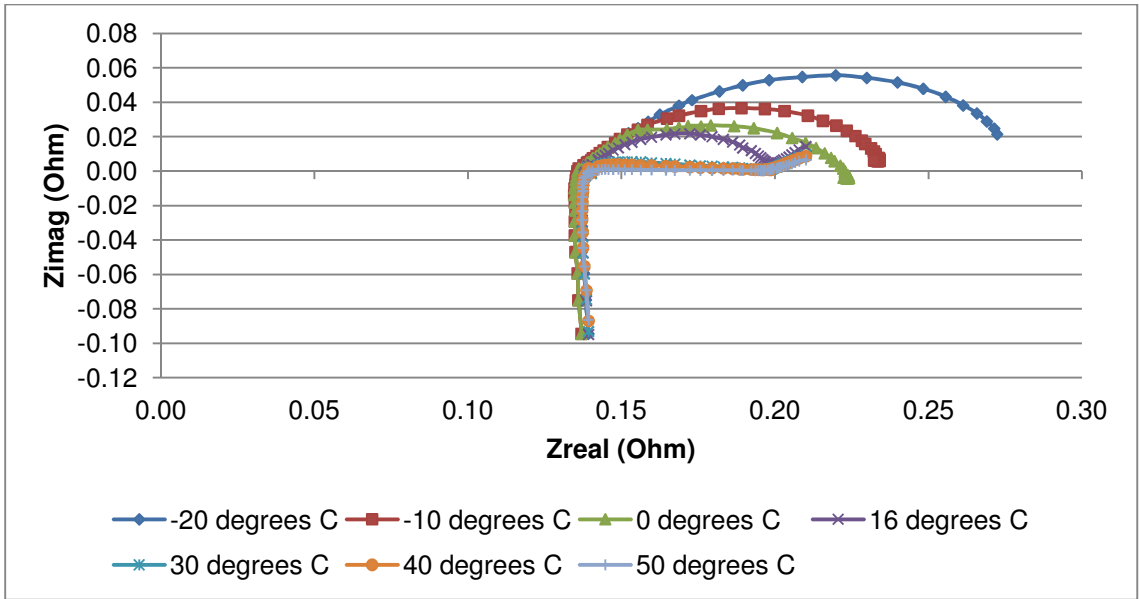


Figure 4.39. EIS spectra of a 1Ah pouch cell at different temperatures.

Very small changes along the Zreal axis were seen for the different temperatures of a fully charged cell. During the 1Ah pouch cell tests, the temperatures had a greater influence on the changes along the Zreal axis than the tests involving different temperatures. However significant changes within the semi-circles were seen. These changes were modelled using the EIS model previously discussed. Larger semi-circles were seen at -20°C, -10°C and 0°C.

The resistances for the different areas within the cell were plotted. Resistances due to current collectors, electrolyte resistance and electrode material resistance were modelled collectively under the circuit resistance parameter of the EIS model selected. The circuit resistance at different temperatures is shown in Fig 4.40.

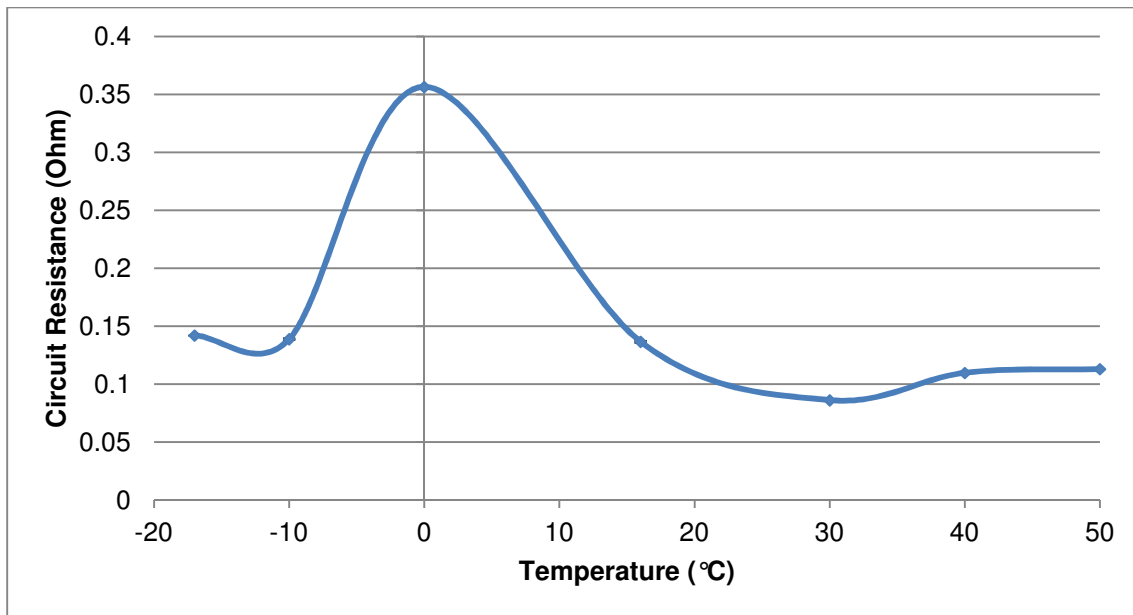


Figure 4.40. Circuit resistance at different temperature.

The highest resistance values were seen at 0°C. The circuit resistance increased from -20°C till 0°C, then decreased again till 30°C. The resistance then increased slightly till 50°C. However overall the resistance values were small.

The resistance associated with the SEI layer at the anode is shown in Fig 4.41.

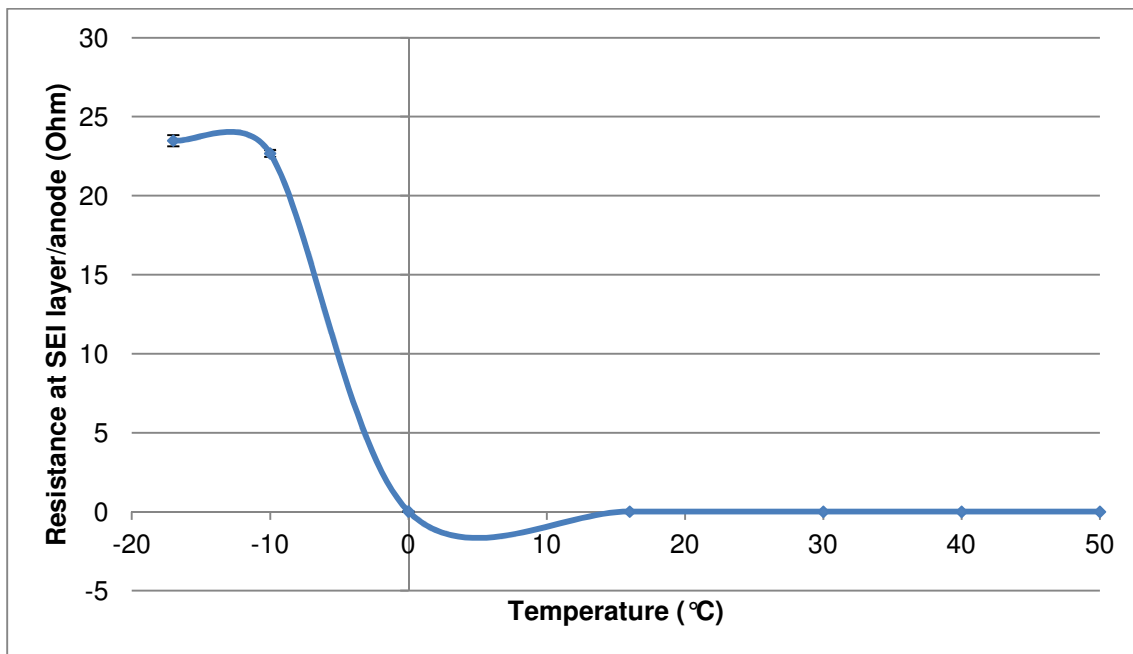


Figure 4.41. Resistance associated with the SEI layer at the anode at the different temperatures.

The resistance gradually decreased from -20°C to 50°C. This resistance was responsible for the increase in the first semi-circle seen for the all EIS spectra at the

different temperatures. A similar trend was seen during the 20Ah pouch cell testing at different temperatures. As the cell heated up, the Li-ions became more energized and were more freely available to move through the SEI layer.

The resistance associated with the double layer capacity and charge transfer resistance at the electrodes is shown in Fig 4.42.

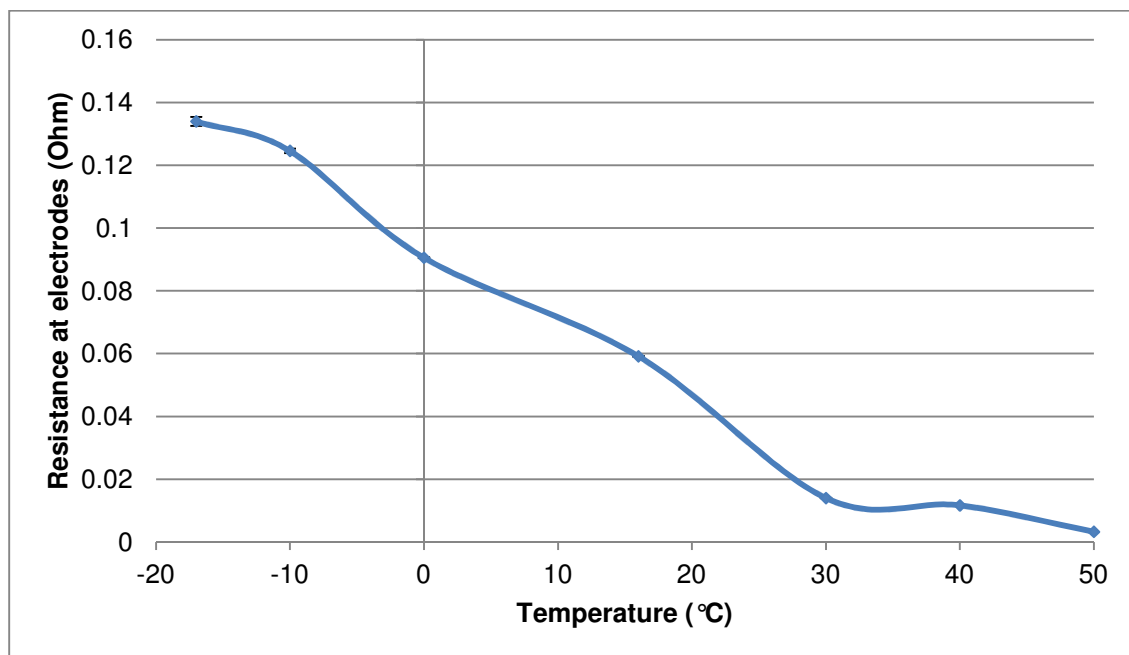


Figure 4.42. Resistance associated with the double layer capacity and charge transfer resistance at the electrode at the different temperatures.

The resistance gradually increased from -20°C to 50°C. Once again a similar trend was seen with the 20Ah pouch cell results.

The capacitance associated with the SEI layer at the anode and the capacitance associated with the double layer capacity and charge transfer resistance at the electrodes at different temperatures was measured and shown in figures 4.43 and 4.44 respectively.

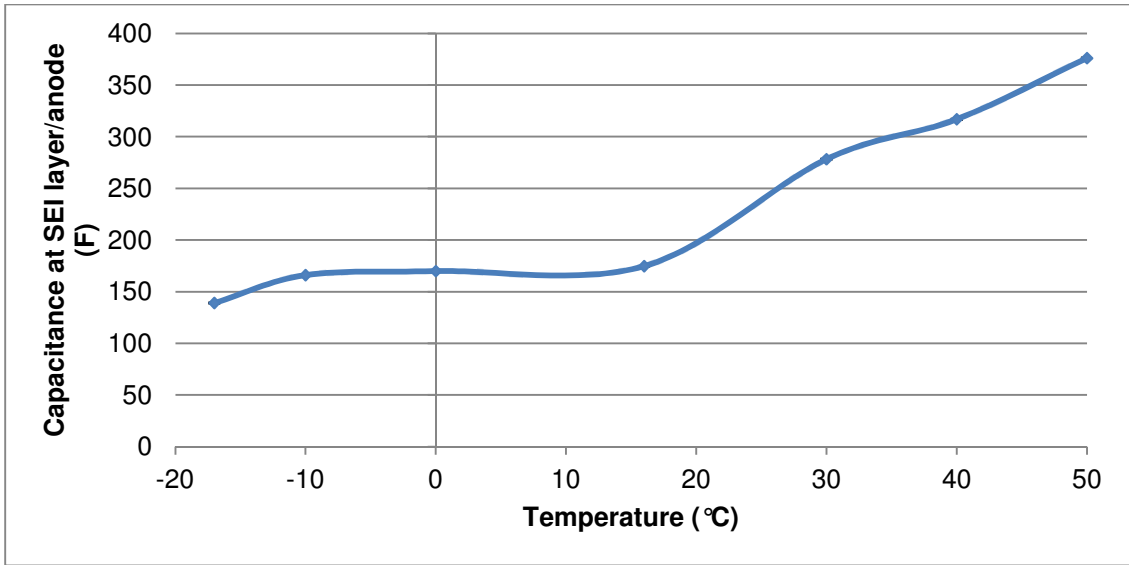


Figure 4.43. Capacitance associated with the SEI layer at the anode at different temperatures.

The capacitance steadily increased as the cell heated up. A sharper increase in capacitance was seen from 16°C till 50°C. This effect could be due to the increased energy within the cell and the ease of movement of the Li-ions through the SEI layer. Heating the cell beyond 40°C did not have the same effect as seen with the 20Ah pouch cell; this could be due to the different chemistry used within the cell.

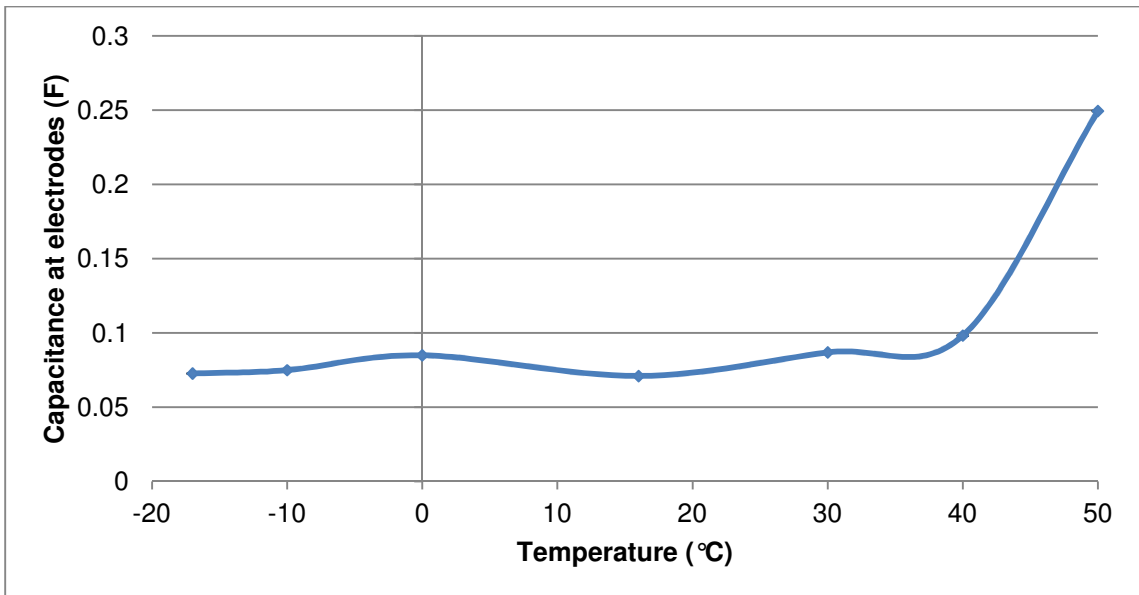


Figure 4.44. Capacitance associated with the double layer capacity and charge transfer resistance at both electrodes over the different temperatures.

The capacitance associated with the double layer capacity and charge transfer resistance at the both electrodes was relatively constant over the temperatures of

-20°C to 40°C. A sharper increase in capacitance was seen at 50°C. This effect could be due to the different chemistry used within the cell.

The time taken for the reactant to diffuse through the Nernst Diffusion layer and is shown in Fig 4.45.

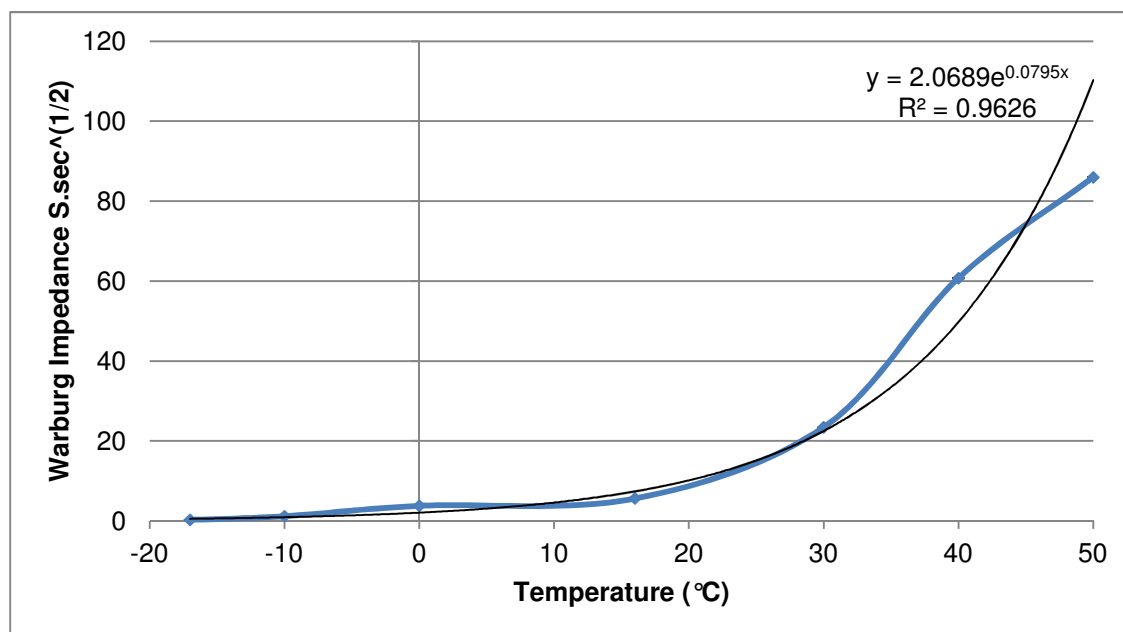


Figure 4.45. The Warburg Effect over the different temperatures.

Once again, the Warburg effect was seen to exponentially increase over the increase in temperature and the values are similar to the values seen in a paper by Jamie Gomez et al⁹⁰.

4.1.6. 2Ah cylindrical cell at different Temperatures

A fully charged cell was placed in a freezer at -20°C for 1hr to equilibrate. The EIS of the cell was measured inside the freezer ensuring that the power to the freezer was switched off. The lower temperature studies were repeated at temperatures of -10°C, 0°C, 7°C and 18°C respectively. The fully charged cells were placed in an oven at 30°C, 40°C and 50°C respectively. After allowing the cells to equilibrate after 1hr, the EIS analyses were done with the cell inside the oven. The power to the oven was switched off during the analysis procedure. All the tests were repeated in duplicate for statistical calculations.

The results of the EIS at the different temperatures are shown in Fig 4.46.

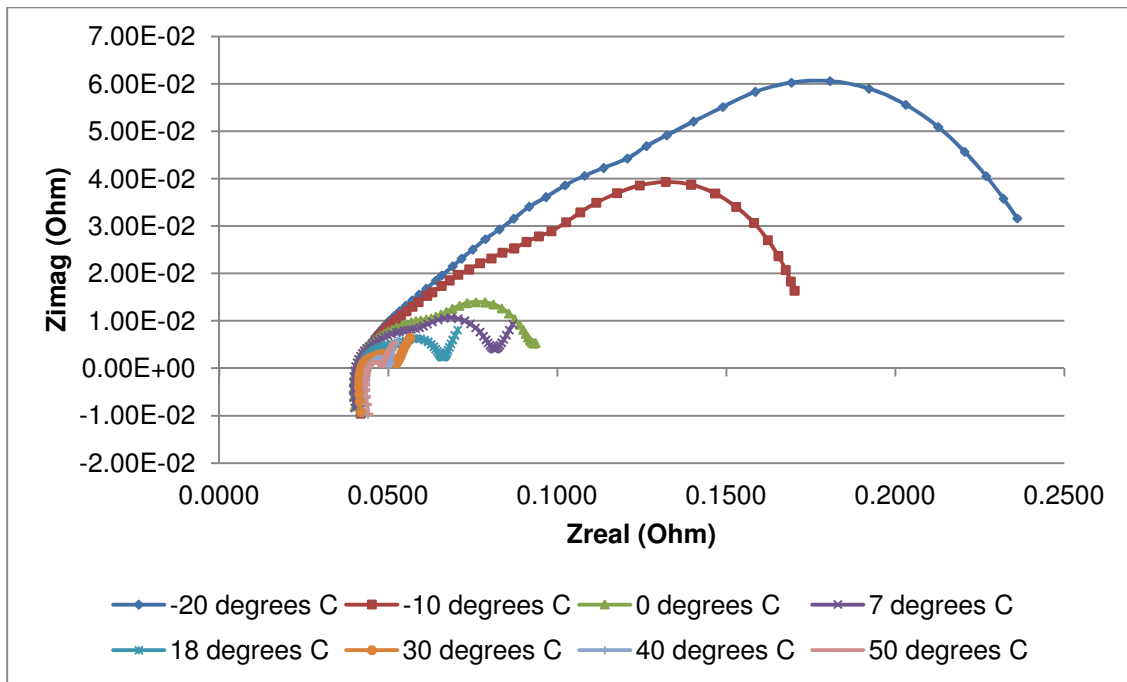


Figure 4.46. EIS spectra of a 2Ah cylindrical cell at different temperatures.

Very small changes along the Z_{real} axis were seen for the different temperatures. However significant changes within the semi-circles were seen. These changes were modelled using the EIS model previously discussed. Larger semi-circles were seen at -20°C, -10°C and 0°C.

The resistances for the different areas within the cell were plotted. Resistances due to current collectors, electrolyte resistance and electrode material resistance were modelled collectively under the circuit resistance parameter of the EIS model selected. The circuit resistance at different temperatures is shown in Fig 4.47.

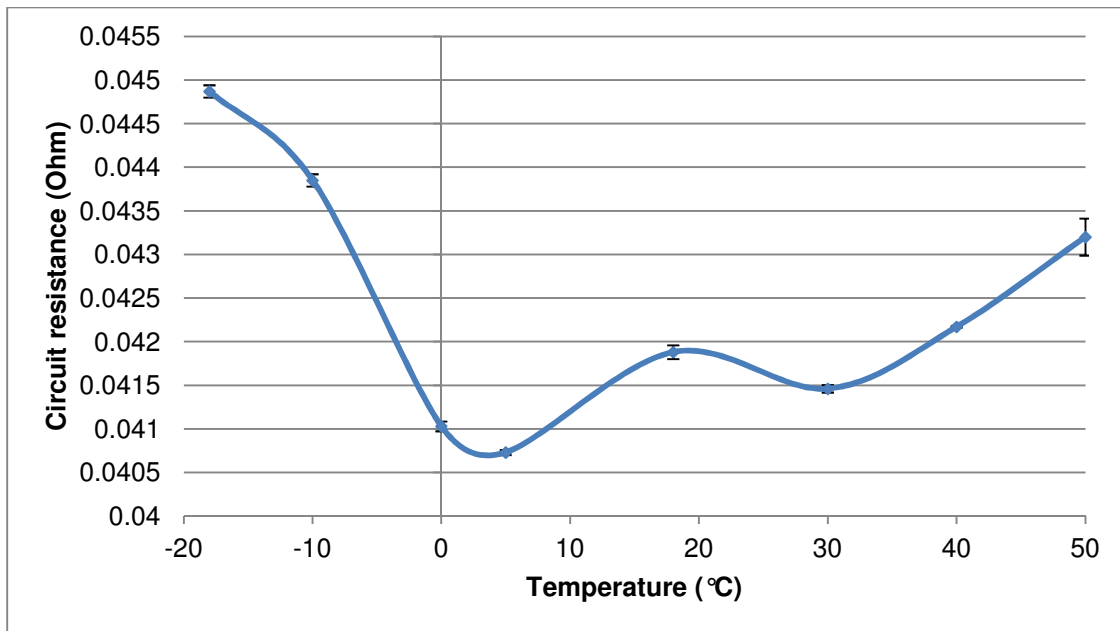


Figure 4.47. Circuit resistance at different temperatures.

The circuit resistance decreased as the cell heated up till 0°C, the resistance then increased till 20°C. The resistance value then decreased slightly to 30°C, followed by a slight increase in resistance at 40°C and 50°C. Overall the changes in resistances were very small. These peaks and valleys in resistance values could be due to the shape of the cell, and the ability of the Li-ions to move through the electrolyte and electrode materials.

The resistance associated with the SEI layer at the anode is shown in Fig 4.48.

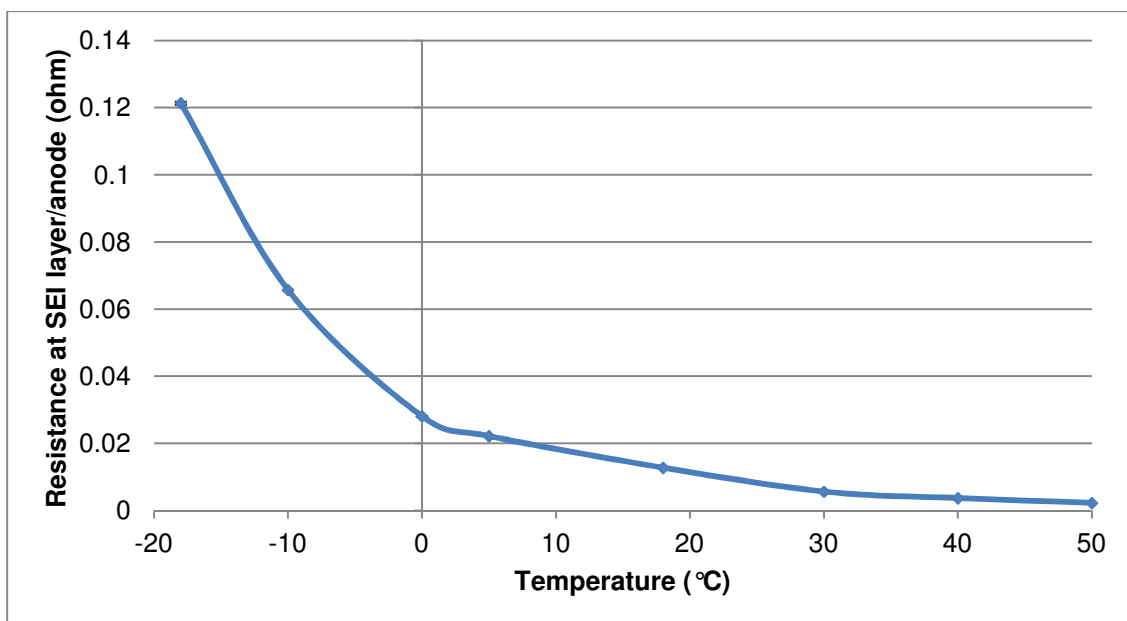


Figure 4.48. Resistance associated with the SEI layer at the anode at the different temperatures.

The resistance gradually decreased from -20 °C to 50 °C. This resistance was responsible for the increase in the first semi-circle seen for the all EIS spectra at the different temperatures. The same trends were seen for both pouch cells. As the cell heated up, the Li-ions were able to move through the SEI layer more freely. The resistance associated with the double layer capacity and charge transfer resistance at the electrodes is shown in Fig 4.49.

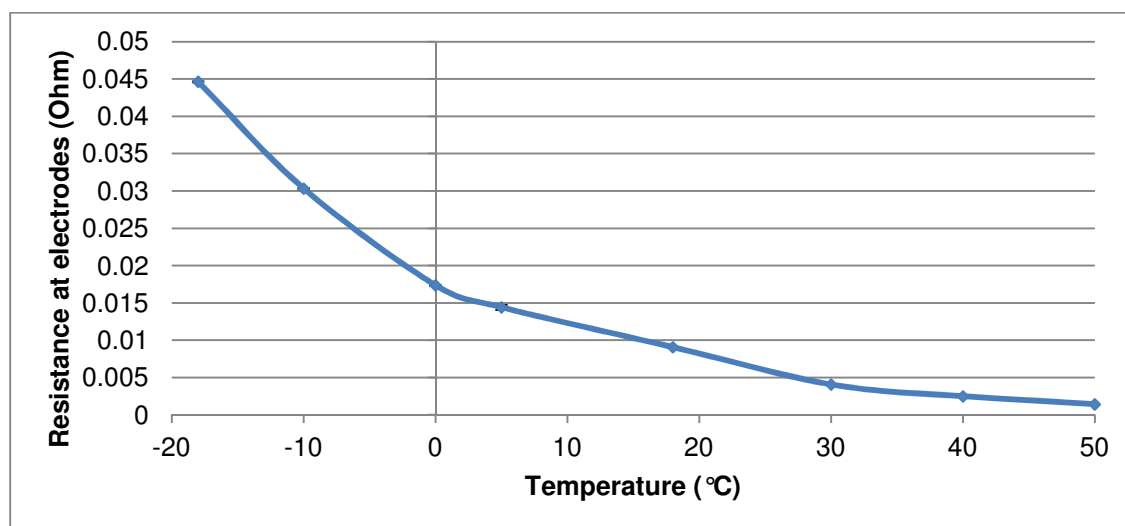


Figure 4.49. Resistance associated with the double layer capacity and charge transfer resistance at the electrode at the different temperatures.

The resistance gradually decreased from -20 °C to 50 °C. This resistance was responsible for the second semi-circle of the EIS spectra.

The capacitance associated with the SEI layer at the anode and the capacitance associated with the double layer capacity and charge transfer resistance at both the electrodes was measured and are shown in figures 4.50 and 4.51 respectively.

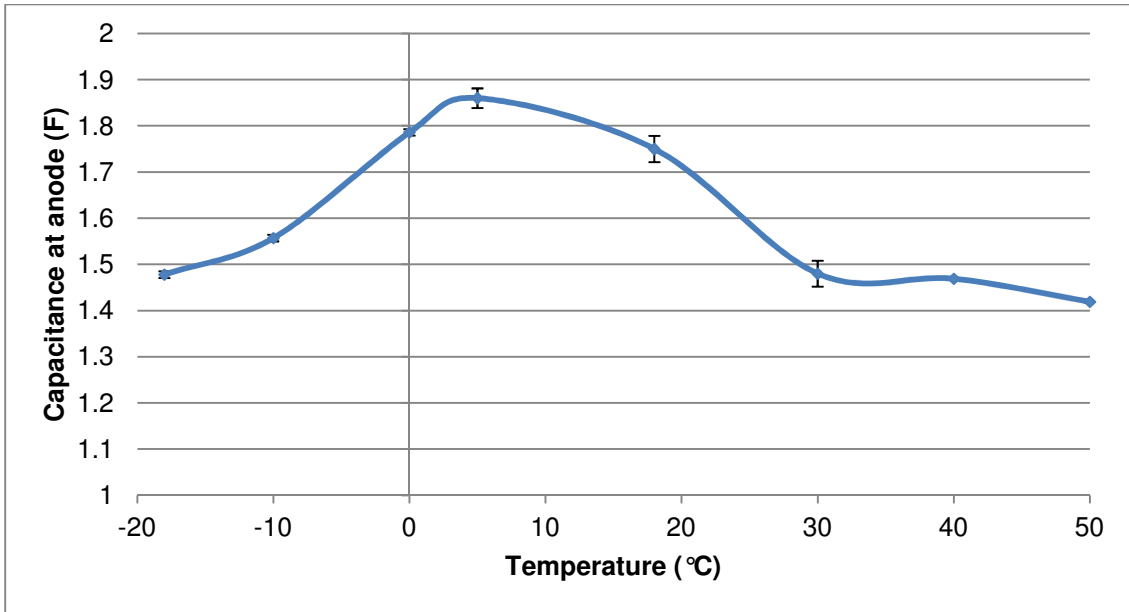


Figure 4.50. Capacitance associated with the SEI layer at the anode over the different temperatures.

This capacitance showed an inverse trend when compared to the trend seen during the circuit resistance. It seems that the circuit resistance had an effect on the capacitance associated with the SEI layer at the anode.

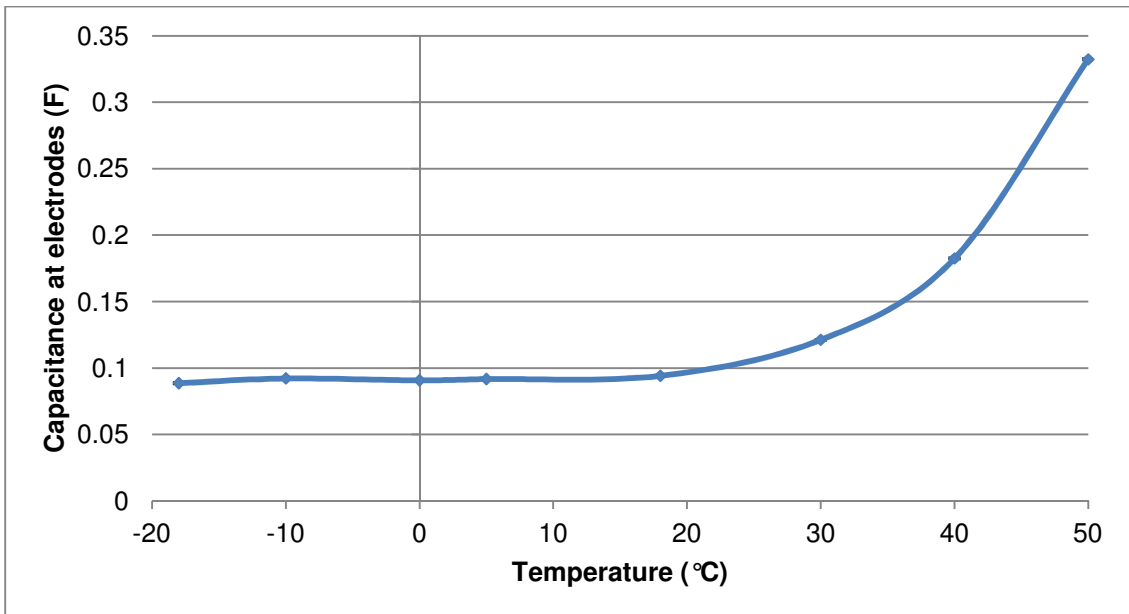


Figure 4.51. Capacitance associated with the double layer capacity and charge transfer resistance over the different temperatures.

The capacitance steadily increased as the cell heated up. A more significant increase in capacitance was seen once the cell was heated higher than 20°C.

The time taken for the reactant to diffuse through the Nernst Diffusion layer is shown in Fig 4.52.

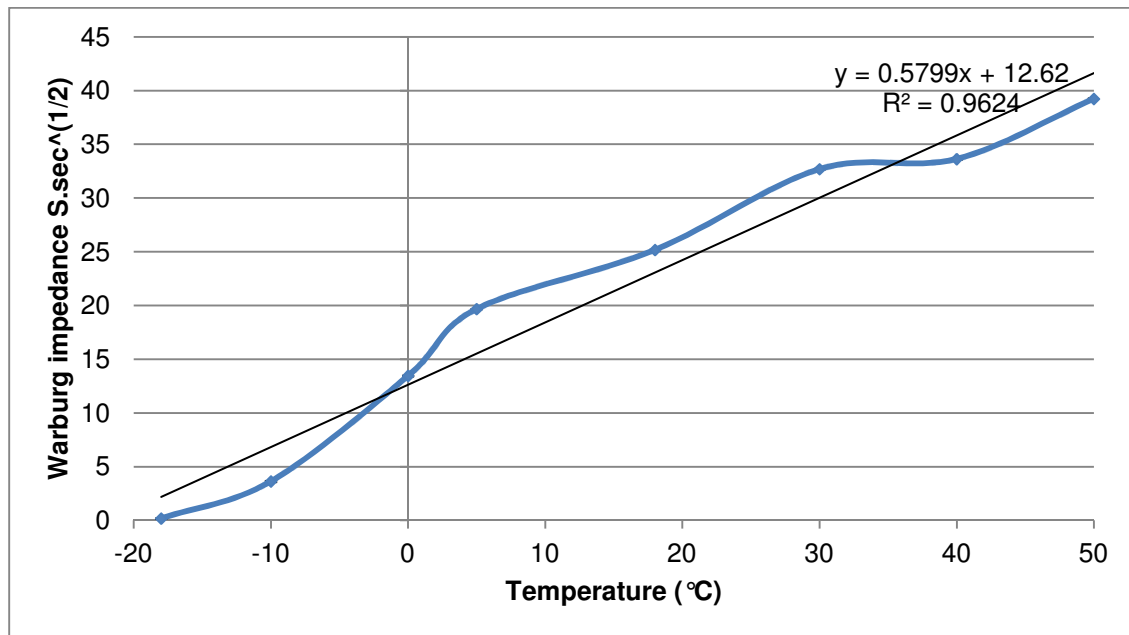


Figure 4.52. The Warburg Effect over the different temperatures.

Once again the Warburg effect increased as the temperature increased, similar to the trend seen in the results of the 20Ah pouch cell.

Summary of Observations made during the EIS testing at different temperatures:

The inductance values for the three different cells are shown in Fig 4.53. Very small values were seen for all three cells which indicated small inductance due to the connectors used, cables and instrumental changes.

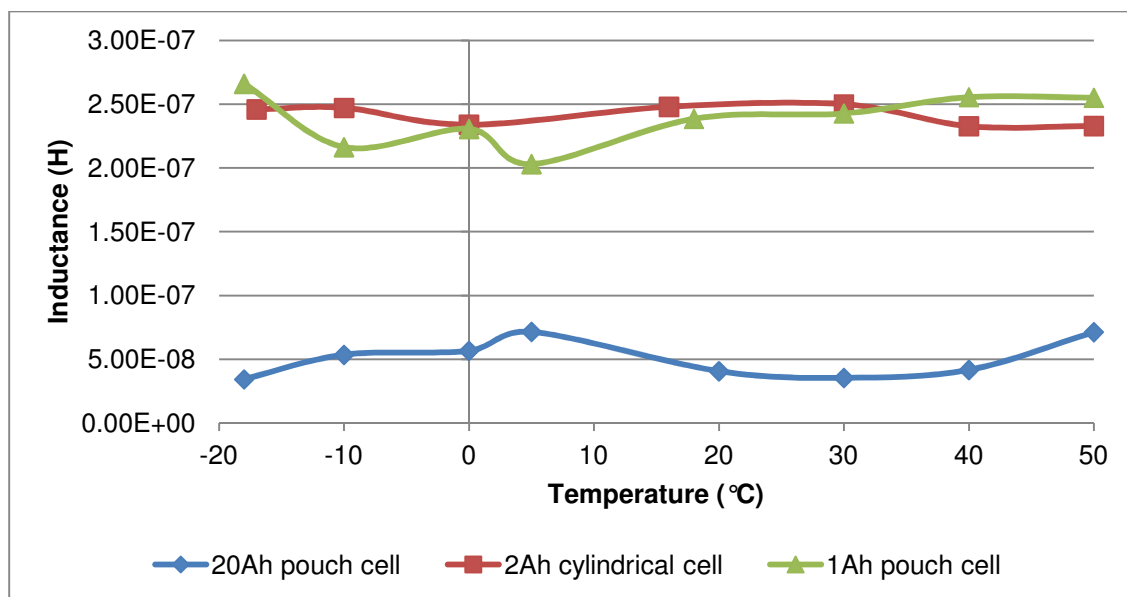


Figure 4.53. Inductance of three different cells at different temperatures.

The circuit resistance for the pouch cells showed higher values at low temperatures with the cylindrical cell showing peak resistances at the lower and higher temperatures. All the cells showed a decrease in resistance associated with the SEI layer at the anode as the cell temperatures increased. All cells showed a decrease in resistance associated with the double layer capacity and charge transfer resistance as the cell temperature increased. Both these decreases in resistance indicate that as the cell heated up, the Li-ions were energized and could move through the layer and to the electrodes easier. In general an increase in capacitance was seen as the temperature of the cell increased. This would also indicate that the Li-ions were more energized as the cell heated. However it was seen that the capacitance dropped at 50 °C for the 20Ah pouch cell, this could be due to the shape and chemistry of the cell. The capacitance associated with the SEI layer at the anode for 2Ah cylindrical cell seemed to have been influenced by the circuit resistance. The reason being that as the circuit resistance decreased at 0 °C and then increased again, an increase in capacitance was seen at 0 °C with a decrease in capacitance at lower and higher temperatures. All the cells showed an increase in the Warburg effect as the cell temperature increased. This observation matched a paper by Jamie Gomez et al⁹⁰. Linear relationships were observed for both the 2Ah cylindrical cell and 20Ah pouch cell. An exponential graph was seen for the 1Ah pouch cell. The linear relationship showed that as the cell heated, the time taken to diffuse through the Nernst Diffusion layer increased. An exponential relationship was seen during the testing of the 1Ah

pouch cell where the Warburg effect increased 2x the increase in temperature. This exponential relationship could be due to the different chemistry within this 1Ah pouch cell and that this cell had been manufactured with thicker electrodes⁸².

In this study, it was seen that both SoC and temperature play a role in the impedance of a cell. The different cells showed different trends due to the different capacity values of the cell.

4.2. Capacity Ageing tests together with EIS:

Capacity ageing tests can be used to determine how long a cell will endure under certain simulated application conditions. Six Li-ion cells were tested, three 20Ah Li-ion pouch cells and three 2Ah Li-ion cylindrical cells. Three different stress regions were determined and were indicated as high, medium and low stress. Different voltage ranges were determined from a typical LiCoO₂ discharge voltage curve⁹¹. The high stress region corresponded to the cycling between 3.0V and 3.58V (high DoD), the low stress corresponded to cycling between 3.58V and 3.94V (middle DoD) and the medium stress corresponded to cycling between 3.94V and 4.2V (low DoD). Electrochemical Impedance Spectroscopy (EIS) was used at various capacity cycling stages during the ageing tests. This was done in order to determine if there were notable changes in the EIS parameters within the cell as it aged due to capacity cycling.

According to the USABC test procedures for EV, a battery that had reached 80% of its original capacity was said to be at its end-of-life and should be replaced³⁴.

4.2.1. 20Ah Li-ion pouch cell capacity ageing results:

The 20Ah pouch cells were capacity cycled at the various DoD regions. After every 50 cycles, the cells would be fully charged and subjected to the C/1 capacity test. The change in the C/1 capacity is shown in fig 4.54.

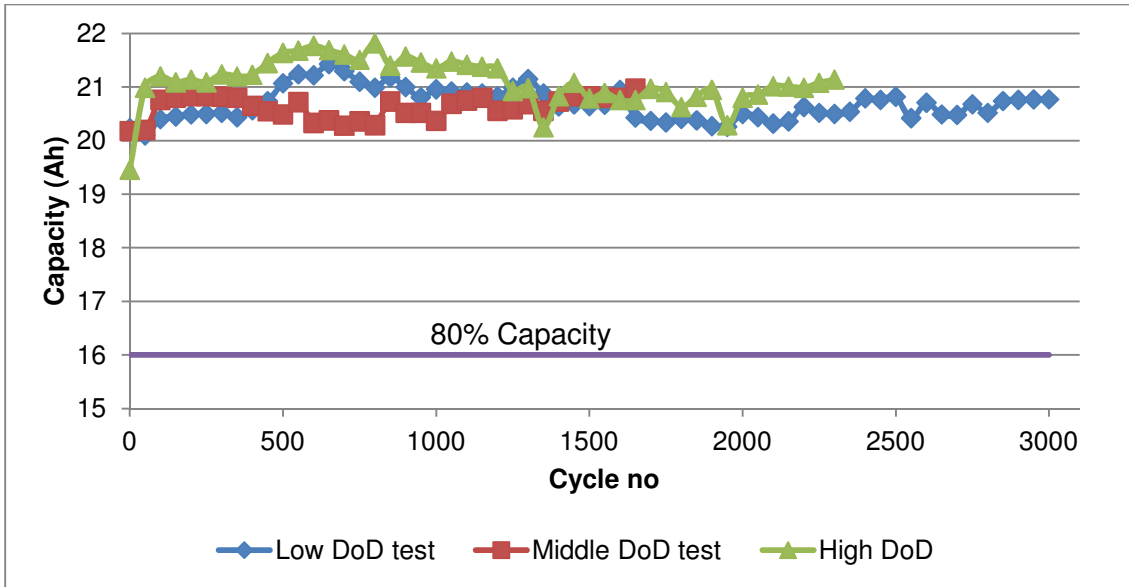


Figure 4.54. Change in capacity over the number of cycles for the different DoD.

The results showed that the cells maintained their capacity for the duration of the capacity cycling test. The proposed test procedure did not accelerate the degradation of the cell even for the region that could be considered to be a high stress region. The tests were conducted for 13 months. The results also showed that based on the true capacity of the cell, the cells capacity actually improved slightly during the initial stages of the capacity cycling test. The initial true capacities of the cells used are shown in Table 4.2.

Cell description	True capacity
Cell 1 – Low DoD	20.23 Ah
Cell 2 – Middle DoD	20.18 Ah
Cell 3 – High DoD	19.46 Ah

Table 4.2. True capacity of each cell.

Within the first 150 cycles the cell capacity increased slightly for each cell and is shown in Figure 4.55.

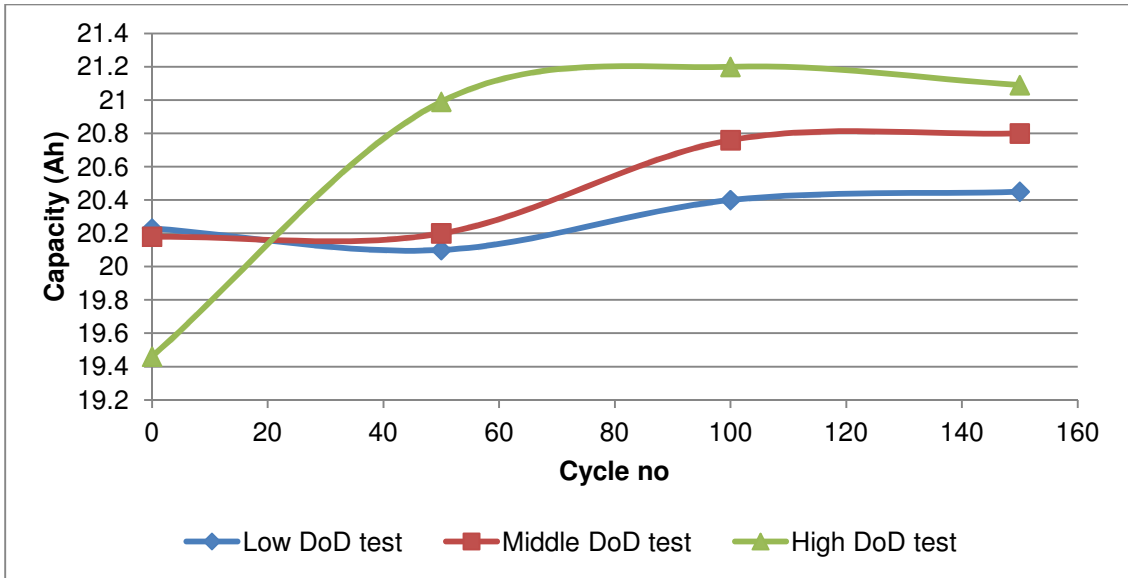


Figure 4.55. Increase in capacity over the initial 150 cycles.

The results showed that an increase in the C/1 rate of the cell was observed within the first 150 cycles, after which the discharge capacity remained relatively constant. By observing the changes in the EIS spectra over the 150 cycles, a similar trend can be seen in that the real impedance decreased initially and then remained relatively constant for the duration of the study (Fig 4.56).

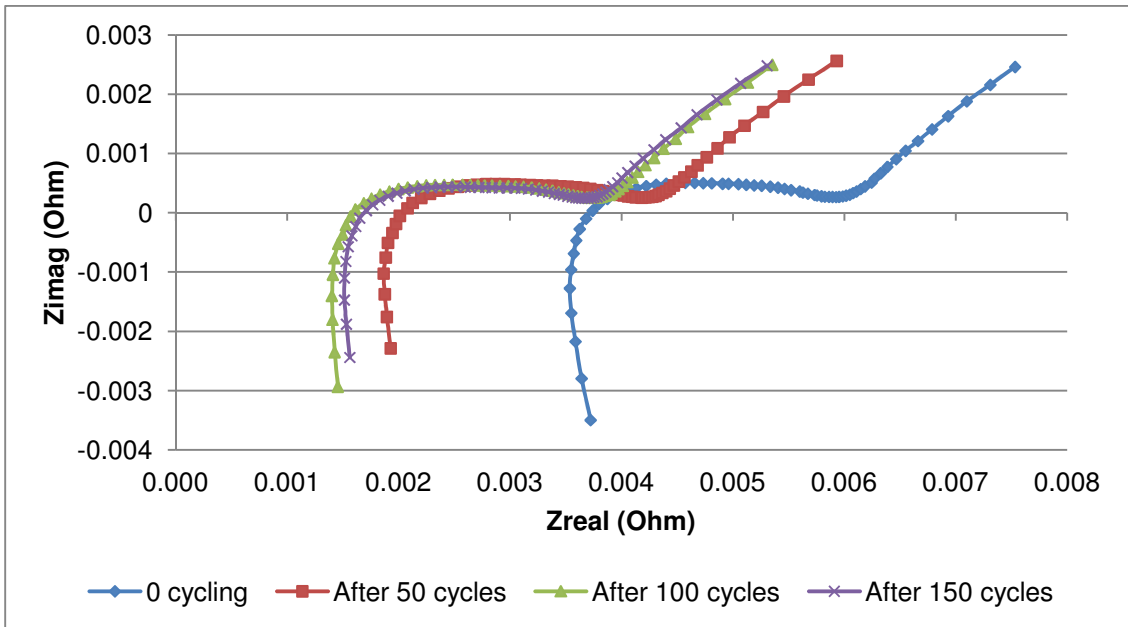


Figure 4.56. First 150 cycle Spectra for the cell at the low DoD window cycling.

The changes within the EIS spectra seen in Fig 4.56 were plotted using the different parameters of the EIS model. Changes in circuit resistance and capacitance were observed in figures 4.57 and 4.58 respectively.

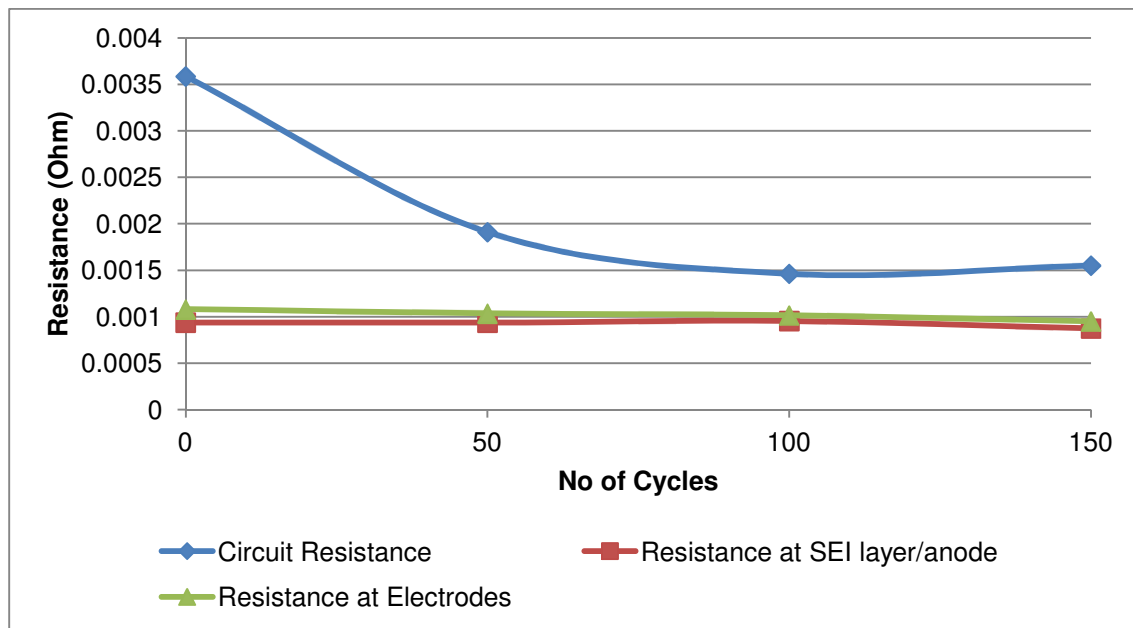


Figure 4.57. Changes in resistances over the initial 150 cycles for the low DoD window.

More significant changes were seen in the circuit resistance, with the resistance decreasing after commencing with the cycling. These results were in agreement with the changes seen in the full EIS spectra (Fig 4.56) where the spectra moved along the x-axis.

There was an increase in capacitance associated with the SEI layer at the anode and the capacitance associated with the double layer capacity and charge transfer resistance at both electrodes and is shown in Fig 4.58.

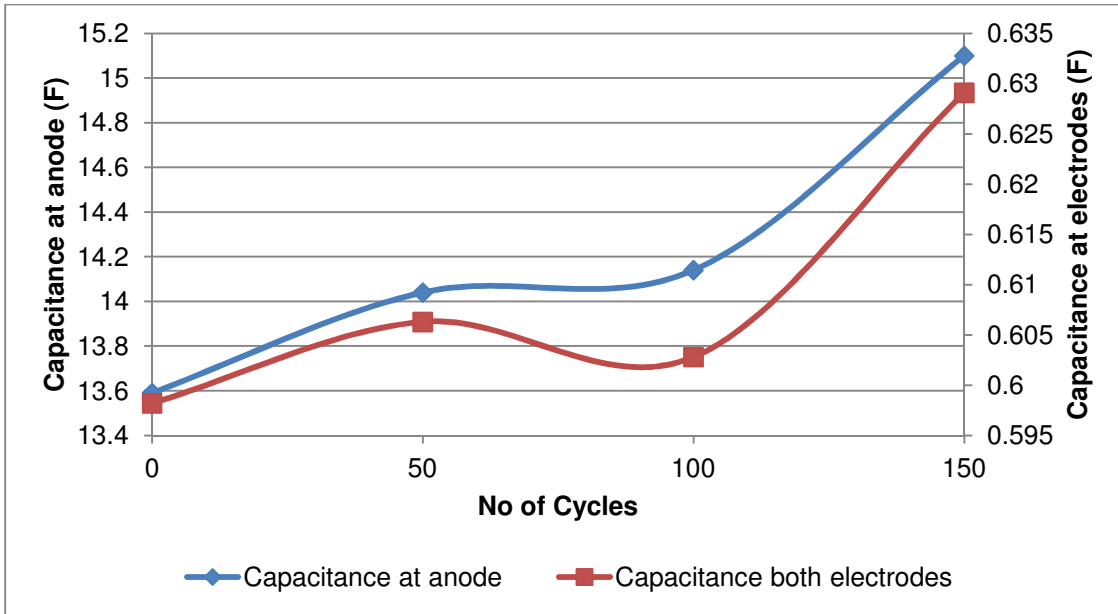


Figure 4.58. Change in capacitance over the initial 150 cycles for middle DoD window.

The EIS spectra for the first 150 cycles for the middle DoD window are shown in Fig 4.59.

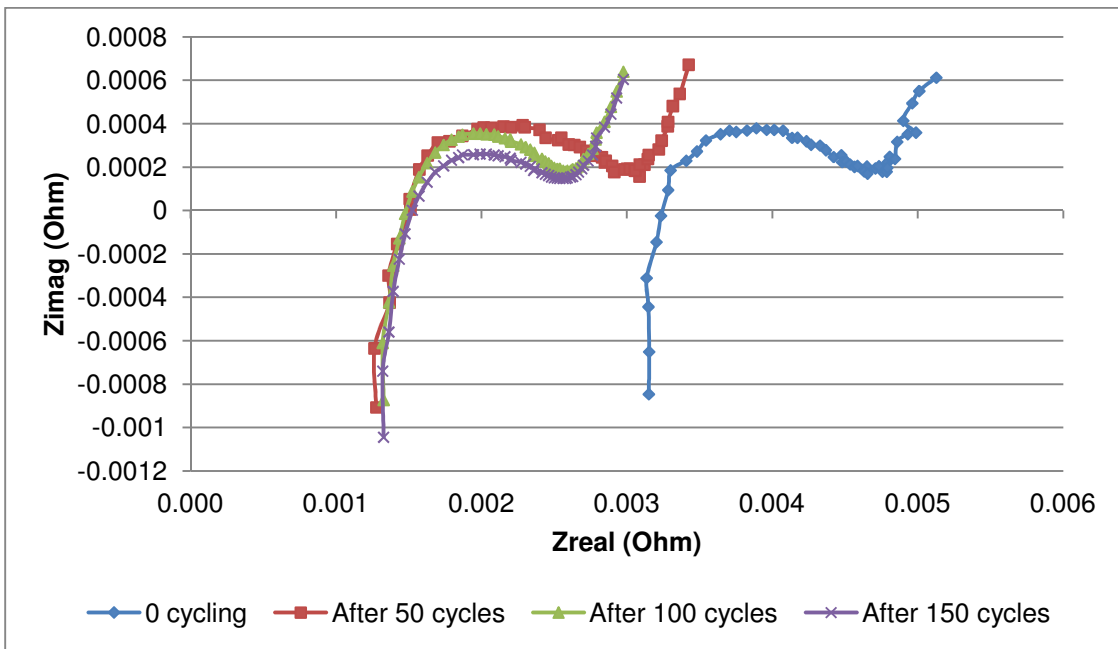


Figure 4.59. First 150 cycle Spectra for the cell at the middle DoD window cycling.

The changes within the EIS spectra seen in Fig 4.59 were plotted using the different parameters of the EIS model. Changes in circuit resistance and capacitance were observed and are shown in figures 4.60 and 4.61 respectively.

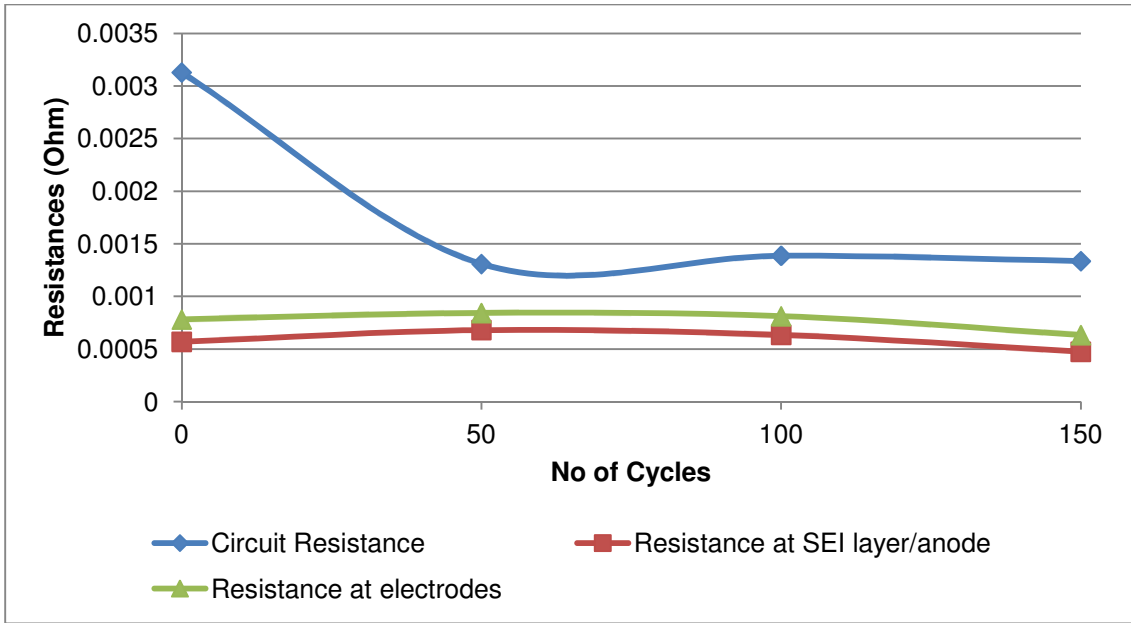


Figure 4.60. Changes in resistances over the initial 150 cycles for the middle DoD window.

There was a decrease in circuit resistance after the commencement of cycling. This decreased in circuit resistance was also seen on the EIS spectra (Fig 4.59) where the spectra shifted along the x-axis.

There was an increase in capacitance associated with the SEI layer at the anode and the capacitance associated with the double layer capacity and charge transfer resistance at both electrodes and is shown in Fig 4.61.

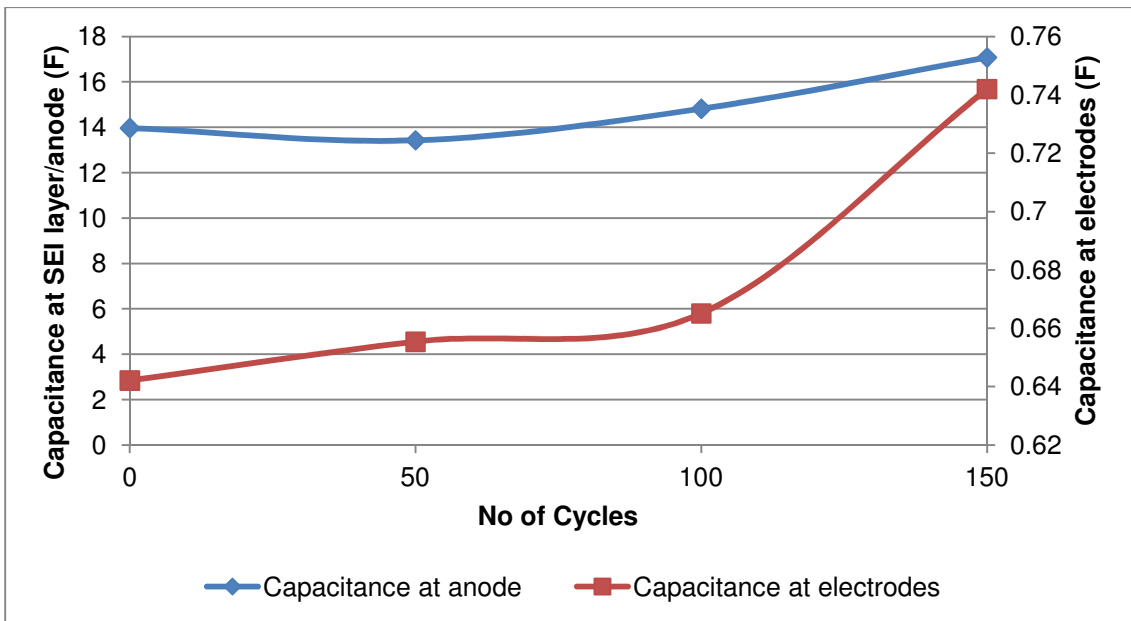


Figure 4.61. Change in capacitance over the initial 150 cycles for the middle DoD window.

The EIS spectra for the first 150 cycles for the high DoD window are shown in Fig 4.62.

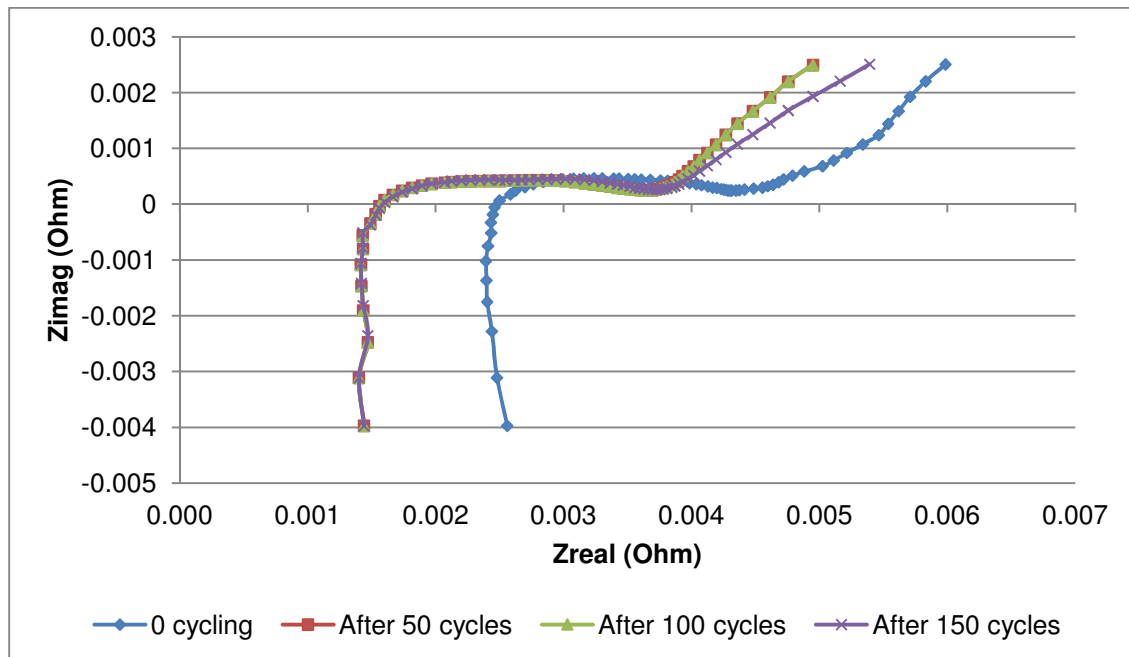


Figure 4.62. First 150 cycle Spectra for the cell at the high DoD window cycling.

The changes within the EIS spectra seen in Fig 4.62 were plotted using the different parameters of the EIS model and the changes in circuit resistance and capacitance were shown in Fig 4.63 and 4.64 respectively.

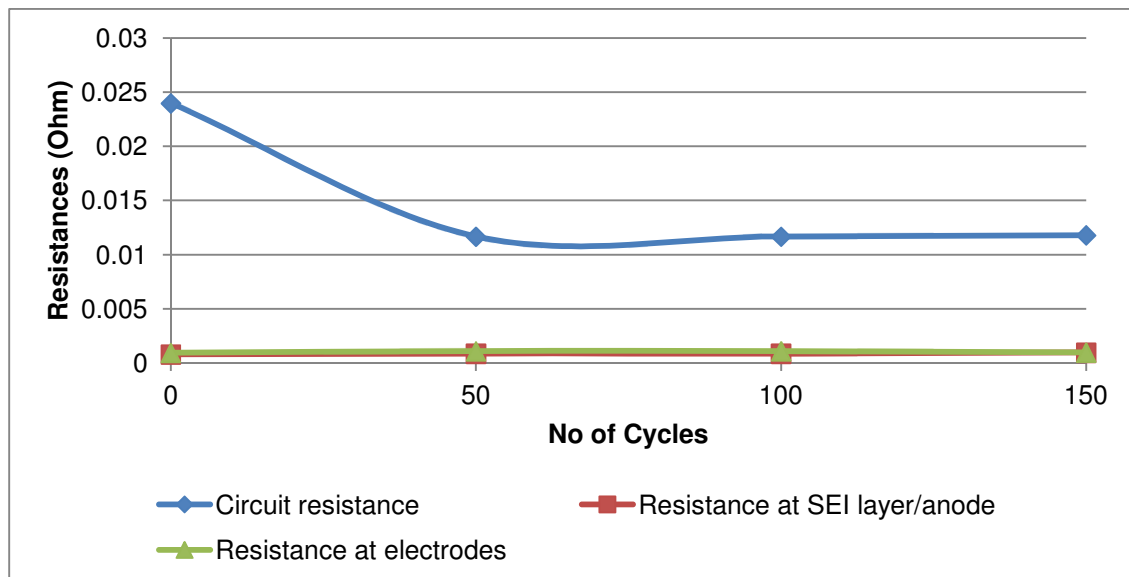


Figure 4.63. Changes in resistances over the initial 150 cycles for high DoD window.

There was a decrease in circuit resistance after the commencement of cycling. This decrease in circuit resistance was also seen on the EIS spectra (Fig 4.62) where the spectra shifted along the x-axis.

There was an increase in capacitance associated with the SEI layer at the anode and the capacitance associated with the double layer capacity and charge transfer resistance at both electrodes and is shown in Fig 4.64.

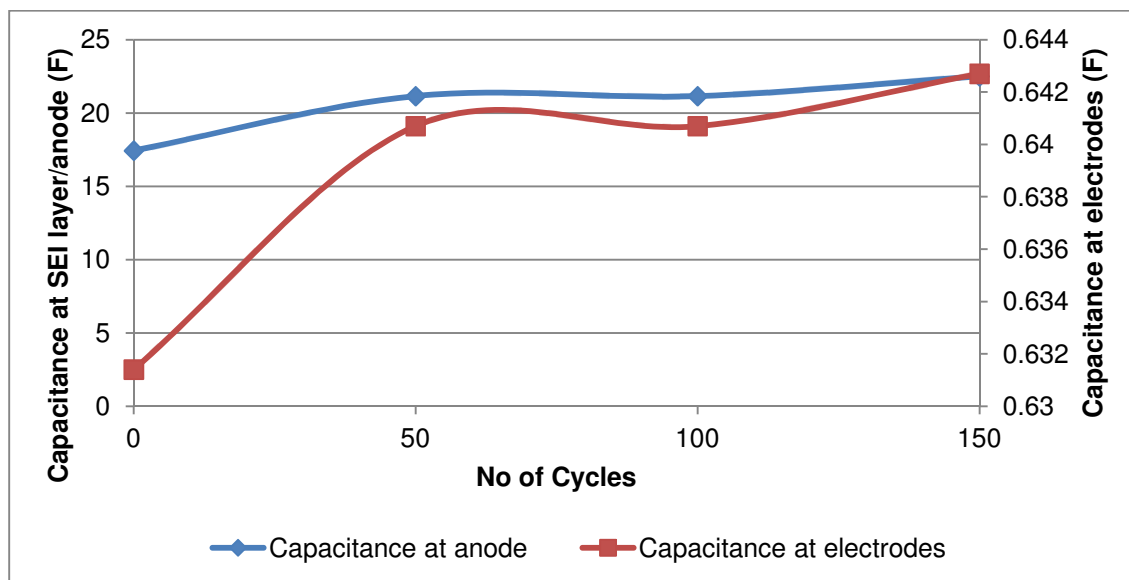


Figure 4.64. Change in capacitance over the initial 150 cycles for high DoD window.

20Ah Li-ion pouch cell capacity ageing results – low, middle and high DoD windows:

The EIS for the 20Ah pouch cell that was cycled in the low DoD window region was cycled for 3000 cycles. The EIS spectra for these 3000 cycles are shown in Fig 4.65 in 500 cycle intervals:

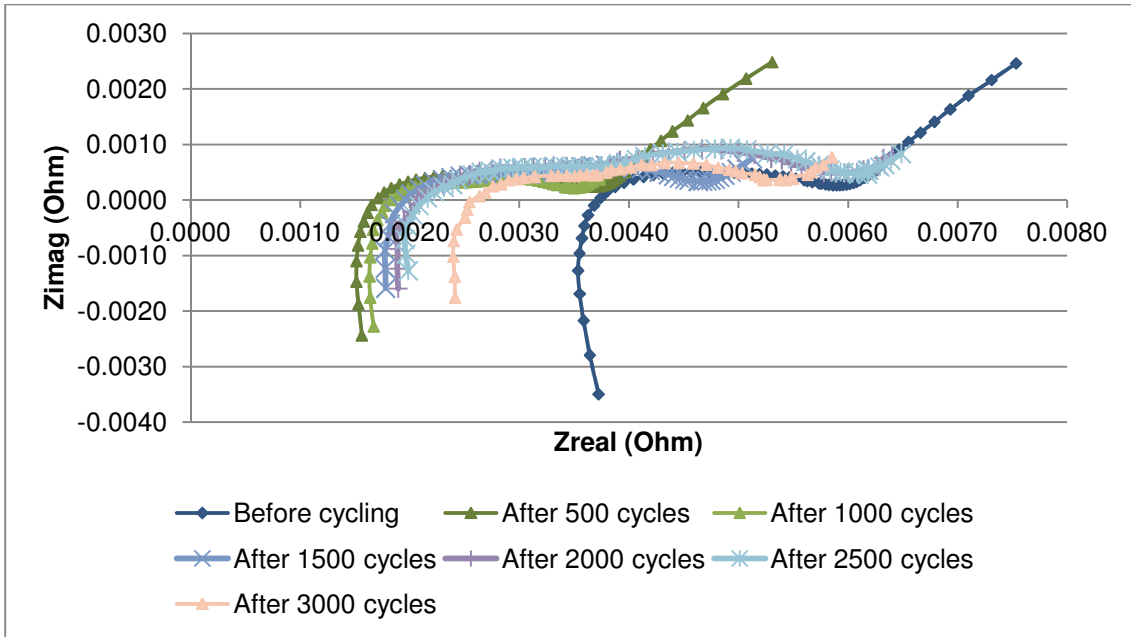


Figure 4.65. EIS for 500 cycle intervals representing the 3000 cycles carried out on a 20Ah pouch cell in the low DoD window region.

The EIS for the 20Ah pouch cell that was cycled in the middle DoD window region was cycled for 1650 cycles. The EIS spectra for these 1650 cycles are shown in Fig 4.66 in 300 cycle intervals:

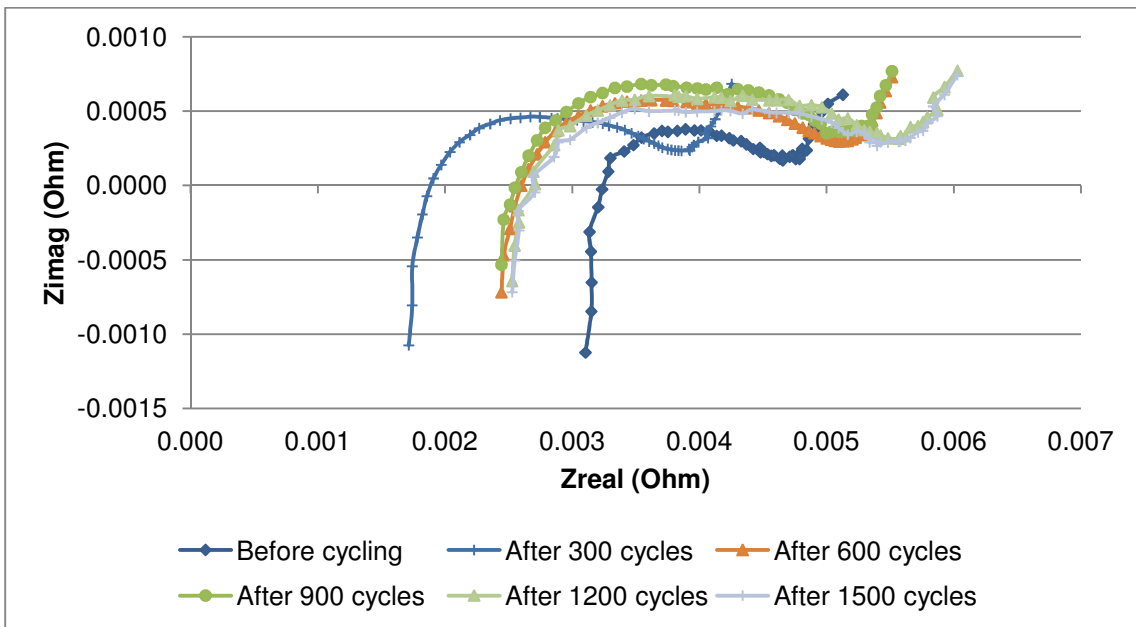


Figure 4.66. EIS for 300 cycle intervals representing the 1650 cycles carried out on a 20Ah pouch cell in the middle DoD window region.

The EIS for the 20Ah pouch cell that was cycled in the high DoD window region was cycled for 2300 cycles. The EIS spectra for these 2300 cycles are shown in Fig 4.67 in 500 cycle intervals:

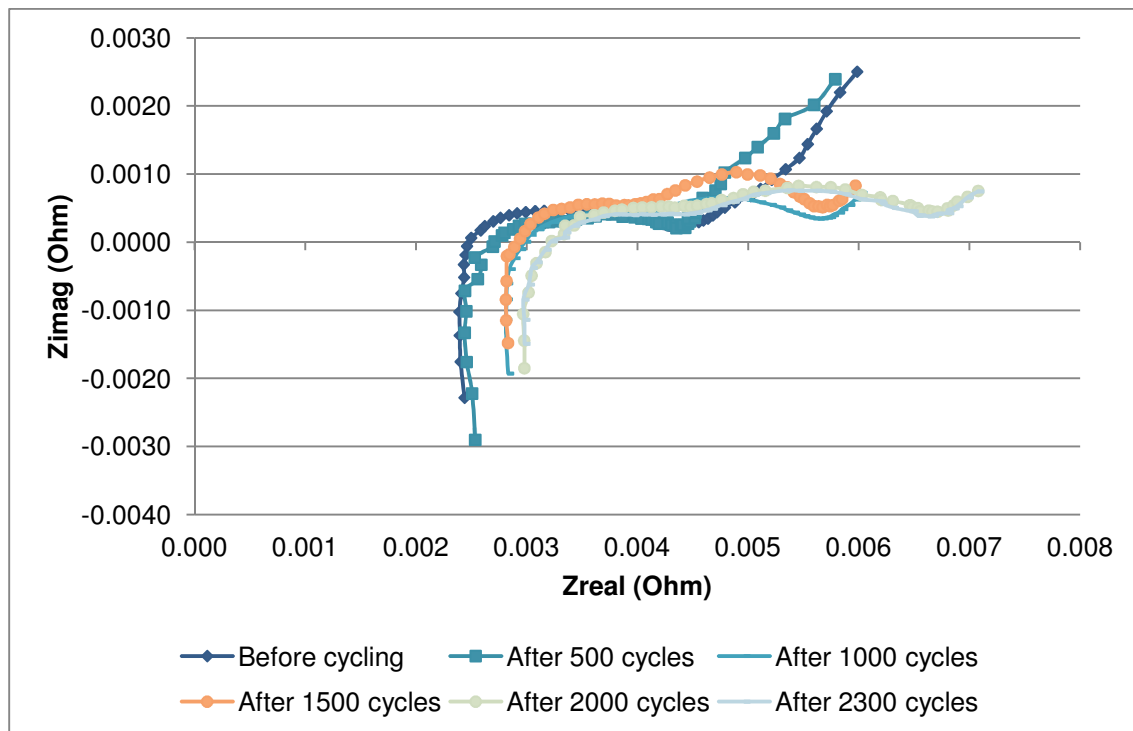


Figure 4.67. EIS for 500 cycle intervals representing the 2300 cycles carried out on a 20Ah pouch cell in the high DoD window region.

The various changes within the cell were modelled according to the EIS model discussed above.

The inductance of all the EIS spectra changed very little between the spectra, which indicated that the inductive reactants of the metallic elements in the cell and wires were low and relatively unchanged over the study.

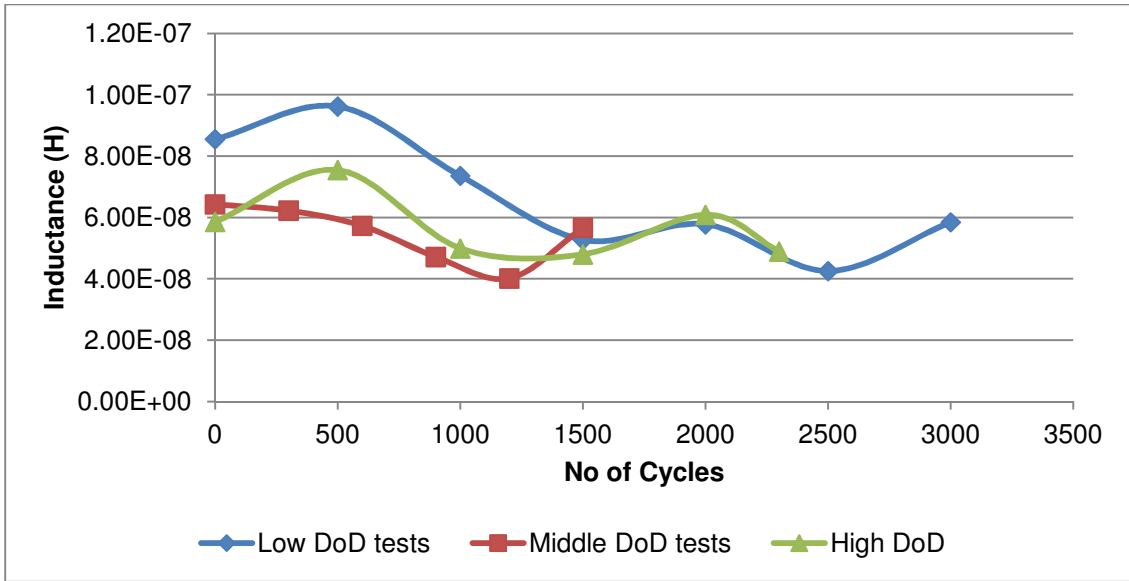


Figure 4.68. Inductance changes during cycling in the three DoD window regions.

Initially the EIS spectrum before commencement of cycling showed the highest Zreal values. As the cycling started, the EIS spectrum was seen to shift towards a smaller Zreal value. As the cycling continued the EIS spectrum shifted along the Zreal axis, which indicated ageing within the cell. These changes along the real impedance axis at zero imaginary impedance were due to the circuit resistance changes and are shown in Fig 4.69. The circuit resistance involved resistances due to the sum of the resistances of the current collectors, the active material, electrolyte and the separator. As a cell ages these materials will change and this is indicated by the small gradual increase in overall resistance shown in the EIS spectra.

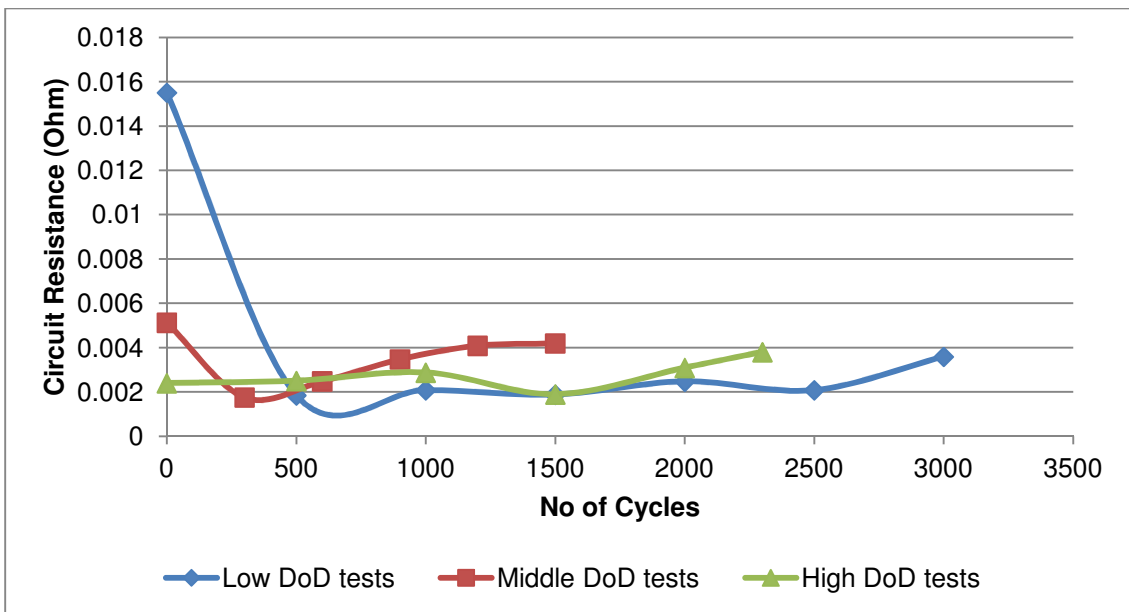


Figure 4.69. Circuit resistance changes during cycling in the three DoD windows.

The resistance value of the circuit initially dropped from the initial EIS spectrum taken before commencement of cycling to the spectrum taken after 50 cycles. From there the circuit resistance gradually increased until the final cycles. This was true for the cycling in the low and middle DoD window regions, however for the high DoD window region, the circuit resistances showed a more gradual increase from before the cycling commenced till the final cycles. In Figure 4.63, there was a decrease in circuit resistance from 0 cycling to 50 cycles. From there the circuit resistance gradually increased. At 500 cycles, the circuit resistance had built up again and was similar to the circuit resistance seen at 0 cycles. During the low and middle DoD window regions the cell required more cycling before the circuit resistance increased to be similar or higher than the initial circuit resistance seen before cycling commenced.

As the cycles continued, small changes were seen in the first semi-circle of the EIS spectra. This first semi-circle is due to changes in resistances associated with the SEI layer at the anode. These results are shown in Fig 4.70.

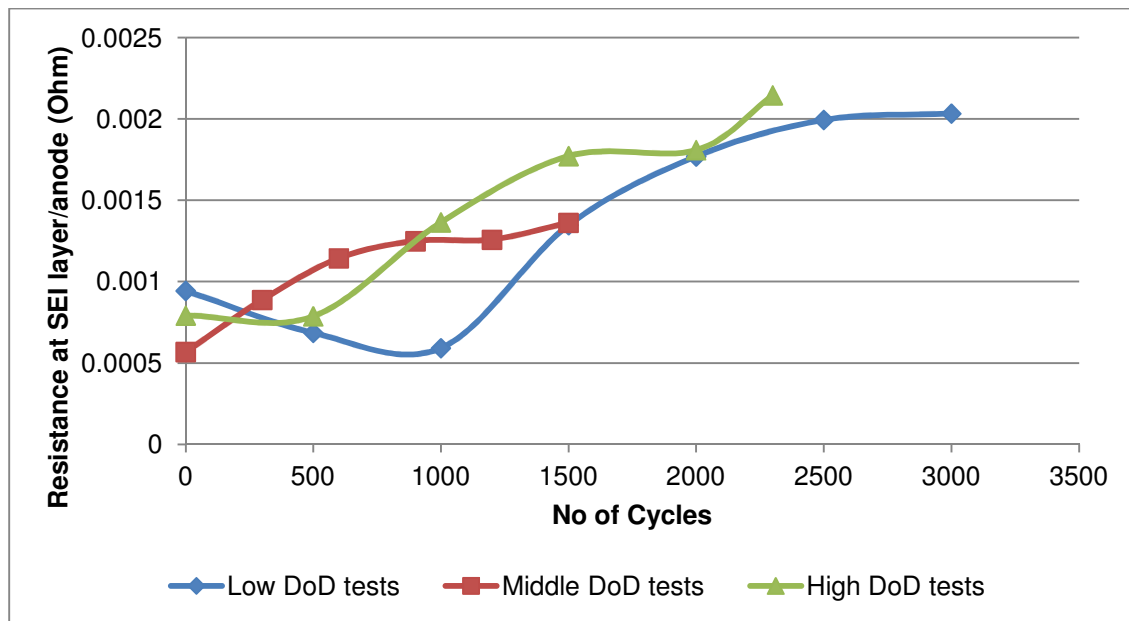


Figure 4.70. Changes in resistance associated with the SEI layer at the anode during cycling in the three DoD window regions.

Resistances associated with double layer capacity and charge transfer resistance at the electrodes are shown for the three DoD window regions (Fig 4.71).

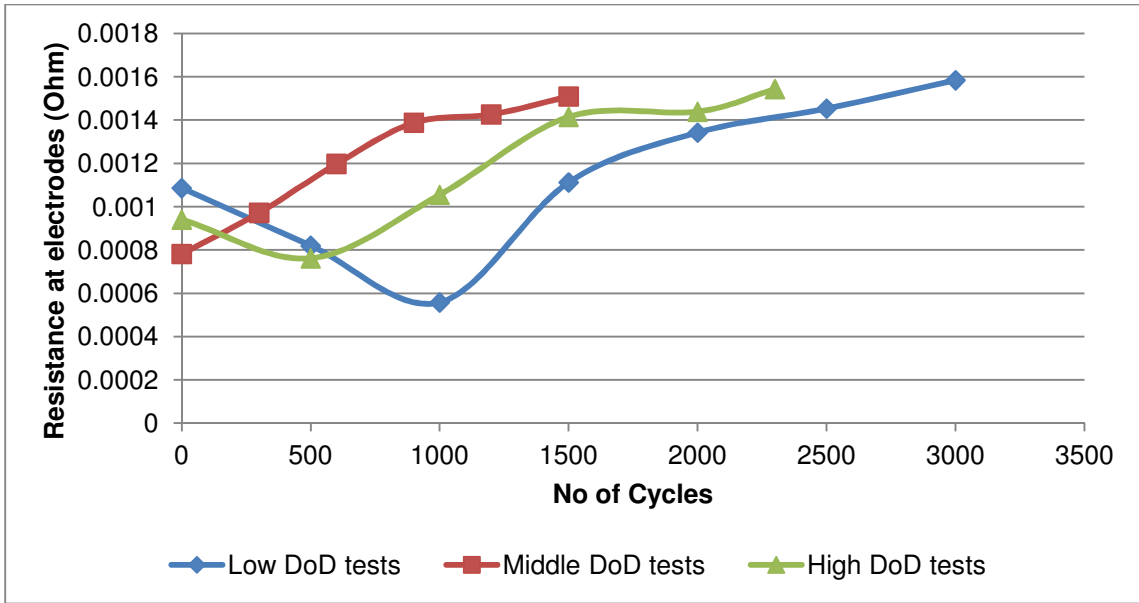


Figure 4.71. Resistance associated with the double layer capacity and charge transfer resistance at the electrodes during cycling in the three DoD window regions.

Similar trends were seen for the resistance associated with the double layer capacity and charge transfer resistance in comparison to the resistance associated with the SEI layer at the anode. Both the low and high DoD window regions saw a drop in resistance, followed by an increase in resistance after 1000 and 500 cycles respectively. During the middle DoD window region cycling, a gradual increase in resistance was seen from the start of cycling.

During cycling, there were a few changes seen in the EIS spectra for the low and high DoD window regions. These changes were then more closely investigated. There was a more significant increase in the first and second semi-circles of the low DoD window region between the cycle numbers 1000 and 1500 cycles. This can be shown in the spectra taken between these points and are illustrated in Fig 4.72.

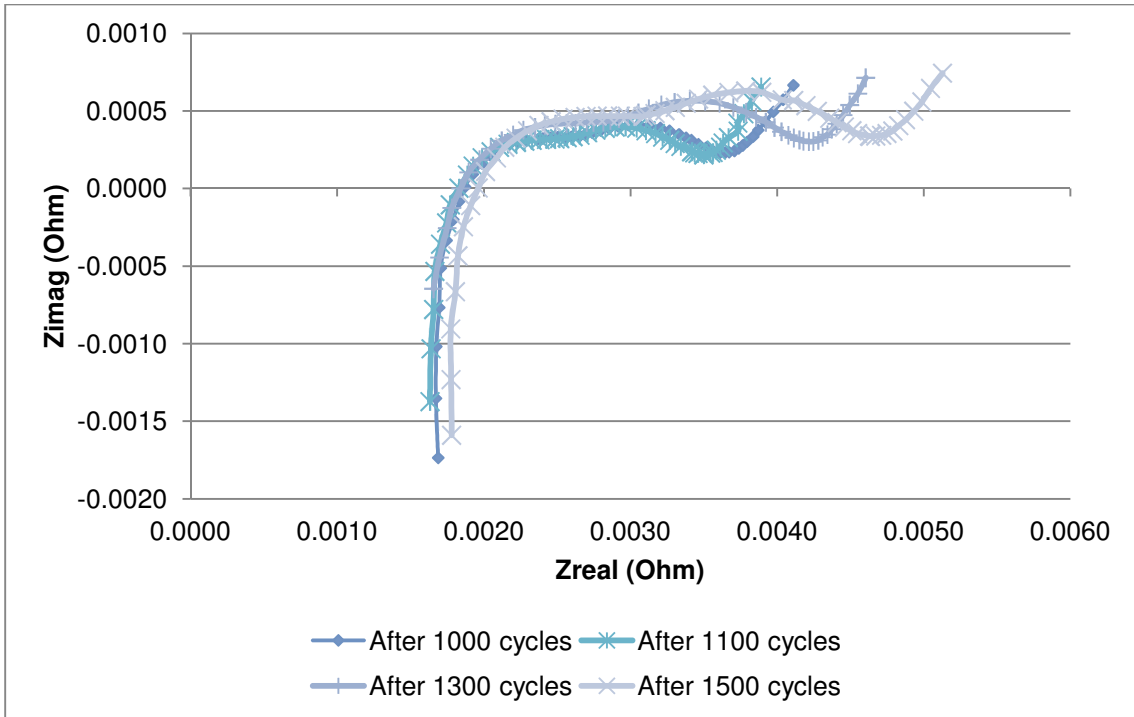


Figure 4.72. EIS spectra taken after cycles 1000 to 1500 in the low DoD window region.

After cycle no 1100 the circumference of the semi-circles become larger which indicated changes in resistances at these areas. These changes can be shown to be due to the resistance associated with the SEI layer at the anode and the resistance associated with the double layer capacity and charge transfer resistance as shown in Fig 4.73.

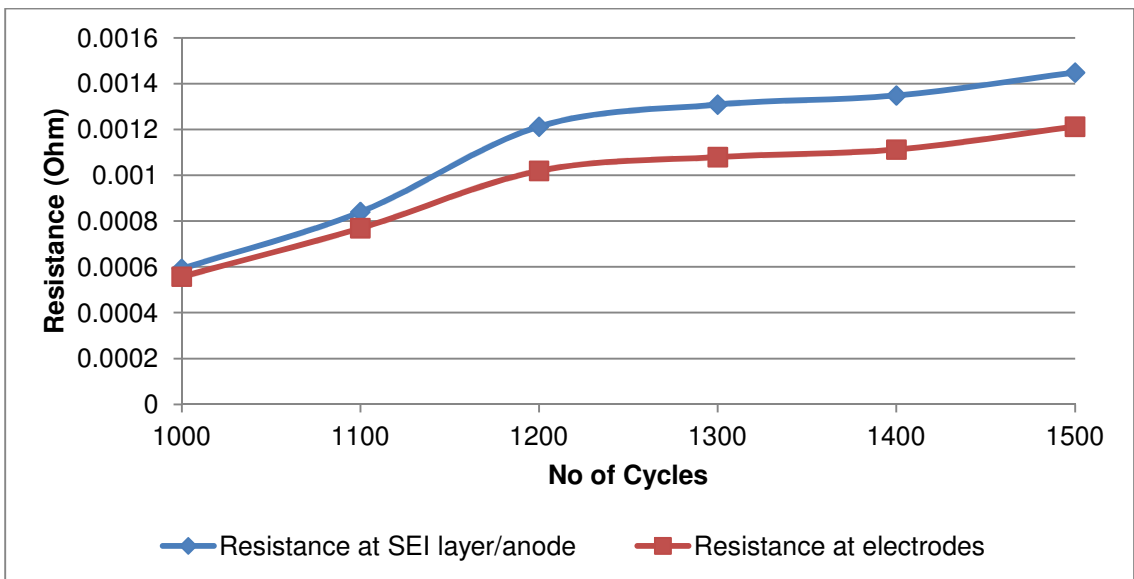


Figure 4.73. Change in resistances over cycles 1000 to 1500 in the low DoD window region.

Overall an increase in resistance was seen where there was a more significant increase in the circumference of the first and second semi-circles of the high DoD window region between the cycle numbers 1000 and 2300 cycles. This was shown in the spectra taken between these points and shown in Fig 4.74.

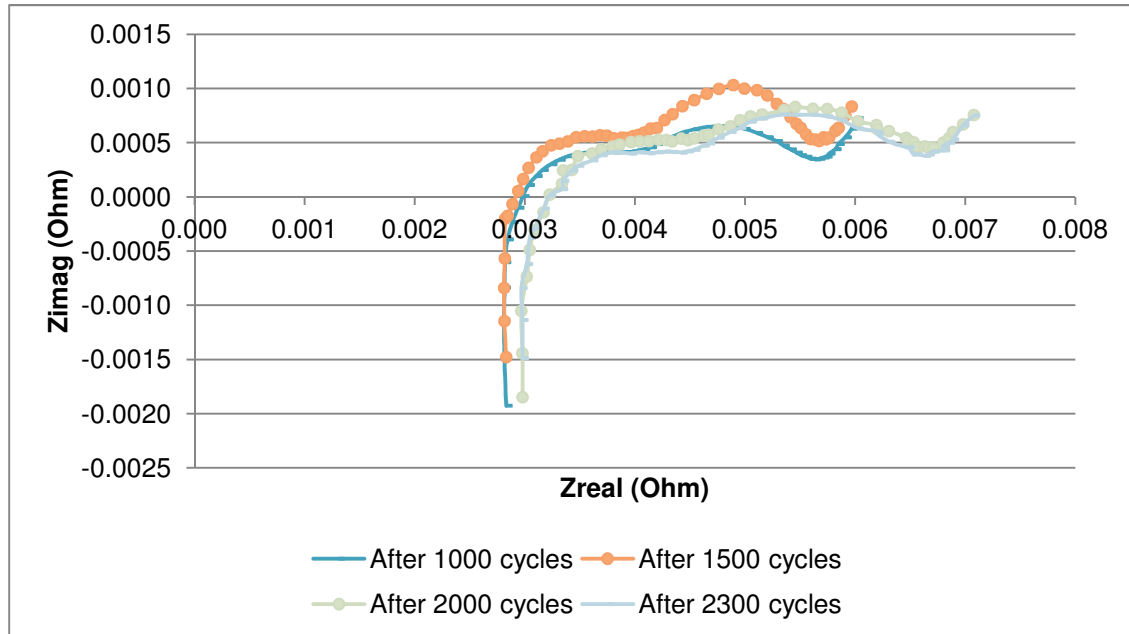


Figure 4.74. EIS spectra taken after cycles 1000 to 2300 in the high DoD window region.

After cycle number 1100 the circumference of the semi-circles in the EIS spectra became larger which indicated changes in resistances associated with the SEI layer at the anode and the resistance associated with the double layer capacity and charge transfer resistance (Fig 4.75).

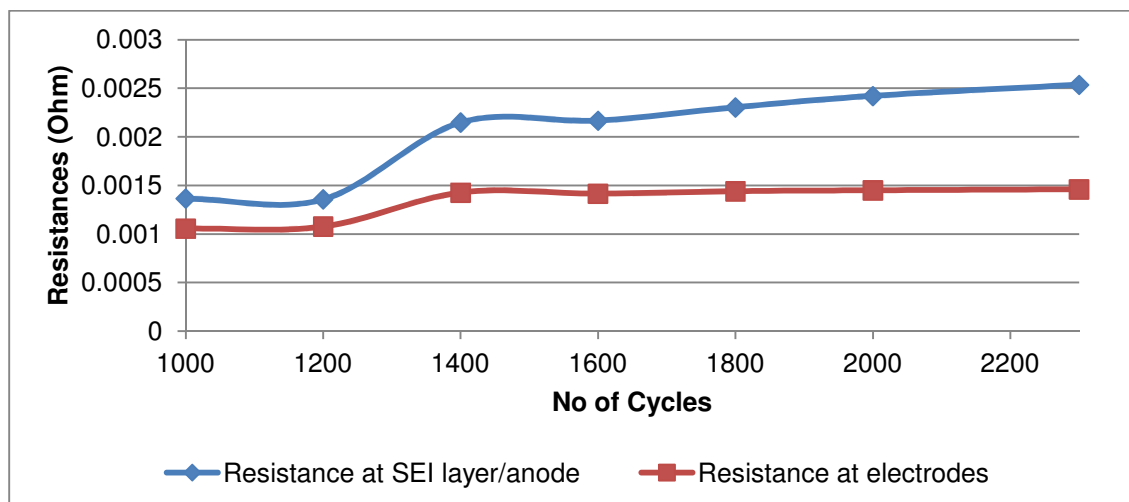


Figure 4.75. Change in resistances over cycles 1000 to 1500 in the high DoD window region.

A steeper increase in resistance was seen between 1200 and 1400 cycles, after which a gradual increase in resistance was seen.

Capacitance associated with the SEI layer at the anode (Fig 4.76) and the capacitance associated with the double layer capacity and charge transfer resistance (Fig 4.77) were measured for the 3 window regions.

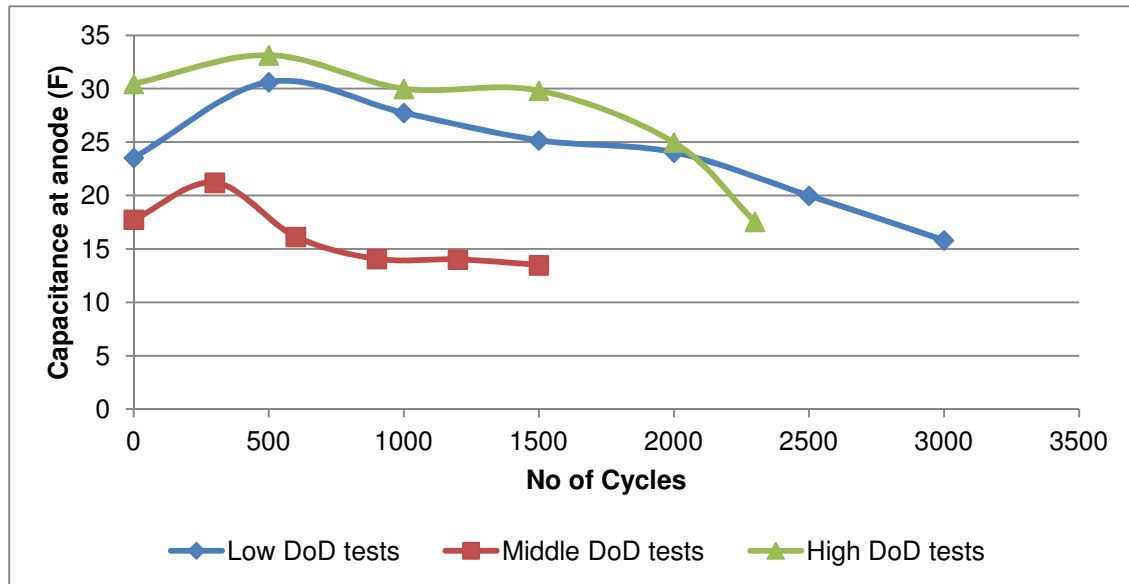


Figure 4.76. Change in capacitance associated with the SEI layer at the anode in the three DoD window regions.

The cell used during the high DoD window test showed the highest capacitance over the cycles until 2000 cycles had been completed. The capacitance then dropped below the capacitance of the cell used for the low DoD window tests at 2300 cycles. The middle DoD window test cell showed the smallest capacitance in comparison to the other cells tested.

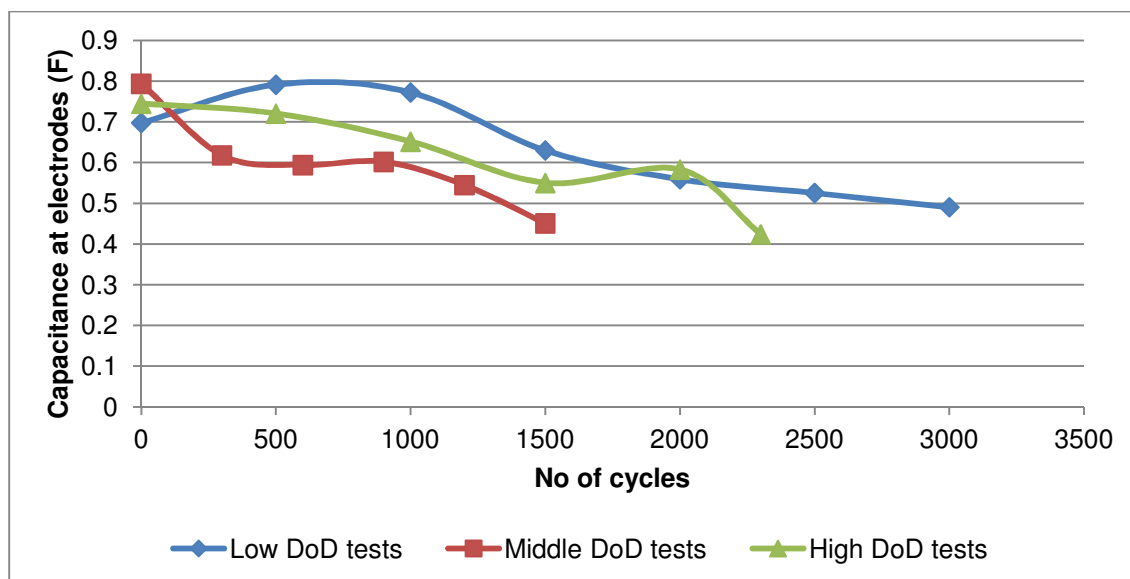


Figure 4.77. Change in capacitance associated with the double layer capacity and charge transfer resistance at both electrodes in the three DoD window regions.

The capacitance of the cell used for the middle DoD window test showed the highest capacitance at the beginning of testing. This capacitance then dropped below the capacitance of the other cells tested, which indicated that the cathode contributed more significantly to the overall capacitance of the cell at the start of cycling, as the capacitance associated with the SEI layer at the anode was low. There was an increase in capacitance of the cell used for the low DoD window tests till the cell had completed 500 cycles after which the capacitance decreased again. The cell used for the low and high DoD window test showed a gradual decrease in capacitance over the cycling.

The overall cell capacitance decreased as the number of cycles increased.

A measure of the time taken for the reactant to diffuse across the Nernst Diffusion layer⁸⁶ was characterized by one of the parameters (YoW) from the model. As the no of cycles increased, the time taken to cross this diffusion layer increased and is shown in Figure 4.78.

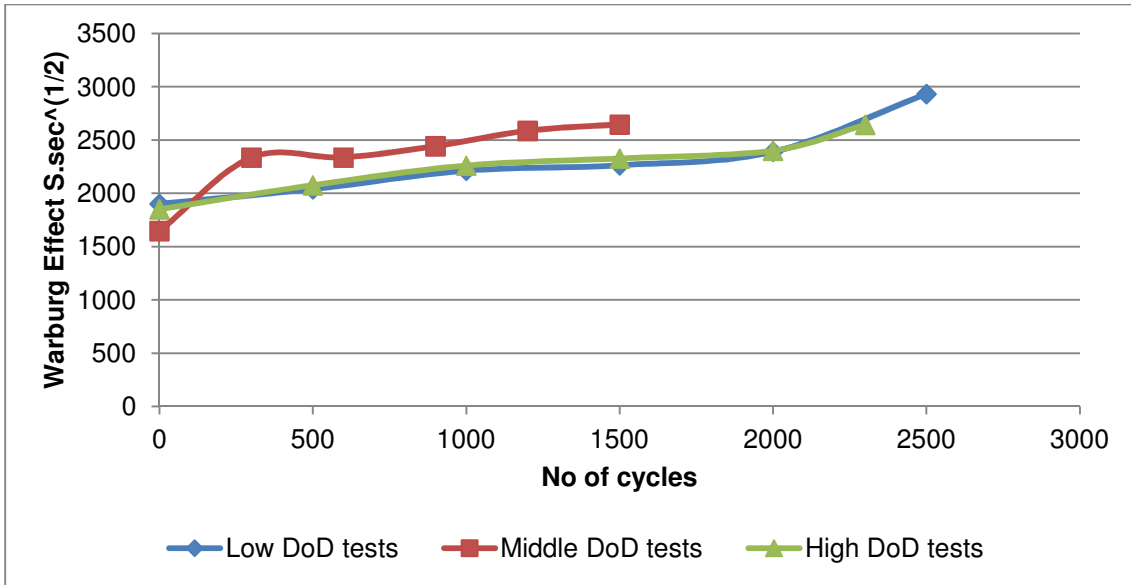


Figure 4.78. Time taken for the reactant to diffuse across the Nernst Diffusion layer in the three DoD window regions.

The time taken for the reactant to diffuse through the Nernst Diffusion layer increased as the cells aged.

When comparing the change in the Warburg effect with the C/1 capacity of the cells at various cycle numbers is shown in Figures 4.79, 4.80 and 4.81.

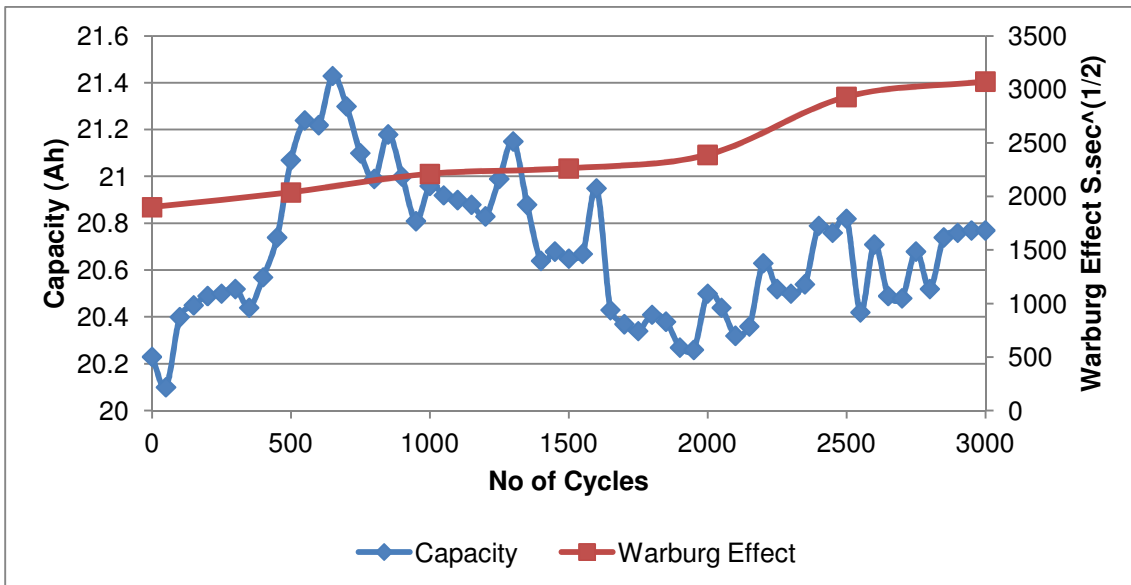


Figure 4.79. Capacity vs. Warburg Effect over the 3000 cycles in the low DoD window test.

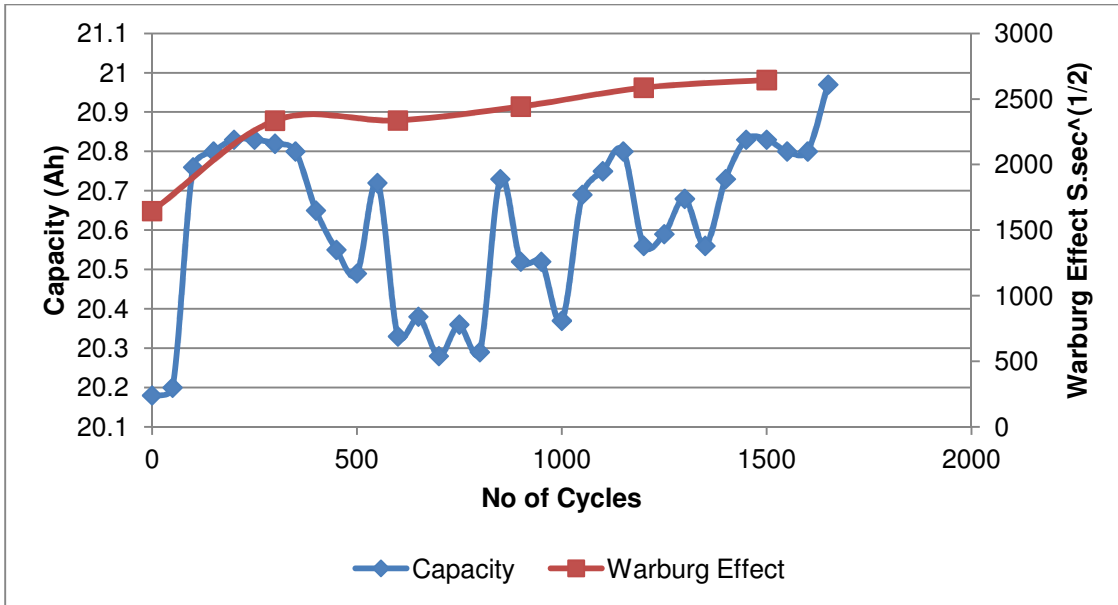


Figure 4.80. Capacity vs. Warburg Effect over the 1650 cycles in the middle DoD window test.

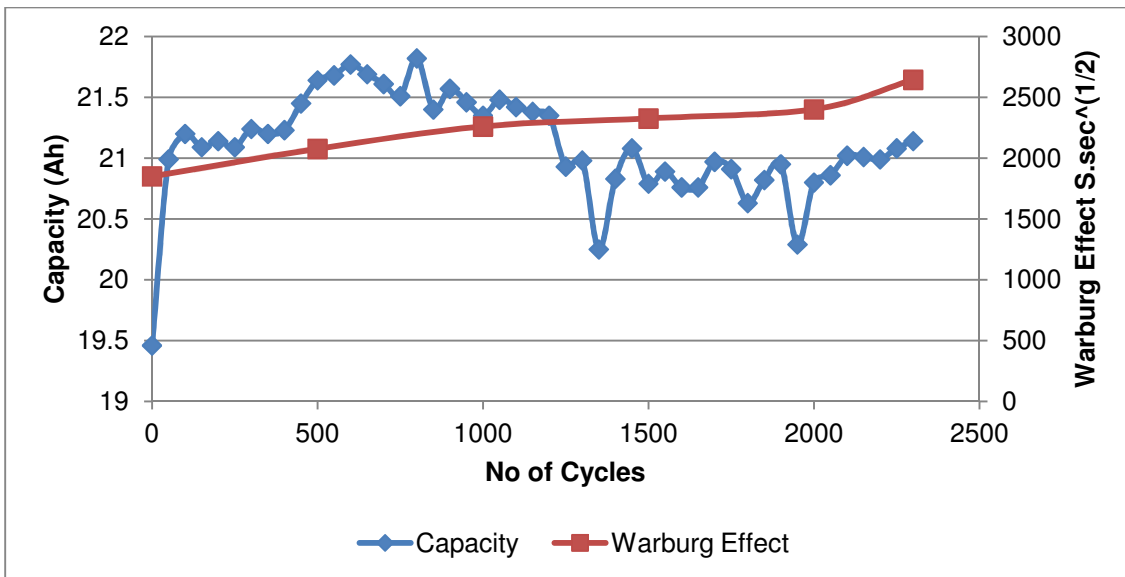


Figure 4.81. Capacity vs. Warburg Effect over the 2300 cycles in the high DoD window test.

During the low DoD tests, the Warburg effect was seen to gradually increase, with an initial increase in capacity. As the capacity began to slightly decrease after 850 cycles, the Warburg effect continued to gradually increase. A sharper increase in the Warburg effect was seen after 2000 cycles where the cell capacity remained fairly constant. During the middle DoD tests, a sharp increase in the Warburg effect was seen during the initial 300 cycles with a sharp increase in cell capacity. The Warburg effect was then seen to steadily increase as the cell capacity cycled between 20.2

Ah and 20.9 Ah. During the high DoD tests, a more gradual increase in the Warburg effect was seen throughout the cycles, while a sharp increase in cell capacity was seen after 50 cycles. The cell capacity decreased slightly as the ageing tests continued. The cells that were tested in this study never reached their end-of-life during the period of this study. However, there were significant changes observed within the cells when the EIS technique was applied that showed some aspects of the cells ageing taking place.

4.2.2. 2Ah Li-ion cylindrical cell capacity ageing results:

One 2Ah cylindrical cell was cycled at the high DoD region, another 2Ah cylindrical cell was cycled at the medium DoD region and one other 2Ah cylindrical cell was cycled at the low DoD region. After cycling the 20Ah pouch cells for about 13 months, the pouch cells still hadn't reached their 80% capacity or end-of-life and no significant accelerated ageing was observed. The Li-ion pouch cells proved to be more robust than initially anticipated. In order to increase the accelerated testing effects, the 2Ah cylindrical cells were tested under a harsher test. This harsher test involved a forced complete discharge within the voltage test window. No charging took place during the 200 cycle set and the results are shown in Figure 4.82.

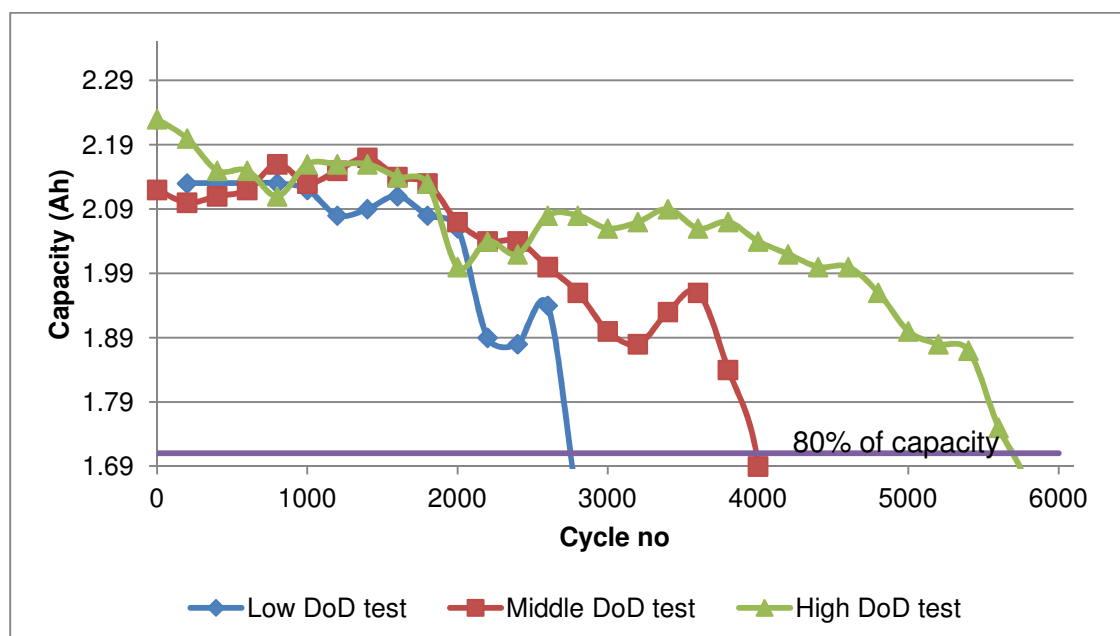


Figure 4.82. Change in capacity over the number of cycles for the different DoD.

The cells were rated by the manufacturer to be 2Ah. However, an initial Peukert test was carried out on the cells and the true capacity was found to be:

Cell description	True capacity
Cell 1 – Low DoD	2.13 Ah
Cell 2 – Middle DoD	2.12 Ah
Cell 3 – High DoD	2.23 Ah

Table 4.3. True capacity of each cell.

2Ah Li-ion cylindrical cell capacity ageing results – low, middle and high DoD windows:

The EIS for the 2Ah cylindrical cell that was cycled in the low DoD window region was cycled for 2600 cycles. The EIS spectra for these 2600 cycles are shown in Fig 4.83 in 400 cycle intervals:

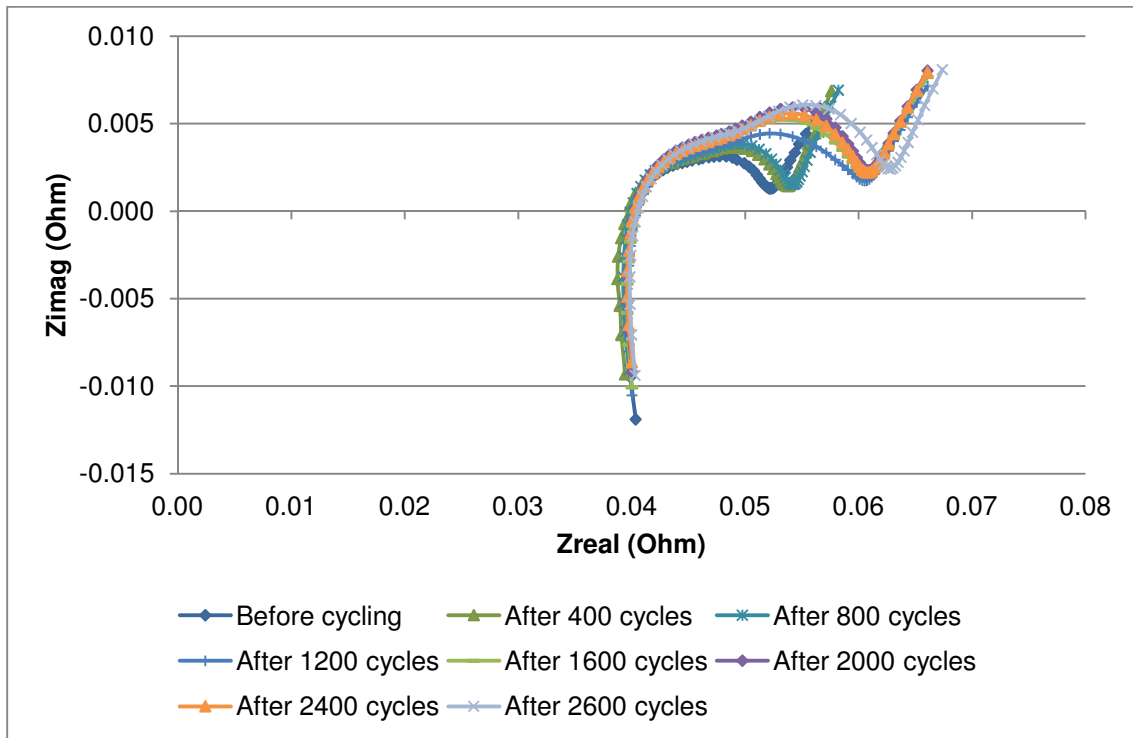


Figure 4.83. 400 cycle intervals representing the 2600 cycles carried out on a 2Ah cylindrical cell in the low DoD window region.

The EIS for the 2Ah cylindrical cell that was cycled in the middle DoD window region was cycled for 4200 cycles. The EIS spectra for these 4200 cycles are shown in Fig 4.84 in 600 cycle intervals:

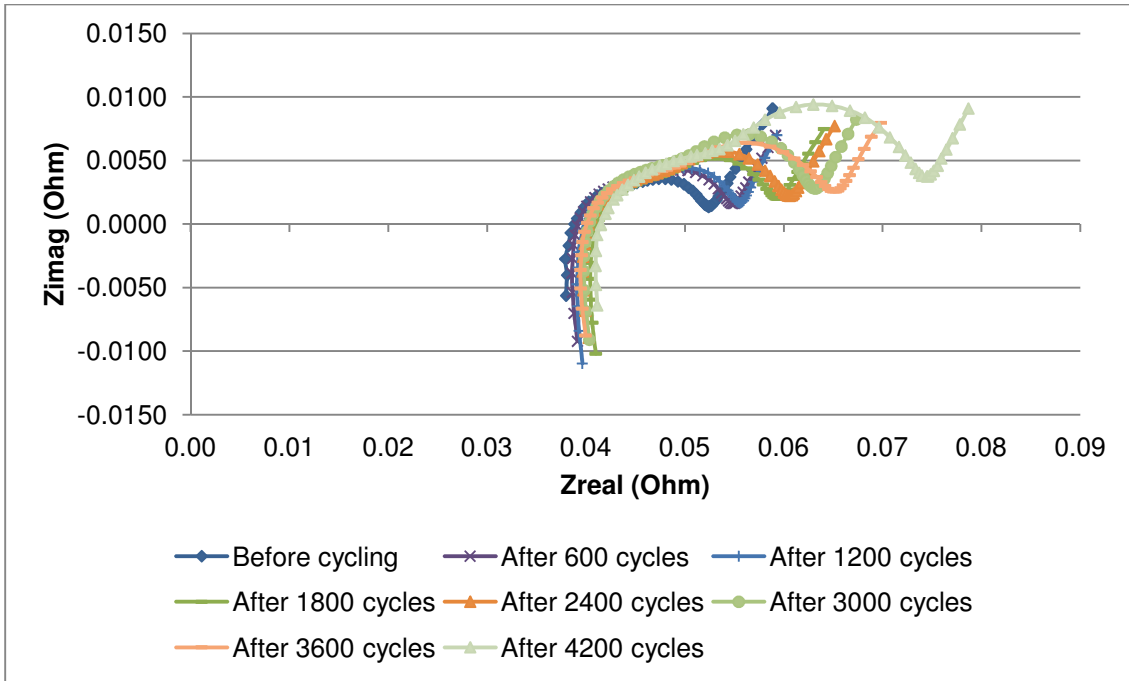


Figure 4.84. 600 cycle intervals representing the 4200 cycles carried out on a 2Ah cylindrical cell in the middle DoD window region.

The EIS for the 2Ah cylindrical cell that was cycled in the high DoD window region was cycled for 5400 cycles. The EIS spectra for these 5400 cycles are shown in Fig 4.85 in 1000 cycle intervals:

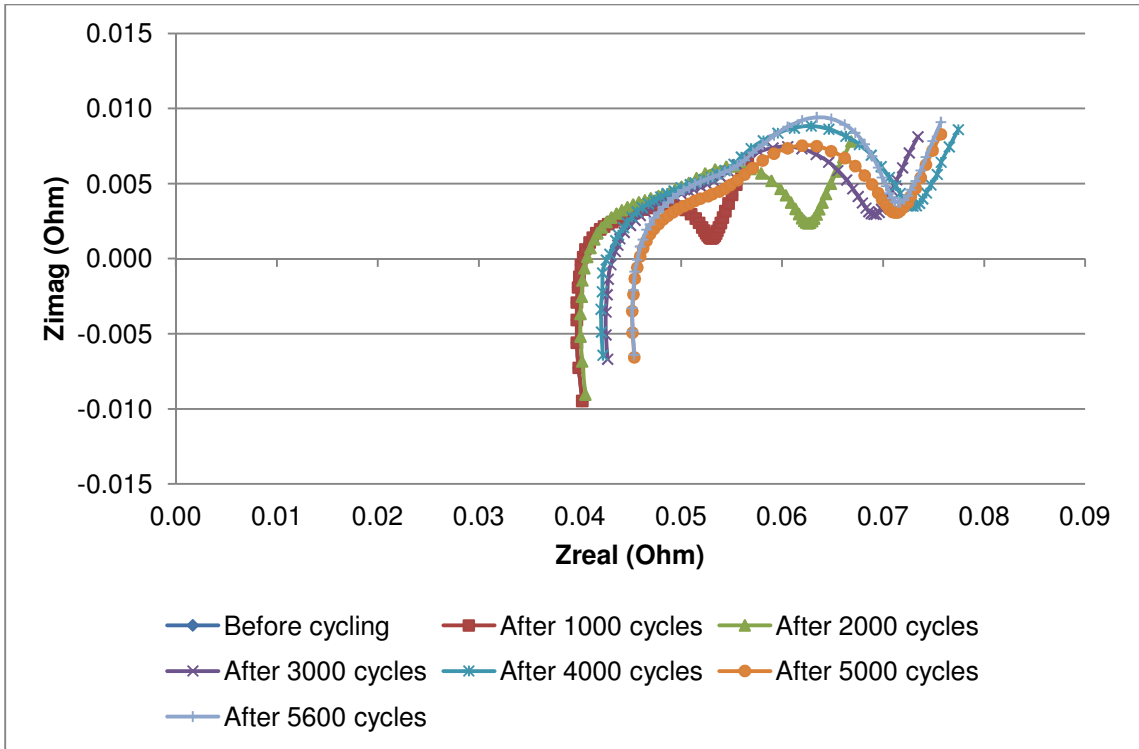


Figure 4.85. 1000 cycle intervals representing the 5400 cycles carried out on a 2Ah cylindrical cell in the high DoD window region.

The various changes within the cell were modelled according to the EIS model discussed above. All the EIS spectra showed similar Zreal values. There were changes in the semi-circle regions.

The inductance of all the EIS spectra changed very little between the spectra. The inductance of the EIS was small, which indicated that the inductive reactants of the metallic elements in the cell and wires were low.

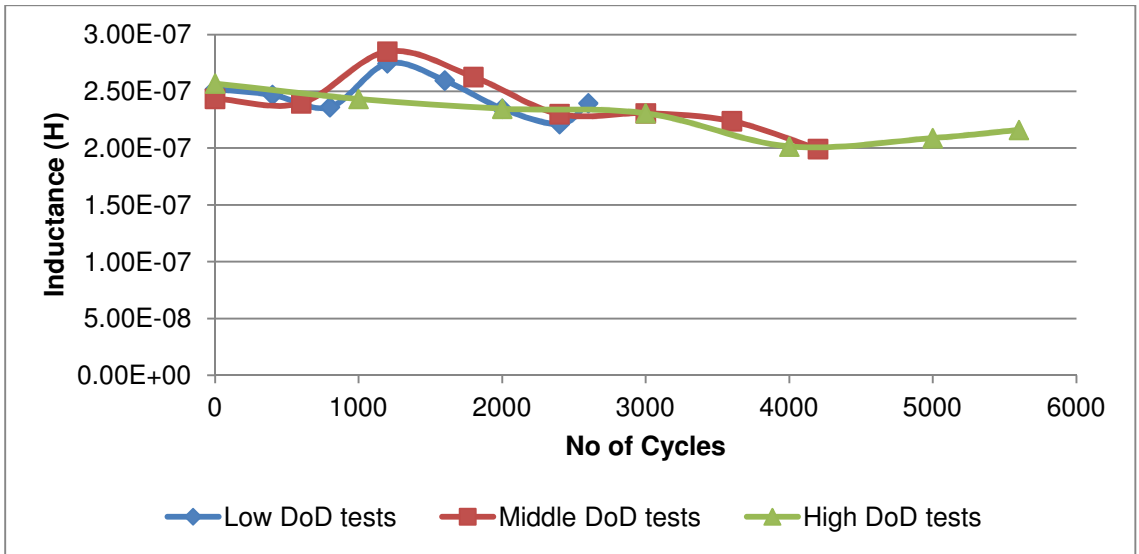


Figure 4.86. Inductance changes during cycling in the three DoD window regions.

Initially the EIS spectrum before commencement of cycling showed the lowest Zreal values. As the cycling started, the EIS spectrum was seen to shift towards a larger Zreal value. As the cycling continued the EIS spectrum shifted along the Zreal axis, which indicated ageing within the cell. These changes along the real impedance axis at zero imaginary impedance were due to the circuit resistance changes and were shown in Fig 4.87. The circuit resistance involved resistances due to sum of the resistances of the current collectors, the active material, electrolyte and the separator. As a cell ages these materials will change and this is indicated by the small gradual increase in overall resistance shown in the EIS spectra.

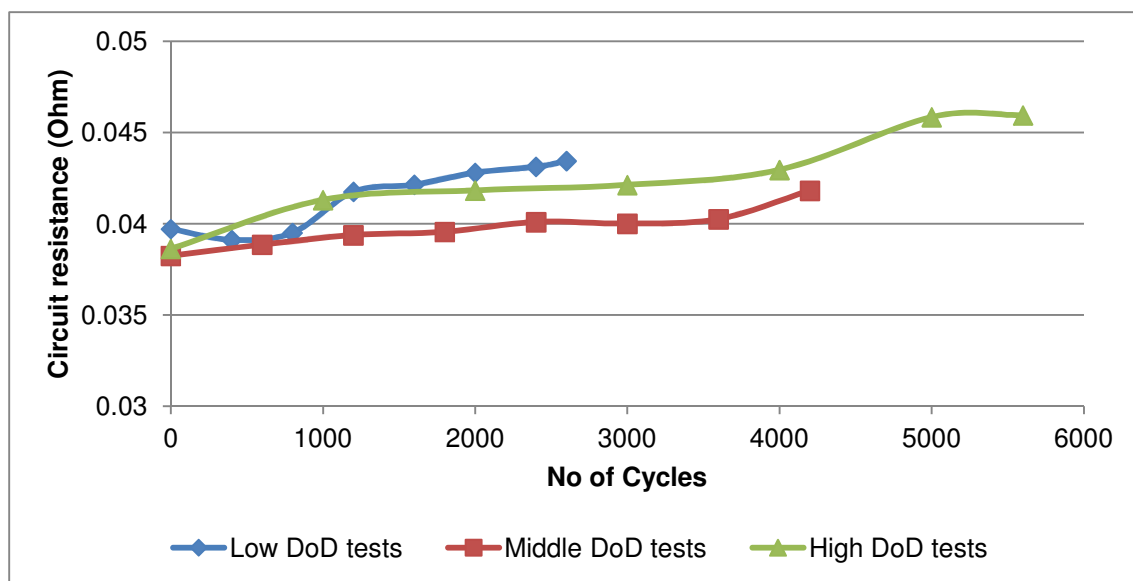


Figure 4.87. Circuit resistance changes during cycling in the three DoD windows.

The circuit resistance gradually increased until the final cycles. As the cycles continued, small changes were seen in the first semi-circle of the EIS spectra. This first semi-circle is due to changes in resistances associated with the SEI layer at the anode.

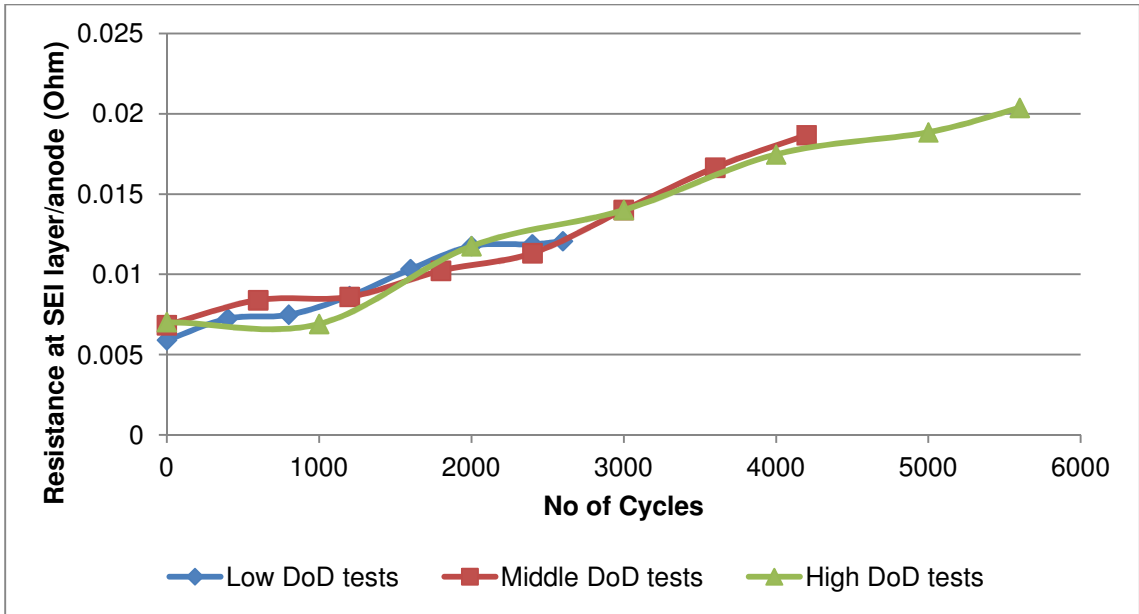


Figure 4.88. Changes in resistance associated with the SEI layer at the anode during cycling in the three DoD window regions.

Once again a gradual increase in the resistance associated with the SEI layer at the anode was seen for all three DoD window regions. Resistances associated with double layer capacity and charge transfer resistance at the electrodes are shown for the three DoD window regions (Fig 4.89).

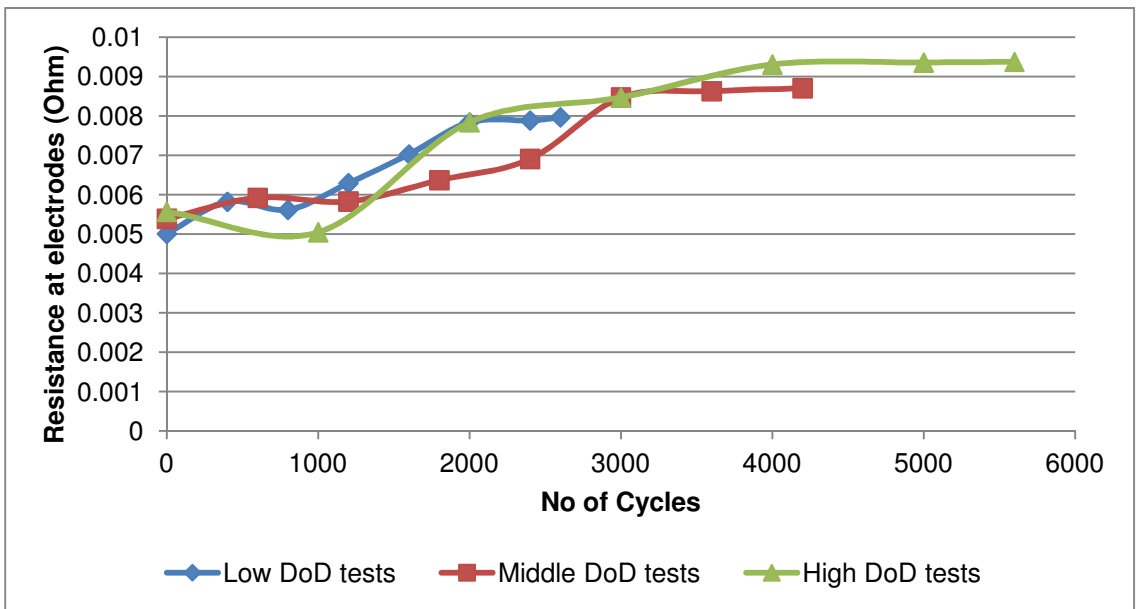


Figure 4.89. Resistance associated with the double layer capacity and charge transfer resistance at the electrodes during cycling in the three DoD window regions.

An increase in resistance associated with the double layer capacity and charge transfer resistance was seen for the three DoD window regions. However the resistance associated with the SEI layer at the anode showed a continuous gradual increase, while the resistance associated with the double layer capacity and charge transfer resistance showed a greater increase in resistance which later tapered off towards the end of the cycling. The reason for this observation could be that the SEI layer continued to increase as the cell aged, which resulted in a continuous increase in resistance associated with the SEI layer at the anode. The resistance associated with the double layer capacity and charge transfer resistance was due to the decrease in effective surface area of the positive and negative electrodes. There seemed to be a greater decrease in the effective surface areas at the start of cycling which later tapered off. According to a paper by Kazuhiko Takeno et al⁷², this resistance will not only be effected by the decreased effective surface areas of both electrodes, but also the loose contact between active materials and current collectors with increased number of cycles. Together with the decrease in liquid electrolyte at the electrodes this caused a decline in the level of electronic conduction in the electrolyte. These factors would have an effect on the resistance associated with the double layer capacity and charge transfer resistance at both electrodes.

Capacitance associated with the SEI layer at the anode (Fig 4.90) and the capacitance associated with the double layer capacity and charge transfer resistance (Fig 4.91) were measured for the three window regions.

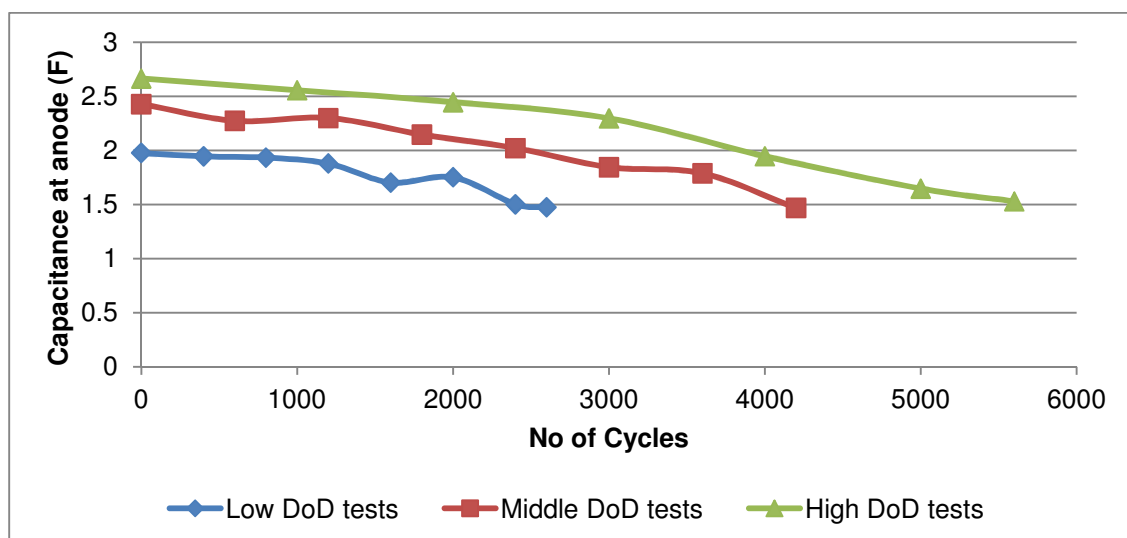


Figure 4.90. Change in capacitance associated with the SEI layer at the anode in the three DoD window regions.

The cell used during the high DoD window test showed the highest capacitance over the cycles until 5600 cycles had been completed. The low DoD window test cell showed the smallest capacitance in comparison to the other cells tested. All the DoD window regions dropped to a capacitance associated with the SEI layer at the anode to 1.5F.

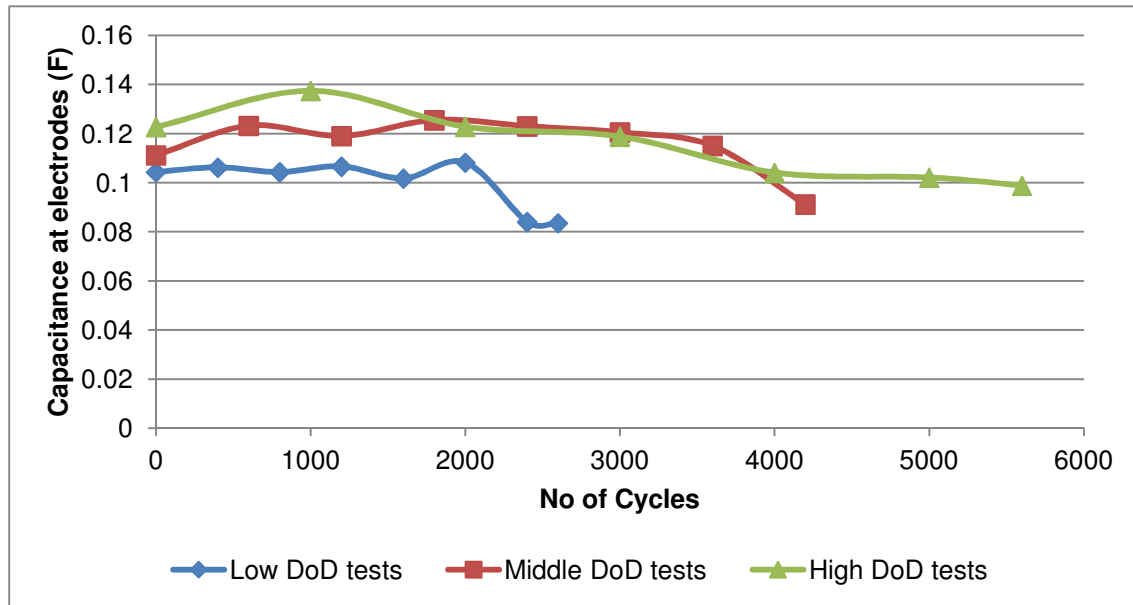


Figure 4.91. Change in capacitance associated with the double layer capacity and charge transfer resistance at both electrodes in the three DoD window regions.

There was an increase in capacitance at the start of the cycling when compared to the capacitance before cycling commenced. The capacitance of the cell used for the high DoD window test showed the highest capacitance at the beginning of testing. There was a gradual decrease in capacitance as the cycling commenced, with a slightly sharper decrease in capacitance towards the end of cycling. This trend matches the drop in capacity at the end of cycling, where a more significant decrease in capacity is seen.

The overall capacitance decreased as the number of cycles completed increased. A measure of the time taken for the reactant to diffuse across the Nernst Diffusion layer⁸⁶ was characterized by one of the parameters (YoW) from the model.

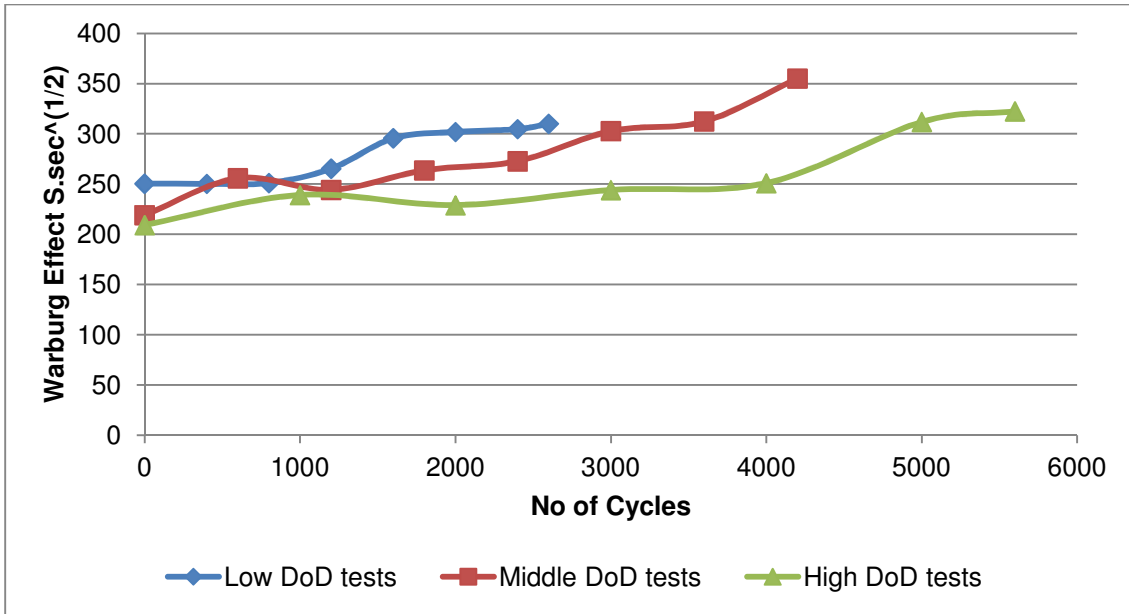


Figure 4.92. Time taken for the reactant to diffuse across the Nernst Diffusion layer in the three DoD window regions.

The time taken to diffuse through the Nernst Diffusion layer increased as the number of cycles increased for the three DoD window regions.

When comparing the change in the Warburg effect with the C/1 capacity of the cells at various cycle numbers is shown in Figures 4.93, 4.94 and 4.95.

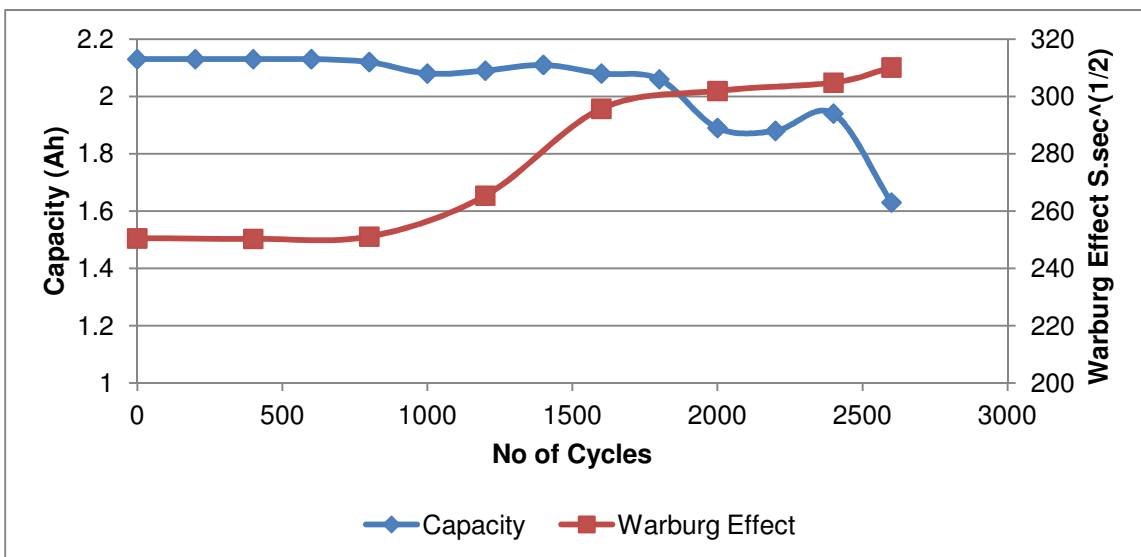


Figure 4.93. Capacity vs. Warburg Effect over the 2600 cycles in the low DoD window test.

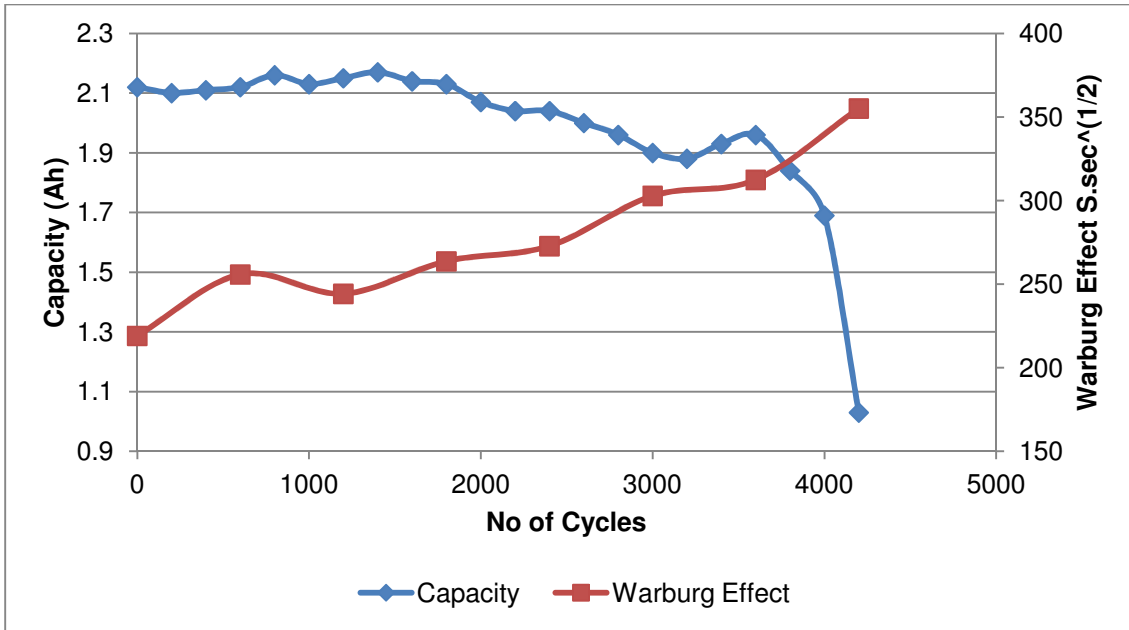


Figure 4.94. Capacity vs. Warburg Effect over the 4200 cycles in the middle DoD window test.

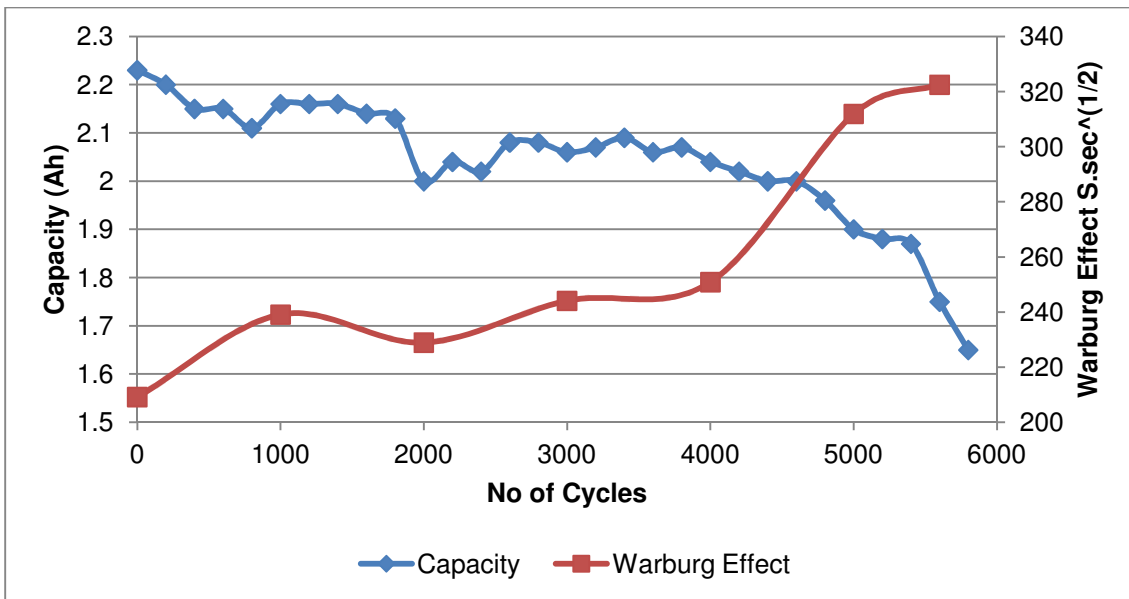


Figure 4.95. Capacity vs. Warburg Effect over the 5800 cycles in the high DoD window test.

As the capacity decreased, the Warburg Effect, representing the Impedance growth, increased as the number of cycles increased. This was seen for the three DoD window regions. These trends are similar to a paper by Kazuhiko Takeno et al⁷², where a decrease in capacity over the number of cycles correlated to an increase in impedance growth. Figure 4.96 shows a plot of the percentage change in the Warburg parameter with the percentage change in the cells capacity over cycle time.

The percentage change was the relative change with respect to the initial values of the new cell.

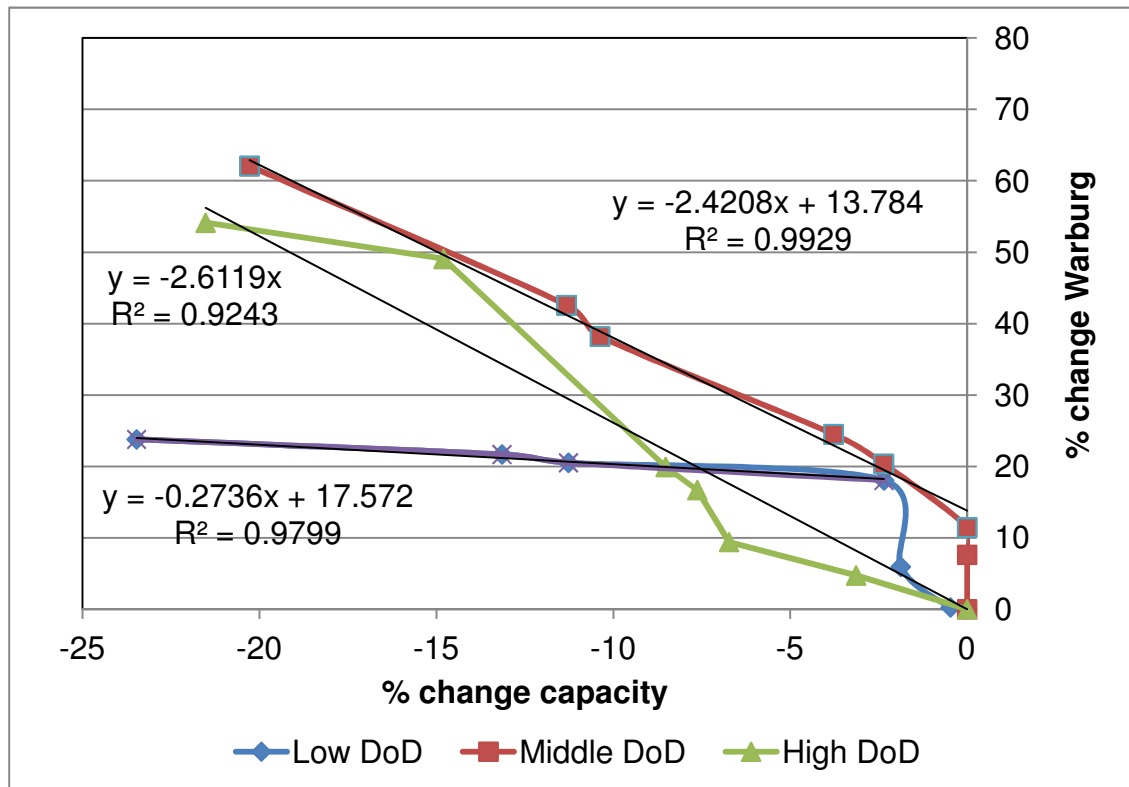


Figure 4.96. Percentage change in capacity vs. percentage Warburg effect for 2Ah cylindrical cell.

The results showed that there was an almost linear change in the Warburg parameter with the loss in cell capacity for the cell tested at the High DoD test sequence, with the percentage change in the Warburg parameter being 2.6 times the corresponding percentage loss in capacity. During first half of cycling of the middle DoD test sequence there was a large notable increase in the Warburg parameter without a significant change in the cells capacity parameter. The second half of the middle DoD cycling, a linear change in the Warburg parameter with change in cell capacity was similar to the slope observed during the high DoD test sequence. During the low DoD test sequence; there was a significantly large initial change in the Warburg parameter within the first few cycles, with only slight changes in the cell capacity. This was followed by a significant loss in cell capacity with little change in the Warburg parameter.

The high and low stress regions (high and middle DoD regions respectively) showed more gradual changes in cell capacity with a comparative change in the Warburg

effect, with both these regions showing high percentage change in Warburg values. The changes seen during the middle stress region (low DoD region) indicate that some significant changes in the cell chemistry had occurred within the first few capacity cycles, followed by small changes in the Warburg parameter at more significant loss in cell capacity. The Warburg parameter is a measure of the time taken for the reactant to diffuse through the Nernst Diffusion layer. At the low DoD window region, the cell operated at the higher voltage region, indicating a cell closer to being fully charged and most of the Li-ions lithiating the cathode. The results suggest that at the start of cycling, most of the Li-ions are freely available and all try to diffuse through the Nernst Diffusion layer at the cathode. As cycling continues and more Li-ions become trapped in the SEI layer at the anode, fewer Li-ions are available to diffuse through the Nernst Diffusion layer at the cathode and the Warburg parameter becomes smaller. The results would also suggest that during the middle and high DoD window cycling, there was a steady increase in the Nernst Diffusion layer at the anode (possibly due to an increase in the SEI layer at the anode) and the time taken for the Li-ions to pass through this layer increases. One of the aims of this study was to investigate if EIS can be used to model ageing within a cell. It can be concluded that EIS can be used to give an indication of the ageing of a cell.

During the EIS study of the 20Ah pouch cell and 2Ah cylindrical cell tests, the inductance parameter remained fairly stable during the repeating tests. The circuit resistance was due to electrolyte resistance, current collectors and other resistances such as electrode bulk resistance and separator resistance. According to a paper by G. Nagasubramanian et al⁹² this resistance was usually small and can be measured at about 0.08Ω. For the 20Ah pouch cells, the circuit resistances ranged from 0.002 to 0.0160Ω. The 2Ah cylindrical cells showed circuit resistances that ranged from 0.04Ω to 0.05Ω. Thus it can be determined that the circuit resistance influenced the overall cell impedance and cell fade but only slightly. During the study of the 20Ah pouch cells, most of the cell impedance can be attributed to the increase in resistance of the SEI layer at the anode and to the increase in resistance associated with the double layer capacity and charge transfer resistance at both electrodes. Stability of most Li-ion cells is due to the reduction of the electrolyte at the negative electrode/electrolyte interface which forms a passivation layer on the anode. This layer remains conductive to the movement of Li⁺ ions. However as the cell begins to

fade, this passivation layer becomes too thick, causing it to become poorly ionic (Li^+) conductive and thus the cell's internal resistance increases⁹³. Most of the overall resistance that contributed to the cell impedance of the 2Ah cylindrical cells was attributed to the resistance associated with the SEI layer at the anode.

During the testing of the 20Ah pouch cells, the capacitance began to drop as the number of cycles increased; however very little change in overall cell capacity was seen during these tests. During testing of all the 2Ah cylindrical cells, the capacitance dropped as the number of cycles increased. These results matched the fact that the capacity of the cells decreased as the number of cycles increased.

In each case when studying the time taken for the reactant to diffuse through the Nernst Diffusion layer, the Warburg effect increased as the number of cycles increased. It was also shown that an overall increase in cell impedance was seen as the cell capacity decreased. During the 20Ah tests, the Warburg effect will have only given an indication of cell deterioration as the cell capacity had not yet decreased.

The EIS values form a pre-emptive indication that ageing is occurring within the cell, which would later lead to a decrease in the cell capacity. Minimal errors in ageing results may have occurred as the cells were not cycled in a temperature controlled environment, but were cycled at ambient temperature. Temperature does have an effect on ageing as discussed in a paper by G. Nagasubramanian et al⁹² where it was shown that at lower temperatures such 0°C and lower or at temperatures higher than 40°C, temperature will have an effect on the capacity that the cell is able to deliver. These capacities will be lower than the capacities seen at room temperature.

The aim of this study was to determine an accelerated ageing test and by using EIS, to model the changes within the cell during these ageing tests. The 20Ah pouch cells never reached the determined end-of-life capacities. Thus it cannot be determined with certainty which DoD window region would age the cell the fastest. It was however noted that the middle DoD window region showed the highest Warburg effect values, with the low and high DoD window regions displaying similar Warburg effect values but lower values than the values seen during the middle DoD test.

During the 2Ah cylindrical cell, the cells were tested until the cells reached the determined end-of-life capacities. It was seen that the cell that was tested in the low DoD window region failed first, followed by the middle DoD window region. The cell tested in the high DoD window region took the longest before achieving 80% of the

expected capacity. Thus it can be determined in this study that the low DoD window region placed the most stress on the cell and aged it the fastest.

CHAPTER 5:

Results and Discussion:

Supercapacitors connected to Li-ion cells and a comparison with Pb-acid cells

Supercapacitors can be added together with a battery in an EV application in order to relieve the battery of severe load demands by meeting the peak power demands. The energy supply system will then be able to supply the average power load without the need for an oversized battery configuration that should be able to supply both the power and energy density needs. This is usually undesirable in vehicle applications where space and weight contribution to the vehicle must be kept to a minimal. In some cases by designing a well optimized battery and supercapacitor configuration, a saving of up to 60% in weight can be made⁴⁴.

A supercapacitor is classified as a capacitor with a capacitance of higher than 1 Farad. Supercapacitors offer higher power densities when compared to batteries systems and offer higher energy densities when compared to conventional capacitors⁹⁴. Batteries are designed to deliver good energy density and usually have poor comparative power density. In comparison supercapacitors would have a poorer energy density with a relative better power density. Supercapacitors can also provide very fast dynamic cycles (close to 1ms) with very little capacity fading over many cycles⁹⁵. By combining the supercapacitor with the battery, the overall system would be able to provide a faster charge acceptance or delivery than when the battery was used alone.

A testing procedure was carried out in order to compare the charge acceptance and discharge ability of a battery alone against a system consisting of a battery and a supercapacitor. Three different Li-ion cells were used for the test, namely a 2Ah Li-ion cylindrical cell, 1Ah Li-ion pouch cell and a 20Ah Li-ion pouch cell. Tests were also carried out using a 7Ah VRLA Pb-acid cell⁷³.

A ratio of 2:1 (supercapacitor : battery) was used for the test. This ratio was based in the results published by M. Fernández et al⁷³ who described a 24Ah Pb-acid battery connected in parallel with a 52F supercapacitor.

In this study, the results from a test sequence consisting of a particular battery type with and without a supercapacitor were compared (figure 5.1 and 5.2) in order to

keep the capacitor and voltage similar between the different battery types, the batteries and supercapacitors were connected in either parallel or series in order to make up the correct system voltage and capacitance.

2Ah Li-ion cylindrical cell and 10F supercapacitor system:

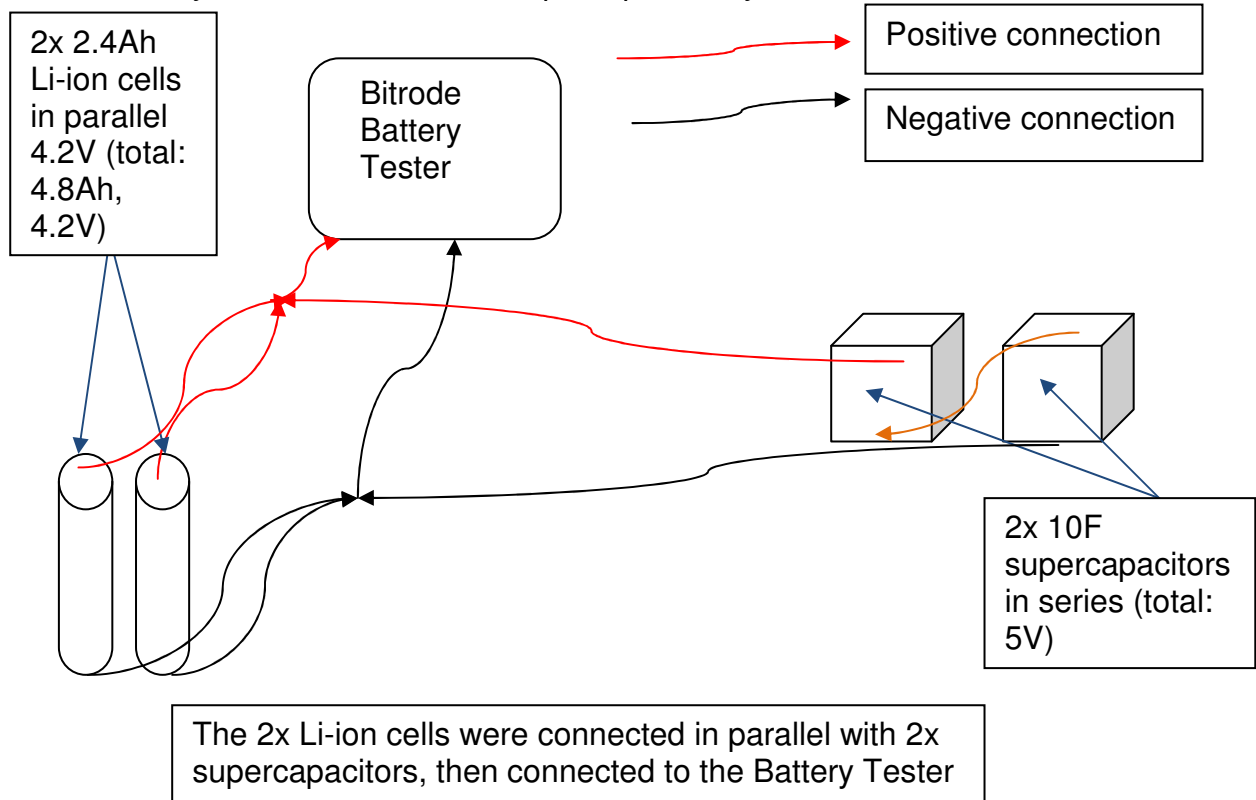


Figure 5.1 2Ah Li-ion cylindrical cell connected to 10F supercapacitor

5.21Ah VRLA Pb-acid cell and 10F supercapacitor system:

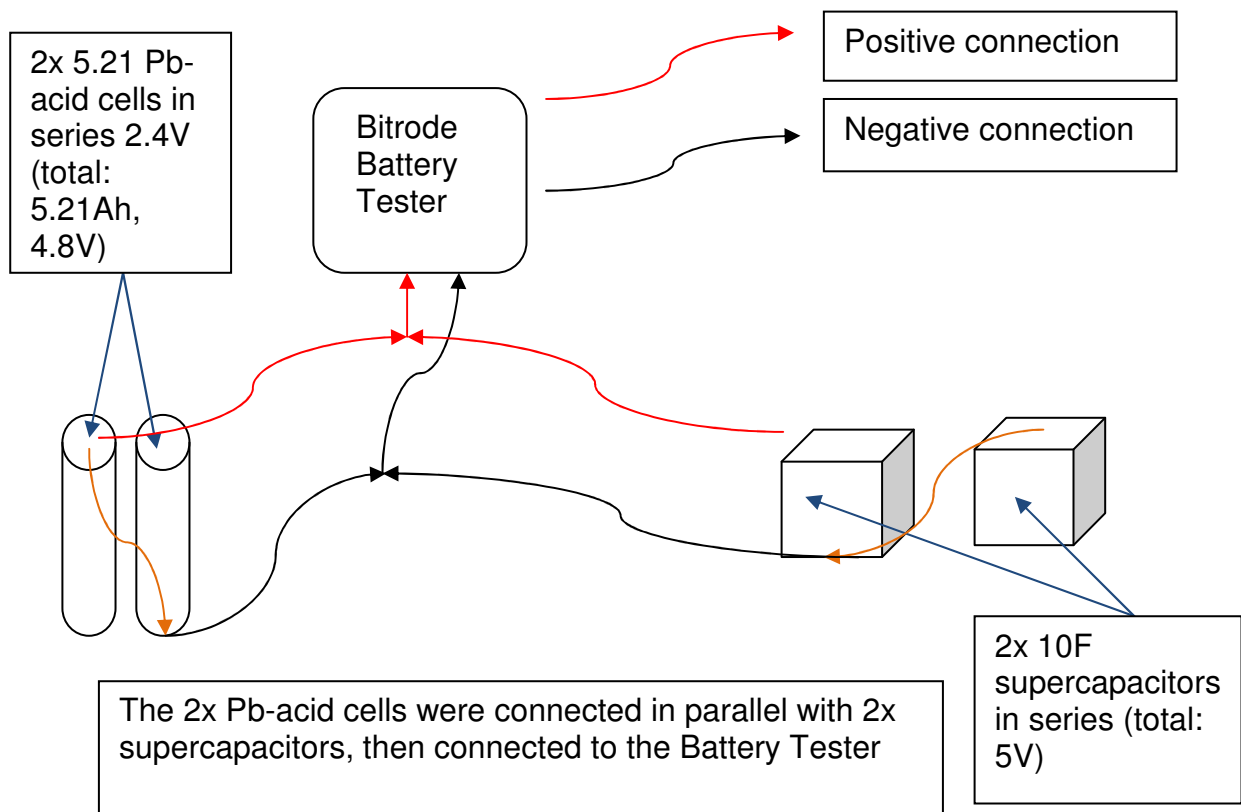


Figure 5.2 5.21Ah VRLA Pb-acid cell connected to 10F supercapacitor.

The supercapacitors were connected in series in order to be similar to the voltage of the Li-ion cells. For comparison reasons two 5.21Ah VRLA Pb-acid batteries were also connected in series. These were then connected in parallel to the two 10F supercapacitor that was already connected in series.

For the 1Ah Li-ion pouch cell made by UWC, only one cell was available for testing and it was connected in parallel to two 3.3F supercapacitors. The 3.3F supercapacitors were connected in series.

The larger 20Ah Li-ion pouch cell would have required 40F supercapacitors. This would have exceeded the current limitations of the 200A battery tester and concern about the weakness of the cell connectors overheating at the high current was observed. The 20Ah Li-ion cell was tested without capacitors. A single 40F supercapacitor was not available for purchasing, which would have required that 4 sets of 10F supercapacitors would be connected in series. According to literature⁹⁶, care must be taken when connecting strings of more than three capacitors in series. This would reduce the overall capacitance of the series and would require voltage

balancing in order to prevent overvoltage of a supercapacitor in the series. This is similar to voltage balancing of batteries.

Electrochemical Impedance Spectroscopy was carried out on all the cells with or without the supercapacitors. EIS spectra were taken at the four SoC and the spectra compared. The spectra were then analysed using the model previously described. All tests were repeated three times for statistical purposes.

5.1. 2.4Ah Li-ion cylindrical cell with two 10F Supercapacitors

The comparison between the high rate charge of the Li-ion cells alone against the system consisting of the Li-ion cells together with the supercapacitors as per the test method can be seen in figure 5.3. The difference between initial maximum acceptance current and the total capacity over the 5 second charge is summarized in Table 5.1.

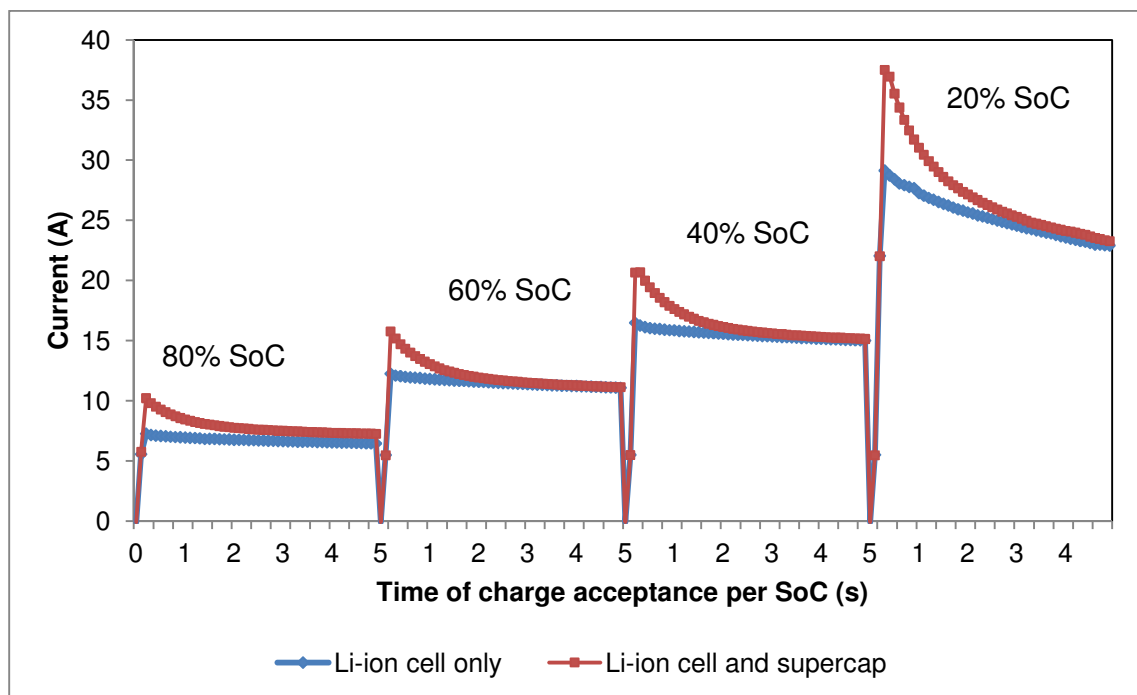


Figure 5.3. Comparison between the Li-ion cells and the system of Li-ion cells and supercapacitors using the high rate charge current.

SoC	Increase in Peak Charge current (A)	Capacity over 5 second step (Ah) - Battery only	Capacity over 5 second step (Ah) - Battery and supercapacitors	Total comparative capacity increase (Ah)
80%	1.73 ± 0.01	0.46 ± 0.01	0.53 ± 0.02	0.07
60%	1.59 ± 0.01	0.78 ± 0.03	0.82 ± 0.01	0.04
40%	1.98 ± 0.01	1.04 ± 0.04	1.10 ± 0.02	0.06
20%	4.04 ± 0.01	1.69 ± 0.03	1.81 ± 0.02	0.12

Table 5.1. The initial increase in current (A) at each SoC and the total comparative capacity increase at each SoC over the 5 second high rate charge.

The result showed that there was an improvement in the maximum peak current that the system could accept at the various SoC of the battery. Notably the maximum peak current increased with a decrease in the SoC except at the 60% SoC. When a comparison was made at each SoC in capacity (Ah), the system consisting of the battery and supercapacitor was able to accept more charge over the 5 second step. However there was not a steady increase in total comparative capacity increase as the SoC decreased over the different SoC except for when the cell was at a 20% SoC. At this SoC, an improvement in 7.1% of capacitance acceptance was observed. The results also showed that the measured results were repeatable where very similar value results were observed over three repeatable analyses with a low standard deviation.

The comparison between the cylindrical Li-ion cells with and without supercapacitors at a high rate discharge is shown in Fig 5.4. The difference between the initial maximum delivery current and the total capacity over the 10 second discharge are summarized in Table 5.2.

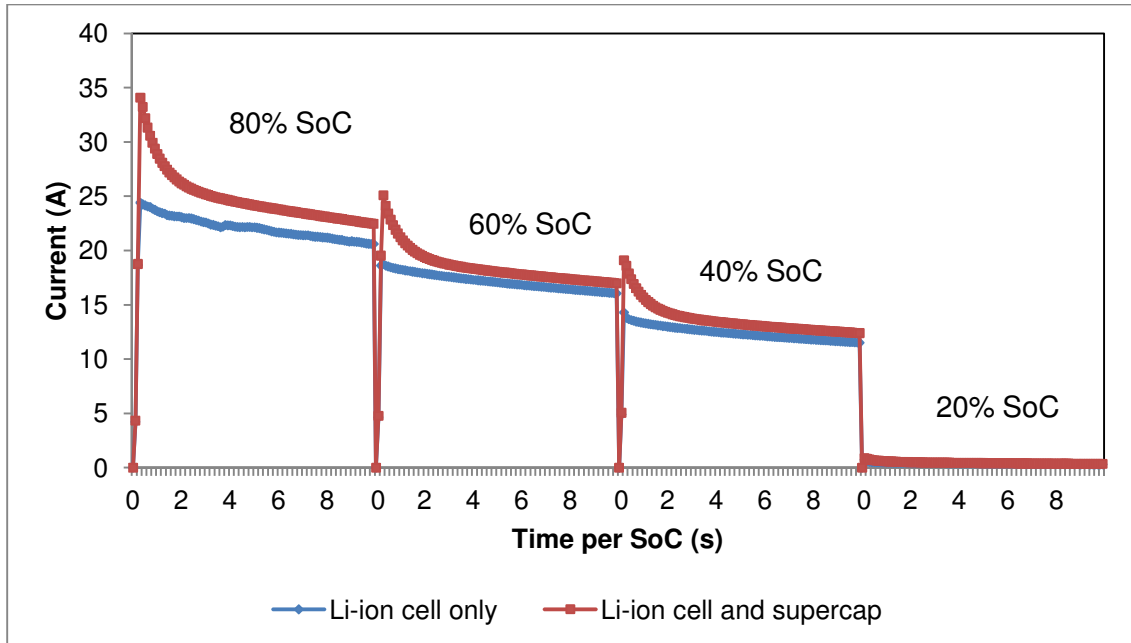


Figure 5.4. Comparison between the Li-ion cells alone against the system consisting of Li-ion cells and supercapacitors using the high rate discharge current.

SoC	Increase in Peak discharge current (A)	Capacity over 10 second step (Ah) - Battery only	Capacity over 10 second step (Ah) - Battery and supercapacitor	Total comparative capacity increase (Ah)
80%	8.82 ± 0.01	6.01 ± 0.13	6.76 ± 0.10	0.75
60%	6.34 ± 0.01	4.68 ± 0.08	5.06 ± 0.04	0.38
40%	4.80 ± 0.01	3.39 ± 0.08	3.73 ± 0.03	0.34
20%	0.15 ± 0.01	0.11 ± 0.01	0.13 ± 0.01	0.02

Table 5.2. The initial increase in current (A) at each SoC and the total comparative capacity increase at each SoC over the 10 second high rate discharge.

The results showed that as the SoC decreased the amount of additional charge that could be delivered decreased. The comparison between the capacity (Ah) of the battery alone against the system consisting of the battery and supercapacitors showed that the system was able to deliver more current at each SoC over the 10 second discharge step. Notably, the cell that was only at 40% SoC could discharge an additional 10% capacity over the 10 second period. The cell that was only at 20% SoC achieved very little comparative discharge capacity even with a supercapacitor. In a paper by C.E. Holland et al⁹⁷, a 50F supercapacitor was added in parallel with a 1.2Ah Li-ion battery. When the Li-ion cell was paired with the supercapacitor only a slight increase in capacity was seen. The battery showed a higher equivalent series resistance in this system while the supercapacitor showed a smaller equivalent series resistance. This meant that the supercapacitor assumed a higher percentage

of the load current. In order to improve the power available from the system, the current would need to be better controlled by sharing the current between the components within the system. Therefore by adding power electronics to the Hybrid system, a greater fraction of the energy stored in the capacitor on each pulse would be used. Also by testing the supercapacitor over a greater voltage range would increase the available power. This may allow for the supercapacitor to be smaller in size and mass. Similar conclusions can be made from the results obtained in this study. However, care needs to be taken not to allow the battery to fully discharge below 20% SoC. Below this SoC of the battery, there is very little benefit of the supercapacitor to allow for some power discharge within the voltage limits. Electrochemical Impedance Spectroscopy (EIS) analyses were done on both the cell alone and the system consisting of the cell and the supercapacitor, and the EIS Nyquist plot of the cells by themselves are shown in figure 5.5.

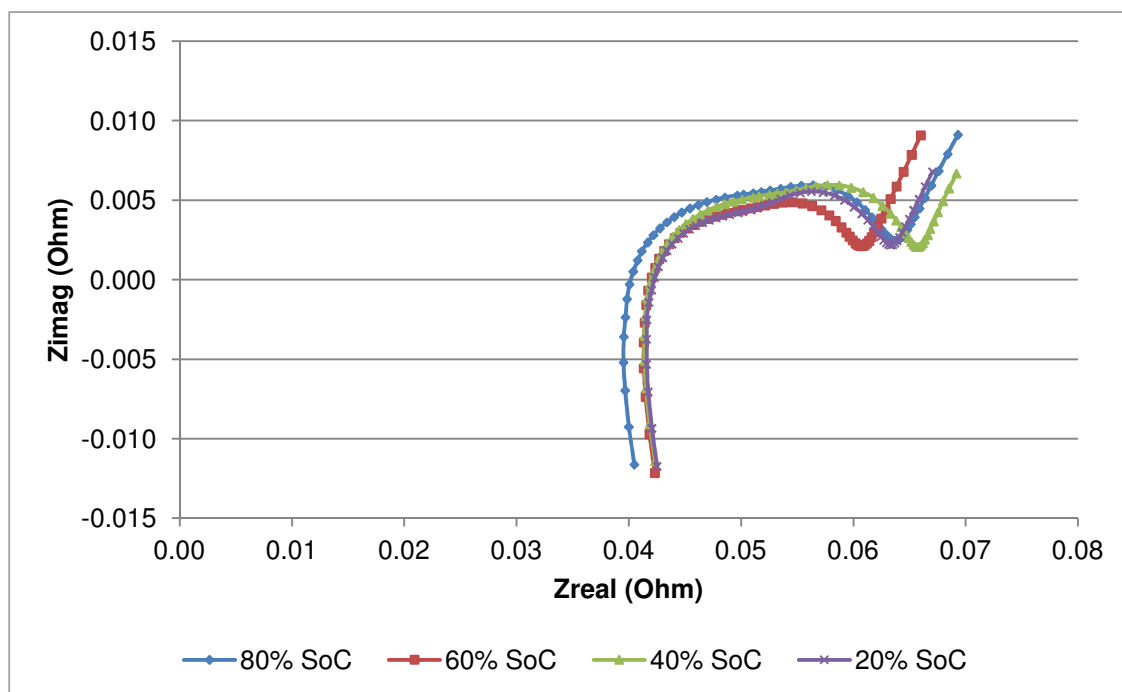


Figure 5.5. The EIS spectra of the cell at different SoC.

The EIS Nyquist spectra of the system consisting of the cells and the supercapacitors are shown in Fig 5.6.

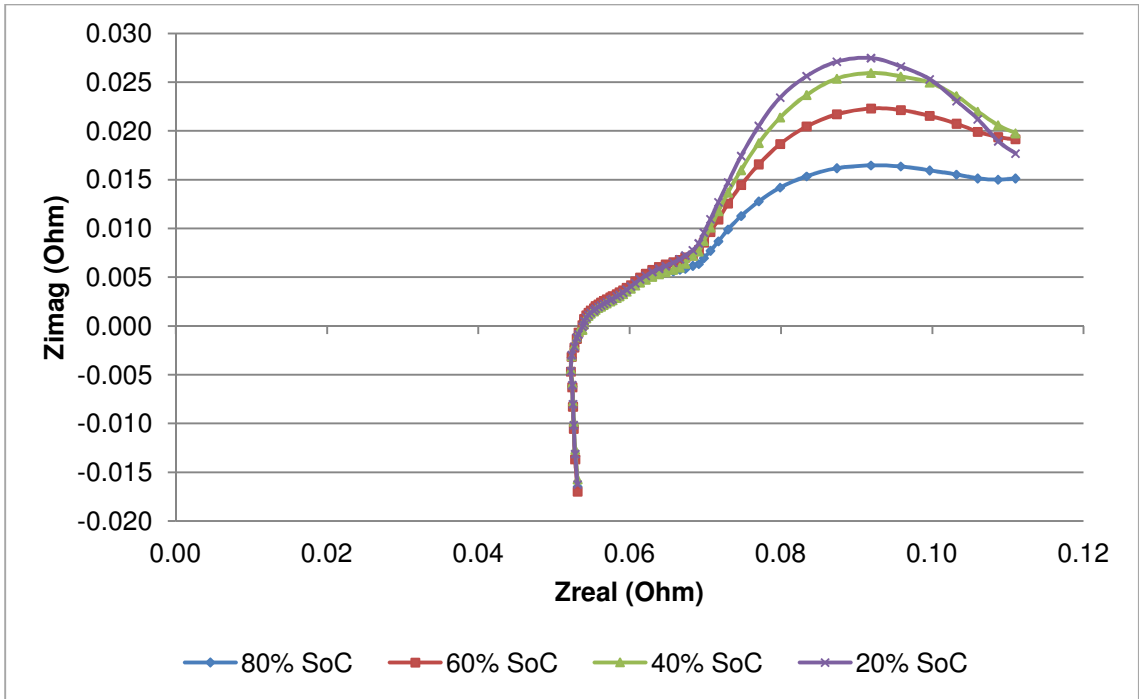


Figure 5.6. The EIS spectra of the cells and supercapacitors at different SoC.

Changes along the real impedance axis at zero imaginary impedance were due to the circuit resistance changes and are shown in Fig 5.7. The circuit resistance involved resistances due to sum of the resistances of the current collectors, the active material, electrolyte and the separator.

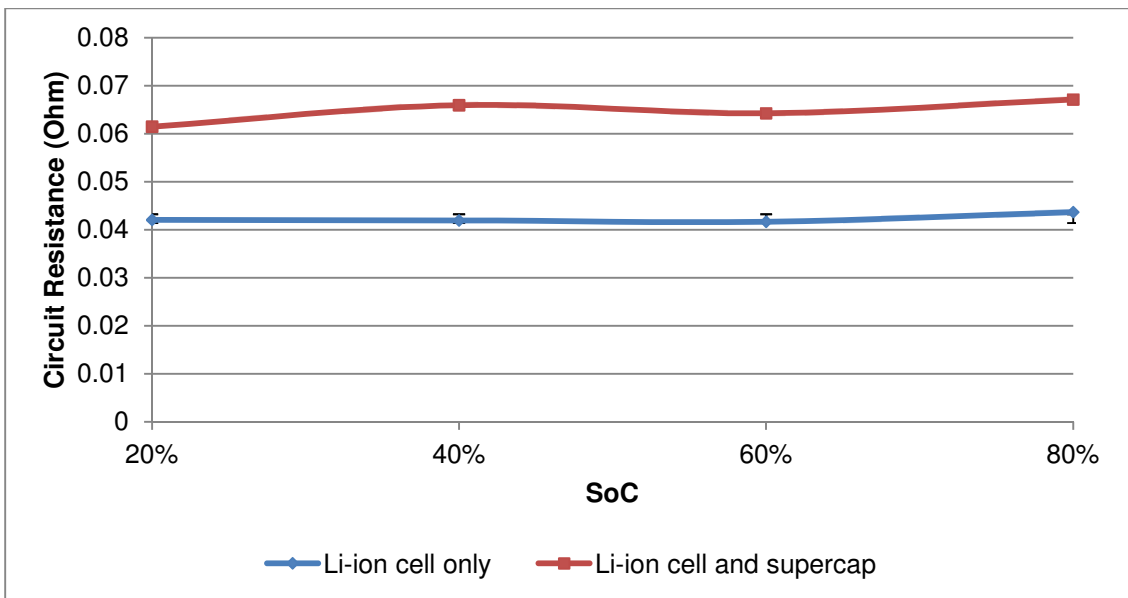


Figure 5.7. Resistance of the circuit at different SoC.

The EIS spectra of the circuit resistance showed that there were little or no differences between the analyses done at the different SoC. The system with the supercapacitor showed a slightly higher circuit resistance which could be mainly

attributed to the connectors and wiring. The results confirm that any differences observed between cells studied would not be due to the connectors and experimental setup.

There were notable comparable changes within the first semi-circle which corresponded to the resistance associated with the SEI that forms on the anode. There were also slight differences within the second semi-circle which corresponded to the resistance associated with the double layer capacity and charge transfer resistance at the electrodes (Fig 5.8 and 5.9).

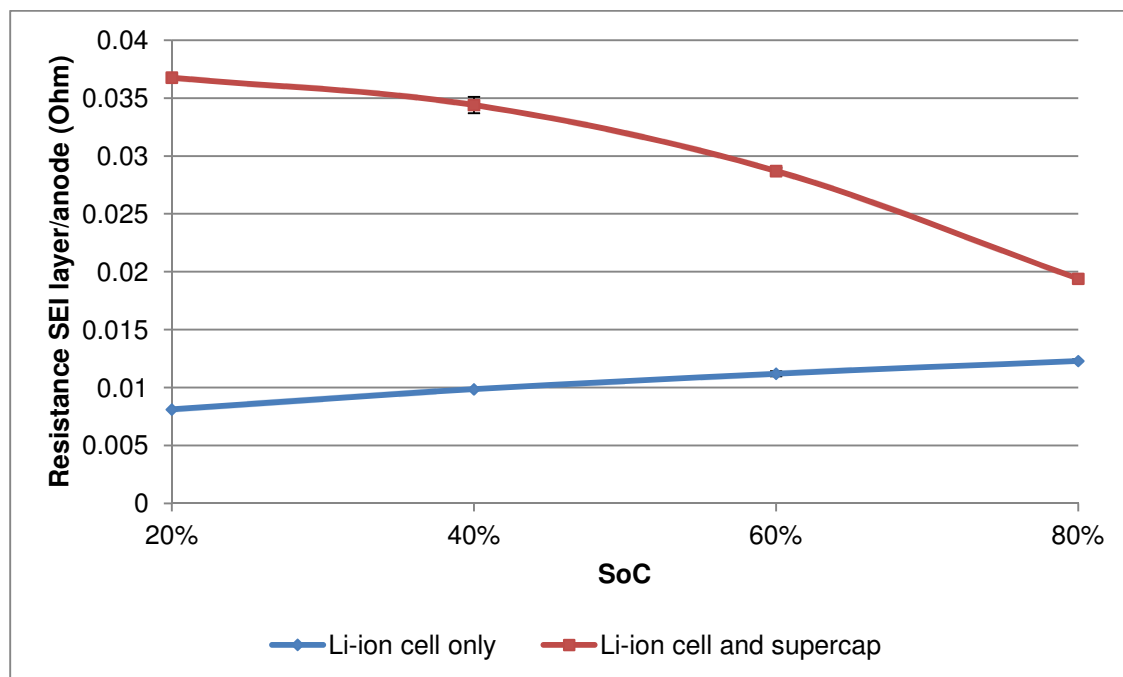


Figure 5.8. Resistance associated with the SEI at the anode at different SoC.

The resistance associated with the SEI layer at the anode was higher at all the SoC for the cells and supercapacitor than for the cells alone. With the resistance decreasing in value as the SoC increased for the combination consisting of the battery and supercapacitor. The opposite was true for the cell alone, i.e. where the resistance increased as the SoC increased. During charging, the resistance due to the cell alone seemed to have contributed higher than the resistance of the system consisting of both the cells and supercapacitors, as the trend is similar to the one seen in the capacity results, i.e. the capacity increased as the SoC increased. During discharging, the resistance of the system consisting of the cells and supercapacitor contributed more towards the decrease in capacity values as the SoC decreased. This implied that the partial resistance within the capacitor due to its low discharge state contributed significantly to this parameter.

The resistances associated with the double layer capacity and charge transfer resistance are shown in Figure 5.9.

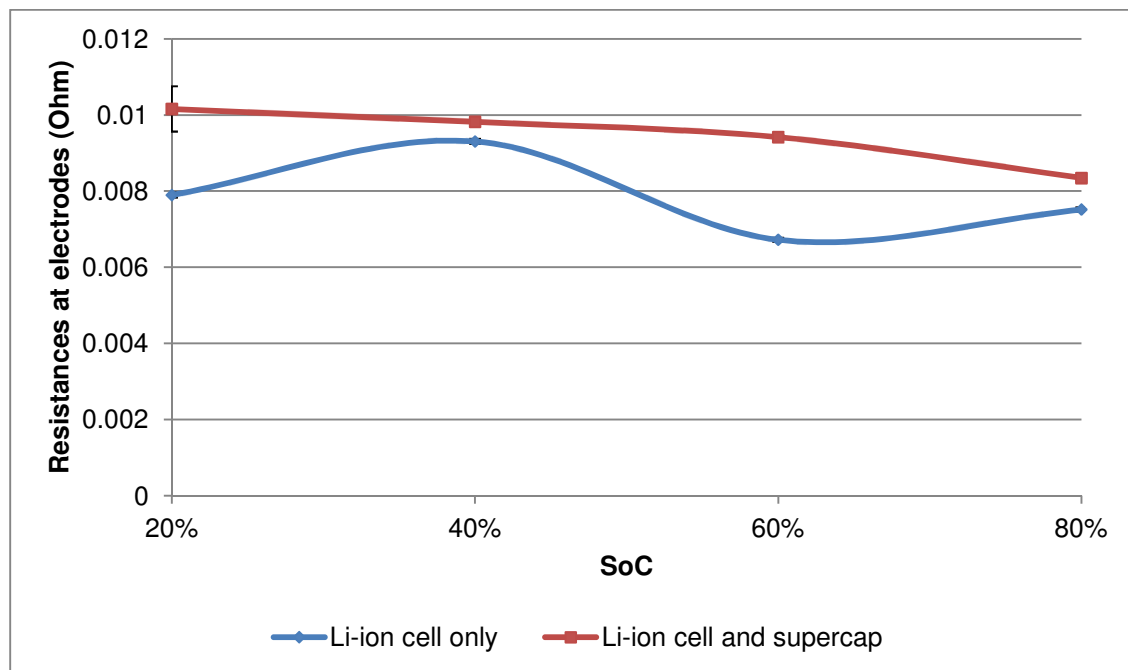


Figure 5.9. Resistance associated with the double layer capacity and charge transfer resistance at the electrodes at different SoC.

The resistances that are normally associated with the electrodes within a cell showed that for the system consisting of the cell and supercapacitor were again slightly higher than the cell alone. Hence, the contribution from the supercapacitor played a role in the overall resistance and a decrease in capacity. A higher resistance for the cell alone was seen at 40%, which is in agreement with the second semi-circle of the EIS spectra.

The resistance associated with the SEI layer at the anode played a larger role in the reduction of capacity at the different SoC as the resistance values were higher than the values observed with the resistance associate with the double layer capacity and charge transfer resistance at the electrodes. These resistance values would have had an influence on the small amount of additional capacity that the system of the cells and supercapacitor was able to accept or deliver in comparison to the cells alone.

The parameters in the model associated with the capacitance are shown in figure 5.10 and 5.11.

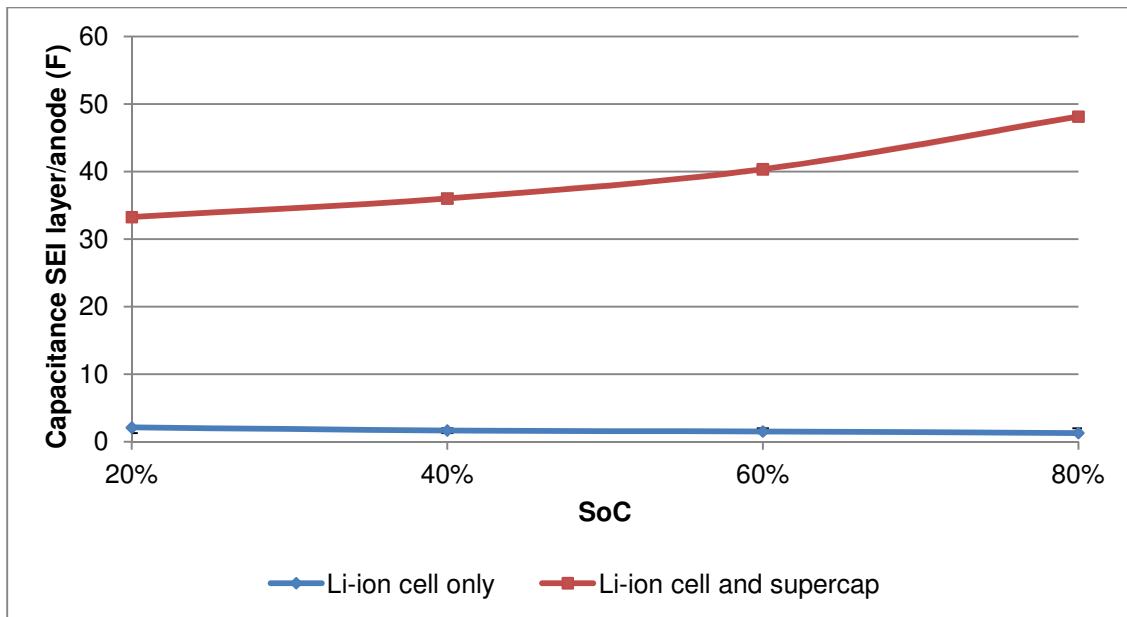


Figure 5.10. Capacitance associated with the SEI layer at the different SoC.

The results showed that the capacitance of the system consisting of the cell and supercapacitor was significantly higher than the cell alone for both the capacitance considered at the SEI layer and at the electrodes. The capacitance associated with the double layer capacity and charge transfer resistance of the system consisting of the Li-ion cell and the supercapacitor showed greater capacitance than the Li-ion cell alone. The capacitance considered at the SEI layer increased from 20% SoC to 80% SoC which was in agreement with the trend in increase in the cells high discharge rate tests. However, the capacity parameter (C2) that considered the capacitance at the electrodes (Fig 5.11) showed a slight decrease from 20 % to 80% SoC. A steady capacitance was seen for the Li-ion cell alone, while the capacitance for the system showed the highest values at 20% SoC.

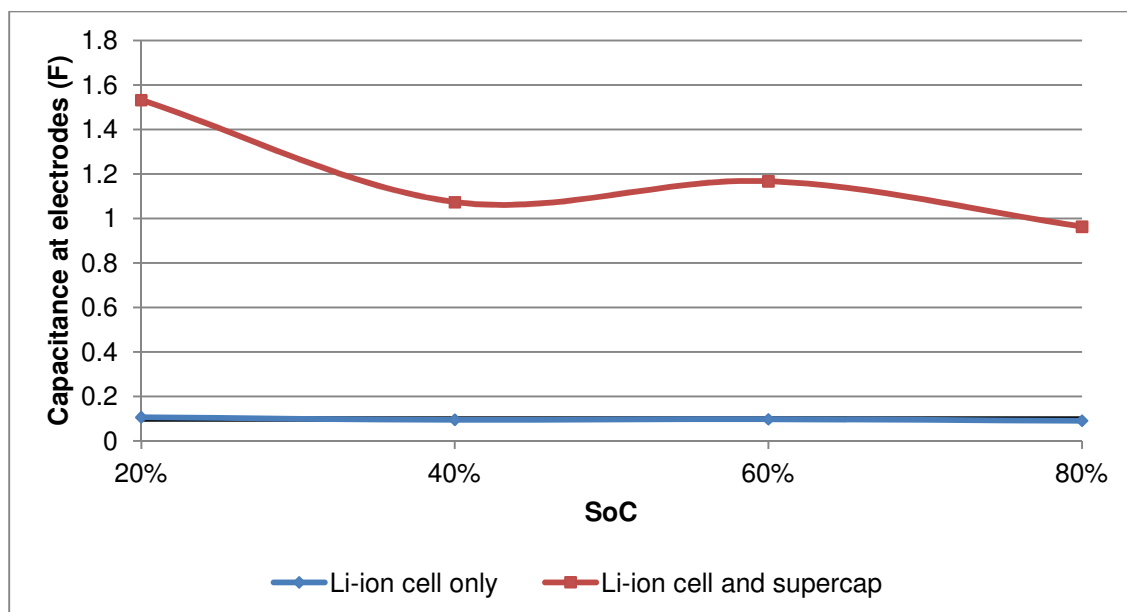


Figure 5.11. Capacitance associated with both electrodes at the different SoC.

During discharge the Li-ions are moved from the anode into the cathode. For the system consisting of the cell only, as the SEI layer influenced the movement of the ions, the resistance would be slightly larger at 80% SoC and become smaller as the SoC decreased (Fig 5.8) with minimal change in the cells capacitance. However the resistance associated with the SEI layer for the system consisting of both the cell and supercapacitor was comparatively higher at 20% SoC, and decreased as the SoC increased, with a notable increase in the SEI capacitance (Fig 5.10). Comparatively, the capacitance associated with the electrodes decreased as the SoC of the system increased. Hence, this implies that the charge was predominantly located at the SEI surface. This supports the observations that during the high rate discharge testing higher charge delivery was seen for the cells with capacitor at 80% SoC.

The Warburg impedance in the equivalent circuit model can be considered as a function that depends on the diffusing ability of the reactants especially at high frequencies, where these reactants don't have to diffuse too far through the Nernst diffusion layer and small impedance would be measured. At lower frequencies, the reactants have to diffuse further and larger impedance will be measured and on the EIS Nyquist plot, the tail end of the spectra would typically relate to the Warburg impedance⁸⁵. The Warburg impedance parameter was measured using the EIS model described in Fig 4.7 in $S.sec^{1/2}$. The results for the different cells at different SoC are shown in figure 5.12.

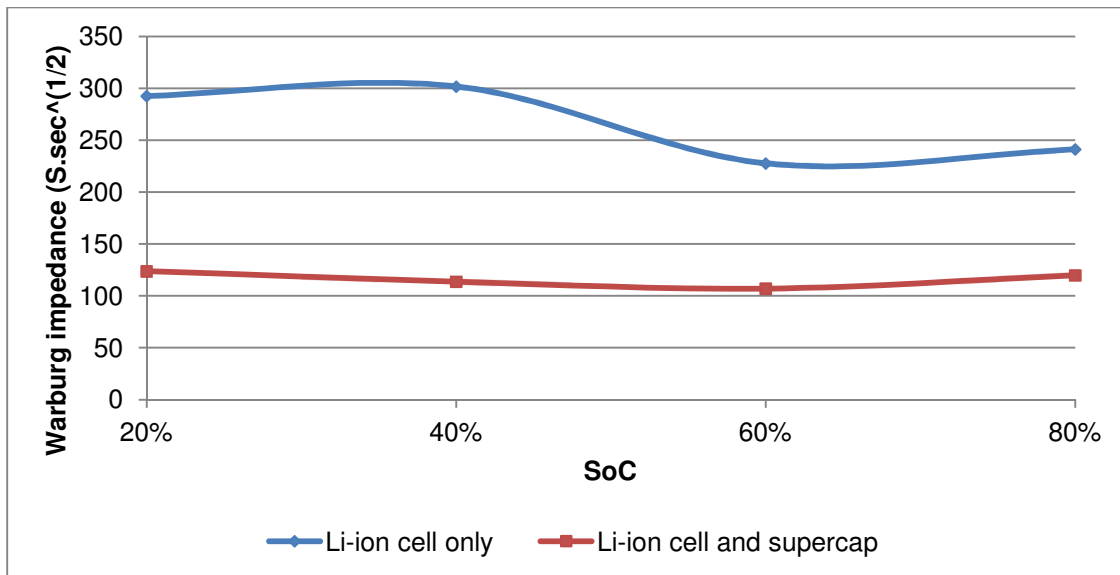


Figure 5.12. Warburg impedance at different SoC.

The results showed that the Warburg impedance parameter determined for the Li-ion cell only showed higher values than the system consisting of the Li-ion cell and supercapacitor. Capacitors have an imaginary impedance component, the current through a capacitor is phase shifted through -90 degrees with respect to the voltage. A capacitor in series to the cell would dominate the imaginary impedance component of the circuit⁹⁸. This would imply that the overall impedance for the system would be lower and a smaller Warburg constant would be seen. The slightly higher Warburg values at the lower SoC of the cell would only indicate that longer time periods for the reactants to diffuse through the Nernst Diffusion layer would be required.

5.2. 5.21Ah VRLA Pb-acid cell with two 10F supercapacitors

The comparison between the high rate charge of the Pb-acid cells alone against the system consisting of the Pb-acid cells together with the supercapacitors as per the test method can be seen in figure 5.13. The difference between initial maximum acceptance current and the total capacity over the 5 second charge is summarized in Table 5.3.

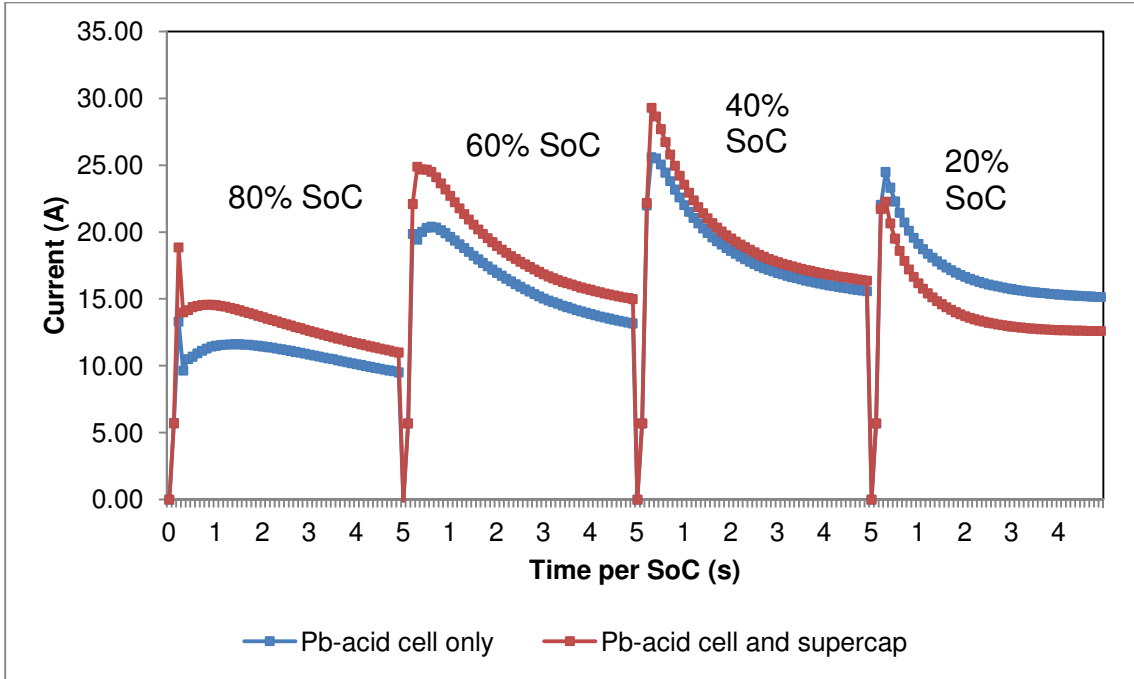


Figure 5.13. Comparison between the Pb-acid battery and the system of Pb-acid cells and supercapacitors using the high rate charge current.

SoC	Increase in Peak charge current (A)	Capacity over 5 second step (Ah) - Battery only	Capacity over 5 second step (Ah) - Battery and supercapacitor	Total comparative capacity increase (Ah)
80%	5.54 ± 0.01	0.73 ± 0.18	0.88 ± 0.04	0.15
60%	5.03 ± 0.01	1.10 ± 0.21	1.25 ± 0.01	0.15
40%	3.69 ± 0.01	1.25 ± 0.16	1.33 ± 0.05	0.08
20%	-1.94 ± 0.01	1.15 ± 0.03	0.97 ± 0.07	-0.18

Table 5.3. The initial increase in current (A) at each SoC and the total comparative capacity increase at each SoC over the 5 second high rate charge.

The results showed that at a maximum peak charging current, with a decrease in SoC, the current that the system could accept was shown to decrease. A slight decrease in the capacitance at the various SoC was observed. However, at the 20% SoC, the battery alone was able to accept more current and charge capacitance than the system consisting of the battery and supercapacitors over this 5 second charge step. At different SoC, the internal resistance of a VRLA Pb-acid cell will have an effect on the charge acceptance and delivery. At a 20% SoC, the internal resistance was reported as high by a paper published by Paul Bentley et al⁹⁹ (Fig 5.14):

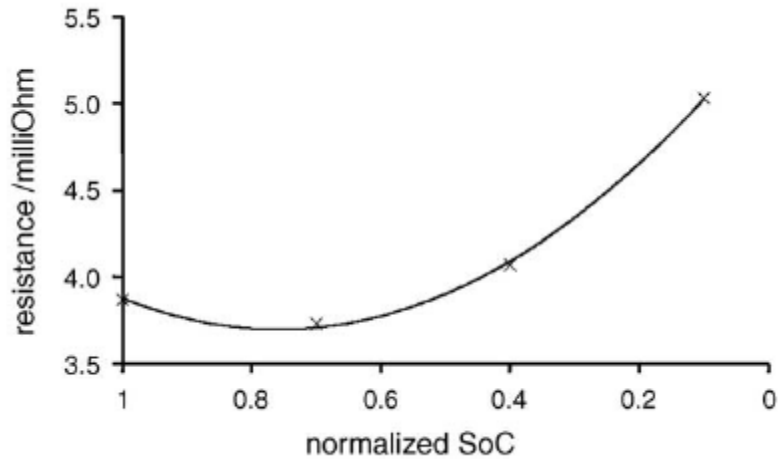


Figure 5.14. Variation of Pb-Acid cell internal resistance with normalized SoC⁹⁹.

The highly sulphated electrodes at the 20% SoC would have a higher internal cell resistance that would result in a lower charge acceptance than the cell that was connected to a set of supercapacitors. An unusual phenomenon was repeatedly observed implying that the resistance of the combined battery and supercapacitor was comparatively higher than the battery at the 20% SoC only. The comparison between the Pb-acid battery alone and the system consisting of the Pb-acid battery and supercapacitors at a high rate discharge was done and shown in Fig 5.15. The difference between initial maximum delivery current and the total capacity over the 10 second discharge are summarized in Table 5.4.

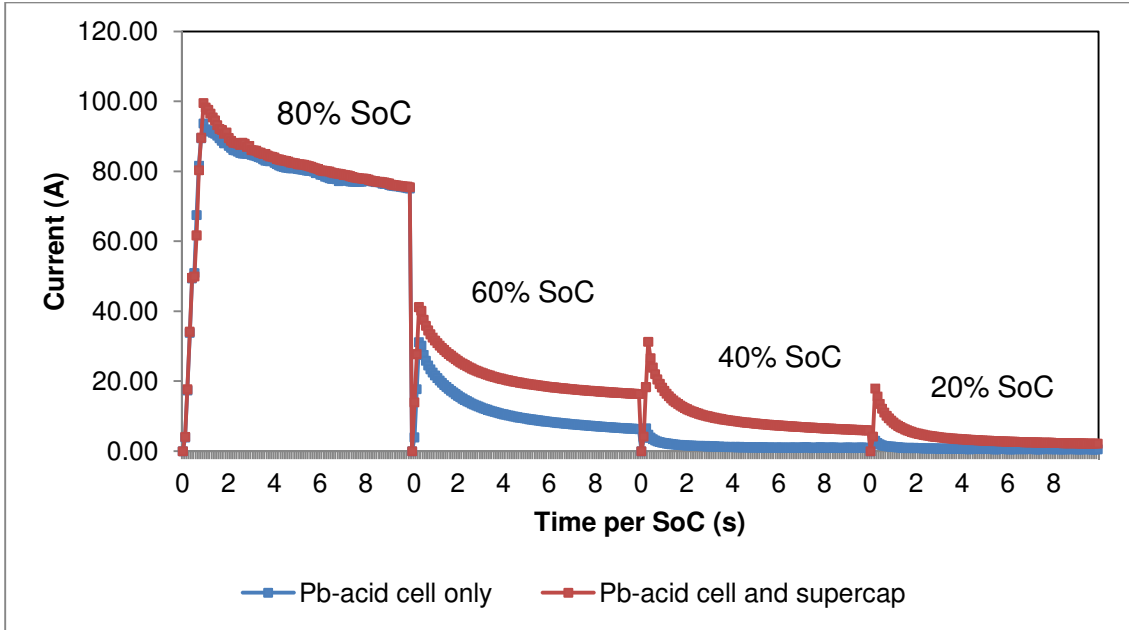


Figure 5.15. Comparison between the Pb-acid battery alone against the system consisting of Pb-acid battery and supercapacitors using the high rate discharge current.

SoC	Increase in peak discharge current (A)	Capacity over 10 second step (Ah) - Battery only	Capacity over 10 second step (Ah) - Battery and supercapacitor	Total comparative capacity increase (Ah)
80%	5.85 ± 0.01	21.62 ± 0.02	22.00 ± 0.01	0.38
60%	10.00 ± 0.01	3.15 ± 0.12	5.90 ± 0.12	2.75
40%	24.69 ± 0.01	0.41 ± 0.01	2.65 ± 0.13	2.24
20%	14.40 ± 0.01	0.23 ± 0.01	1.14 ± 0.06	0.91

Table 5.4 The initial increase in current (A) at each SoC and the total comparative capacity increase at each SoC over the 10 second high rate discharge.

The results showed that at 60% and 40% SoC, a significant improvement in the discharge capacity could be delivered when compared to the discharge ability at 80% and 20% SoC respectively. Notably the maximum peak discharge current increased as the SoC decreased, except at 20% SoC. This could be due to the increase in internal resistance of the battery and supercapacitors.

Electrochemical Impedance Spectroscopy (EIS) analyses were done on both the battery alone and the system consisting of the battery and the supercapacitor. For comparative reasons, the same equivalent circuit model (Fig 4.7) was used for this test of analysis. However Pb-acid battery does not build SEI layers at the electrodes. There are surface changes due to sulfation, the crystallization of lead sulfate which will have an effect on both the resistance and capacitance of the battery. The sizes

of the surfaces include the active materials absorbing sulfate from the acid within the cell¹⁰⁰.

The EIS spectra of the battery alone at different states of charge are shown in Fig 5.16. For the system consisting of the battery and the supercapacitors and is represented in Fig 5.17.

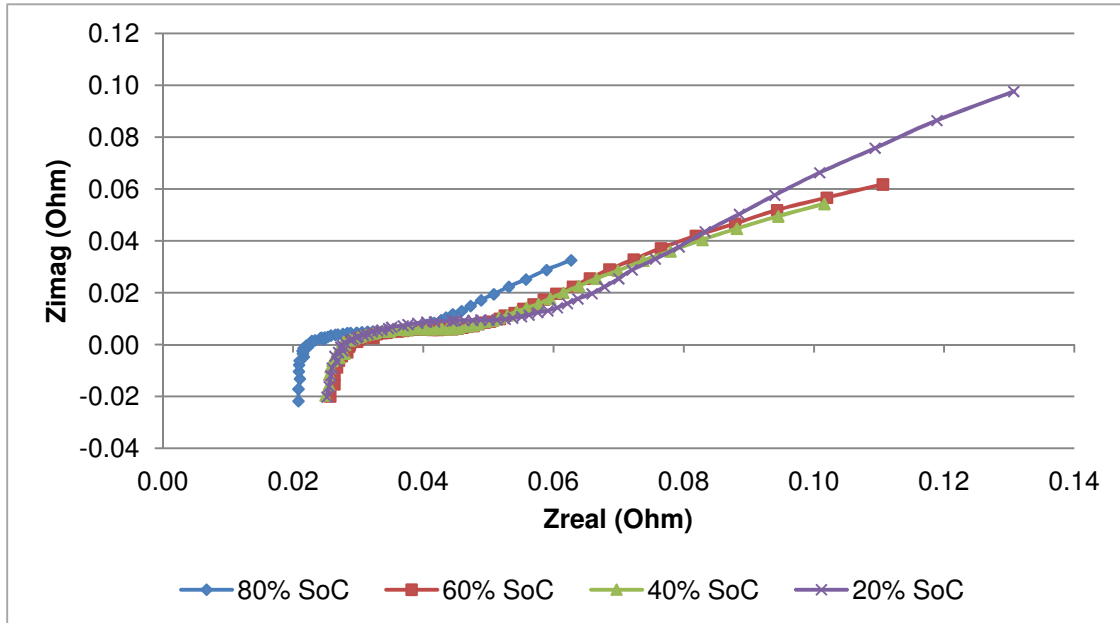


Figure 5.16. The EIS spectra of the battery at different SoC.

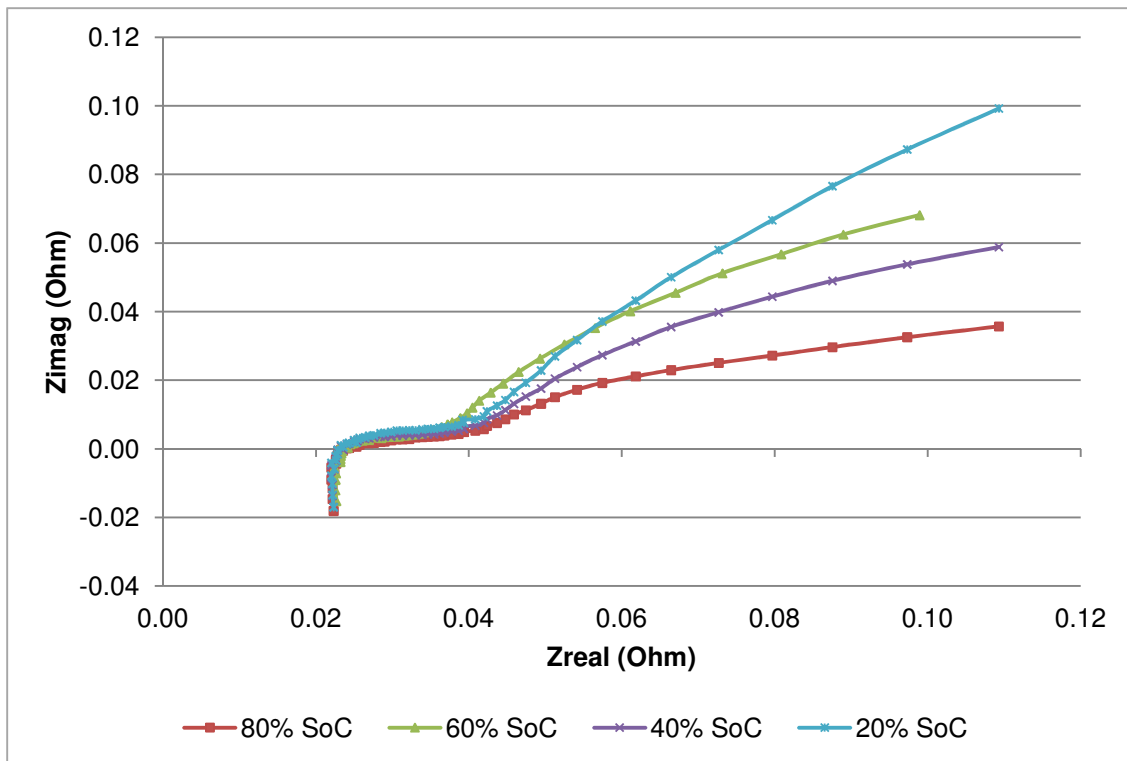


Figure 5.17. The EIS spectra of the battery and supercapacitors at different SoC.

The areas of resistance and capacitance were modelled on the EIS spectra obtained from both the cell only and the system consisting of the battery and supercapacitor.

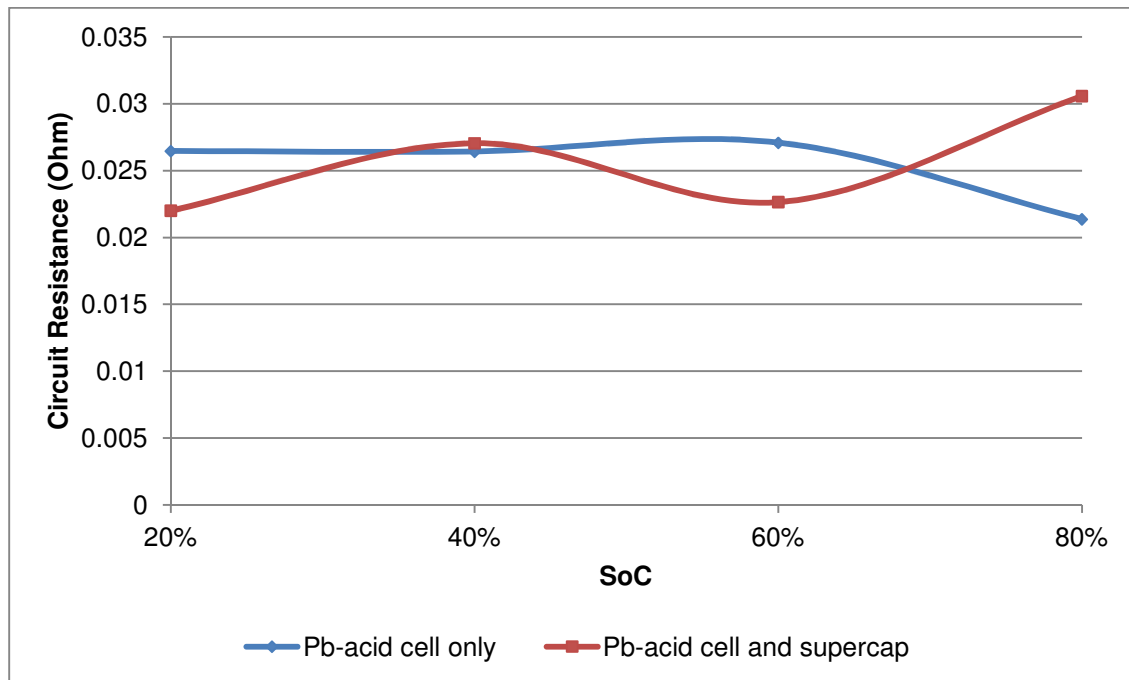


Figure 5.18. Resistance of circuit at different SoC.

The results showed that for the Pb-acid battery with and without a capacitor at different SoC, that there was little variation between the circuit resistance. This implies that there were very little differences observed between cells studied due to the connectors and experimental setup.

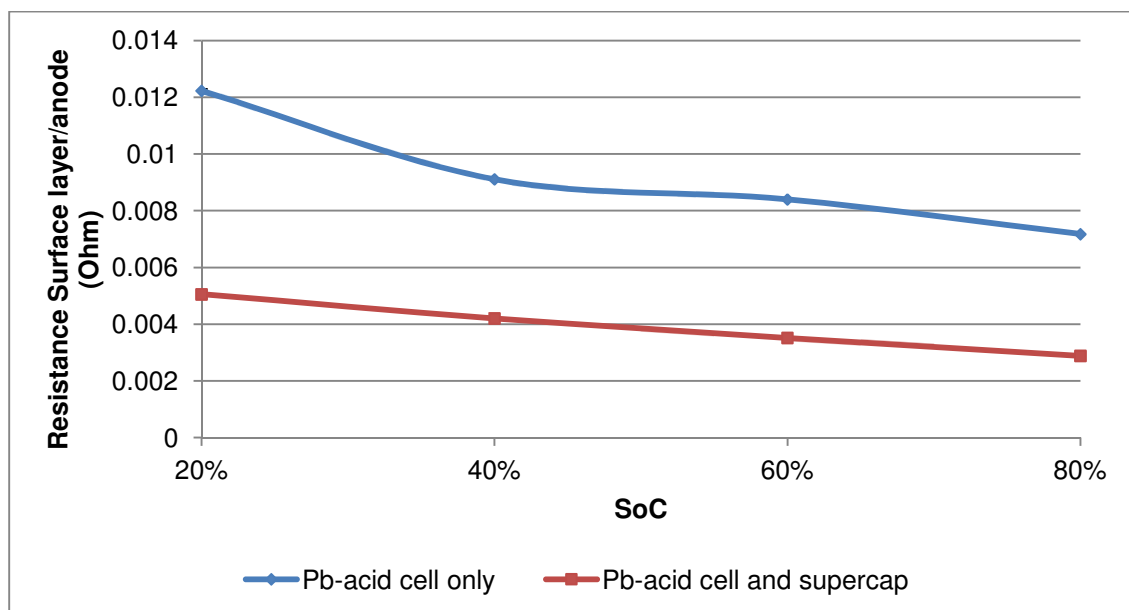


Figure 5.19. Resistance associated with the surface layer at the anode at different SoC.

The resistance contribution associated with the surface layer at the anode was significantly higher at 20% SoC for the battery only when compared to the system combination of battery and supercapacitor. The associated resistance with a capacitor in series was lower and in comparison different to the results observed for the Li-ion cells (Fig 5.10). The surface resistance on the anode at low SoC would occur due to the formation of a predominantly insulating layer of PbSO_4 .

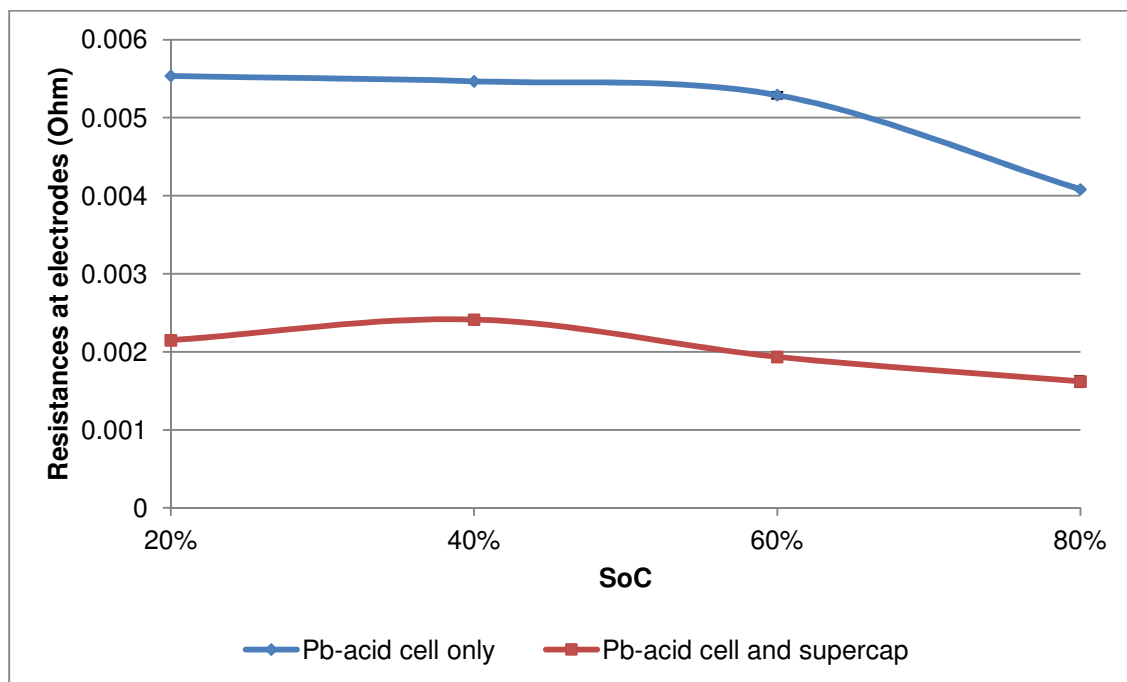


Figure 5.20. Resistance associated with the double layer capacity and charge transfer resistance at both electrodes at the different SoC.

A similar trend was observed for the parameter that considers the resistance at electrodes. The contribution of the resistance associated with the double layer capacity and charge transfer resistance at both electrodes was the highest at 20% SoC, with a small decrease in resistance at 80% SoC. The resistances for the battery with the supercapacitor were comparatively similar across the various SoC and lower than the battery only. Overall the resistance values associated with the surface layer at the anode contributed the most to the overall resistance of the system to the resistance associated with the double layer capacity and charge transfer resistance at the electrodes.

In considering the capacitance of the surface layer (EIS parameter C1) (Fig 5.21) and at the electrodes (EIS parameter C2) (Fig 5.22), a considerable increase in capacitance value was observed for the cell at 80% SoC. Notably, the cell with the

capacitor had a significantly higher capacitance value at 80% SoC than the cell without the capacitor.

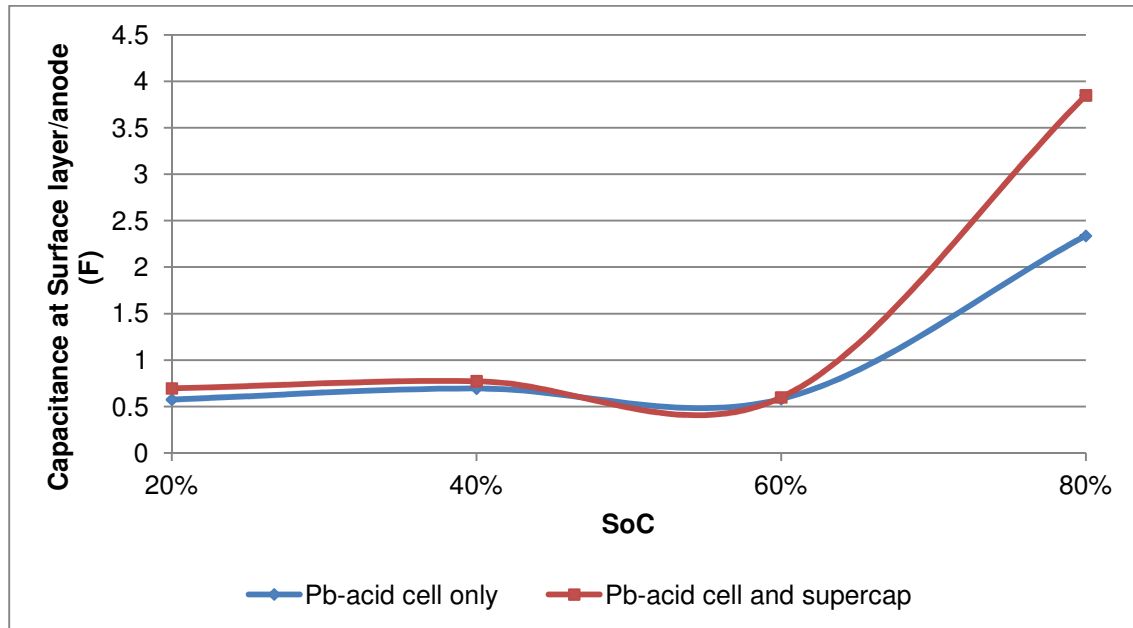


Figure 5.21. Capacitance associated with the surface layer at the anode at different SoC.

For the capacitance at the electrodes, the values were slightly larger for the cell with the capacitor than the ones without the capacitor.

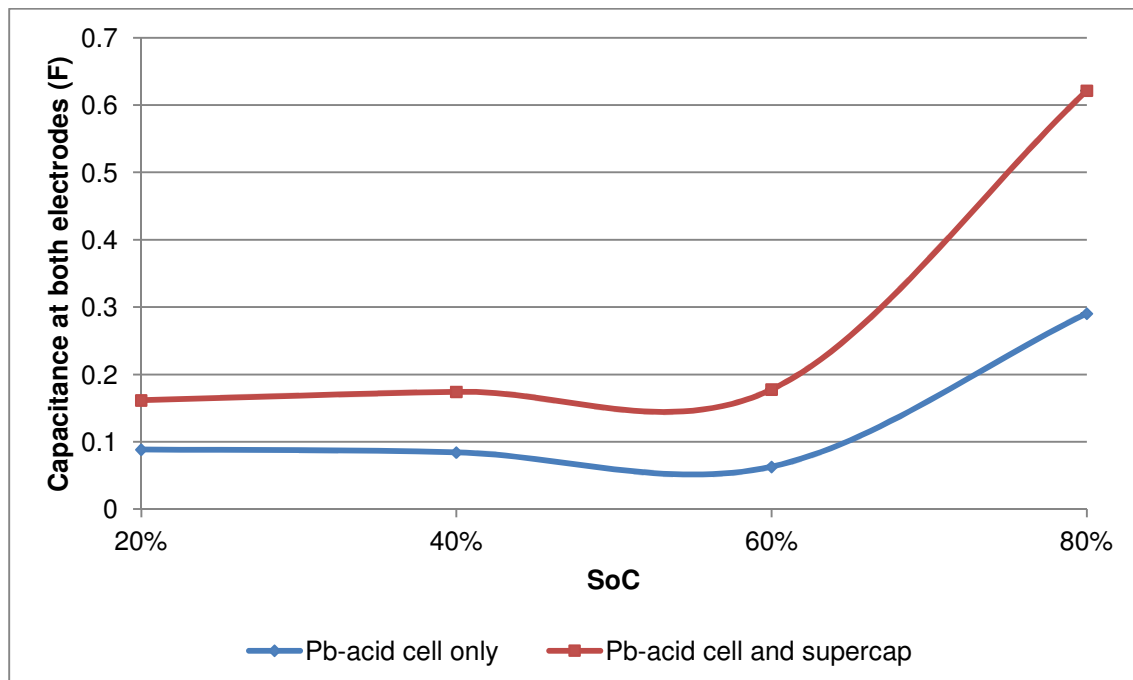


Figure 5.22. Capacitance associated with the double layer capacity and charge transfer resistance at both electrodes at different SoC.

From the results it was seen that the combination with the supercapacitors allowed the system to have a slightly higher capacitance associated with the surface layer at the anode. For both types of capacitance the values were similar for 20%, 40% and 60% SoC and higher values were seen for the capacitance at 80% SoC.

The Warburg impedance of the battery only and with a capacitor is shown in Figure 5.23.

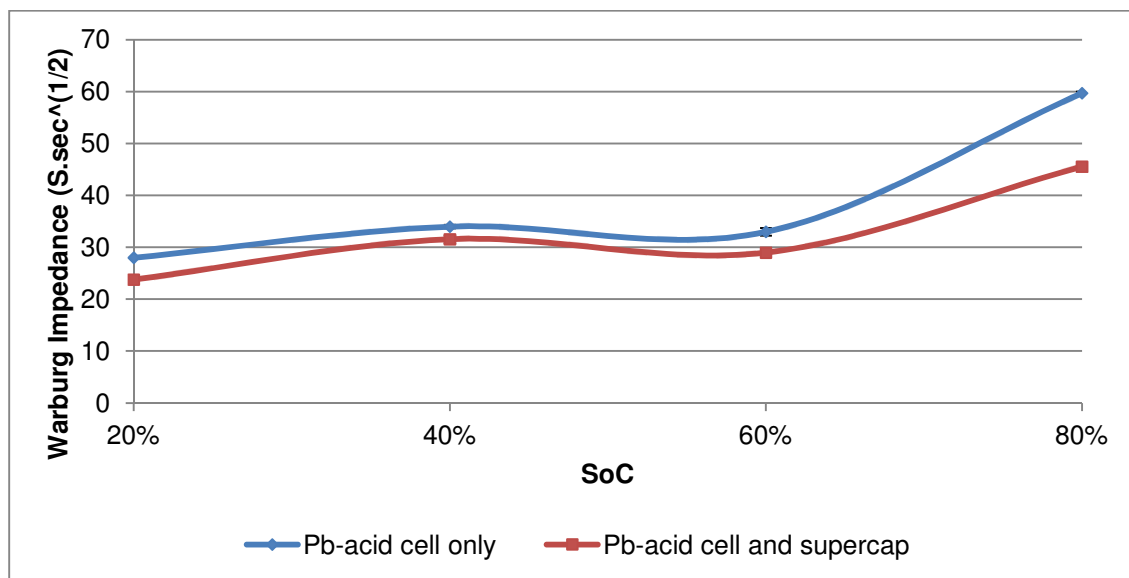


Figure 5.23. Warburg impedance at different SoC.

The Warburg effect trends were similar for both systems, with the battery showing slightly higher values at the different SoC. Notably, the cell at 80% SoC showed the highest value implying that it showed a slightly higher ability for the charge delivery to occur. The lower values for the battery and supercapacitor combination would indicate the influence of the Warburg effect by the supercapacitor, which was also seen on the Li-ion cell Warburg effect results. As mentioned with the Li-ion cell, the supercapacitor has only an imaginary impedance component and thus reduced the overall impedance of the system. The lower Warburg impedances values correlate with the 20%, 40% and 60% SoC tests that show a lower charge delivery during the high rate discharge steps.

The comparison between the capacity (Ah) of the battery alone against the system consisting of the battery and supercapacitors showed that the system was able to deliver more current at each SoC over the 10 second discharge step. The total comparative capacity increased from the 80% SoC to the 60% and 40% SoC. These results were different to the work published in the paper by M. Fernández et al⁷³; they showed a consistent increase in both charge acceptance and discharge at all

comparative SoC (Fig 5.24 & 5.25). Their graphical results from the article are shown for discussion purposes.

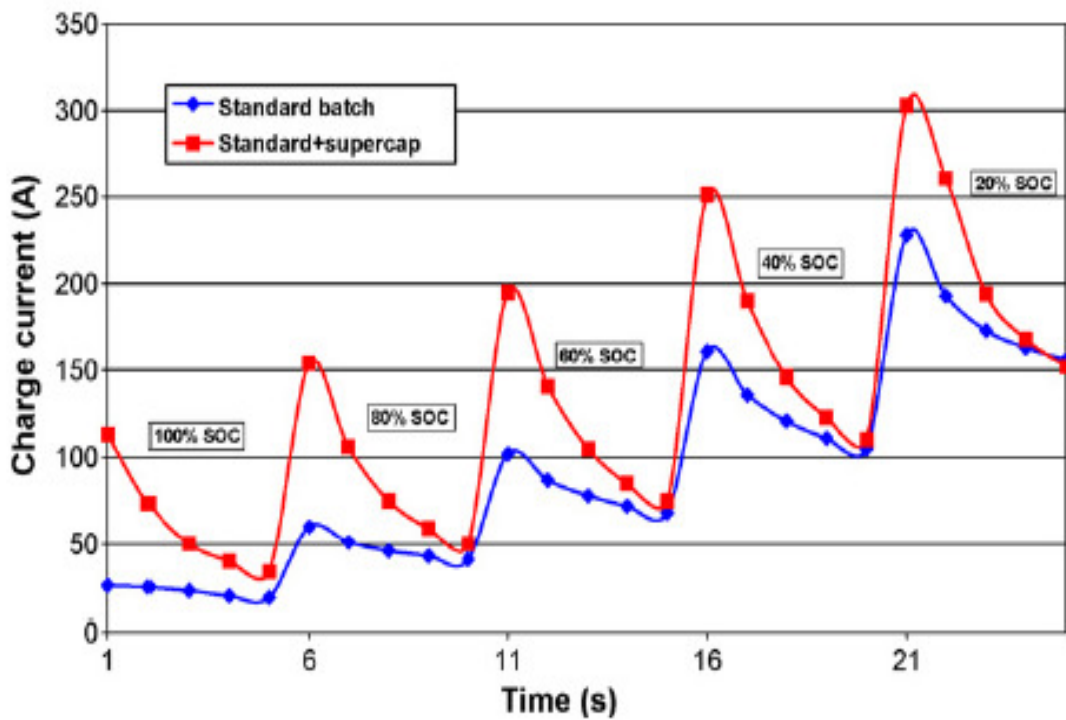


Figure 5.24. 6V/24 Ah battery + supercapacitor. Charge acceptance power, 8V, 5s 25 °C⁷³.

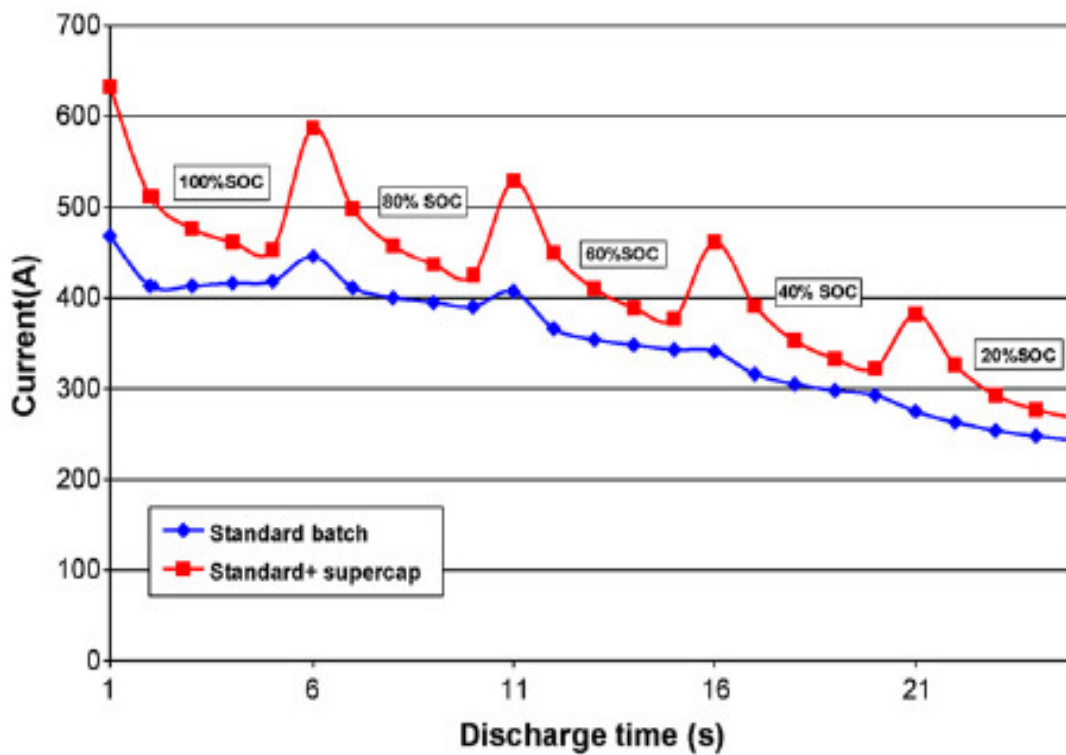


Figure 5.25. 6V/24 Ah battery + supercapacitor. Discharge power, 5V, 10s 25 °C⁷³.

The reasons for the very different results could be due to a slightly different test procedure being done. Very little information was given in the paper as to the exact testing parameters used. This study procedure was based primarily on the graphical representations of their results assuming that the accurate SoC represented in the graph are their true values. In this study, the cells were always recharged and subsequently discharged to the exact SoC before commencing with the testing. The results in the article could infer that the different SoC were achieved sequentially without a recharge step as shown in the x-axis of the total discharge time. A notable difference was the fact that the study was done on a 4 V battery system, whereas the article considered a 12 V battery. Different-sized Pb-acid cells were used this test (5.21 Ah) compared to the Pb-acid battery in the paper (24Ah). A VRLA Pb-acid cell was used in this study. In this study, the battery and the system consisting of the battery and supercapacitor was fully charged after each high rate charge or high rate discharge. This may not be the case in the paper as it is seen at 100% SoC the battery alone is still able to accept charge during the high rate charge step. At all SoC, it was seen in the paper that a consistent increase in charge acceptance or charge delivery of about 100A for the system consisting of the battery and supercapacitor and internal resistance seems to have had no effect. In this study, internal resistance in both the battery and the combination of the battery and supercapacitor was seen. This internal resistance had an effect on the charge acceptance or charge delivery.

Some important points should be considered between the two different battery type systems (Li-ion and Pb-acid cells) with and without supercapacitors:

- The VRLA Pb-acid battery can be discharged to a lower voltage limit of 3.3V. For the Li-ion cell the voltage limit was 3.0V.
- The VRLA Pb-acid cell can be charged at a higher voltage limit of 5.0V with limited damage to its internal chemistry. The Li-ion cell was limited in its charge voltage to 4.2V and could not be exceeded due to possible damage to its internal chemistry.

5.3. 1Ah Li-ion pouch cell with two 3.3F supercapacitors

The comparison between the high rate charge of the Li-ion cell alone against the system consisting of the Li-ion cell together with the supercapacitors can be seen in figure 5.26. The difference between initial maximum acceptance current and the total capacity over the 5 second charge is summarized in Table 5.5.

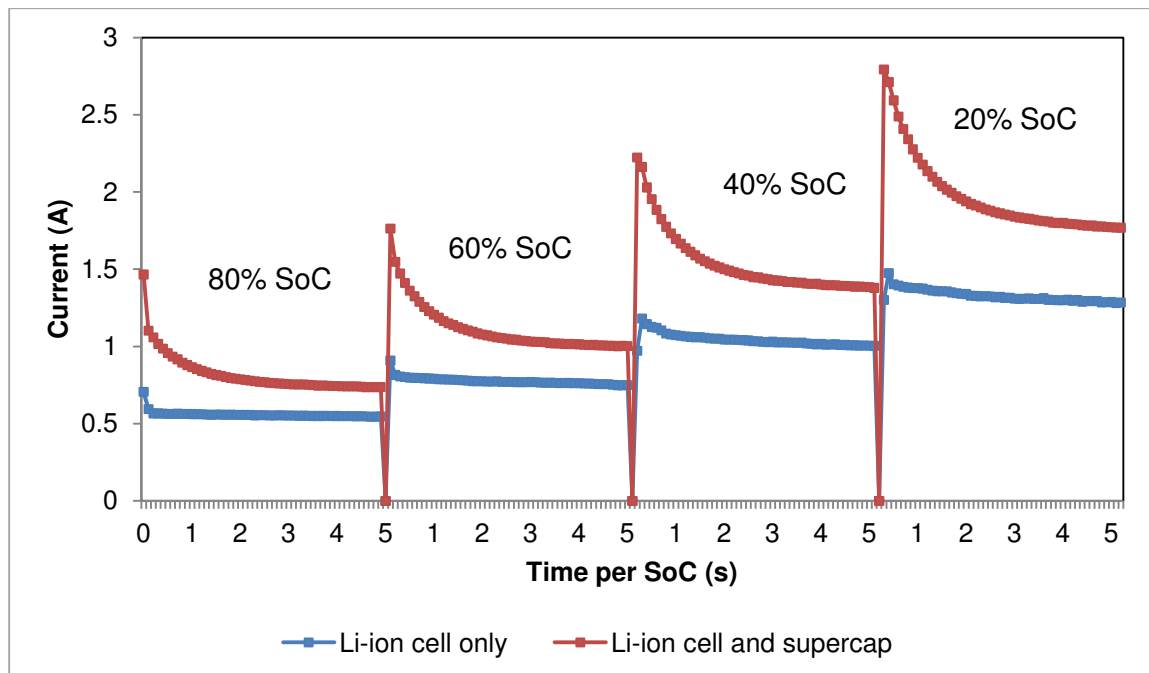


Figure 5.26. Comparison between the Li-ion cell and the system of Li-ion cells and supercapacitors using the high rate charge current.

SoC	Increase in peak charge current (A)	Capacity over 5 second step (Ah) - Battery only	Capacity over 5 second step (Ah) - Battery and supercapacitor	Total comparative capacity increase (Ah)
80%	0.76 ± 0.01	0.04 ± 0.01	0.06 ± 0.01	0.02
60%	0.86 ± 0.01	0.05 ± 0.01	0.08 ± 0.01	0.03
40%	1.04 ± 0.01	0.07 ± 0.01	0.11 ± 0.01	0.04
20%	1.32 ± 0.01	0.09 ± 0.01	0.14 ± 0.01	0.05

Table 5.5. The initial increase in current (A) at each SoC and the total comparative capacity increase at each SoC over the 5 second high rate charge.

The results showed that there was an improvement in the maximum peak current that the system could accept at the various SoC of the battery. Notably the maximum peak increased with a decrease in the SoC. When a comparison was made at each SoC in capacity (Ah), the system consisting of the battery and supercapacitor was

able to accept more charge over the 5 second step. There was a steady increase in total comparative capacity increase as the SoC decreased over all the SoC.

The comparison between the Li-ion cell alone and the system consisting of the Li-ion cell and supercapacitors at a high rate discharge was also carried out can be seen in figure 5.27. The difference between initial maximum delivery current and the total capacity over the 10 second discharge is summarized in Table 5.6.

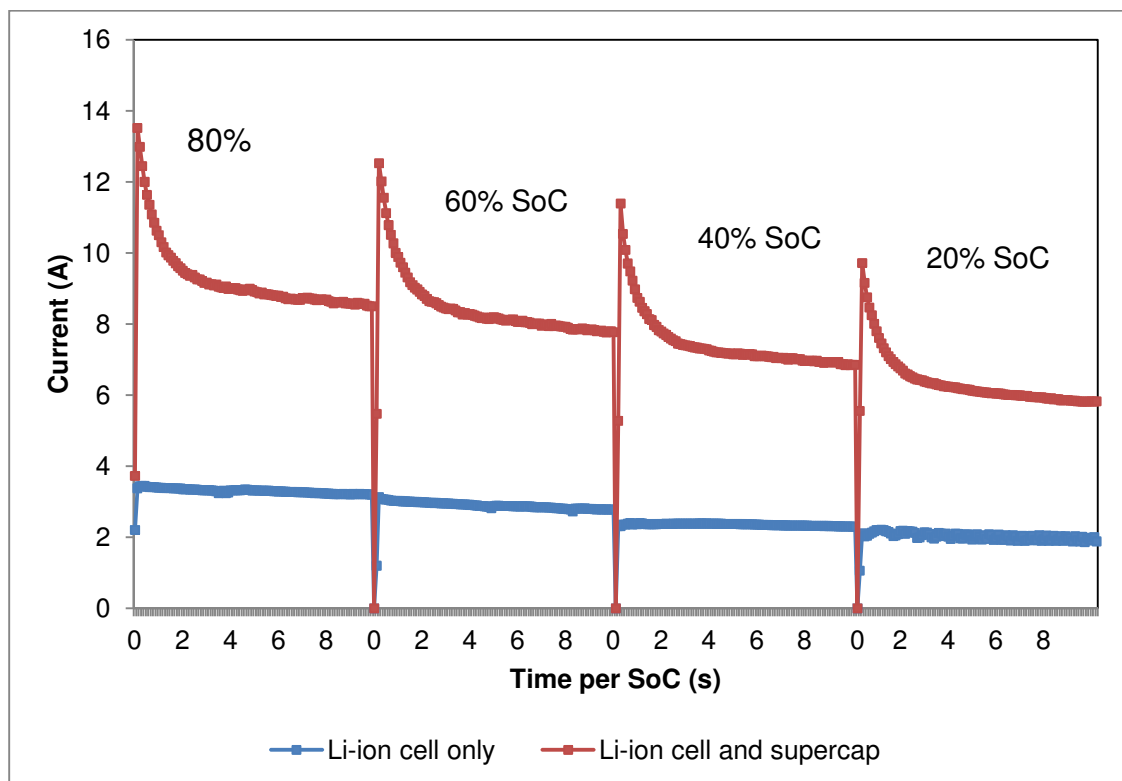


Figure 5.27. Comparison between the Li-ion cell alone against the system consisting of Li-ion cell and supercapacitors using the high rate discharge current.

SoC	Increase in peak discharge current (A)	Capacity over 10 second step (Ah) - Battery only	Capacity over 10 second step (Ah) - Battery and supercapacitor	Total comparative capacity increase (Ah)
80%	10.07 ± 0.01	0.91 ± 0.02	2.55 ± 0.02	1.64
60%	9.39 ± 0.01	0.8 ± 0.03	2.35 ± 0.02	1.55
40%	9.01 ± 0.01	0.65 ± 0.04	2.06 ± 0.02	1.41
20%	7.60 ± 0.01	0.56 ± 0.04	1.77 ± 0.02	1.21

Table 5.6. The initial increase in current (A) at each SoC and the total comparative capacity increase at each SoC over the 10 second high rate discharge.

The results showed that as the SoC decreased the total amount of discharge capacity that could be delivered decreased. Notably the maximum peak discharge current decreased as the SoC decreased.

The cathode cell chemistry used for this cell was LiMn_2O_4 . The material has the advantages of being of relatively low cost, thermally more stable and has relatively good rate capabilities due to its three-dimensional framework structure¹⁰¹. In most cases, a high charge rate is limited in a battery by the solid-state diffusion of the Li-ions into the bulk of the active mass particles¹⁰². The smaller resistance of a Li-ion battery having the Manganese chemistry seems to have an effect on the overall system consisting of the battery and supercapacitors. This will allow for even greater charge acceptance and delivery. A fairly consistent increase in charge acceptance and delivery was seen over all the SoC.

Electrochemical Impedance Spectroscopy (EIS) analyses were done on both the cell alone and the system consisting of the cell and the supercapacitor and the Nyquist plots are shown in figure 5.28 and 5.29.

The EIS spectra of the cell alone are shown in Fig 5.28.

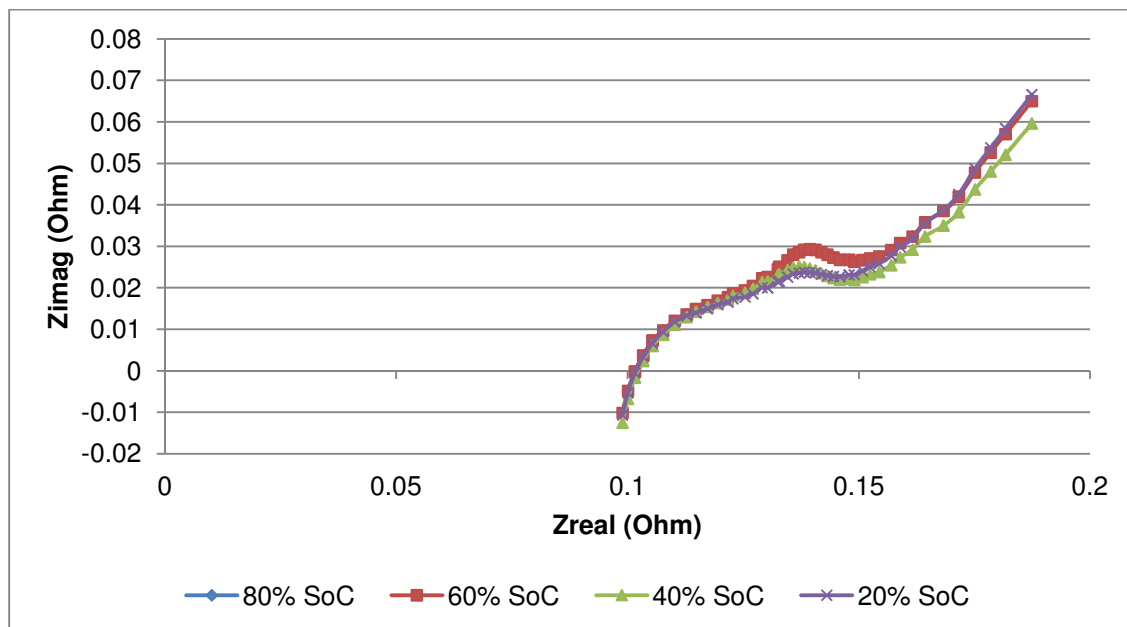


Figure 5.28. The EIS spectra of the cell at different SoC.

The EIS spectra of the system consisting of the cell and the supercapacitors are shown in Fig 5.29.

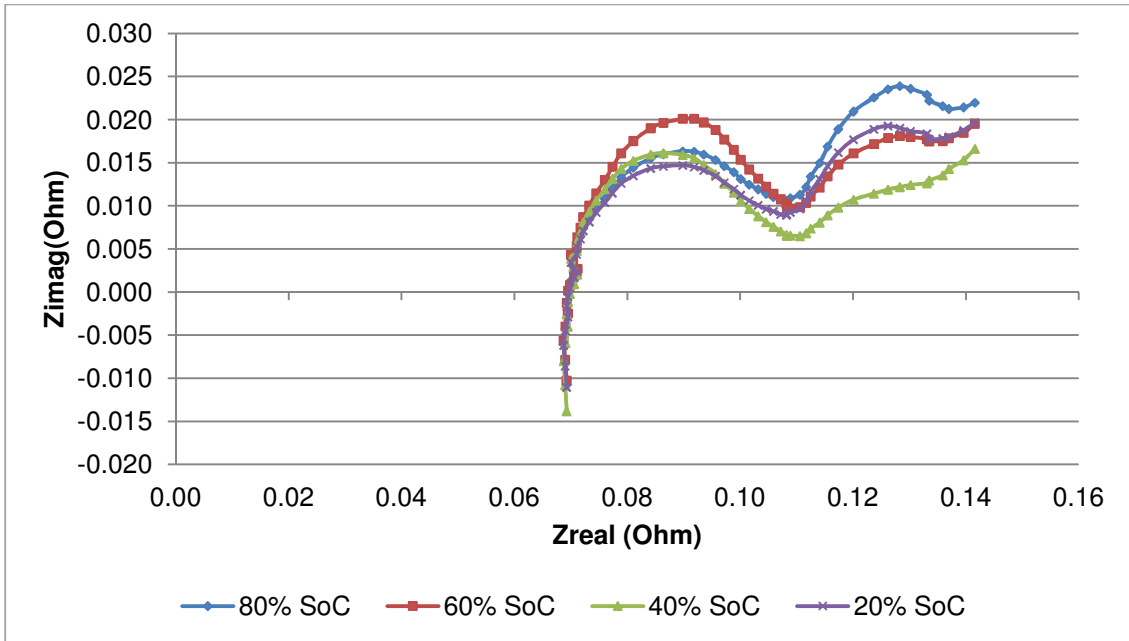


Figure 5.29. The EIS spectra of the cell and supercapacitors at different SoC.

Various parameters of the EIS model were examined in order to explain the differences seen in the EIS spectra.

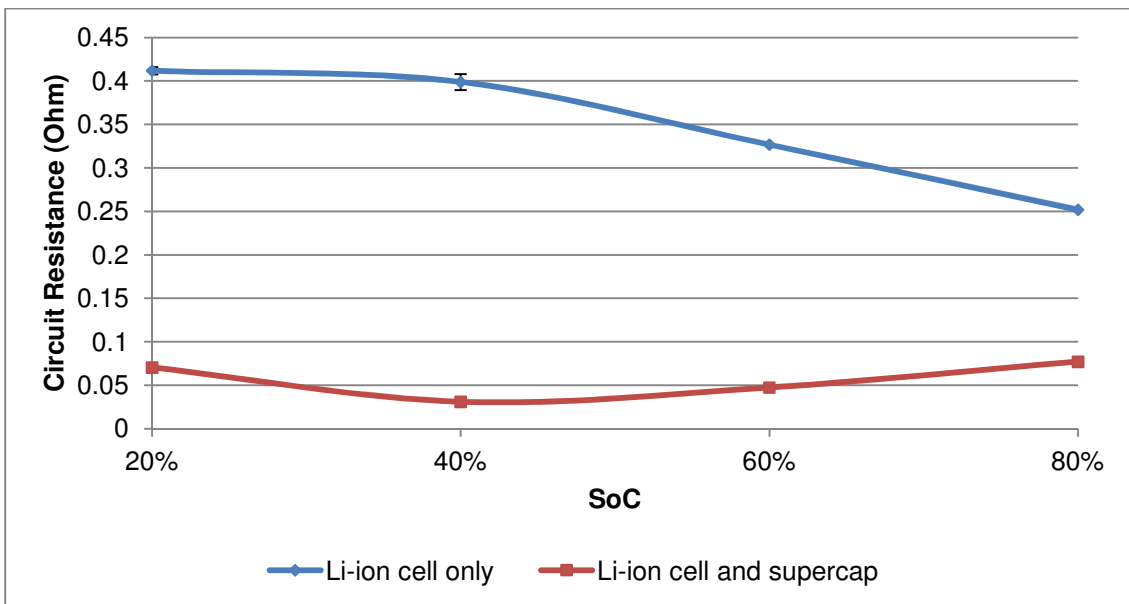


Figure 5.30. Circuit resistance at different SoC.

Both EIS spectra showed small changes in the circuit resistance. The cell alone showed a slightly higher circuit resistance which was in agreement with the EIS spectra seen in Fig 5.28 where the spectra start at a higher Zreal value.

There were small changes within the first semi-circle which correspond to the resistance associated with the SEI that forms on the anode.

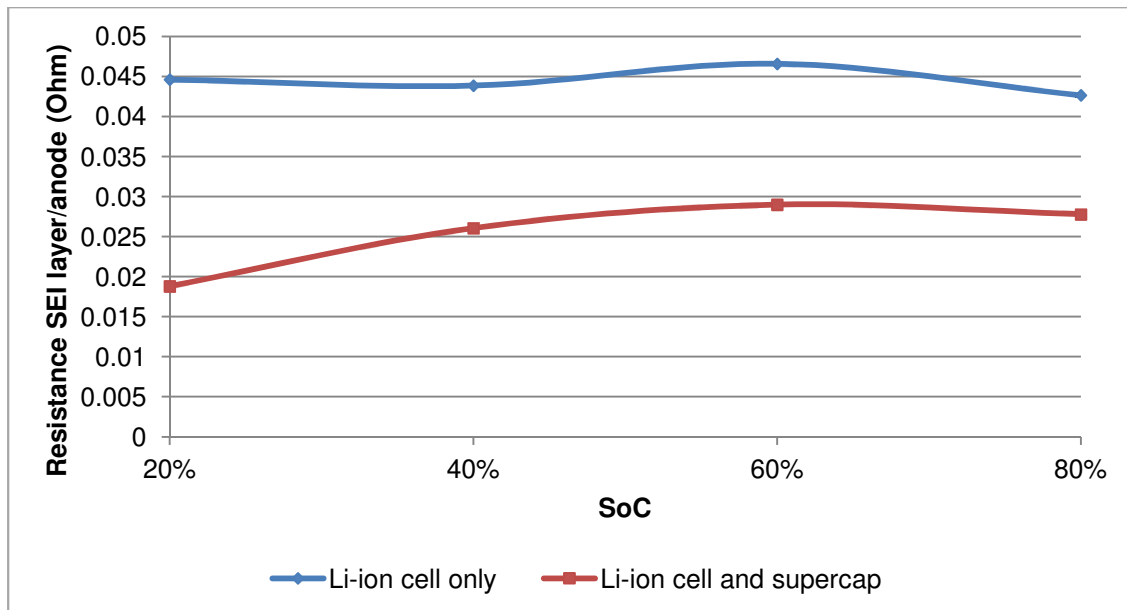


Figure 5.31. Resistance associated with the SEI layer at the anode at the different SoC.

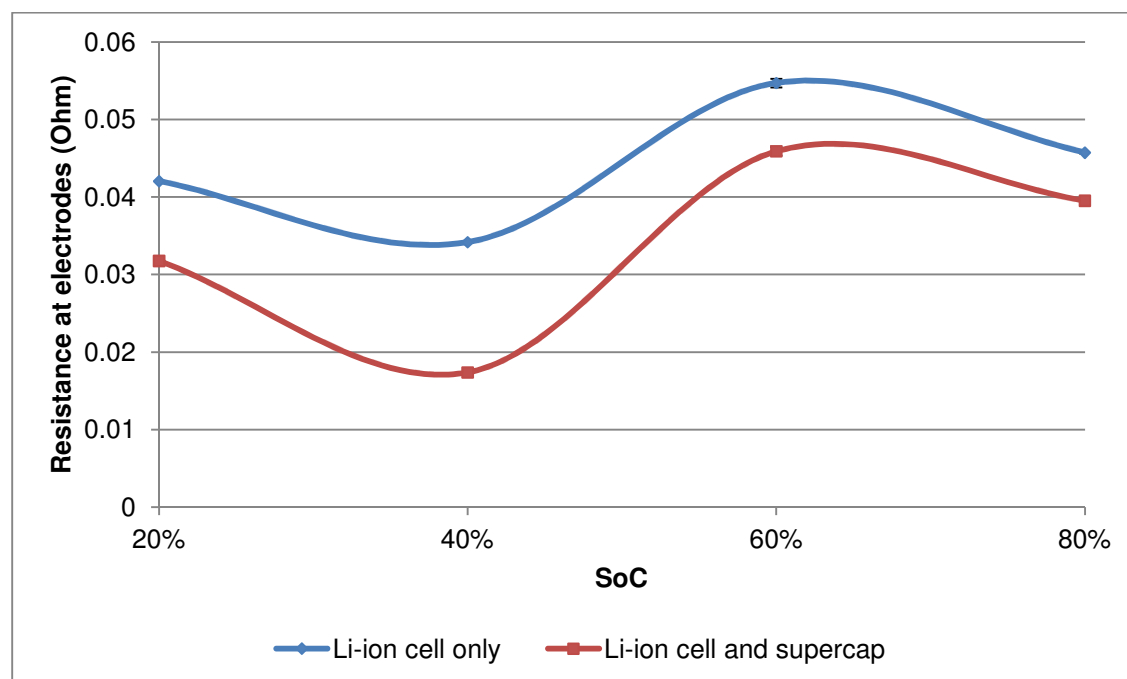


Figure 5.32. Resistance associated with the double layer capacity and charge transfer resistance at the electrodes at different SoC.

The resistance associated with the SEI layer at the anode of the system of the cell only showed higher values than the system consisting of the cell and supercapacitor. The resistances associated with the double layer capacity and charge transfer resistance at the electrodes for the cell only also showed higher values than the system consisting of the cell and supercapacitor. These resistances could have an effect on the amount of charge delivery and acceptance during the testing, whereby

the resistance of the cell only could have hindered the charge delivery and acceptance.

The capacitance associated with the SEI layer at the anode and the capacitance associated with the double layer capacity and charge transfer resistance was measured.

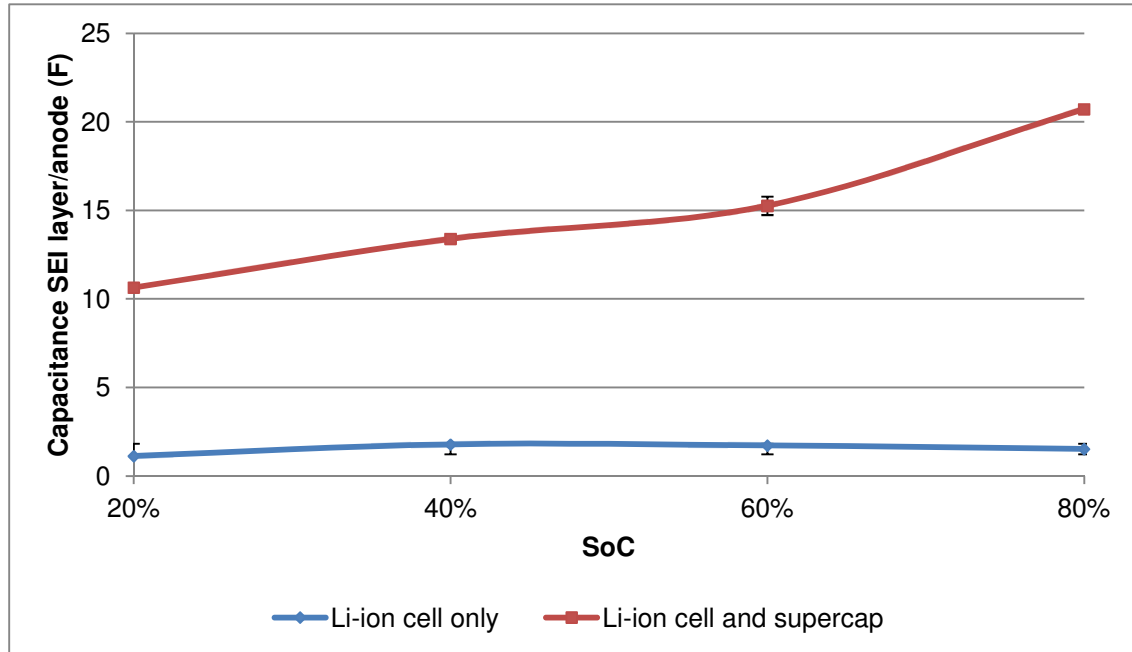


Figure 5.33. Capacitance associated with the SEI layer at the anode at the different SoC.

The capacitance of the system consisting of the cell and supercapacitor was higher than the cell alone. The capacitance increased from 20% SoC to 80% SoC which is in agreement with the trend in increase in capacitance during the high discharge rate tests.

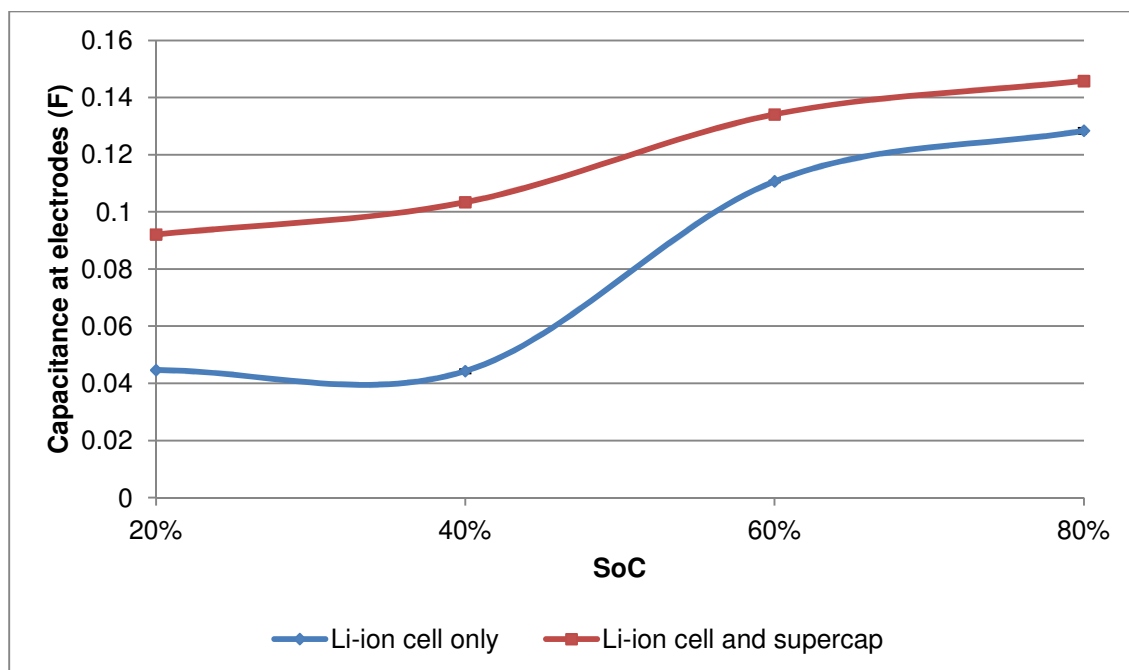


Figure 5.34. Capacitance associated with both electrodes at the different SoC.

Once again the capacitance of the system consisting of the Li-ion cell and the supercapacitor showed greater capacitance than the Li-ion cell alone. However the capacitance values associated with both electrodes was smaller than the values of capacitance associated with the SEI layer. A steady capacitance was seen for the Li-ion cell alone, while the capacitance for the system showed the highest values at 80% SoC.

Both the resistances and capacitances associated with the SEI layer at the anode over the different SoC showed the largest values when compared to the resistances and capacitances associated with both the electrodes. These resistances and capacitance trends were different to the trends seen with the 2Ah cylindrical cells. These differences could be the reason why so much extra charge acceptance and delivery was seen for the 1Ah pouch cell over the 2Ah cylindrical cell. Increases in capacitance and decreases in resistance of the 1Ah pouch cell over the 2Ah cylindrical cell could be due to the chemistry within the cell and/or the geometry of the cell.

The Warburg impedance was measured on both systems.

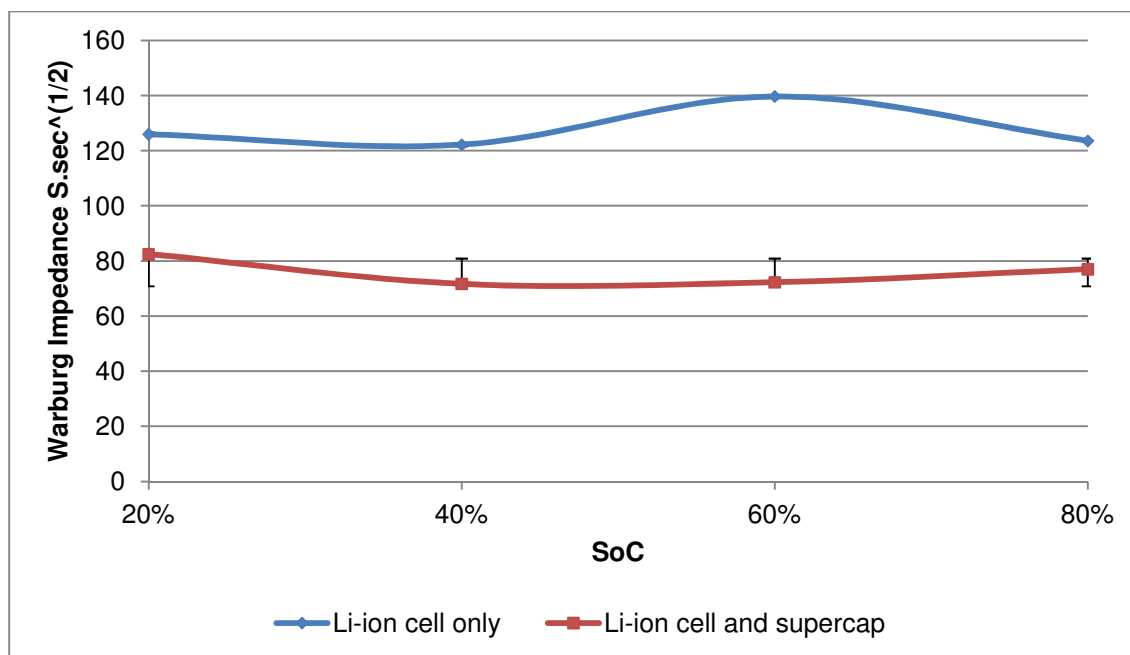


Figure 5.35. Warburg impedance at different SoC.

There was a marked increase in values in the Warburg effect of the system of the cell only against the system consisting of the cell and supercapacitor. Once again the impedance due to the capacitors played a role in reducing the Warburg impedance of the system.

The resistances associated with the electrodes and the SEI layer at the anode was higher for the cell alone when compared to the system consisting of the cell and the supercapacitor. These resistances played a role in the high charge acceptance and charge delivery and the higher combination of resistances for the cell alone resulted in there being significant increases in charge acceptance and delivery for the system consisting of the cell and supercapacitors.

5.4. 20Ah Li-ion pouch cell

A 20Ah pouch Li-ion cell was also tested for charge acceptance and discharge ability at different SoC. However the maximum charge or discharge rate available was 200A. As the cell would have required more than 200A for the cell alone, the study did not consider the cells with a supercapacitor (Fig 5.36 and 5.37).

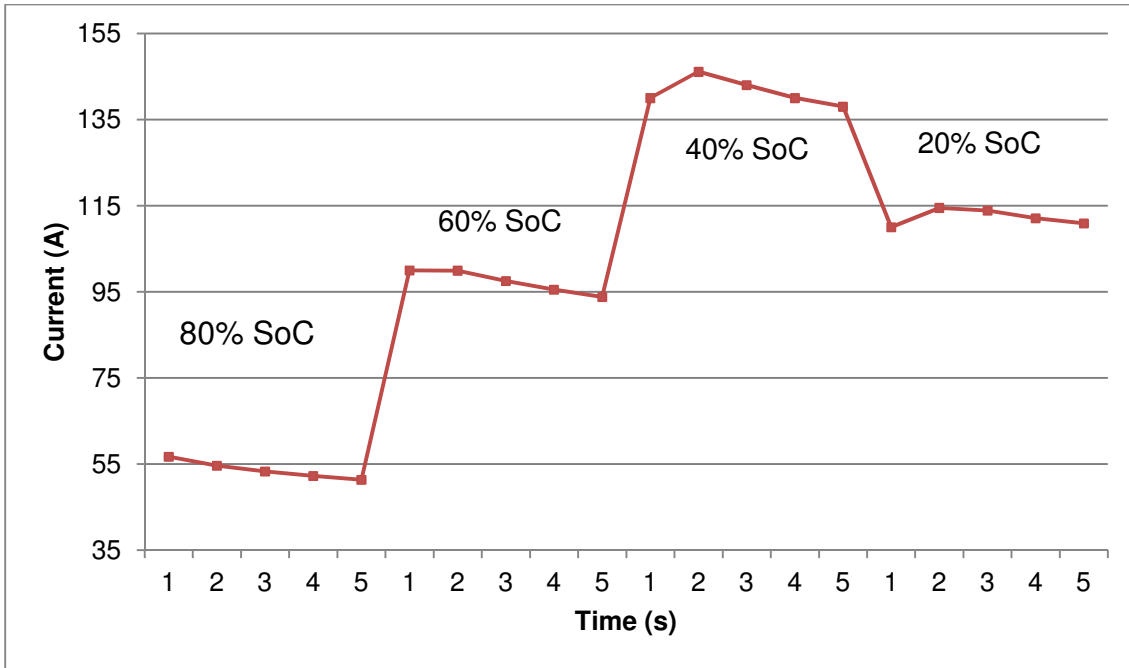


Figure 5.36: 20Ah Li-ion pouch cell showing the charge acceptance at different SoC.

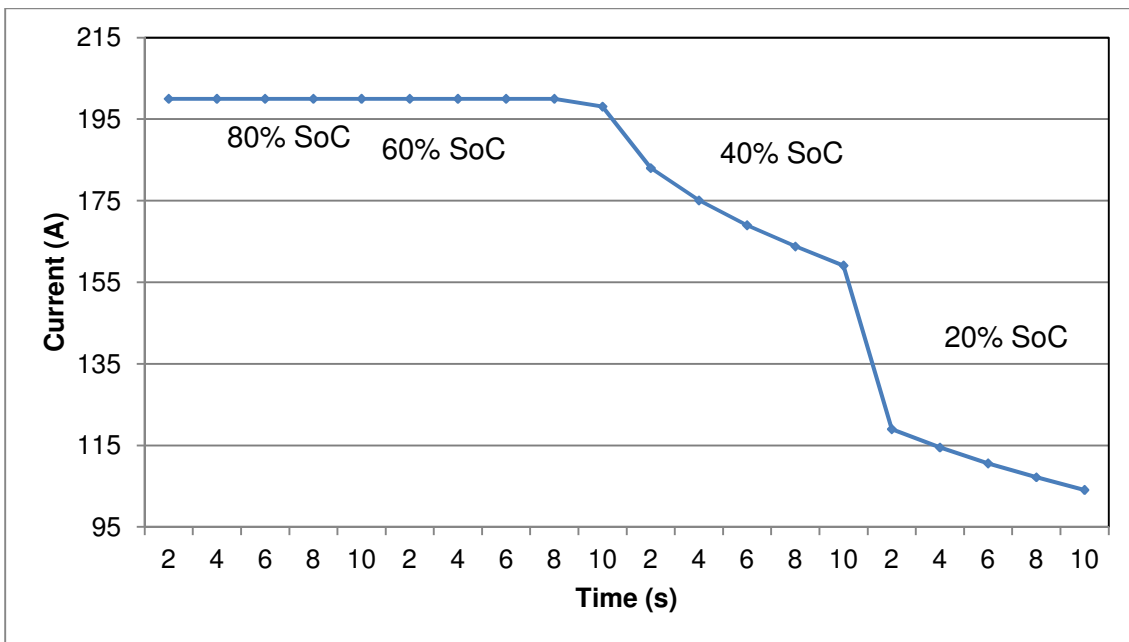


Figure 5.37: 20Ah Li-ion pouch cell showing the discharge delivery at different SoC.

The results showed that the 20Ah pouch cell current discharge was limited to the available current limits on the Battery Tester and there were safety concerns about the large amount of heat build-up observed at the electrode tab connections on the pouch cell. In order for these tests to be completed, better thermal management of the tab connectors with high power battery testing equipment would be required.

Observations made during these tests:

The results of the study showed that by placing a suitable sized supercapacitor in parallel with a battery such as a Li-ion or Pb-acid can improve the charge acceptance of the system during regenerative braking. Different Li-ion chemistries have an influence on the charge acceptance and delivery when the Li-ion cells are connected to the supercapacitors. At low SoC Pb-acid cells have a marked increase in internal resistance. This internal resistance seems to have an effect at low SoC on the charge acceptance and delivery. A small influence from the internal resistance of the Pb-acid cell on the charge delivery at 80% SoC was seen. EIS analysis was also carried out on all the cells and the combination of battery and supercapacitors. The EIS analysis was used to explain the charge acceptance and charge delivery at the different SoC.

Overall it was seen that the 1Ah Li-ion pouch cell was able to accept additional charge of about 31% at each SoC and deliver additional charge of 66% at each SoC when the cell was connected to the supercapacitors. The 2Ah Li-ion cylindrical cell was only able to accept additional charge of between 5 and 15% over the different SoC when connected to the supercapacitors. It was able to deliver additional charge of between 7 and 14% over the different SoC when connected to the supercapacitors. The 5.21Ah Pb-acid battery connected to the supercapacitors was able to accept additional charge of between 5 and 17% over the different SoC except at 20%, where the Pb-acid battery without the supercapacitors accepted more charge. The 5.21Ah Pb-acid battery connected to the supercapacitor was able to deliver additional charge of 2 and 85% over the different SoC. The 1Ah Li-ion pouch cell was seen to provide a more constant charge acceptance and delivery when connected to the supercapacitors over all the SoC. The information gained from these tests could also be factored into the battery management system when dealing with regenerative braking and possible use of this energy in auxiliary systems, or even for smoother power delivery.

CHAPTER 6:

Conclusion

During this study, electrochemical testing procedures were investigated in order to determine the capacity characteristics of various Li-ion cells under various simulated application conditions. One such test included a technique such as the Peukert test that was commonly used in characterizing Pb-acid cells. It was found to be a suitable technique in evaluating the discharge characteristics of Li-ion cells. These Li-ion cells are normally rated at a specific capacity at a certain discharge rate. This test demonstrated that it would be possible to determine the true capacity of a cell under certain discharge rates. The true capacity becomes important in accurately discharging the cells where their discharge voltage limits are not exceeded, especially if a set of cells with slightly different nominal capacities were connected in series to make up a battery that was then capacity cycled under various high rate conditions. The particular poorer cell in a battery pack would discharge to a lower DoD during discharge and could discharge below its cell voltage limits thereby causing irreversible cell damage. The long term effect of connecting cells with dissimilar true capacities would have a negative effect on the overall health and life cycle ability of the battery. The Peukert test also showed that the shape or geometry of the cell assembly played a role in how the temperature increased during high discharge rates.

Ragone tests of electrochemical cells looked at comparing the energy and power densities of different chemistry technologies. The Ragone tests were done by using constant current discharge and constant power discharge methods. There were slight differences in values of the measured power and energy densities of the different cells using the different discharge methods. The study showed that the Li-ion cells showed similar energy densities but different power densities due to different capacity rated cells. Differences in energy and power densities were seen when different chemistry cells were compared, i.e. the energy and power densities of the Pb-acid were lower in value in comparison to the Li-ion cells tested.

Accelerated simulated application testing included the capacity cycling of the Li-ion cells within different DoD window regions of a typical LiCoO₂ discharge voltage curve. Accelerated capacity life cycle testing is an important property of Li-ion cells

that are used in a variety of applications such as electric vehicles. Very little information was available to try and correlate a type of capacity cycling test with true calendar life of a battery in application. The different DoD window regions were determined according to the amount of stress that the cell may undergo when discharged only within those specified voltage regions. Electrochemical Impedance Spectroscopy (EIS) was successfully used to demonstrate that certain parameters of an EIS model would give an indication of the cells ageing as the cell was capacity cycled within these different DoD regions. Significant observations made during these tests showed that the larger 20Ah pouch cells had an increase in cell capacity during the initial 50 to 100 cycles. This increased capacity corresponded to a decrease in overall cell resistance. The 20Ah pouch cells were cycled for 13 months without significant cell capacity loss or increased cell impedance. The 20Ah cell was not subjected to a severe life cycle testing sequence but included a short recharge step at constant power. The testing sequence was modified to consider a harsher capacity cycling sequence within a certain cell voltage window that considered a continuous discharge to a voltage limit for 200 cycles. This ensured that any residual capacity within the active material would be fully depleted to the lower voltage limit, which resulted in a faster cell failure with significant changes in EIS measurements. An increase in cell impedance matched a decrease in cell capacity. A significant contributor to the cell impedance was shown to be due to an increase in resistance at the SEI layer at the anode.

It was determined that EIS analysis of the Li-ion cells was a sensitive enough technique to demonstrate that there are significant changes within the Li-ion cells impedance under different State of Charge (SoC) or temperature. The significant observations made during the SoC studies showed that the resistances within the cells gradually decreased as the SoC increased. This observation could be due to a reduction in the restriction of the Li-ions between the electrodes as the cell's charge increased. A gradual decrease in capacitance was also seen as the SoC decreased. The Warburg effect for all the cells showed a peak at 40% SoC, indicating an increase in time taken to diffuse through the Nernst Diffusion layer at both electrodes due to similarly charged electrodes. The observations made during the temperature studies of a fully charged cell showed that the cell resistance decreased as the cell's temperature increased. These decreases in resistance indicated that as the cell heated up, the Li-ions became more energized and were able to more freely move

between the electrodes. The cell capacitance however increased as the cell temperature increased. This observation could be due to increased energy within the cell. Both the 20Ah pouch and 2Ah cylindrical cells showed a linear relationship with the Warburg effect. As the temperature increased, so too did the time taken to diffuse through the Nernst Diffusion layer. This increase in time could be due to the amount of energy the Li-ions gained as the cell heated, which resulted in more collisions and longer time periods. The 1Ah pouch cell that was made by UWC showed an exponential relationship of the Warburg effect. The reason for the exponential relationship could be due to the thicker electrodes manufactured for this cell.

The study considered the use of supercapacitors that are connected in parallel with supercapacitors that would be subjected to high rate charge and discharge steps at different SoC. These high rate charge and discharge steps were similar to the work published by M. Fernández et al⁷³ that carried out the evaluation only on a VRLA Pb-acid battery. The results showed that a 2Ah LiCoO₂ cylindrical cell and the VRLA Pb-acid battery were not able to significantly accept or deliver more charge when connected to the supercapacitor. During the VRLA Pb-acid battery tests at 20% SoC, a larger charge acceptance was seen when using the battery alone. EIS studies were insufficient in determining the reason for this observation. A possible reason for this observation could be an increased resistance of the battery in combination with the supercapacitor at this specific SoC. A 1Ah LiMn₂O₄ pouch cell did show significant charge acceptance and delivery at all the SoC. These observations were explained by the EIS studies where a significant decrease in resistance and an increased capacitance of the cell and supercapacitor was seen in comparison to the cell alone. The reduction in resistance and increase in capacitance could be due to the thicker electrodes manufactured within this pouch cell. A 20Ah LiCoO₂ pouch cell was tested, however the cell without a supercapacitor was able to accept and deliver more charge than our instrumentation could control. The study did show that it is only slightly beneficial to use supercapacitors in parallel with Li-ion cells. There was no significant improvement in the charge acceptance of the cell with the capacitor, and that the small improvement in discharge ability was only evident at relatively higher SoC of the cells, below which the supercapacitor had no marked improvement.

Further studies could include connection of the Li-ion cells to the supercapacitors via an energy convertor such as a transistor or diode, which may lead to better voltage equalizing. The high rate charge and discharge step testing procedure would then be repeated on the new combination set-up.

References

1. Iran F. Machado, Silva F. De M. Figueirôa, 500 years of mining in Brazil: a brief review. *Resources Policy* **27** (2001) 9-24
2. Properties of Lithium. Retrieved 6 June 2011
<http://www.chemicool.com/elements/Lithium.html>
3. More properties of Lithium. Retrieved 6 June 2011
<http://www.lenntech.com/periodic/elements/li.html>
4. P. Kurzweil, Gaston Planté and his invention of the lead–acid battery—The genesis of the first practical rechargeable battery. *J. of Power Sources* **195** (2010) 4424-4434
5. The Rechargeable battery market 2008-2009, Avicenne March 2009
6. Colin A. Vincent, Lithium batteries: a 50-year perspective, 1959-2009. *Solid State Ionics* **134** (2000) 159-16
7. Y.P. Wua, C. Jianga, C. Wana, R. Holze, Modified natural graphite as anode material for lithium ion batteries. *J. of Power Sources* **111** (2002) 329-334
8. *Advances in Lithium-Ion Batteries*, W.A. van Schalkwijk and B. Scrosati. Published by Kluwer Academic/Plenum Publishers (2002) **Chapter 4** 135-155 **Chapter 5** 155-185 **Chapter 11** 309-345 **Chapter 13** 393-433
9. Yoshiaki Asami, Kenji Tsuchiya, Hiroyoshi Nose, Shintaro Suzuki, Kiyoto Mizushina, Development of coin-type lithium-ion rechargeable batteries. *J. of Power Sources* **54** (1995) 146-150
10. M.A. Fetcenko, S.R. Ovshinskya, B. Reichmana, K. Younga, C. Fierroa, J. Kocha, A. Zallena, W. Maysa and T. Ouchi, Recent advances in NiMH battery technology. *J. of Power Sources* **165** (2007) 544-551
11. *SECONDARY BATTERIES - LEAD- ACID SYSTEMS Automotive Batteries: Conventional*. E. Meissner. *Encyclopaedia of Electrochemical Power Sources*, pages 829-850
12. Bruno Scrosati, Jugen Garche, Lithium batteries: Status, prospect and future. *Journal of Power Sources Review* **195** (2010) 2419-2430
13. WG Pell, BE Conway, Quantitative modelling of factors determining Ragone plots for batteries and electrochemical capacitors. *J. of Power Sources* **63** (1996) 255-266
14. Electronic Design: Retrieved 10 August 2011

<http://electronicdesign.com/>

15. Ambuj D. Sagar, Automobiles and global warming: Alternative fuels and other options for carbon dioxide reduction. Environmental Impact Assessment Review **15** (1995) 241-274
16. Engineering Supercapacitor Storage Systems Tutorial. Presented by Dr. Roland Gallay from Garmanage at the AABC in Mainz, Germany, June 2011
17. Chemistry **Second Edition**, McMurray and Fay. Prentice Hall publishers. 1998. Pages 742
18. Jeffrey W. Fergus, Recent developments in cathode materials for lithium ion batteries. J. of Power Sources **195** (2010) 939-954
19. Hui Xie and Zhentao Zhou, Physical and electrochemical properties of mix-doped lithium iron phosphate as cathode material for lithium ion battery. Electrochimica Acta **51** (2006) 2063-2067
20. Background information and diagrams. Retrieved 15 August 2011.
<http://batteryuniversity.com>
21. J Li, E Murphy, J Winnick, PA Kohl, Studies on the cycle life of commercial lithium ion batteries during rapid charge-discharge cycling. Journal of Power Sources **102** (2001) 294–301.
22. Introduction into Lithium Battery Materials Tutorial. Presented by Prof Martin Winter from the University of Muenster at the AABC in Mainz, Germany, June 2011
23. Yujie Zhu, Chunsheng Wang, Strain accommodation and potential hysteresis of LiFePO₄ cathodes during lithium ion insertion/extraction. J. of Power Sources **196** (2011)1442-1448
24. Jae Hyun Lee, Hyang Mok Lee and Soonho Ahn, Battery dimensional changes occurring during charge/discharge cycles—thin rectangular lithium ion and polymer cells. J. of Power Sources **119-121** (2003) 833-837
25. A.F. Bower, P.R. Guduru and V.A. Sethuraman, A finite strain model of stress, diffusion, plastic flow, and electrochemical reactions in a lithium-ion half-cell. J. of Power Sources **59** (2011) 804 - 828
26. Jeffrey W. Fergus, Recent developments in cathode materials for lithium ion batteries. J. of Power Sources **195** (2010) 939-954

-
27. S. Albrecht, J. Kümpersb, M. Krufta, S. Malcusa, C. Voglerc, M. Wahlb and M. Wohlfahrt-Mehrens, Electrochemical and thermal behavior of aluminium- and magnesium-doped spherical lithium nickel cobalt mixed oxides $\text{Li}_{1-x}(\text{Ni}_{1-y-z}\text{Co}_y\text{M}_z)\text{O}_2$ (M = Al, Mg). J. of Power Sources **119-121** (2003) 178-183
 28. Mojtaba Mirzaeian, Peter J Hall, Characterizing capacity loss of lithium oxygen batteries by impedance spectroscopy. J. of Power Sources **195** (2010) 6817-6824
 29. Testing and Characterisation of Large High-Energy Lithium-Ion Batteries for Electric and Hybrid Electric Vehicle. Dennis Doerffel. PhD Thesis, University of SOUTHAMPTON, March 2007
 30. Colin A. Vincent, Lithium batteries: a 50-year perspective, 1959–2009. Solid State Ionics **134** (2000) 159-167
 31. J. Vetter, P. Novák, M.R. Wagner, C. Veit, K.-C. Möller, J.O. Bensenhard, M. Winter, M. Wohlfahrt-Mehrens, C. Vogler, A. Hammouche, Ageing Mechanisms in Lithium-ion batteries. Journal of Power Sources **147** (2005) 269-281
 32. Battery Performance Characteristics - How to specify and test a battery. Retrieved 22 July 2011.
<http://mpoweruk.com/performance.htm>
 33. Presentation by Walter A. Van Schalkwijk on Lithium-ion chemistry and Battery Management Systems – Cape Town, July 2010
 34. ELECTRIC VEHICLE BATTERY TEST PROCEDURES MANUAL Revision 2. Published January 1996
Advanced Technology Development Program For Lithium-Ion Batteries. Battery Technology Life Verification Test Manual. February 2005. Idaho National Laboratory Idaho Falls, ID 3415 Operated by Battelle Energy Alliance, LLC. FreedomCAR & Vehicle Technologies Program.
 35. R Spotnitz, Simulation of capacity fade in lithium-ion batteries. J. of Power Sources **113** (2003) 72-80
 36. Presentation by Dr. Shan Ji - Energy Storage for Fuel Cell Vehicles. HySA System Competence Centre 14th April 2010
 37. Discharge curve. Retrieved 30 June 2011.

<http://www.teslamotorsclub.com>

38. Peter Georén and Göran Lindbergh, On the use of voltammetric methods to determine electrochemical stability limits for lithium battery electrolytes. *J. of Power Sources* **124** (2003) 213-220
39. I Bloom, BW Cole, JJ Sohn, SA Jones, EG Polzin, VS Battaglia, GL Henriksen, C Motloch, R Richardson, T Unkelhaeuser, D Ingersoll, HL Case, An accelerated calendar and cycle life study of Li-ion cells. *J. of Power Sources* **101** (2001) 238-247
40. Battery Education. Retrieved 22 August 2011.
<http://pvcdrom.pveducation.org/BATTERY/charlead.htm>
41. M. Thele, J. Schiffer, E. Karden, E. Surewaard, D.U. Sauer, Modelling of the charge acceptance of lead-acid batteries. *J. of Power Sources*; **168** (2007) 31-39
42. Steven T. Mayer, Electric Vehicle Dynamic-Stress-Test Cycling Performance of Lithium-ion Cells. May 1994. Lawrence Livermore National Laboratory
43. Mattieu Dubarry, Bor Yann Liaw, Identify capacity fading mechanism in a commercial LiFePO₄ cell. *Journal of Power Sources* **194** (2009) 541-549
44. Pawan Sharma, TS Bhatti, A review on electrochemical double-layer capacitors. *Energy Conversion and Management* **51** (2010) 2901-2912
45. PSA group. Retrieved 15 June 2011.
<http://www.psa-peugeot-citroen.com>
46. Yong Zhang, Hui Feng, Xingbing Wu, Lizhen Wang, Aiqin Zhang, Tongchi Xia, Huichao Dong, Xiaofeng Li, Linsen Zhang, Progress of electrochemical capacitor electrode materials: A review. *International Journal of Hydrogen Energy* **34** (2009) 4889-4899
47. W. Peukert, *Elektrotechnische Zeitschrift* **20** (1997) 20–21
48. Kathryn Striebel, Joongpyo Shim¹, Azucena Sierra, Hui Yang, Xiangyun Song, Robert Kosteki and Kathryn McCarthy, The development of low cost LiFePO₄-based high power lithium-ion batteries. *J. of Power Sources* **146** (2005) 33-38
49. Anna M. Lackner, Elena Sherman, Paul O. Braatz and J. David Margerum, High performance plastic lithium-ion battery cells for hybrid vehicles. *J. of Power Sources* **104** (2002) 1-6

-
50. Dennis Doerffel, Suleiman Abu Sharkh, A critical review of using the Peukert equation for determining the remaining capacity of lead-acid and lithium-ion batteries. *J. of Power Sources* **155** (2006) 395 -400
 51. V. Yufit, N.P. Brandon, Development and application of an actively controlled hybrid proton exchange membrane fuel cell – Lithium-ion battery laboratory test-bed based on off-the-shelf components. *J. of Power Sources* **196** (2011) 801-807
 52. Dong Hyup Jeon and Seung Man Baek, Thermal modelling of cylindrical lithium ion battery during discharge cycle. *Energy Conversion and Management* **52** (2011) 2973 - 2981
 53. D. Ragone. *Prac. Soc. Automotive Engineers Conference*, Detroit, MI, USA, May 1968.
 54. Peter Van den Bossche a, Frédéric Vergels, Joeri Van Mierlo, Julien Matheys, Wout Van Autenboer, SUBAT: An assessment of sustainable battery technology. *Journal of Power Sources* (article in press) (2005)
 55. S.G. Stewart, V. Srinivasan, J.Newman, *J. of Electrochem Soc.* **155 A664** (2008)
 56. International Workshop on Distributed Energy Systems: The role of Chemical Sciences and Technologies. Milano 06/04/2009 conference.
 57. G Nagasubramanian, RG Jungst, Energy and power characteristics of the lithium-ion cells. *J. of Power Sources* **72** (1998) 189-193
 58. Andrew Chu, Paul Braatz, Comparison of commercial supercapacitors and high-power lithium-ion batteries for power-assist applications in hybrid electric vehicles I: Initial characterization. *J. of Power Sources* **112** (2002) 236-246
 59. Uwe Tröltzsch, Olfa Kanoun, Hans-Rolf Tränkler, Characterizing ageing effects of Lithium ion batteries by Impedance spectroscopy. *Electrochimica Acta* (2006) 1664-1672
 60. EIS conference PE, South Africa. Presentation by Dr Jacob Ketter, Gamry Instruments
 61. EIS conference PE, South Africa. Presentation by Martjin van Dyck, Metrohm Instruments

-
62. G. Palasantzas and G. M. E. A. Backx, Roughness effects on the double-layer charge capacitance: the case of Helmholtz layer induced roughness attenuation. *Surface Science* Volume **540**, (2003) 401-406
 63. Impedance Analysis Notes. By Prof Loyson, NMMU 2010
 64. Double layer Education. Retrieved 15 September 2011.
http://web.nmsu.edu/~snsm/classes/chem435/Lab14/double_layer.html
 65. Impedance Spectroscopy, Theory, Experiment and Applications. **Second Edition**. Edited by: E. Barsoukov and J.R. Macdonald. Published by: John Wiley and Sons Inc. In 2005
 66. Jeremy P. Meyers, Marc Doyle, Robert M. Darling and John Newman, The Impedance Response of a Porous Electrode Composed of Intercalation Particles. *J. of Electrochemical Society* **147** (8) 2930-2940 (2000)
 67. Gamry Instrument Application Notes for the basics of Electrochemical Impedance Spectroscopy. Retrieved 6 September 2011.
http://www.gamry.com/App_Notes/EIS_Primer/Basics_Of_%20EIS.pdf
 68. D. Andre, M. Meiler, K. Steiner, H. Walz, T. Soczka-Guth, D.U. Sauer, Characterization of high-power lithium-ion batteries by electrochemical impedance spectroscopy. I: Experimental investigation. *J. of Power Sources* **196** (2011) 5341-5348
 69. D. Andre, M. Meiler, K. Steiner, H. Walz, T. Soczka-Guth, D.U. Sauer, Characterization of high-power lithium-ion batteries by electrochemical impedance spectroscopy. II: Modelling. *J. of Power Sources* **196** (2011) 5356-5363
 70. Masayuki Itagaki, a, Nao Kobaria, Sachiko Yotsudaa, Kunihiro Watanabea, Shinichi Kinoshitab and Makoto Ue, In situ electrochemical impedance spectroscopy to investigate negative electrode of lithium-ion rechargeable batteries. *J. of Power Sources* **135** (2004) 255-261
 71. J Li, E Murphy, J Winnick, PA Kohl, Studies on the cycle life of commercial lithium ion batteries during rapid charge-discharge cycling. *J. of Power Journals* **102** (2001) 294-301
 72. Kazuhiko Takeno, Masahiro Ichimura, Kazuo Takano, Junichi Yamaki, Shigeto Okada, Quick testing of batteries in lithium-ion battery packs with impedance-measuring technology. *J. of Power Sources* **128** (2004) 67-75

-
73. M. Fernández, J. Valenciano, F. Trinidad, N. Muñoz, The use of activated carbon and graphite for the development of lead-acid batteries for Hybrid vehicle applications. *J. of Power Sources* **195** (2010) 4458-4469
 74. R.A. Dougal, Power and Life Extension of Battery-Ultracapacitor Hybrids. *IEEE Transactions on Components and Packaging Technologies* Vol. **25** no 1 March 2002
 75. Eric Wood, Marcus Alexander, Thomas H. Bradley, Investigation of battery end-of-life conditions for plug-in hybrid electric vehicles. *J. of Power Sources* **196** (2011) pages 5147-5154.
 76. M. Dubarry, Vojtech Svoboda, Ruey Hwu, Bor Yann Liaw, Capacity and power fading mechanism identification from a commercial cell evaluation. *J. of Power Sources*; **165** (2007) 566-572
 77. Entropy explanation. Retrieved 10 October 2011.
<http://www.thefreedictionary.com/entropy>
 78. Joule Heating explanation. Retrieved 10 October 2011.
<http://www.physics.isu.edu/~hackmart/spl1ejh.pdf>
 79. Battery and Energy Technologies. Retrieved 21 July 2011.
http://www.mpoweruk.com/cell_construction.htm
 80. Tomohiko Ikeyaa, Nobuyuki Sawadab, Sakae Takagic, Jun-ichi Murakamic, Kazuyuki Kobayashid, Tetsuya Sakabee, Eiichi Kousakaf, Haruki Yoshiokag, Satoru Katoh, Masanori Yamashitai, Hayato Narisokoj, Yuichi Mitaa, Kazuo Nishiyamak, Kazuyuki Adachil and Kaoru Ishiharaa, Multi-step constant-current charging method for electric vehicle, valve-regulated, lead/acid batteries during night time for load-levelling. *J. of Power Sources* **75** (1998) 101-107
 81. Kaushik Das, Aparesh Mondal, Discharge behaviour of electro-deposited lead and lead dioxide electrodes on carbon in aqueous sulfuric acid. *J. of Power Sources* **55** (1995) 251 - 254
 82. Personal communication with Professor Linkov of the University of the Western Cape.
 83. Gamry Instrument Technical Note: Quick check of EIS System Performance. Retrieved 2 October 2010

-
- <http://www.gamry.com/assets/Application-Notes/Quick-Check-of-EIS-System-Performance.pdf>
84. Gamry Instrument Application Notes: Testing Supercapacitors, Part 1 – CV, EIS and Leakage current. Retrieved 2 July 2011.
<http://www.gamry.com/assets/Application-Notes/Testing-Supercaps-Part-1.pdf>
 85. Gamry Instrument Application Notes for the basics of Electrochemical Impedance Spectroscopy. Retrieved 2 July 2011.
http://www.gamry.com/App_Notes/EIS_Primer/Basics_Of_%20EIS.pdf
 86. Electrochemical Impedance at a Rotated Disk Electrode. Gamry Instruments Manual. Retrieved 2 July 2011.
http://www.gamry.com/Newsletter/2005Feb/RDE_Impedance.htm
 87. Nernst Diffusion layer explanation. Retrieved 10 November 2010
<http://events.nace.org/library/corrosion/Kinetics/nernstdiffusion.asp>
 88. Capacitance and capacitors explanation. Retrieved 25 November 2010.
<http://physics.bu.edu/~duffy/py106/Capacitors.html>
 89. W.B. Gu, C.Y. Wang, Thermal-electrochemical coupled modelling of a Lithium-ion cell. GATE Centre for Advanced Energy Storage. Department of Mechanical Engineering & Pennsylvania Transportation Institute, The Pennsylvania State University, USA.
 90. Jamie Gomez, Ruben Nelson, Egwu E. Kalu, Mark H. Weatherspoon, Jim P. Zheng, Equivalent circuit model parameters of a high-power Li-ion battery: Thermal and state of Charge effects. J. of Power Sources (2011). Article in Press
 91. Personal communication with Dr Wim Fuls, Optimal Energy, Cape Town 2010.
 92. G. Nagasubramanian, R.G. Jungst, D.H. Doughty, Impedance, power, energy, and pulse performance characteristics of small commercial Li-ion cells. J. of Power Sources **83** (1999) 193-203.
 93. M.Broussely, S. Herreyre, P. Biensan, P. Kasztejna, K. Nechev, R.J. Staniewicz, Ageing mechanism in Li ion cells and calendar life predictions. J. of Power Sources **97-98** (2001) 13-21
 94. Godfrey Sikha and Branko N. Popov, Performance optimization of a battery–capacitor hybrid system. J. of Power Sources **134** (2004) 130-138

-
95. Phatiphat Thounthonga, Stephane Raëlb and Bernard Davat, Energy management of fuel cell/battery/supercapacitor hybrid power source for vehicle applications. J. of Power Sources **2206** (2009) 376-385
 96. The role of supercapacitors. <http://batteryuniversity.com>
 97. C.E Holland, J.W. Weidner, R.A. Dougal and R.E. White, Experimental characterization of Hybrid power systems under pulse current loads. J. of Power sources **109** (2002) 32-37
 98. Application Note: EIS on Primers by Gamry Instruments. Retrieved 10 October 2010.
http://www.gamry.com/App_Notes/EIS_Primer/EIS_Primer.htm
 99. Paul Bentley, David A. Stone, Nigel Schofield, The parallel combination of a VRLA cell and supercapacitor for use as a hybrid vehicle peak power buffer. J. of Power Sources **147** (2005) 288-294
 100. Basics of Lead-acid batteries. Retrieved 10 October 2011.
<http://rollsbatteryne.com/docs/A%20Sulfated%20Battery.pdf>
 101. K. Amine, J. Liu , S. Kang , I. Belharouak , Y. Hyung , D. Vissers and G. Henriksen, Improved lithium manganese oxide spinel/graphite Li-ion cells for high-power applications. J. of Power Sources **129** (2004) 14-19
 102. B. Frenzela, P. Kurzweil and H. Rönnebecka, Electromobility concept for racing cars based on lithium-ion batteries and supercapacitors. J. of Power Sources **196** (2011) 5364 - 5376